Downscaling large-scale ocean-basin solutions in coastal tri-dimensional hydrodynamic models

Guillaume Riflet
MARETEC IST

July 21, 2010

Abstract

The aim of this thesis is to evaluate the quality of open boundary conditions of regional Ocean models downscaled in large-scale Ocean basin solutions by calculating the Okubo-Weiss parameter, which qualifies the type of flow.

The scope of the open boundary conditions evaluation encompasses schematic test-cases as well as realistic regional Ocean models.

The test-cases consist in a gaussian elevation release, a freshwater cylinder, a schematic upwelling situation (to be implemented) and regional Ocean models of Western Iberia and the bay of Biscay, both forced with realistic conditions. A two-level, one-way nesting experiment was considered. The idea is to provide an unbounded reference solution to compare with the nested model and to provide adequate external forcing when required. A shallow waters equations numerical model was developed for the schematic experiments, whereas the hydrodynamic model, MOHID, was used for the regional applications.

It was found that systematic flow-type inversions tend to occur near the open boundaries, even in situations where the unbounded reference solution displays monotonic flow types at the same location. The Okubo-Weiss criterion is arguably found by this thesis to provide an objective measurement of the performance of the open-boundary condition.

The downscaling methodology applied to the regional applications yields robust results, capable of sustaining an operational system for regional Ocean forecasts.

ABSTRACT

Resumo

O objectivo da presente tese de doutoramento consiste em avaliar a qualidade das condições de fronteira aberta em modelos matemáticos de circulação oceânica regionais, aninhados em modelos globais. O parâmetro de Okubo-Weiss é proposto para identificar o tipo de escoamento.

O âmbito da avaliação das condições de fronteira aberta engloba casos de teste esquemáticos assim como aplicações realistas a regiões do Oceano.

Os casos de teste consistem na evolução duma elevação de nível gaussiana, dum cilíndro de água doce, numa situação de afloramento costeiro, e em aplicações à península Ibérica e à baía da Biscaia com forçamentos realistas. Uma experiência de aninhamento unidireccional de dois modelos foi concebida. A ideia consiste em garantir a existência duma solução de referência localmente sem fronteiras para permitir a comparação com a solução do modelo aninhado. Um modelo numérico das equações de águas rasas foi desenvolvido para implementar os casos de teste esquemáticos. O modelo hidrodinâmico MOHID foi utilizado para as aplicações regionais.

Foi descoberto que uma inversão sistemática do tipo de escoamento tende a occorer junto às fronteiras abertas, mesmo em situações quando a solução de referência apresenta, para a mesma região, um tipo de escoamento uniforme. É sugerido que o critério de Okubo-Weiss permite uma medida objectiva da performance da condição de fronteira aberta.

A metodologia de *downscaling* aplicada a modelos regionais ocêanicos retorna resultados robustos, capazes de suster um sistema operacional de previsão de correntes.

Keywords

- Regional Ocean model
- Open boundary condition
- Okubo-Weiss scalar
- Downscaling
- Numerical model
- Baroclinic hydrodynamical model

KEYWORDS

Palavras-chave

- Modelo regional do Oceano
- Condição de fronteira aberta
- Escalar de Okubo-Weiss
- Aninhamento
- Modelo numérico
- Modelo hidrodinâmico baroclínico

Acknowledgments

Here goes the list of credits for all the people that contributed, or inspired me in some way, during this thesis journey.

I would like to thank for the hospitality and the good working conditions provided by my thesis supervisor professor Ramiro Neves and for all the encouragement. I would also like to thank my thesis co-supervisor, doctor Paulo Chambel Leitão for being my mentor in MOHID.

I would like to thank professor Aires dos Santos for the many interesting discussions in geophysical fluids. I would like to thank professor Manuela Juliano of the University of the Azores for her collaboration and fruitful involvment with MOHID.

I would like to thank the team at Maretec and all their past members that I met and worked with. They are a fantastic group of persons with whom I spent pleasurably most of my time for the last five years.

I would like to thank the team at Hidromod. They are a dynamic, hard-working engineering company and I wish them the best of successes. I would also like to thank Frank Braunschweig, founder of ActionModelers and MOHID guru, for all his fundamental work on the MOHID GUI and MOHID GIS. I also wish his company the best of successes.

I would like to thank the team at Mercator-Océan for their professionalism and for their continuous support in providing real-time large-scale Ocean forecasts for western Iberia.

I would like to thank Guillaume Reffray and Mercator-Océan, for letting us collaborate in the regional modeling intercomparison for the bay of Biscay. The ferret scripts and the design of the experiments for the analysis of

the intercomparison are mostly his.

I would like to thank Rosa Trancoso and J. J. Delgado Domingos for their continuous support in providing real-time accurate atmospheric forcing. Without their effort the regional Ocean models wouldn't have been realistic.

I would like to thank Paulo Chambel and Rodrigo Fernandes for teaming up with me and make the bay of Biscay modeling a reality. Rodrigo, in particular, did all the hard work of running week after week the model and solving all the problematic bathymetric regions.

I would like to thank Paulo Chambel Leitão, for teaching me the downscaling methodology in regional Ocean modeling that he was the first to implement successfully in MOHID.

I would like to thank Luis Fernandes, for making a great Ocean forecasting system for western Iberia, PCOMS. His version is a lot less buggy and more elegant than mine, which was an early pre-operational prototype. Luis relieved me from the burden of having to monitor and maintain a very complex system and for that, I'm very grateful. I still provide him some support with the Thredds server and with some Linux tricks. I hope someday we'll see the PCOMS system acknowledged by society as a very useful and important tool.

I would like to thank João Nogueira for the geostrophic initialization implementation in MOHID.

I would like to thank Ângela Canas for all her work in the development of the MOHID tools, such as ConvertToHdf5, and her documentation in the MOHID wiki.

I would like to thank Ana Luísa Pinho for challenging me in developing a shallow waters model in Matlab, that she could use for her work. I later reused all the code and added diverse open boundary conditions. The shallow-waters Matlab code turned out to be a fundamental tool for the rapid prototyping of barotropic experiments and for the first tests on the Okubo-Weiss scalar.

I would like to acknowledge the privilege it was for me participating in

some of the bi-monthly geophysical fluid discussions organized by professor Juha Videman and professor Aires dos Santos. As they made me read with great depth Gill (1982) and Kundu and Cohen (2002), they expanded my horizons in geophysical fluids and proved to be very influential for most of the implemented schematic test-cases.

I would like to thank my wife, Alexandra Pimentel Riflet, for all her support and uncondicional love. She helped me a great deal with the editing and the typing of the document.

I would like to thank my parents for their unconditional support. I would also like to thank my family, my parents-in-law, my brother-in-law and my brother.

I would like to thank Nathalie Verelst, with whom I learned what mentoring meant, Pedro Almeida, with whom I learned many useful aplications in solid mechanics and hydraulics, and the students of the class of environmental modeling which helped me reach a next level of understanding of numerical modeling.

I would like to thank João Rodrigues for all the interesting conversations.

I would like to thank Jorge Cham and Randall Munroe, the authors of PhD Comics and XKCD, respectively, for their fantastic work and moral support.

I would like to thank Fundação para a Ciência e Tecnologia (FCT) through the Ph.D. grant SFRH/BD/17631/2004 and research projects.

I would also like to thank the following artists whose music made my days brighter while I was writing this thesis: Jeff Buckley, Nina Simone, Ella Jenkins, Leonard Cohen, Chico Buarque, Bob Dylan, Lou Reed, David Bowie, Queen, The Pink Floyd and Booker-T and the MGs.

I would like to thank all my friends.

Contents

Contents **xi**

List of figures **xvii**

List of tables **xxviii**

Nomenclature **xxxi**

1 Introduction **1**
1.1 The problem and the hypothesis 1
1.2 The background in numerical modeling of Oceans 2
1.3 The state-of-the-art in OBCs for regional oceanic models . . . 5
1.3.1 Relaxing type conditions 6
1.3.2 Radiative type conditions 7
1.3.3 Model adapted conditions 9
1.3.4 Overall appreciation 9
1.4 The planning 10

2 Fundamentals in geo-fluid physics and coastal physical processes **13**
2.1 Mathematical fundaments 13
2.1.1 The Fundamental Theorem of Calculus 14
2.1.2 Leibniz integration rule 15
2.1.3 Reynold's transport theorem: a deeper insight 16
2.2 Continuum medium 31
2.2.1 The continuity equation 32
2.2.2 The advection-diffusion equation 33
2.3 Fluid dynamics 39
2.4 Geofluid physics 41
2.4.1 The Primitive Ocean Equations 41

2.4.2 General Vertical coordinates 44
2.4.3 Energy equations 54
2.4.4 Mixing 61

3 Discretizing and modeling the physics of fluids 65
3.1 Implementing a 1D vertical model in MOHID 65
3.1.1 Preliminary results 67
3.1.2 Application to a test-case: PAPA station 72
3.1.3 Review of the state-of-the-art on static stability 81
3.1.4 The principle of Archimedes 82
3.1.5 The equivalence of the interpretation 86
3.1.6 Discussion 87
3.2 The freshwater cylinder test-case 88
3.2.1 Objectives 88
3.2.2 Description 88
3.2.3 Model setup 91
3.2.4 Battery tests 91
3.2.5 Results 95

4 Proposing a scalar to assess the influence of the open boundary condition 113
4.1 The scalar of Okubo-Weiss 113
4.1.1 A conserved quantity coined by Rossby as potential vorticity 113
4.1.2 Quantitative flow characterization 115
4.1.3 Qualitative flow characterization 117
4.2 Developing a shallow waters model in MATLAB 118
4.2.1 From the continuum to the discrete 118
4.2.2 Calculating the barotropic force 120
4.2.3 The mathematical model 126
4.2.4 The mesh 128
4.2.5 Boundary conditions 129
4.2.6 The numerical scheme 133
4.2.7 Validation 139
4.2.8 Appying the Okubo-Weiss scalar to assess the open-boundary condition 171
4.2.9 Conclusions 173

5 Application and assessment to real-world case studies 175
5.1 The continental Portuguese coast operational model 175
5.1.1 Introduction 175
5.1.2 Downscaling 176
5.1.3 Results 184
5.1.4 Conclusions 194
5.2 The bay of Biscay inter-comparison 194
5.2.1 Circulation and processes in the Bay of Biscay 194
5.2.2 Modelling strategies 202
5.2.3 Results comparison, validation and analysis 213
5.2.4 Conclusion 240

6 Conclusion 243

Bibliography 247

A Topics on geometry 263
A.1 The divergence theorem 263
A.1.1 Defining the problem 263
A.1.2 Defining the geometry 263
A.1.3 Calculating the flux of **E** through one elemental volume 264
A.1.4 Summing the infinitesimal elements of the open set . . 267
A.1.5 Summing up 269

Index 271

List of Figures

2.1 Representation of the control volumes V_A, V_B and V_C near time instant $t = t_0$ and their relative deformation rate of change, represented by the vector fields $\mathbf{v}_{A|B}$ and $\mathbf{v}_{B|C}$ over their control surfaces. On the left panel are represented volumes V_B and V_A at time instants $t = t_0$ and $t = t_0 + \delta t$ in a reference frame fixed in volume V_B. The deformation rate of change of V_A relative to V_B is represented by the vector field $\mathbf{v}_{A|B}$ at time instant $t = t_0$. On the right panel are represented volumes V_B and V_C at time instants $t = t_0$ and $t = t_0 - \delta t$ in a reference frame fixed in volume V_B. The deformation rate of change of V_B relative to V_C is represented by the vector field $\mathbf{v}_{B|C}$ at time instant $t = t_0 - \delta t$. 18

3.1 Ekman spiral projected along the U-component of velocity, under a constant wind forcing of 6 m/s, in a 30 layers and 30 meters depth domain. The arrows indicate the intensity and direction of the U-component of velocity. The color map indicate the velocity intensity. 70

3.2 The four topmost panels are profile timeseries of the velocity intensity for different test-cases of the same 30 layered model. The top left panel represents a monthly profile timeseries excluding the Coriolis force in the solved equations. The top right panel included the full one-dimensional equation but with constant vertical turbulent viscous coefficients for the same period. The middle left panel shows the same configuration but with the GOTM turbulent model. The middle right panel displays a zoom-in in time of the top-right panel, displaying a 2 day timeserie. The bottom panel displays the timeserie FFT frequency spectrum for the vertical model results with Coriolis force. 71

3.3 In the upper left panel: the temperature profile given by MOHID with pressure correction. In the upper right panel: the temperature profile given by GOTM v3 with pressure correction. In the lower left panel: the experimental data temperature profile. In the lower right panel: the SST given by GOTM, MOHID and in-situ data. All the isopleth are spaced of a half degree between the extrema of the color scale. 73

3.4 In the upper left panel: the accumulated heat integrated in the water column and the accumulation of heat exchanged at the surface. In the upper right panel: the X-Y scatter plots of accumulated heat of GOTM and MOHID versus the accumulation of heat exchanged at the surface. In the lower left panel: the relative difference in heat between MOHID and GOTM. In the lower right panel: the relative difference in heat of MOHID and GOTM with the surface exchange. . . 75

3.5 Evolution of the square of the Brünt-Vaisalla frequency in depth over time. Upper left panel: results from MOHID. Upper right panel: results from GOTM. Lower left panel: Differences of MOHID related to GOTM. In all the panels, the extrema values are beyond the range of the color scale. This is so in order to put in evidence the differences of patterns between the results. Extrema values are (0, ¿0.01) for the upper left panel; (-0.002, ¿0.008) in the upper right panel and (-0.01, ¿0.01) for the lower panel. The isopleth of the upper panels is set to 2E-4 s-2 and the isopleths of the lower panel are set to -8E-4 and 8E-4. 76

3.6 In the upper left panel: the temperature profile of MOHID without the pressure correction. In the upper right panel: the temperature profile of GOTM without the pressure correction. In the lower left panel: the temperature profile of in-situ data. In the lower right panel: the Sea Surface Temperature of MOHID, GOTM without the pressure correction and in-situ data. All isopleths spaced of half degree between the extrema of the color scale. 78

3.7 The square of the Brünt-Vaisalla frequency. In the upper left panel: the result of MOHID without the pressure correction. In the upper right panel: the result of GOTM without the pressure correction. The isopleth is of 2E-4 s-2. In the lower panel: the differences between MOHID and GOTM with isopleths of -1E-4 and 1E-4 s-2. 79

3.8 Illustration of an adiabatic and isohaline transformation of a seawater TMV, from a state of rest, to a perturbated state, away from equilibrium. The transformation is slow enough, so that compression forces have time to restore the pressure inside the TMV along the way. 85

3.9 freshwater cylinder, pressure gradient and gravity forces. . . . 89

3.10 Model results after 6 days run. The color scale represents the velocity intensity and the isohalines are spaced by 0.15. On the left panel is the test result with a time-step of 60s. On the right panel is the test result with a time-step of 300s. . . 96

3.11 Potential Energy, Kinetic Energy, Enstrophy and Salinity extrema for runs with several time increments of 60s, 150s and 300s. 97

3.12 Surface currents after 6 days of simulation. The colour scale maps velocity intensity. The vector field represents the velocity field. On the left panel, single precision results. On the right panel, double precision results. 97

3.13 Potential Energy, Kinetic Energy, Enstrophy and Salinity extrema for runs with single (pink) and double (blue) precision. 98

3.14 Surface currents after 6 days. Cartesian coordinates in the left panel and sigma coordinates in the right panel. 100

3.15 Surface currents after 6 days. No level radiation was implemented in the left panel. Flather level radiation was implemented in the right panel. 100

3.16 Potential Energy, Kinetic Energy, Enstrophy and Salinity extrema for runs with Cartesian, Sigma and Lagrangean w/o radiation coordinates. 101
3.17 Timeserie of the perturbation of initial mass, volume and level for runs with Cartesian, Sigma, Lagrangean (w/ FRS) and Lagrangean (w/ radiation) coordinates. 102
3.18 The top panels are showing surface currents. The bottom panels are showing 10 m depth currents. All results are shown after 6 days of simulation. The left panels display the uniform method to calculate the baroclinic force. The right panels display the linear method. 103
3.19 The top panels are showing surface currents. The bottom panels are showing 10 m depth currents. All results are shown after 6 days of simulation. The left panels display the Leibniz method to calculate the baroclinic force. The right panels display the Leibniz2 method. 104
3.20 Potential Energy, Kinetic Energy, Enstrophy and Salinity extrema for runs with uniform, linear, Leibniz or Leibniz 2 methods for calculating the horizontal density gradient. . . . 105
3.21 Surface currents and isohalines after 6 days run. Left panel, upwind first order scheme, right panel, upwind 2nd order scheme. 106
3.22 Surface currents and isohalines after 6 days run. Left panel, upwind third order scheme, right panel, TVD superbee scheme. 106
3.23 Surface currents and isohalines after 6 days run. Left panel, scheme equivalent to MU in Tartinville et al. (1998), right panel, scheme equivalent to DE in Tartinville et al. (1998). . 107
3.24 Surface currents and isohalines after 6 days run with a scheme equivalent to CL in Tartinville et al. (1998). 107
3.25 Potential Energy, Kinetic Energy, Enstrophy, Salinity extrema, total mass, total volume and level for runs of ID 1, 2, 3, 4, 5, 6 and 7 as described in table 3.2.4. 108
3.26 Potential Energy (in 10^9 J), Kinetic Energy (in 10^9 J), Enstrophy (in m^3/s^2), surface area with one percent less salinity than ambient value (in 10^8 m^2) and Salinity extrema (in psu). CL gets a circle; DE gets a square; IF gets a diamond; MU gets a triangle and PO gets a star. Courtesy of Tartinville et al. (1998) 109

4.1 Bi-dimensional cartesian elements of volume representing geometrical distortion through a) growth, b) spin, c) stretch and d) shear operations. The geometrical operation is performed by computing the integral circulation of the scalar product of the vector field (u, v) with the unit vectors represented in the figure. The Kelvin-Stokes theorem and the divergence theorem are easily derived in the particular respective cases of spin and growth. 124

4.2 Unidimensional equivalent of the Arakawa C staggered grid. Two T-cells on the left panel. One U-cell on the right panel. . 125

4.3 System depicted by the mathematical model. The reference level is indicated by a dash-dotted line. η is the water elevation from the reference level, d is the depth from the reference level and H is the total depth. The forces acting on the system are illustrated by vector arrows. g is the gravitational acceleration, τ_w is the wind stress, τ_b is the bottom stress and $\Omega \times \mathbf{v}$ is the Coriolis acceleration. 126

4.4 Arakawa C staggered grid patterns. From left to right: the T-cell, where η and H are evaluated at the centres, and u and v are evaluated at the eastern, western faces and southern, northern faces respectively. The U-cell where u is evaluated at the centre, η and H are evaluated at the eastern, western faces, and v is evaluated at the corners. The V-cell, where v is evaluated at the centre, η and H are evaluated at the southern, northern faces, and u is evaluated at the corners. The distance between two consecutive cells of the same type is Δx, zonally, and Δy, meridionally. The indices i and j correspond to the i-th zonal cell and the j-th meridional cell counted in the South-North direction and in the West-East direction respectively. 128

4.5 Detailed mesh emphasizing the boundaries. Composite of T, U and V-cells, the mesh illustrates the zone of integration of each type of cell: the blue rectangle contains the T-cells computed nodes, the thin green rectangle contains the U-cells computed nodes, the thin red rectangle contains the V-cells computed nodes. The thick green and red rectangles, however, delimit respectively the faces of the U and V-cells computed nodes. 131

4.6 The oscillatory motion of particles caused by wave propagation is characterized by the wave amplitude, h_0, and time period, $T = \frac{\lambda}{\sqrt{g\,(h_0+d)}}$. Their mean linear velocity is estimated to be $U = \frac{2\,\pi\,h_0}{T} = \frac{2\,\pi\,h_0\,\sqrt{g\,(h_0+d)}}{\lambda}$. 146
4.7 Gaussian elevation test-case energy time evolution in inviscid, frictionless conditions at initial instant. 148
4.8 Gaussian elevation test-case in inviscid, frictionless conditions at time instant 1.8×10^5 s. 148
4.9 Gaussian level velocity field in inviscid, frictionless conditions at time instant 1.8×10^5 s. 149
4.10 Time evolution of the volume. The boundaries are closed and the volume is conserved at $4.9 \times 10^1 2$ m^3. 150
4.11 Curl at instant 1.8×10^5 s. The order of magnitude of the extrema is roughly 10^{-7} s^{-1}. The curl is locally zero everywhere, except in a line near the boundary. Its integration yields zero nonetheless, as is confirmed by the global curl results. 150
4.12 Evolution with time of the global curl. Global curl is conserved, as expected. 151
4.13 Velocity modulus at instant 3500 s. The maximum velocity is estimated to be around 2×10^{-3} m s^{-1}. 153
4.14 Velocity modulus at instant 180000 s. The maximum velocity is estimated to be around 1×10^{-3} m s^{-1}. 154
4.15 Time evolution of the the u and v components of velocity integrated in the whole domain. The erratic behavior ranging 10^{-7} m^4 s^{-1} is strictly due to numerical errors. 154
4.16 Gaussian elevation test-case energy time evolution in inviscid, frictionless conditions for a 180000 s run. The energy decay is strictly due to numerical diffusion. 155
4.17 TE decay with time for several viscosities, ν, ranging from 0 to 5×10^4 m^2 s^{-1}. The horizontal line represents exactly one half of the initial energy. 156
4.18 Dependence of the total energy half-life with viscosity. The viscosity axis is logarithmic. The initial energy of the gaussian bump was 2.86×10^9 J. Three regions are separated by the vertical dashed lines: the low viscosity region for $0 < \nu < 2 \times 10^2$ m^2 s^{-1}, the transition region for $2 \times 10^2 < \nu < 2 \times 10^3$ m^2 s^{-1} and the high viscosity region for $2 \times 10^3 < \nu < 10^5$ m^2 s^{-1}. 158

4.19 Evolution of $\frac{TE}{TE_0}$ with $t^\star$ for several values of σ and for a value of $\nu = 5000$ m^2 s^{-1}. The several time-series with the same ν show a perfect overlap. $t^\star = 1$ is equal to T_σ, the characteristic time of dissipation proposed in equation 4.49. . 160

4.20 Gaussian elevation test-case energy time evolution with $\sigma =$ 60 km and with $\nu = 5000$ m^2 s^{-1}. The TKE summed with the TE returns a near constant value as expected, proving that the TKE model accurately reproduces the loss in KE by viscous forces. 161

4.21 Domain volume evolution in time. The transient perturbation in the volume occurs when the gravity wave reaches the OB while making its exit. The final volume is slightly less than the original volume, as the gaussian bump exits the domain. The volume difference is roughly of the order of $\sim 10^8$ m^3. . . 163

4.22 Mechanical, kinetic and potential energy evolution with time. When the gravity wave reaches the boundary, the energy, which was concentrated in the wave wake, exits the domain. . 164

4.23 Domain volume evolution in time. The transient perturbation in the volume occurs when the gravity wave reaches the OB while making its exit. The final volume oscillates and is slightly above the original volume, as the gaussian bump exits the domain. The volume difference is roughly of the order of $\sim 10^7$ m^3. 167

4.24 Mechanical, kinetic and potential energy evolution with time. When the gravity wave reaches the boundary, part of the total energy, (the part concentrated in the wave wake,) exits the domain. The remnant part is distributed half in potential energy and half in kinetic energy to form the geostrophic (stationary) equilibrium of water elevation with currents. . . 168

4.25 Okubo-Weiss field of the geostrophic balance, after the gravity wave exited the domain. The central eddy signature is defined by the negative OW, surrounded by positive OW at the edges. 169

4.26 Adjustement of a gaussian elevation in a rotating domain. Left panels display the gravity wave elevation and right panels display the flow velocity field. a) The top panels show the transient state of the system shortly after the initial gaussian elevation was released and before the gravity wave front arrive at the boundaries. b) The middle panels show the gravity wave front crossing the boundaries and the instauration of the central eddy evolving towards geostrophic equilibrium. c) The bottom panels show the geostrophic equilibrium, well after the gravity wave front was radiated at the boundaries. . 170

4.27 Contour plots of the Okubo-Weiss scalar for the same region. On the left panel, the large domains result. On the right panel, the small domain results. Positive OW contours are dashed and represent hyperbolic flow. Negative OW contours are solid and represent elliptic flow. The null-OW contour is the thick solid line and marks the transition from hyperbolic to elliptic flow. 172

5.1 On the left panel, the Western Iberia coast baroclinic model bathymetry. The domain is labeled *P*. Bounded by $[-12.6^\circ$ $-5.5^\circ]$ W $\times$ $[34.4^\circ$ $45.0^\circ]$N. 0.06° spatial resolution. On the right panel, Portugal continental central regional coastal model bathymetry, labeled *C*. Bounded by $[-11.2^\circ$ $-8.8^\circ]$W $\times$ $[40.3^\circ$ $37.5^\circ]$N. 0.02° spatial resolution. Baseline data from ETOPO $2'$(Etopo, 1988) on both panels. 178

5.2 To the left, the interpolated temperature fields of the *M-O* solution. To the right, the superposition of the temperature fields of the *C* model over the *P* model. The temperature scale's interval is $[14.5$ $20.0]^\circ C$ at the surface (top) and $[12.0$ $14.7]^\circ C$ at 250 m (bottom). The graphical tool is Mohid GIS. 185

5.3 Horizontal distribution of velocity ensemble average at 2 m depth for the top panel and 645 m depth for the bottom panel. Two main branches of the MW spreading pathways are well pronounced in the bottom panel: the poleward slope current branch, and the cyclonic recirculation flowing southward. . . 186

5.4 On the left panel, ensemble averages of salinity contours of [35.5, 35.52, 35.83, 35.94, 36.05, 36.16, 36.27, 36.38, 36.49, 36.6] and color maps in the interval [35.5 36.6]. On the right panel, ensemble averages of zonal velocity contours of [-.15, -.12, -.09, -.06, -.03, .0, .03, .06, .09, .12, .15] m s^{-1} and color maps in the interval [-.15 .15] m s^{-1}. The plots are meridional sections in the Gulf of Cádiz at longitudes 7.23 °W, 7.83 °W and 8.73 °W from top to bottom, respectively. They show how the MO shifts from a bottom current to a buoyancy driven intermediate depth jet current. 188

5.5 On the top panels, ensemble averages of meridional velocity contours of 0.1 $m\,s^{-1}$ apart and color maps in the interval $[-.1\ .1]$ $m\,s^{-1}$ are shown. Positive velocities are equatorward and negative velocities are poleward. On the middle panels, ensemble averages of salinity contours of [35.6, 35.66, 35.72, 35.78, 35.84, 35.90, 35.96, 36.02, 36.08, 36.14, 36.2] and color maps in the interval [35.6 36.2] are shown. On the bottom panels, ensemble averages of temperature isocontours of 1°C apart and color maps in the interval [6 16]°C are shown. The plots are zonal sections off the Portuguese coast at latitudes 38.25 °N, for the left panel; and 40.95 °N, for the right panel. 189

5.6 Color map and contours of salinity distribution ensemble average at 1000 m depth ranging in interval [35.6 36.2] showing the spreading pathway of the MO off western Iberia. Contour lines are valued [35.6, 35.78, 35.84, 35.9, 35.96, 36.02, 36.08, 36.14, 36.2]. 191

5.7 The Mercator solution sea surface temperature daily average on the September 9th 2006, at the bottom left. A NOAA sea surface temperature satellite image taken during the same day, at the top. At the bottom right, the Mohid instantaneous solution taken the same day at 19h00 hours. The temperature scale is set to [17°C 22°C]. However, the color palettes differs between the satellite images and the model's fields. The graphical tool used is *Mohid GIS*. 193

5.8 Proposed circulation pattern of the Atlantic Ocean in the northern hemisphere of the earth. The circle represents the Bay of Biscay region. 195

5.9 The Ushant front as described in the literature. A homogeneous water column (in light blue) separating, at the surface, stratified warmer waters in the inner shelf and in the outer-shelf (red). 200
5.10 Upwelling regions in the Bay of Biscay in blue. Warmpool region, with weak winds, in red. 201
5.11 The cold water mass in the Bay of Biscay in deep blue. Seasonal stratified surface waters in red. Well mixed water column in light blue. 202
5.12 Original bathymetry used for the intercomparison. 205
5.13 Bias of temperature (left panel) and salinity (right panels) profiles between PSY2V1 and IFREMER climatology, during 2004. 208
5.14 PSY2V1 TS diagram in the Bay of Biscay. Left, 01/01/2004 diagram (initial condition for the regional models). Right, 2004 annual mean diagram. The red curves represent the climatology minima and maxima. 209
5.15 Adour, Loire and Garonne rivers daily flow used to simulate year 2004. 211
5.16 Temperature (left panels) and salinity (right panels) differences between each model and PSY2V1. The top panels display the difference in temperature and salinity between NEMO-OPA and PSY2V1, whereas the bottom panels display the difference between MOHID and PSY2V1. 214
5.17 TS diagrams of each model. The left panels represent the initial condition. The right panels represent the annual mean. The red contours are the TS minima and maxima from the PSY2V1 reference solution. The top panels represent the results of NEMO-OPA. The bottom panels represent the results of MOHID. 215
5.18 Thermal (left panel) and haline (right panel) balance normalized to the initial value obtained for each model. The climatology is also represented. 217
5.19 SST bias of NEMO-OPA and MOHID relatively to monthly MODIS images. Left panel, bias in the whole region. Right panel, bias in the Ushant area (6°W to 4°W and 47.5°N to 49°N). 218
5.20 Yearly average tide-removed EKE and velocity fields during 2004 at 15 m depth. Top left panel, PSY2V1. Top right panel, NEMO-OPA. Bottom panel, MOHID. 220

5.21 Buoys (left panel) and tidal stations (right panel) positions. . 222

5.22 Comparison of SST time series between data from the Cherbourg buoy (black line), model results without tide (red line), and model results with tide (blue line). Black dots represent data from cloud-free MODIS images. Left panel, NEMO-OPA. Right panel, MOHID. 223

5.23 Comparison of SST time series between data from the Minquiers buoy (black line), model results without tide (red line), and model results with tide (blue line). Black dots represent data from cloud-free MODIS images. Left panel, NEMO-OPA. Right panel, MOHID. 223

5.24 SST MODIS comparison with the models NEMO-OPA and MOHID for the June 15th. Top-left panel, MODIS image. Top-right panel, NEMO-OPA model. Bottom panel, MOHID model. 228

5.25 SST MODIS comparison with the models NEMO-OPA and MOHID for the June 15th. Top-left panel, MODIS image. Top-right panel, NEMO-OPA model. Bottom panel, MOHID model. The SST average difference between the models and MODIS was removed. 229

5.26 June 3rd event in the Ushant area. Top panels: MODIS and litterature data. Middle panels: NEMO-OPA results. Bottom panels: MOHID results. Left panels: SST. Center panels: SST with the average difference with MODIS removed. Right panels: Cross-section at 48.2°N, between 6°W and 4°W. . . . 231

5.27 July 6th event in the Ushant area. Top panels: MODIS and litterature data. Middle panels: NEMO-OPA results. Bottom panels: MOHID results. Left panels: SST. Center panels: SST with the average difference with MODIS removed. Right panels: Cross-section at 48.2°N, between 6°W and 4°W. . . . 232

5.28 Hovmuller diagrams of the temperature offset relatively to the minimal temperature found along the Ushant section (6°W to 4°W at 48.15°N), of the MODIS SST (leftmost panels) and the models SST (middle panel and rightmost panel). 233

5.29 left panel: Minimum SST evolution of the Ushant section section (6°W to 4°W at 48.15°N). Right panel: Position evolution of the SST minimum in the Ushant section (right panel).233

5.30 Cross-section from 46ºN, 4ºW to 47.2ºN, 2.8ºW of the la Vasière cold water mass during August. Temperature comparison between literature (top left), climatology (top right) and the models (bottom). 235
5.31 Cross-section from 46.5ºN, 5ºW to 47.6ºN, 3ºW of the la Vasière cold water mass during PELGAS campaign. Temperature comparison between PELGAS (top left), NEMO-OPA (top right) and MOHID (bottom). 236
5.32 Cross-section from 46.3ºN, 4.4ºW to 47.1ºN, 2.4ºW of the la Vasière cold water mass during EVHOE campaign. Temperature comparison between EVHOE (top left), NEMO-OPA (top right) and MOHID (bottom). 237
5.33 Upwelling indexes measured and modelled by NEMO-OPA (top panels) and MOHID (bottom panels) at latitudes 44°N (left), 44.5°N (center) and 45°N (right) between May and September. Superposed are the results from NAR (square), NEVIRI (triangle), MODIS (cross) and MODIS Acqua (vertical cross) satelitte SST imagery. 238
5.34 Comparing MODIS warmpool (grey area) with the models (red contour and temperature colour scale) NEMO-OPA (left) and MOHId (right) between the 20th and the 30th August. . 239
5.35 Time evolution of the number of cells (vertical axis on the left) defining the warmpool by MODIS (blue line) and by the models (black line). The blue squares stand for the cloud-free area percentage (vertical axis on the right). NEMO-OPA results are on the left panel and MOHID results are on the right panel. 240
5.36 Average temperature comparison between MODIS (red) and the models (black) NEMO-OPA (left panel) and MOHID (right panel) in the area bounded by 4°W and 1°W and by 43.5N and 45N. The error bars (in red) are proportional to the cloud-coverage percentage for the area. 241

A.1 Cartesian element of volume $\Delta\Omega$ of width, length and height of Δx, Δy and Δz, respectively. The local uniform vector field $\mathbf{E}$ is represented in the volume's center of coordinates $P = (P_i, P_j, P_k)$. 264

List of Tables

3.1 Description of the model setup 92

3.2 Battery of time increment tests 93

3.3 Battery of precision tests 94

3.4 Battery of vertical discretizations tests 94

3.5 Battery of pressure gradient error tests (Sigma mesh only) . . 94

3.6 Battery of advection schemes tests. The first number is the advection scheme ID. The second number (optional) is the ID of the TVD type of scheme. Both numbers seen in table 3.2.4 94

3.7 ID numbers of advection schemes and of TVD schemes (variants of the TVD). 95

3.8 Numerical models and their advection schemes, as tested by Tartinville et al. (1998). 95

3.9 Optimal numerical parameters summary 100

3.10 Integrated quantities averaged in time over the last two-hundred iterations with a time-step of 300 s. 112

4.1 Configuration of the model for a non-rotating fluid with a gaussian initial elevation. 147

4.2 Configuration of the model for a non-rotating fluid with a gaussian initial elevation and with open boundaries. 162

4.3 Configuration of the model for a rotating fluid with a gaussian initial elevation and with open boundaries. 166

4.4 Configuration of the models for a non-rotating fluid with a gaussian initial elevation and with open boundaries. 172

5.1 Nested models boundary conditions. The abbreviations definitions are: Zonal and meridional velocity components (U, V), potential temperature (T) and salinity (S), water level relative to a reference level (η), flow relaxation scheme (FRS), Mercator-Océan solution(M-O), western Iberia barotropic model (WI), portuguese Iberian coastal model(P), Estremadura promontory model (C). 177
5.2 Nested models' initial conditions, assimilations and spin-up. The abbreviations definitions are: Zonal and meridional velocity components (U, V), potential temperature (T) and salinity (S), water level relative to a reference level (η), flow relaxation scheme (FRS), modèles de Mercator-Océan (M-O), western Iberia barotropic model (WI), portuguese Iberian coastal model(P), Estremadura promontory model (C). . . . 179
5.3 Water masses in the North-eastern Atlantic Ocean. 196
5.4 Description of the models used in the intercomparison 204
5.5 Bathymetry filtering method for NEMO-OPA and MOHID . 206
5.6 Numerical OBC schemes. 210
5.7 Initialization methods used in NEMO-OPA and in MOHID. . 212
5.8 Statistical comparison in temperature between the models and the Brittany buoy. 224
5.9 Statistical comparison in temperature between the models and the Cabo Penhas buoy. 224
5.10 Statistical comparison in temperature between the models and the Cherbourg buoy. 225
5.11 Statistical comparison in temperature between the models and the Estacabares buoy. 225
5.12 Statistical comparison in temperature between the models and the Gascogne buoy. 226
5.13 Statistical comparison in temperature between the models and the Minquiers buoy. 226
5.14 Statistical comparison in temperature between the models and the Ushant buoy. 227
5.15 Statistical comparison in temperature between the models and the Villano-Sisargas buoy. 227

Nomenclature

$(\tilde{t},\ \tilde{x},\ \tilde{y},\ \tilde{z})$ Space-time coordinates in a generalized vertical coordinates frame of reference, page 45

(u_g, v_g) Coordinate cartesian components of the geostrophic velocity, page 165

$(x,\ y,\ z)$ Coordinate components of position in a cartesian reference frame, page 41

$\alpha,\ \beta$ Thermal and haline contraction coefficients, respectively, page 82

Δx Space step or cell width along the x-axis, page 120

Δy Space step or cell width along the y-axis, page 120

$\frac{D}{Dt}$ Material derivative operator, page 27

ϵ Internal dissipation rate of kinetic energy (by action of viscous forces), page 57

η Sea-level free surface, page 41

$\frac{d}{dt}$ Time derivative, page 16

Γ Adiabatic lapse rate, page 82

γ Robert-Asselin filter parameter, page 137

ι Specific internal energy, page 60

κ Specific kinetic energy, page 57

$\kappa = 0.4$ von Karman constant, page 44

$\left(\frac{\partial}{\partial t},\ \frac{\partial}{\partial x},\ \frac{\partial}{\partial y},\ \frac{\partial}{\partial z}\right)$ Coordinate partial derivatives operators in cartesian reference frame, page 41

$\left(\tau_b^x,\, \tau_b^y\right)$ Coordinate components of bottom stress, page 43

$(\tau_s^x,\, \tau_s^y)$ Coordinate components of surface stress, page 43

$(u,\, v,\, w)$ Coordinate components of velocity in a cartesian inertial reference frame, page 40

$(u_{10m},\, v_{10m})$ Wind speed horizontal components at 10 m height, page 43

$(u_b,\, v_b)$ Bottom velocities components at the depth of the grid point nearest to the bottom, page 44

ζ Velocity curl, page 114

$\mathbf{F_{rad}}$ Radiative flow, page 59

$\mathbf{n}$ Outward normal vector to a manifold, page 15

$\mathbf{p}$ Coordinate point in $\mathbb{R}^3$ or $\mathbb{R}^n$ according to context, page 16

$\partial\mathcal{M}$ The boundary of $\mathcal{M}$, page 14

$\mathcal{M}$ An oriented differentiable manifold, page 14

d The exterior derivative, page 14

μ Specific entropy, page 59

$\nabla\cdot$ Divergence operator, page 15

$\nabla\times$ Curl operator, page 15

∇ Gradient operator, page 15

ν Molecular viscosity, page 62

ω A generic differential form, page 14

$\overline{f}$ Average of function f over an interval or a volume domain, page 26

π Specific potential gravitational energy, page 58

ψ A transformation of coordinates and its dual transformation, page 45

ρ density, page 32

$\tilde{\rho}$ TMV density, page 83

$\sharp, \flat$ Musical isomorphisms, page 15

σ Sigma vertical coordinate, page 46

$\star$ Hodge star operator, page 15

$\tau_{1/2}$ Half-life, page 156

Fr Froude adimensional number, page 142

θ Potential temperature, page 59

υ_H Horizontal viscosity coefficient, page 42

υ_t Vertical viscosity coefficient, page 41

ϱ Specific total energy, page 61

$\mathbf{v}$ Velocity vector, page 17

b Buoyancy, page 41

c Gravity waves celerity, page 142

C_a Air drag coefficient, page 43

C_D Bottom drag coefficient, page 44

C_p Heat capacity of sea-water, page 43

c_p Specific heat at constant pressure, page 59

D_E Ekman depth, page 69

e Internal energy per unit mass, page 59

F The primitive of f, page 14

f A real integrable and differentiable function, page 14

f Local Coriolis acceleration coefficient, page 41

g Gravitational acceleration of the local vertical, page 41

H Height from the reference gravitational equipotential to the bottom, page 41

I Internal energy, page 58

K Fick's law diffusion coefficient, page 34

K Kinetic energy, page 58

k Thermal conductivity, page 59

K_H Horizontal turbulent diffusivity coefficients, page 42

K_t Vertical turbulent diffusivity coefficients, page 42

M Atomic mass, page 32

m Mass, page 40

m_s Specific mass, page 32

m_T Land mask, page 129

m_U and m_V Null-fluxes masks, page 129

N Brunt-vaisalla frequency, page 82

N Number of particles in a control volume, page 31

P Potencial gravitational energy, page 58

P fluid property concentration, page 34

p Pressure relative to reference atmospheric pressure, page 41

p_r Reference pressure, page 59

p_{atm} Atmospheric pressure at sea-surface, page 41

Q Potential vorticity, page 115

Q_H Net heat transfer at the water-air interface, page 42

S Salinity, page 40

S_{ss} Salinity source term, page 42

Sc Source term in the advection-diffusion equation, page 34

Sk Sink term in the advection-diffusion equation, page 34

T Potential temperature, page 42

t time coordinate, page 18

T_σ Characteristic dissipation time of a gaussian bump of isotropic width given by σ, page 145

T_f Relaxation Time, page 6

T_{ss} Temperature source term, page 42

TE Total energy, page 58

U Characteristic velocity of the flow, page 142

u^i Represents any component of velocity, page 57

$u^{\hat{k}}$ Represents the horizontal components of velocity, page 57

V Volume of $\mathbb{R}^3$ or $\mathbb{R}^n$ according to context, page 16

v_s Specific volume, page 32

W Okubo-Weiss parameter, page 118

z_0 Bottom characteristic roughness length, page 44

ADI Alternate Direction Implicit, page 202

ALADIN Aire Limitée Adaptation Dynamique Développement International, page 206

BC Boundary Condition, page 120

CFD Computational Fluid Dynamics, page 3

CFL Courant-Friedrich-Levy stability criterion (Courant et al., 1959), page 138

CTCS Centered in Time and Centred in Space, page 133

EOS Equation Of State, page 4

ETOPO Electronic TOPOgraphic maps, page 203

FD Finite Difference, page 119

FFT Fast Fourier Transform, page 69

FLA Flather radiation condition, page 162

FRS Flow Relaxation Scheme, page 6

GOTM General Ocean Turbulence Model, page 66

GWE Gravity Wave Explicit radiation condition, page 162

HYCOM Hybrid Coordinate Ocean Model, page 4

IC Initial Condition, page 120

IFREMER Institut Français de Recherche pour l'Exploitation de la MER, page 208

LHS Left-hand side, page 17

MODIS MODerate resolution Imaging Spectro-radiometer, page 216

MOHID MOdelo HIDrodinâmico, page 67

MOM Modular Ocean Model, page 82

NEMO Nucleus for European Modelling of the Ocean, page 203

NERC Natural Environment Research Council, page 203

NVIE Normal Velocity Inside the Elevation Node, page 132

NVOE Normal Velocity Outside of the Elevation Node, page 130

OB Open Boundary, page 7

OBC Open Boundary Condition, page 2

OGCM Ocean General Circulation Model, page 209

OPA Ocean PArallel model, page 203

PAPA One of the oldest oceanic station situated in the Pacific ocean at 50°N, 145°W, page 67

PDE Partial Difference Equation, page 3

PML Perfectly Matched Layer, page 7

POM Princeton Ocean Model, page 87

PRM Polarization Relation Method, page 9

PSY2V1 System name of the Mercator-Océan operational forecasting solution of the north-Atlantic ocean basin, page 208

RHS Right-hand side, page 17

ROFI RegiOn of Freshwater Influence, page 66

ROMS Regional Ocean Modeling System, page 4

SHOM Service Hydrographique et Océanographique de la Marine, page 203

SST Sea Surface Temperature, page 72

SWE Shallow Waters Equations, page 120

TKE Turbulent Kinetic Energy, page 144

TMV Test Material Volume, page 82

TVD Total Variation Diminishing, page 93

UKMO UK Met Office, page 203

MOG2D Modèle d'Ondes de Gravité 2D, page 207

Chapter 1

Introduction

1.1 The problem and the hypothesis

Implementing regional Ocean applications, designed to model coastal and estuarine systems, usually downscaled in larger-scale Ocean basin solutions, always causes considerable challenges to the modeller when it comes to choose (and implement) an adequate open boundary condition. On the one hand, there is the need to let perturbations generated within the solution to leave the domain unperturbed. On the other hand, the realism of the solution depends on the presence of physical processes that are generated at scales of length and time far beyond and below the scales possibly resolved by the regional numerical model. Thus there is the need to provide to the regional model with exterior, accurate information in order to ensure the existence of the externally generated physical processes and features, and in order for the solution developed within the regional model to be realistic. In the latter case, several mathematical models that solve the turbulent equations of motion were put forward based on the hypothesis of Reynolds (Boussinesq, 1877; Reynolds, 1895), and later by Prandtl (1931) and Kolmogorov (1942, 1962). However, despite substantial positive experimental results corroborating the latter hypothesis, the scientific field of turbulence and ocean turbulence in general is still an open and unsolved problem of physics in this twenty-first century. In the former case (the physical processes of the larger scales), the solution is deterministically solved by the equations of motion as a boundary value problem. The problem lies in implementing the mapping of information from the large scale model to the regional scale model. There is now a considerable family of different types of open boundary conditions. Each performing better than the others under well-defined circumstances.

The challenge lies in choosing the correct ones. Poorly chosen open boundary conditions (OBC) could return worse results than a closed wall at the sytem. Thus, which OBC to choose from? This is the biggest question each modeler must consider, for each new system he considers.

The aim of this thesis is to assess the performance of OBC of regional ocean models downscaled in large-scale Ocean basin solutions, under the hypothesis that there must exist some scalar diagnostic quantity that can qualify the type of flow locally (hyperbolic, elliptic), and that this quantity should be a guide in helping to measure the negative effects of the open boundary condition on the local flow. The quantity put forward to this aim by this thesis was independently found by Okubo (1970) and Weiss (1991), and it is sometimes referred in the literature (Zavala Sanson and Sheinbaum, 2008; Isern-Fontanet et al., 2004; Lapeyre et al., 2001; Hua and Klein, 1998; Basdevant and Philipovitch, 1994) as the function, or parameter, of Okubo-Weiss. The global objective is to have a practical tool, objectively capable of classifying the nature of the flow, and to design experimentations that guide the modeller in the process of identifying where does the implemented OBC yields undesired results and, if possible, by how much.

Another aspect of this thesis, concerning the downscaling of large-scale Ocean basin solutions in regional models, is to propose a consistent methodology capable of yielding realistic results for any regional domain of application, provided the input of a large-scale solution, a realistic atmospheric forcing and a data flow from the major rivers.

1.2 The background in numerical modeling of Oceans

Numerical models are a fundamental tool to study the behavior of plausible solutions to the equations that describe the motion of fluids. Historically, to better understand the complex physics of fluids, approximate solutions to simplified forms of the equations of motion of momentum and of continuity were considered. The simplified equations would yield only the dominant terms in the general non-linear equations of motion, each depending on the type of system in study. The richness and diversity in the predominant type of forces acting on fluids, from the gravitacional force to the capillary force, make the complete equations of motion a very complex and challenging system to study. For some of these systems, sometimes, but very few times, an analytical solution is found. But very often the solution is quite simple and doesn't represent the complex flows we are accustomed to view in nature, in the rivers, in the atmosphere or in the seas.

However, even if many processes can be studied with simplified versions of the equations of motion, modeling the full hydrodynamics of coastal and estuarine systems requires the use of the primitive Ocean equations, which consist of the full three-dimensional Navier-Stokes equations in a rotating reference frame. Granted, the validity of the hydrostatic approximation and the near-incompressible hypothesis help a great deal in simplifying the full Navier-Stokes equations. But still, a very rich and complex range of processes lies within the primitive Ocean equations. A numerical approach in solving the non-linear equations of motion is often tempting, and many numerical algorithms were implemented to solve partial difference equations (PDE) in the past century, accompanying the advances of modern computing. One of the first scientific fields where the first modern calculators were dedicated, was the field of meteorology, for the sheer sake of its usefulness. Richardson was one of the first person to imagine such a machine capable of predicting the state of the weather in the late nineteenth century by means of a finite-differencing scheme, at a time when a computer was a person that performed calculations for a living. However, little could he imagine at the time that the discretized equations of continuum fields would yield more often divergent solutions rather than convergent ones. Little could he imagine the richness of convergent solutions from numerical models that are unrealistic.

Since the late nineteenth century, many numerical algorithms based on the finite-differences (Courant et al., 1959) were implemented, and many practicalities were tackled, solved and, if not completely solved, properly identified and classified. Just to mention a few, the long term stable integration of PDE numerical solvers (Arakawa, 1966) and the pressure-gradient error in topography following Ocean models (Beckmann and Haidvogel, 1993) were some issues identified that are not yet completely solved. Another class of approach at solving PDE with numerical models are the finite-elements methods. Even if finite-elements are in a rising trend in computational fluid dynamics (CFD), the broad class of available numerical models is entrinched on a legacy dating with more than a century of development based on finite-differences methods. Specifically for the Ocean, todays numerical models are all descendant from the original model of Bryan (1969) and Cox and Bryan (1984). The several new classes of models that appeared were due to transformations on the vertical coordinate (from cartesian spherical coordinates, known as z-level coordinates(Bryan, 1969; Cox and Bryan, 1984), to topography following coordinates, known as σ (Blumberg and Mellor, 1987) and generalized s-coordinate (Gerdes, 1993), and finally to isopycnal following coordinates (Bleck, 1978)). Griffies (2004) makes an overall review on

the matter and further discusses the different types of vertical coordinates in Chassignet and Verron (2006, Ch. 2). Furthermore, Griffies (2004) assesses some key aspects of Ocean and regional Ocean modeling that remain unsolved or are only partially solved. Namely:

- The need to create a common modeling environment or platform that makes it easy to switch between numerical schemes. Furthermore, the need to define standards of data formatting in order to optimize the global modeling community workload.
- The validity of the hydrostatic approximation when simulating domains with less than 1 km of horizontal resolution. In this thesis, the maximum resolution of regional Ocean models is roughly 2 km. Nevertheless, some regions are known to be prone to double-diffusive processes (Huppert and Turner, 2006) like the Gulf of Cadiz where occurs the Mediterranean outflow. Such question definitively would be worth it to be raised.
- The equation of state (EOS) of the Ocean for density. How accurate should the thermodynamics of the Ocean be? Fairly complex polynomial approximation to the full non-linear EOS are available (Mcdougall et al., 2003; Jackett and Mcdougall, 1995). To which extent does this complexity is required?
- To properly define OBCs.

Today, there exists several regional ocean modeling tools such as HYCOM, the hybrid generalized vertical coordinate ocean model, based on isopycnal-following vertical coordinates (Bleck, 2002); ROMS, the regional ocean modeling system based on a generalized topography-following vertical coordinate (Shchepetkin and McWilliams, 2005); NEMO-OPA, based on a generalized equipotential-following vertical coordinate. The latter models are dedicated to hydrodynamics alone, but some try to be more comprehensive and implement water-quality, biological and geochemical models, in order to model the full marine system, such as MOHID (Miranda et al., 1999; Braunschweig et al., 2003, 2004; Leitão et al., 2005) and ROMS. During the course of this work, MOHID will be the tool of choice to model regional ocean systems. MOHID is a full modeling suite developed in fortran95 in an object-oriented modular philosophy (Miranda et al., 1999; Braunschweig et al., 2004) consisting of a finite-volume hydrodynamical model, a water-quality model (Saraiva et al., 2007), a sand and cohesive sediments transport model, an ecological model (Mateus and Neves, 2008; Trancoso et al.,

2005), an oil-dispersion model (Balseiro et al., 2003), a lagrangian tracer model and a jet (submarine outfall) lagrangian-eulerian model. MOHID is capable to model complex water systems with its integrated approach. It models lakes, lagoons (Malhadas et al., 2009b, 2010, 2009a), rivers and estuaries (Vaz et al., 2009, 2007, 2005; Canas et al., 2009), regions of freshwater influence in the Ocean (Marin and Campuzano, 2008) and regional Oceanic domains (Leitão et al., 2005). Thus its scope is quite broad, scaling from the meter to the hundreds of kilometers. It cannot model global Oceanic systems because it doesn't integrate the spherical coordinates system.

1.3 The state-of-the-art in OBCs for regional oceanic models

There are two main approaches to regional Oceanic modeling and both come from the need of providing external information to the models, given the fact that the mathematical model is intrinsically a boundary value problem. The approaches are either the one-way nesting or the two-way nesting. In the one-way nesting (or downscaling approach) there are, typically, a large-scale domain and a smaller scale domain, usually with finer resolution, embedded in the first. The large-scale model runs independently of the smaller-scale model. The small-scale model, however, extracts information from the large-scale model to provide adequate values at its open boundaries and even to the interior of its domain. In the two-way nesting however, there are two regional models patched in one another and each providing to each other boundary conditions. In the occurence that one model has a larger-scale with a coarser resolution, and that the finer-scale model is patched within the large-scale model, then one can talk of downscaling and upscaling. In this case, the large-scale model acts as a reference solution to the smaller-scale model (downscaling), and the large-scale model also needs information at its boundaries coming from the small-scale model. This work will focus exclusively on the downscaling approach. For the two-way nesting, the reader is referred to Debreu et al. (2005) and Cailleau et al. (2008). The best known recent review on OBCs for regional ocean models is from Blayo and Debreu (2005) and is somewhat further discussed in Chassignet and Verron (2006, Ch. 5). Basically most authors separate the boundary conditions in two types: the radiative and the relaxing type conditions. The former type consists in letting perturbations generated within the local model to leave seamlessly and the latter type consists in transmitting information from an exterior model into the local model. Both ypes consist in han-

dling a linearized form of the equations. More complex non-linear forms of the equations of motion is also considered by Blayo and Debreu (2005) and known as characteristics methods, but restricts itself to hyperbolic type of PDEs. Boundary conditions following the exact equations of motion were proposed by Engquist and Majda (1977), but are computationally costly to implement.

1.3.1 Relaxing type conditions

The Dirichelet condition (clamped) can be regarded as the simplest form of active boundary condition where the field, Φ, is connected at the boundary to a reference solution, Φ_{ext},

$$\Phi = \Phi_{\text{ext}}.$$

Blayo and Debreu (2005) generalizes the concept with the linear boundary operator B, and a general class of simple active boundary condition follow the relation

$$B\,\Phi = B\,\Phi_{\text{ext}}, \tag{1.1}$$

where the particular case of the clamped condition considers $B = id$. In fact, Blayo and Debreu (2005) goes further arguing that equation 1.1 must be ensured by any OBC scheme in order to be consistent. A typical relaxation (damping or nudging) scheme would be of the type

$$\frac{\partial \Phi}{\partial t} = -\frac{\Phi - \Phi_{\text{ext}}}{T_f},$$

where T_f is a relaxation time period corresponding to the time scale of the incoming external information entering the model. This relaxation scheme is often combined with Sommerfeld (1949) type radiation schemes, as proposed by Blumberg and Kantha (1985). However, Blayo and Debreu (2005) recommend to enforce the consistency criterion in equation 1.1 and propose alternatively a scheme of the genre of

$$\frac{\partial \Phi - \Phi_{\text{ext}}}{\partial t} = -\frac{\Phi - \Phi_{\text{ext}}}{T_f}. \tag{1.2}$$

A more progressive relaxation scheme, known as a flow relaxation scheme (FRS) originally introduced by Davies (1976), then later adapted by Martinsen and Engedahl (1987). It uses a layer of cells near the boundary, called

the sponge layer, and in this sponge layer the solution, Φ, is relaxed to an external solution at each time step by

$$(1-\alpha)\ \Phi + \alpha\,\Phi,$$

where α is a relaxation coefficient varying between 0 (at the limit between the sponge layer and the inner domain) and 1 (at the limit between the open boundary (OB) and the sponge layer). The sponge layer also contains an artificially increased viscosity designed to damp out any inwards reflection that occurs near the boundary. Martinsen and Engedahl (1987) adapted the above scheme, to something more similar to equation 1.2, and varied the relaxation time coefficient, T_f. T_f is very large (towards infinity) in the inner domain and at the edge in the sponge layer limit with the inner domain. T_f decreases gradually in the sponge layer towards the OB. Comparative studies seem to indicate that the Martinsen and Engedahl (1987) type schemes perform quite well (Palma and Matano, 1998; Nycander and Doos, 2003).

Finally, the perfectly matched layer technique (PML), originally introduced by Berenger (1994) for electromagnetic waves, is an alternative method to sponge layered relaxation type schemes. Blayo and Debreu (2005) acknowledges the fact that it should be implemented for the primitive Ocean equations and duely tested. Tam et al. (1998); Hu (2001, 2008) implemented a PML OB scheme in the Euler equations and in the shallow waters equation. Lavelle and Thacker (2008) performs an implementation derivated from the PML that he calls *pretty good sponge*. He then tests it for an equatorial soliton wave and for a geostrophical eddy. The *pretty good sponge* seems to perform better than typical relaxation schemes (Martinsen and Engedahl, 1987; Marchesiello et al., 2001).

1.3.2 Radiative type conditions

Radiative type conditions are passive boundary conditions by design. They are meant to let information get out of the model. Nevertheless, they can be accomodated within an active boundary scheme. According to Blayo and Debreu (2005), there are radiative type conditions such as the ones defined by Sommerfeld (1949), where an apriori knowledge of the phase wave celerity is required,

$$\frac{\partial \Phi}{\partial t} + \mathbf{c}\cdot\mathbf{n}\,\frac{\partial \Phi}{\partial n} = 0 \tag{1.3}$$

where $\mathbf{c}$ is the phase celerity vector of the dependent variable Φ, $\mathbf{n}$ is the outwards normal vector to the boundary and $\frac{\partial}{\partial n}$ is the normal derivative to the boundary. Though the Neumann boundary condition (null-gradient) doesn't

fit the radiative type, it does enter the class of passive boundary condition. The radiative type condition is also a passive boundary condition designed to radiate out of the model non-dispersive mono-phasic wave-like perturbations. Several approaches are considered when calculating the mono-phase wave speed and incidence relative to the OB. Either the classical shallow approximation wave celerity is considered

$$c = \sqrt{g\,H}$$

where H is the domain depth and g is the local acceleration, either an Orlanski (1976) type celerity is considered

$$c(x\,t) = -\frac{\frac{\partial \Phi}{\partial t}}{\frac{\partial \Phi}{\partial n}},$$

which obeys the following equation

$$\frac{\partial \left(\frac{\frac{\partial \Phi}{\partial t}}{\frac{\partial \Phi}{\partial n}} \right)}{\partial t} + \frac{\Delta x}{\Delta t} \frac{\partial \left(\frac{\frac{\partial \Phi}{\partial t}}{\frac{\partial \Phi}{\partial n}} \right)}{\partial x}. \tag{1.4}$$

For the latter type, the Orlanski (1976) radiation condition is shown in Blayo and Debreu (2005) to be consistent with equation 1.4 for mono-phasic waves. Wave groups with different celerities will not respond adequately to such schemes and reflect partially at the boundaries. In fact, most OBC used in regional Ocean models consider a combination of a radiative type scheme with a relaxation type scheme, depending if the sign of c is inward (relaxation) or outward (radiation) such as proposed by Blumberg and Kantha (1985). Nevertheless, for realistic complex baroclinic flows, Treguier et al. (2001) suggests that most of the effectiveness of the Blumberg and Kantha (1985) scheme comes from the relaxation type part of it.

Finally, Flather (1976) proposed a radiative/relaxing type of condition

$$u - \sqrt{\frac{g}{H}}\,\eta = u_{\text{ext}} - \sqrt{\frac{g}{H}}\,\eta_{\text{ext}} \tag{1.5}$$

which appears to yield best performances in comparative studies of OBC such as Palma and Matano (1998); Marchesiello et al. (2001); Nycander and Doos (2003). The Flather type condition is deduced from the Sommerfeld radiation condition applied to water elevation

$$\frac{\partial \eta}{\partial t} + \sqrt{g\,H}\,\frac{\partial \eta}{\partial x} = 0,$$

and the 1D continuity equation,

$$\frac{\partial \eta}{\partial t} + \frac{\partial H\, u}{\partial x} = 0,$$

by subtracting one another and considering that H is a constant. Blayo and Debreu (2005) suggests that the apparent better performance of the Flather radiation condition is due, in fact, to the use of the clamped condition,

$$w = w_{\text{ext}},$$

on the incoming characteristic, $w = u - \sqrt{\frac{g}{H}}\,\eta$, of the 2D linearized inviscid shallow waters equation.

Marsaleix et al. (2009) proposes a polarization relation method (PRM) to radiate internal gravity waves. He further discusses the non-rotating case as well as the rotating case. The radiation of internal gravity are an important aspect of regional Ocean modeling. Mostly every other radiation condition only addresses the external gravity waves, thus the PRM technique is an important progress towards radiation techniques capable of propagating outwards of the model the multi-modal propagating waves.

1.3.3 Model adapted conditions

So far, linearized versions of the model equations were considered at the boundaries to prescribe OBCs, but Engquist and Majda (1977) proposed OBCs depending on the full model equations. Nevertheless, Blayo and Debreu (2005) considers that prescribing OBCs with the full model equations is unpractical and that some approximations need to be made. There are various types of model adapted conditions found independently but all are based on the transformed characteristic equations of the original equations of motion. There are the absorbing radiation conditions proposed by Engquist and Majda (1977); Nycander and Doos (2003) and the characteristic waves amplitudes methods proposed by Roed and Cooper (1987) for the linearized inviscid shallow water equations. Blayo and Debreu (2005) propose a characteristics method for the shallow water equations.

1.3.4 Overall appreciation

Blayo and Debreu (2005) makes the fundamental point that all the most successful OBC (Flather, 1976; Nycander and Doos, 2003) follow the criteria of considering incoming characteristics variables and consistently verifying equation 1.1. The clamped Dirichelet condition is not recommended since

its outward propagation does not rely on the interior solution. The radiation methods are discarded as well since they only radiate outgoing single phase waves and don't perform well in complex flows. For instance, internal waves are consistently reflected at the OB. Nevertheless, Marsaleix et al. (2009) addresses this issue and proposes the PRM to radiate internal gravity waves. Relaxation schemes with sponge layers are computationally more costly but they yield quite good results in complex flows. Lavelle and Thacker (2008) proposes a PML implementation for shallow water equations that he recommends as being the best sponge layered type scheme, so far. Herzfeld (2009) showed recently that OBC schemes can be implemented in several ways and can yield quite different results. Herzfeld (2009) performed two types of implementation to the Sommerfeld radiation scheme and to the Flather scheme. He then exposed the differences of these implementations from a physical point of view. The final idea of the state-of-the-art concerning OBC is that it remains an open subject prone to modifications and improvements.

1.4 The planning

The idea is to assess if the state-of-the-art in OBC for regional Ocean models in order to plan and steer the future development of numerical OB schemes for MOHID, as a model capable of forecasting the Ocean circulation at the regional level.

To do that, a part of the thesis is devoted to validate MOHID in typical Ocean processes, namely that of the Ocean vertical turbulence and the generation of barotropic and baroclinic instabilities. The Ocean vertical turbulence process validation envolved the development of a vertical unidimensional hydrodynamical model in MOHID, which reduced dramatically the computational cost, and it allowed to correct an important bug in the Brunt-Vaisalla frequency calculation which would yield a significant excess of stratification.

The barotropic and baroclinic instabilities generated by MOHID were tested with the schematic test-case of the freshwater cylinder (Tartinville et al., 1998).

An idealized numerical experiment to test both passive and active boundary conditions was devised as a two-level, one-way nesting experiment, much

like the ones found in Marsaleix et al. (2009); Herzfeld (2009); Lavelle and Thacker (2008). The concept was generalized to both schematic test-cases and realistic regional Ocean applications.

For the schematic test-case, a gaussian water elevation is released and the subsequent wave front is propagated outwards of the domain. This experiment is designed to test passive boundary conditions. To allow rapid prototyping of boundary conditions, a shallow water equations numerical model was developped in Matlab, using a leapfrog, face centred second order numerical scheme. The gravitational wave radiation condition was developed in a NVOE Herzfeld (2009) stencil, as well as the Flather radiation condition. The application of the Okubo-Weiss scalar to the flow near the open-boundaries will yield insight on the effect of the boundary condition, particularly when compared with the unbounded reference solution.

Another schematic test-case considering a coastal upwelling event is considered to pass to the three-dimensional case and is yet to be implemented with MOHID.

Two regional Ocean applications were implemented with MOHID, both with realistic forcing, in Western Iberia (Riflet et al., 2007a) and in the bay of Biscay. A downscaling methodology is presented based on the works of Leitão et al. (2005). The scalar of Okubo-Weiss is yet to be implemented, in offline mode.

Due to computational costs, only the schematic test-cases can be tested with several OBC.

Chapter 2

Fundamentals in geo-fluid physics and coastal physical processes

2.1 Mathematical fundaments

The fundamental mathematical tools required to properly expose and study the motion of fluids, or the physics of any continuum medium, were developed by Newton and Leibniz, independently, roughly during the late seventeenth century. In particular, they developed the infinitesimal calculus, which allowed them to define the instant velocity, and acceleration, of objects. The mean velocity was intuitively taken as the ratio between the length traveled and the time taken to travel that length, however the instant velocity required infinitesimal lengths, δx, and infinitesimal time periods, δt. Thus the need to define instant velocities, and accelerations, led to the formal concept of derivative, known today as the limit when δt tends to 0 of the ratio of δx and δt. In fact, the most powerful concepts from infinitesimal calculus were revised and more rigorous mathematical methods were enforced during the nineteenth century, under the Weierstrass school, which defined real analysis or real *standard* calculus, and which used the notion of *limit* rather than that of *infinitesimal*. The infinitesimal techniques, heuristically used by Leibniz, were formalized much later, during the 1960's, by Abraham Robinson in his non-standard analysis treaty, where he introduced the concept of *hyperreals*(Robinson, 1974). Basically, the concepts devised by both Newton and Leibniz lie in the derivative, the primitive and the integral which are adequate to study rates of change in continuum spaces.

Particularly important are the *Fundamental Theorem of Calculus* and the *Theorem of Leibniz* which will be developed in the following section 2.1.1 and 2.1.2. After real analysis, or one-dimensional analysis, came naturally the calculus in $\mathbb{R}^n$, which was suitable to study functions in orthonormal reference frames. However, when came the issue to tackle analysis of functions on non-cartesian reference frames, with more irregular geometries, like the sphere, the torus, etc, came also the need to find continuous transformation functions that would map mathematical objects from one frame onto another. This challenge was heavy-lifted by Riemann, amongst others, and modern geometry and differential geometry was founded which proved to be a fundamental tool in Physics, in domains such as General Relativity. Differential geometry is important as it introduces the concept of form and exterior derivative, which is an interesting tool that generalizes important theorems used in tensor calculus and other engineering fields such as solid mechanics and fluid mechanics.

2.1.1 The Fundamental Theorem of Calculus

The most important and recurrent theorem to develop all the fluid dynamics equations, in the scope of this text, is the *Fundamental Theorem of Calculus* which, in a common modern differential geometry language, states as

$$\int_{\mathcal{M}} \mathrm{d}\omega = \oint_{\partial\mathcal{M}} \omega \tag{2.1}$$

where ω is a form, $\mathcal{M}$ is an oriented differentiable manifold, $\partial\mathcal{M}$ is its outward oriented boundary and d is the exterior derivative. This theorem has an equivalent classic counterpart in real Calculus,

$$\int_a^b f(x)dx = F(b) - F(a),$$

where f is any real function, F is its primitive, and a, b are any bounded reals. Furthermore, the *Fundamental Theorem of Calculus* is also perfectly equivalent, in tensor calculus, to what we'll call herein, for simplicity, the *curl theorem*, the *divergence theorem* and the *gradient theorem*, respectively expressed as

$$\int_M \nabla \times \mathbf{F} = \oint_{\partial M} \mathbf{F}, \tag{2.2}$$

$$\int_M \nabla \cdot \mathbf{F} = \oint_{\partial M} \mathbf{F} \cdot \mathbf{n} \tag{2.3}$$

and

$$\int_M \nabla \mathbf{F} = \oint_{\partial M} \mathbf{F}\,\mathbf{n}, \tag{2.4}$$

where is M is any real n-dimensional finite volume, $\mathbf{F}$ is any differentiable vector field and $\mathbf{n}$ is the outward normal vector on the finite volume surface. It can be easily seen, though it will not be properly demonstrated here, that they're equivalent expressions of equation 2.1 by noting that

$$\nabla \times \mathbf{F} = \left[\star\left(\mathrm{d}\mathbf{F}^{\flat}\right)\right]^{\sharp},$$

$$\nabla \cdot \mathbf{F} = \star\mathrm{d}\left(\star\mathbf{F}^{\flat}\right),$$

$$\nabla\mathbf{F} = (\mathrm{d}\mathbf{F})^{\sharp},$$

where $\star$ is the Hodge star operator and $\sharp$ and $\flat$ are the musical isomorphisms. The Hodge star operator may be seen as the natural extension of the cross product to arbitrary dimensional spaces while the latter couple of operators raise and lower the index in tensors (and are analogue with the flat and sharp symbols that raise and lower one semitone in music). Equations 2.2-2.3 are classicaly known as Kelvin-Stokes and Gauss-Ostrogradsky theorems, named after their respective founders and promoters. Equations 2.2-2.4 will be recurrently used throughout this text and they evidence that the integrated inner motion of any continuum medium can be described by accounting solely the motion at the boundary. On the other hand, these equations, by construction, are valid to any finite volume, or control volume, that is embedded in a continuum medium and to any property of this continuum medium. However, of little use they would be if the rates of change of the continuum medium properties weren't computable. This insinuates the fact that the derivatives applied to properties integrated in a control volume must be summoned, and it also implies that a sound method to swap the derivative with the volume or surface integral is badly needed. To our aid comes *Leibniz's Integral Rule*.

2.1.2 Leibniz integration rule

Probably the most important and useful theorem of real Calculus after the *Fundamental Theorem of Calculus* is *Leibniz's integration rule*, which states how the derivative is applied to an integral property in a continuum medium. It is best known in Calculus textbooks as

$$\frac{d}{dt}\int_a^b f(x,t)\,dx = \int_a^b \frac{df}{dt}(x,t)\,dx, \tag{2.5}$$

where $\frac{d}{dt}$ is the time derivative, a and b are the limits of an open interval of $\mathbb{R}$ and f is a real integrable and differentiable function relative to coordinate points $(x,\, t) \in \mathbb{R}^2$. Switching the derivative with the integral is quite straightforward to prove, as seen in Zorich (2004, p. 409). An extended version of the *Leibniz's integration rule* where the boundary limits are evolving with the coordinate of the derivative is (Zorich, 2004, p. 411)

$$\begin{aligned}\frac{d}{dt}\bigg|_{t_0} \int_{a(t)}^{b(t)} f(x(t),t)\,dx = \int_{a(t_0)}^{b(t_0)} \frac{\partial f}{\partial t}(x(t_0),t)\,dx \\ + \frac{db}{dt}\bigg|_{t_0} f(b(t_0),t_0) - \frac{da}{dt}\bigg|_{t_0} f(a(t_0),t_0),\end{aligned} \tag{2.6}$$

where a and b are any two real functions of t, and t_0 is the time instant when the derivative is taken. Notice how the time derivative of the interval's boundary points is required in order to switch the integral with the derivative operator. The difference with equation 2.5 is that, when dealing with moving boundaries, the *Reynolds transport theorem* concept was implicitly used (and invoked or proved during the proof). In fact, one aspect of the author's displeasure concerning today's Newton-Leibniz modern continuum mechanics approach is that too often the extended version of *Leibniz's integration rule* in equation 2.6 is presented without prior introduction to the also important and insightful *Reynolds transport theorem*. Thus, in the next section 2.1.3, the *Reynolds transport theorem* and the generalized multi-dimensional *Leibniz's integration rule* will be described. Needless to say that the former, in conjunction with equation 2.5, will be used to prove the latter. However, it is straigtforward to express the equivalent of equation 2.5 to a multi-dimensional volume $V \subset \mathbb{R}^n$ where $n \in \mathbf{N}$:

$$\frac{d}{dt}\int_V f(\mathbf{p},t)\,dV = \int_V \frac{df}{dt}(\mathbf{p},t)\,dV,$$

where $\mathbf{p}$ is any point in V.

2.1.3 Reynold's transport theorem: a deeper insight

The *Reynolds transport theorem*, in physics, simply states that the rate of change in time of some quantity within a control volume bounded by a control surface is equal to what comes in (through the control surface) minus what goes out (through the control surface) summed to what is created (within the control volume) minus what is destroyed (within the control volume). This practical and intuitive definition describes exactly what

equation 2.6 represents for one dimension: a balance between what changes within the control volume in the first term of the right hand side (RHS) and what flows through the control volume boundary in the last term of the RHS. However, traditionally, the control volume used is always represented fixed at a given time instant, such as seen in equation 2.7.

$$\left.\frac{d}{dt}\right|_{t_0} \int_{V(t)} f(\mathbf{p}(t),\, t)\, dV \;=\; \int_{V(t_0)} \left.\frac{\partial f(\mathbf{p}(t_0),\, t)}{\partial t}\right|_{t_0} dV + \oint_{\partial V(t_0)} f(\mathbf{p}(t_0),\, t_0)\mathbf{v}\cdot\mathbf{n}\, dS, \qquad (2.7)$$

where $V \in \mathbb{R}^3$ is a moving control volume, f is any real function, ∂V is its control surface, $\mathbf{v}$ is the velocity of the control surface relative to the coordinate reference frame and $\mathbf{n}$ is the outward normal to the control surface. Although it is convenient and required to fix the control volume in time when one wishes to properly switch the derivative with the integral sign, i.e. apply the classic Leibniz integration rule in equation 2.5, it is not mandatory; particularly if one wishes to study only what comes in and what goes out, and is not particularly interested in calculating explicitly what is created and what is destroyed within the control volume. This is a strong enough reason to define a deeper *transport theorem*. In this work it is believed that this aspect is key to study finite volume modeling of Navier-Stokes equations (or similar equations of motions for fluids) using a mesh with time evolving control volumes, (but not necessarily with lagrangian volumes, in the classical sense,) while managing to prescribe constraints such as local mass or volume convervation, vorticity conservation and so on. In fact, the first reported application that was found in the literature was applied to a one-dimensional two-phase flow by Collado (2007) where the author suggested a new particle control volume fixed relative to one of the fluid phases as to adequately describe mass conservation and continuity. Of course, several numerical models already implemented such time-evolving meshes (Bleck, 2002; Martins et al., 1998) but they don't explicitly consider the mind-framework that this work emphasizes. Furthermore, at the time of Leibniz, or even Reynolds, when these theorems were first discovered, numerical modeling (and modern geometry) was still a faraway fantasy, thus it is only natural that their contemporary saw no need in developing any further equation 2.6.

In this novel framework, several control volumes, V_A, V_B, V_C, ..., V_Z, are considered evolving continuously in time through a cartesian referenced three-dimensional space that happen to coincide (exactly) in shape and vol-

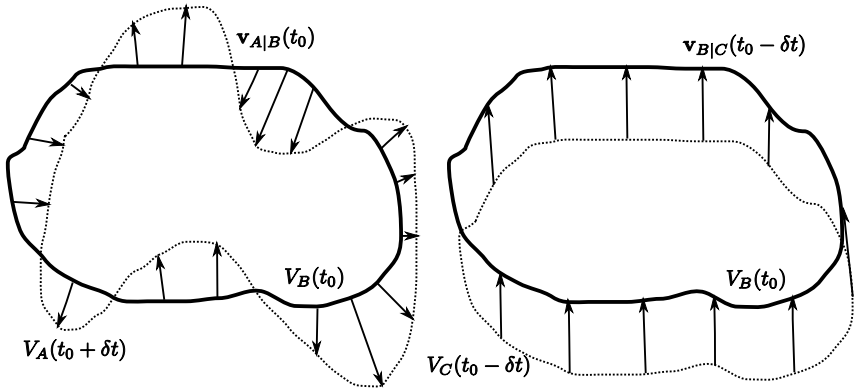

Figure 2.1: Representation of the control volumes V_A, V_B and V_C near time instant $t = t_0$ and their relative deformation rate of change, represented by the vector fields $\mathbf{v}_{A|B}$ and $\mathbf{v}_{B|C}$ over their control surfaces. On the left panel are represented volumes V_B and V_A at time instants $t = t_0$ and $t = t_0 + \delta t$ in a reference frame fixed in volume V_B. The deformation rate of change of V_A relative to V_B is represented by the vector field $\mathbf{v}_{A|B}$ at time instant $t = t_0$. On the right panel are represented volumes V_B and V_C at time instants $t = t_0$ and $t = t_0 - \delta t$ in a reference frame fixed in volume V_B. The deformation rate of change of V_B relative to V_C is represented by the vector field $\mathbf{v}_{B|C}$ at time instant $t = t_0 - \delta t$.

ume with a fixed volume V at one time instant $t = t_0$. This constrasts with the classical framework where only one moving lagrangian volume and one fixed control volume were considered. For the sake of rigor, let us consider that there always exists a diffeomorphism(Zorich, 2004, p. 142) between any two control volumes V_X and V_Y. Let $\mathbf{v}_{X|Y}(t)$ be the relative deformation rate of change with time of any two control volumes $V_X(t)$ and $V_Y(t)$ near instant $t = t_0$. $\mathbf{v}_{X|Y}$ is basically the relative velocity between the two volumes V_X and V_Y and is best represented by a vector field evolving with time as seen in figure 2.1 near time instant $t = t_0$. Thus, the real integrable and differentiable function f, whose domain is $\mathbb{R}^3 \times \mathbb{R}$ and whose coordinate points are of type $(\mathbf{p}, t)$, is well determined, within each moving volume, and its rate of change in time within volume V_X is related to the rate of change in time within volume V_Y around instant $t = t_0$ by means of its relative velocity. Hence, the *new transport theorem* yields

$$\left.\frac{d}{dt}\right|_{t_0} \int_{V_A(t)} f_A \, dV = \left.\frac{d}{dt}\right|_{t_0} \int_{V_B(t)} f_B \, dV + \oint_{\partial V_B(t_0)} f_B \, \mathbf{v}_{A|B} \cdot \mathbf{n}_B \, dS, \quad (2.8)$$

where f_A is the function f restricted to the moving domain V_A, i.e. $f_A \equiv f|_{V_A} \equiv f(p_A(t), t)$, and for every point in V_A there is a path p_A in $\mathbb{R}^3$ parametrized by t such that $\forall t \in \mathbb{R}, p_A(t) \in V_A(t)$. $\mathbf{n}_B$ is the outward oriented normal on the surface boundary of V_B. It follows naturally that the relative velocity between V_A and V_B is defined, by construction, as

$$\mathbf{v}_{A|B} \equiv \frac{d}{dt}(\mathbf{p}_A - \mathbf{p}_B). \tag{2.9}$$

Furthermore the relative velocity for any two diffeomorphic volumes, possess the distinct properties of anti-symmetry and of chaining with any third diffeomorphic volume:

1. $\mathbf{v}_{X|Y} = -\mathbf{v}_{Y|X}$,
2. $\mathbf{v}_{X|Y} + \mathbf{v}_{Y|Z} = \mathbf{v}_{X|Z}$.

The proof for anti-symmetry is straightforward from equation 2.9:

$$\begin{aligned} \mathbf{v}_{X|Y} &= \frac{d}{dt}(\mathbf{p}_X - \mathbf{p}_Y) \\ &= -\frac{d}{dt}(\mathbf{p}_Y - \mathbf{p}_X) \\ &= -\mathbf{v}_{Y|X}. \quad \square \end{aligned}$$

Idem for chaining:

$$\begin{aligned} \mathbf{v}_{X|Y} + \mathbf{v}_{Y|Z} &= \frac{d}{dt}(\mathbf{p}_X - \mathbf{p}_Y) + \frac{d}{dt}(\mathbf{p}_Y - \mathbf{p}_Z) \\ &= \frac{d\mathbf{p}_X}{dt} - \frac{d\mathbf{p}_Y}{dt} + \frac{d\mathbf{p}_Y}{dt} - \frac{d\mathbf{p}_Z}{dt} \\ &= \frac{d}{dt}(\mathbf{p}_X - \mathbf{p}_Z) \\ &= \mathbf{v}_{X|Z}. \quad \square \end{aligned}$$

This approach, as seen in equation 2.8, rather than aiming at switching the derivative with the integral, lies in using generic moving diffeomorphic volumes that happen to coincide at a given point in space and time, thus making equation 2.8 an equation of a more general class than the classic *Reynolds transport theorem* while still carrying the concept of transportation: the rate of change of a property within a volume is equal to the rate of change of the property within another overlapping volume, temporarily coincident with the first, summed to the relative flow of the property through the

surface of the overlapping volume. Though the chaining property of velocity in equation 2.9 was explicitly deduced in Collado (2007), Collado (2007) used it simultaneously with the *Leibniz integration rule*, thus shadowing its intrinsic interest. In fact, the study of two-phase and multi-phase flows often consider such relative velocities between each phase of the flow(Gray, 2002; Hassanizadeh and Gray, 1990). The other insightful aspect is that the velocity field defined by equation 2.9 may be custom-built to meet some specific requirements of the control volumes, such as, in geophysical fluids, to follow isopycnals, isentropic or geopotential lines. In opposition, the traditional physics approach was to consider the velocity of the boundaries as the velocity of the fluid relative to the reference frame. However, this is not a requirement when, for instance, the motion of isopycnals is considered to determine the motion of the finite volume boundaries, within the context of numerical models. An insightful and interesting applied exercise consists in deducing the two-dimensional barotropic shallow water equations of motion, seen in section 4.2, where the top surface of the control volumes is free moving. The classical approach consists in integrating the Navier-Stokes equations in the required control volumes, whereas the approach in this exercise will spearhead directly the correct equations of motion, thus completely bypassing the Navier-Stokes equations.

In fact, the *Reynolds Transport Theorem* contains powerful symmetries that derive from equations 2.8 and 2.9. Exposing them more clearly is evidencing the inherent algebra of the *Reynolds Transport Theorem* and, by doing so, a simpler notation is introduced:

Definition 1. *Let us define the flow of f through a volume adopting the following square bracket notation:*

$$[A,\, B]_f \equiv \oint_{\partial V_B} f_B\, \mathbf{v}_{A|B} \cdot \mathbf{n}_B\, dS,$$

which, invoking the divergence theorem, is equivalent to

$$[A,\, B]_f \equiv \int_{V_B} \nabla \cdot \left(f_B\, \mathbf{v}_{A|B}\right)\, dV.$$

Thus, definition 1 creates an operator that acts over any real field f that also inherits anti-simmetry and chaining properties from equation 2.9:

Property 1. *$\forall f$, $\forall_{V_A, V_B}$, the square bracket operator is anti-symmetric*

$$[A,\, B] = -\,[B,\, A]\,.$$

Property 2. $\forall f, \forall_{V_A,V_B,V_C}$, *the square bracket operator is chainable*

$$[A,\, B] + [B,\, C] = [A,\, C]\,.$$

Proof. The proof consists in noting that at instant t_0, $V_A = V_B = V_C$, so that we have $\partial V_A = \partial V_B = \partial V_C$, $f_A = f_B = f_C$ and $\mathbf{n}_A = \mathbf{n}_B = \mathbf{n}_C$. Hence, by using the anti-symmetric and chaining qualities of $\mathbf{v}_{X|Y}$, the square bracket anti-symmetric and chaining properties are respectively proved.

1. $\oint_{\partial V_B(t_0)} f_B\, \mathbf{v}_{A|B} \cdot \mathbf{n}_B\, dS = -\oint_{\partial V_A(t_0)} f_A\, \mathbf{v}_{B|A} \cdot \mathbf{n}_A\, dS$,
2. $\oint_{\partial V_B(t_0)} f_B\, \mathbf{v}_{A|B} \cdot \mathbf{n}_B\, dS + \oint_{\partial V_C(t_0)} f_C\, \mathbf{v}_{B|C} \cdot \mathbf{n}_C\, dS$
   $= \oint_{\partial V_C(t_0)} f_C\, \left(\mathbf{v}_{A|B} + \mathbf{v}_{B|C}\right) \cdot \mathbf{n}_C\, dS$
   $= \oint_{\partial V_C(t_0)} f_C\, \mathbf{v}_{A|C} \cdot \mathbf{n}_C\, dS$.

□

Property 3. $\forall_f,\ \forall_{V_A}$,

$$[A,\, A] = 0.$$

Proof. It suffices to remark that $\mathbf{v}_{A|A} = 0$, $\forall_{V_A}$. A more conventional proof would invoke the anti-symmetric property of the square bracket:

$$[A,\, A] = -\,[A,\, A]$$

if and only if, $\forall_{V_A}$

$$[A,\, A] = 0.$$

□

Lemma 1. $\forall_f$,

$$[A,\, B]_f = 0$$

if and only if

$$V_B = \oslash \ \ or \ \ V_A = V_B.$$

Proof. If $V_A = V_B$, then, according to property 3, $[A,\, B] = [A,\, A] = 0$.
If $\forall_f,\ [A,\, B]_f = 0$ then $\forall_f,\ \oint_{\partial V_B} f\, \mathbf{v}_{A|B} \cdot \mathbf{n}\, dS = 0$ if and only if $V_B = \oslash$ or $\mathbf{v}_{A|B} = 0$. $\mathbf{v}_{A|B} = 0 \Leftrightarrow \frac{d}{dt}\mathbf{p}_A = \frac{d}{dt}\mathbf{p}_B \Leftrightarrow \mathbf{p}_A = \mathbf{p}_B + C$. At $t = t_0$ we have $V_A(t_0) = V_B(t_0)$, thus $\mathbf{p}_A(t_0) = \mathbf{p}_B(t_0)$ if and only if $\forall t,\ C = 0$. Hence $\forall_t,\ \mathbf{p}_A = \mathbf{p}_B$ and, thus, $V_A = V_B$. □

Definition 2. *Let us define the RHS of equation 2.8 using the* bra-ket *notation:*

$$\begin{aligned} < A \,|\, f \,|\, B >_{t_0} &\equiv \left.\frac{d}{dt}\right|_{t_0} \int_{V_B(t)} f_B \, dV + \oint_{\partial V_B(t_0)} f_B \, \mathbf{v}_{A|B} \cdot \mathbf{n}_B \, dS \\ &= \left.\frac{d}{dt}\right|_{t_0} \int_{V_B(t)} f_B \, dV + [A,\, B]_{f(t_0)} \,. \end{aligned}$$

Property 4. *It immediately follows that,* $\forall f$*,*

$$< A \,|\, f \,|\, A >_{t_0} = \left.\frac{d}{dt}\right|_{t_0} \int_{V_A(t)} f_A \, dV.$$

Proof. It suffices to remark that $\mathbf{v}_{A|A} = 0$, $\forall V_A$. □

Property 5. $\forall f$, $\forall_{V_B}$ *coincident at one time instant* t_0 *and diffeomorphic to* V_A*, the equivalent of the* Reynolds transport theorem *in equation 2.8 in the bracket notation is*

$$< A \,|\, f \,|\, A >_{t_0} = < A \,|\, f \,|\, B >_{t_0},$$

or, stated alternatively,

$$< A \,|\, f \,|\, A >_{t_0} = < B \,|\, f \,|\, B >_{t_0} + [A,\, B]_{f(t_0)} \,.$$

Proof. From property 4,

$$< A \,|\, f \,|\, A >_{t_0} = \left.\frac{d}{dt}\right|_{t_0} \int_{V_A(t)} f_A \, dV,$$

from property 2,

$$< A \,|\, f \,|\, B >_{t_0} \equiv \left.\frac{d}{dt}\right|_{t_0} \int_{V_B(t)} f_B \, dV + \oint_{\partial V_B(t_0)} f_B \, \mathbf{v}_{A|B} \cdot \mathbf{n}_B \, dS,$$

from equation 2.8

$$\left.\frac{d}{dt}\right|_{t_0} \int_{V_A(t)} f_A \, dV = \left.\frac{d}{dt}\right|_{t_0} \int_{V_B(t)} f_B \, dV + \oint_{\partial V_B(t_0)} f_B \, \mathbf{v}_{A|B} \cdot \mathbf{n}_B \, dS,$$

hence

$$< A \,|\, f \,|\, A >_{t_0} = < A \,|\, f \,|\, B >_{t_0},$$

or

$$< A \,|\, f \,|\, A >_{t_0} = < B \,|\, f \,|\, B >_{t_0} + [A,\, B]_{f(t_0)} \,.$$

□

The above couple of definitions and their following five properties are enough to prove any other property using purely the bracket notation algebra.

Property 6. $\forall f, \forall_{V_B}$ *coincident at one time instant* t_0 *and diffeomorphic to* V_A*, the square bracket notation is none other than a commutator operator,*

$$\begin{aligned}[A,\,B]_{f(t_0)} &= < A \,|\, f \,|\, B >_{t_0} - < B \,|\, f \,|\, A >_{t_0} \\ &= < A \,|\, f \,|\, A >_{t_0} - < B \,|\, f \,|\, B >_{t_0} .\end{aligned}$$

Proof.

$$\begin{aligned}& < A \,|\, f \,|\, A >_{t_0} - < B \,|\, f \,|\, B >_{t_0} \\ = \;& < A \,|\, f \,|\, B >_{t_0} - < B \,|\, f \,|\, A >_{t_0},\end{aligned}$$

from property 4, and

$$\begin{aligned}& < A \,|\, f \,|\, B >_{t_0} - < B \,|\, f \,|\, A >_{t_0} \\ = \;& < A \,|\, f \,|\, B >_{t_0} - < B \,|\, f \,|\, B >_{t_0} \\ = \;& < B \,|\, f \,|\, B >_{t_0} + [A,\,B]_{f(t_0)} - < B \,|\, f \,|\, B >_{t_0} \\ = \;& [A,\,B]_{f(t_0)} ,\end{aligned}$$

□

using properties 4 and 5.

Property 7. *In the special case of* $f = 1$*, by defining* $< A \,|\, A > \equiv < A \,|\, 1 \,|\, A > \forall_{V_A}$*, then* $\forall t$

$$< A \,|\, A > = \frac{dV_A}{dt}.$$

Proof.

$$\begin{aligned}\forall t,\, < A \,|\, A > &\equiv < A \,|\, 1 \,|\, A > \\ &= \frac{d}{dt} \int_{V_A} 1 \, dV \\ &= \frac{d}{dt} V_A,\end{aligned}$$

□

using definition 2.

Property 8. *A special case of property 6 consists in imposing f as the identity:*

$$\begin{aligned}[A,\,B]_1 &= <A\,|\,B> - <B\,|\,A> \\ &= <A\,|\,A> - <B\,|\,B>\end{aligned}$$

Proof. The proof is self-evident, it suffices to replace f with 1 in property 6. □

Property 8, stated back in integral notation, yields the following relevant results:

$$\left.\frac{dV_A - V_B}{dt}\right|_{t=t_0} = \int_{V_B(t_0)} \nabla \cdot \mathbf{v}_{A|B}\, dV \tag{2.10}$$

Property 9. *V_0 is a volume fixed relative to the reference frame if, and only if,*

$$<0\,|\,0>=0.$$

Proof. If V_0 is a volume fixed relative to the reference frame, then

$$\begin{aligned}<0\,|\,0> &\equiv <0\,|\,1\,|\,0> \\ &= \frac{d}{dt}\left(\int_{V_0} 1\, dV\right) \\ &= \frac{d\,V_0}{dt} \\ &= 0.\end{aligned}$$

If $<0\,|\,0>=0$ then, by definition, $\frac{d\,V_0}{dt}=0$ and $\frac{d\,V_0}{dt}=0$ if, and only if, V_0 is fixed in time relative to the reference frame. □

Property 10. $\forall_f$ *the* Leibniz integration rule*, in bracket notation, states,*

$$<0\,|\,f\,|\,0>=\int_V \frac{\partial f}{\partial t}\, dV,$$

where the derivative is annotated partial derivative, $\frac{d}{dt} \equiv \frac{\partial}{\partial t}$*, whenever the derivative is applied to an integral whose domain of integration is fixed in time. The* Leibniz Integration Rule *allows to switch the derivative from the outside to the inside of the integral.*

Proof.

$$\begin{aligned} & < 0 \,|\, f \,|\, 0 > \\ = \;& \frac{d}{dt}\left(\int_V f \, dV\right) \\ = \;& \int_V \frac{\partial f}{\partial t} \, dV, \end{aligned}$$

□

using property 4.

Property 11. $\forall_f, \forall_{V_A}$ *diffeomorphic and coincident at instant* t_0 *with* V_0*, the classic* Reynolds Transport Theorem *states, in bracket notation,*

$$< A \,|\, f \,|\, A >_{t_0} = < 0 \,|\, f \,|\, 0 >_{t_0} + [A,\, 0]_{f(t_0)} \,.$$

Proof. By using property 5 and property 10 and substituting in

$$< A \,|\, f \,|\, A >_{t_0} = < 0 \,|\, f \,|\, 0 >_{t_0} + [A,\, 0]_{f(t_0)} \,,$$

yields

$$\begin{aligned} \left.\frac{d}{dt}\right|_{t_0} \int_{V_A(t)} f(\mathbf{p}(t),\, t)\, dV \;=\; & \int_{V_0} \left.\frac{\partial f(\mathbf{p}(t_0),\, t)}{\partial t}\right|_{t_0} dV \\ & + \oint_{\partial V_0} f(\mathbf{p}(t_0),\, t_0) \mathbf{v}_{A|0} \cdot \mathbf{n} \, dS, \end{aligned}$$

which is equation 2.7. □

The bracket notation applied to the *Reynolds Transport Theorem*, along with its properties, becomes really interesting when powerful properties get easily proved. For example, the following lemma is very important to construct the constitutive relations for geometry in a continuum medium:

Lemma 2. $\forall_{V_A}$ *coincident at instant* t_0 *and diffeomorphic to a control volume,* V_0*, fixed relative to the reference frame,*

$$< A \,|\, A >_{t_0} = [A,\, 0]_{1(t_0)}.$$

Proof.

$$\begin{aligned} & < A \,|\, A >_{t_0} \\ = \;& < 0 \,|\, 0 >_{t_0} + [A,\, 0]_{1(t_0)} \\ = \;& [A,\, 0]_{1(t_0)}, \end{aligned}$$

□

using properties 5 and 3, The lemma 2 translates, back into integral notation by using property 7 and definition 1, as

$$\left.\frac{d}{dt}\right|_{t_0} V_A(t) = \int_{V_0} \nabla \cdot \mathbf{v}_{A|0}\, dV. \tag{2.11}$$

$\forall_{V_0} \in \mathbb{R}^3$, $\forall_{V_A}$ diffeomorphic and coincident at instant t_0 with V_0, which is equivalent to, for short, $\forall_{V_A}$ that moves in space through time.

A special case, within the scope of the continuum medium, consists in considering only diffeomorphic control volumes V_A and V_B and scalar fields f that are well-behaved. In particular, if the motion of the control volumes and the scalar field is smooth enough such that $\forall \mathbf{p}$, t in the domain of f there always exists an infinitesimal neighbourhood v_A, v_B contained within the domain of f whose volume is small enough such that

1. f and the spatial gradient of f are similar to their respective average in v_A and v_B, $\overline{f}$ and $\overline{\nabla f}$,

2. $\mathbf{v}_{A|B}$ and the spatial gradient of $\mathbf{v}_{A|B}$ are similar to their respective average in v_A and v_B, $\overline{\mathbf{v}_{A|B}}$ and $\overline{\nabla \mathbf{v}_{A|B}}$,

then the open sets v_A and v_B, which form a neighbourhood of $\mathbf{p}$, are defined as *specific volumes*. By "similar" it is meant that, $\forall\, \mathbf{p} \in v$

$$\frac{f - \overline{f}}{\overline{f}} \ll 1, \tag{2.12}$$

whereas, by "average", it is meant that

$$\overline{f^a} \equiv \frac{\int_{v_A} f\, dV}{\int_{v_A} dV}, \tag{2.13}$$

where the superscript notation indicates the averaging specific volume. Of course, the bracket notation may be extended to contemplate and to study the properties of specific volumes. It may seem paradoxal to integrate a property within a specific volume, and it may actually be conceptually wrong as well, since a specific volume is an infinitesimal volume. Thus, the author itself is doubtful of the consistency and meaning of equation 2.13. Perhaps a more consistent way is simply to accept infinitesimals as a valid and solid notion, well-posed and proved from Non-standard analysis (Robinson, 1974). In that case we would have

$$f - \overline{f} = 0$$

and

$$\overline{f^a} = f(\mathbf{p}_a),$$

where $\mathbf{p}_a$ is the point whose neighbourhood is v_A.

Definition 3. *$\forall f$ well behaved, $\forall \mathbf{p}$ in the domain of f, $\forall v_A$ forming a neighbourhood of $\mathbf{p}$ and contained in the domain of f, the bracket-notation yields*

$$< a \,|\, f \,|\, a > \equiv \frac{d}{dt}\left(\overline{f^a}\, v_A\right),$$

where the lower-case letter in the brackets emphasis the fact that the control volume is a specific volume. It is also noteworthy that the time derivative, when applied to a physical property integrated in a specific volume that contains the same mass particles (without taking into account molecular diffusion), is often designated by mechanical engineers as the material derivative *and is usually annotated $\frac{d}{dt} \equiv \frac{D}{Dt}$.*

Property 12. *$\forall f$ well behaved, $\forall v_A$ specific volume contained in the domain of f,*

$$\begin{aligned} < a \,|\, f \,|\, a > &= \frac{D}{Dt}\left(\overline{f^a}\, v_A\right) \\ &= \frac{D\overline{f^a}}{Dt}\, v_A + \overline{f^a}\, \frac{Dv_A}{Dt}, \end{aligned}$$

and

$$< a \,|\, a > = \frac{dv_A}{dt}.$$

Proof.

$$\begin{aligned} < a \,|\, f \,|\, a > &\equiv \frac{d}{dt}\int_{v_A} f\, dV \\ &= \frac{D}{Dt}\left(\overline{f^a}\int_{v_A} dV\right) \\ &= \frac{D}{Dt}\left(\overline{f^a}\, v_A\right) \\ &= \frac{D\overline{f^a}}{Dt}\, v_A + \overline{f^a}\, \frac{Dv_A}{Dt}, \end{aligned}$$

and

$$\begin{aligned} < a \,|\, a > &\equiv \frac{d}{dt}\int_{v_A} 1\, dV \\ &= \frac{dv_A}{dt}. \end{aligned}$$

□

Property 13. *$\forall f$ well behaved, for all specific volume v_B, for all specific volume v_A contained in the domain of f and diffeomorphic and coincident with v_B at instant t_0,*

$$[a,\, b]_f = \overline{\nabla \cdot \left(f\, \mathbf{v}_{A|B}\right)}^{\,b} v_B.$$

Proof.

$$\begin{aligned} [a,\, b]_f &= \oint_{\partial v_B} f\, \mathbf{v}_{A|B} \cdot \mathbf{n}\, dS \\ &= \int_{v_B} \nabla \cdot \left(f\, \mathbf{v}_{A|B}\right)\, dV \\ &= \overline{\nabla \cdot \left(f\, \mathbf{v}_{A|B}\right)}^{\,b} v_B. \end{aligned}$$

For the above equation to hold true, it is required to note that the average of a sum is the sum of the averages and that the average of a product is the product of the averages. □

Property 14. *For all specific volume v_B, for all specific volume v_A diffeomorphic and coincident with v_B at instant t_0,*

$$\frac{1}{v_B}\, \frac{D\left(v_A - v_B\right)}{Dt} = \overline{\left(\nabla \cdot \mathbf{v}_{A|B}\right)}^{\,b}.$$

Proof. From property 6 we have

$$< a \,|\, a > - < b \,|\, b >= [a,\, b]_1,$$

and by substitution into the integral notation (properties 12 and 13) we get

$$\begin{aligned} \frac{Dv_A}{Dt} - \frac{Dv_B}{Dt} &= \overline{\left(\nabla \cdot \mathbf{v}_{A|B}\right)}^{\,b} v_B, \\ \frac{1}{v_B}\, \frac{D\left(v_A - v_B\right)}{Dt} &= \overline{\left(\nabla \cdot \mathbf{v}_{A|B}\right)}^{\,b}. \end{aligned}$$

□

A particular case of property 14 arises when the specific volume v_B is held fixed in time,

$$\frac{1}{v_0}\frac{Dv_A}{Dt} = \overline{\left(\nabla \cdot \mathbf{v}_{A|0}\right)}^{\,o}.$$

Property 14 will also be helpful to extend the classical definition of the material derivative, usually known as

$$\frac{D}{Dt} \equiv \frac{\partial}{\partial t} + \mathbf{v} \cdot \nabla,$$

in most textbooks.

Property 15. *For all f well-behaved and defined in $\mathbb{R}^3 \times \mathbb{R}$, the extended Lagrangian derivative can be expressed as*

$$\frac{D\overline{f^a}}{Dt} = \frac{D\overline{f^b}}{Dt} + \overline{\left(\mathbf{v}_{A|B}\right)^b} \cdot \overline{\nabla f^b},$$

or, equivalently, as

$$\frac{1}{\overline{f^b}} \frac{D\left(\overline{f^a} - \overline{f^b}\right)}{Dt} = \overline{\left(\mathbf{v}_{A|B}\right)^b} \cdot \frac{\overline{\nabla f^b}}{\overline{f^b}}.$$

Proof. From property 5 we have

$$\begin{aligned}
< a \,|\, f \,|\, a > &= < b \,|\, f \,|\, b > + [a,\, b]_f, \\
\Leftrightarrow \frac{d}{dt}\bigg|_{t_0} \int_{v_A(t)} f \, dV &= \frac{d}{dt}\bigg|_{t_0} \int_{v_B(t)} f \, dV + \int_{v_B(t_0)} \nabla \cdot \left(f \, \mathbf{v}_{A|B}\right) \, dV, \\
\Leftrightarrow \frac{D\left(\overline{f^a}\, v_A\right)}{Dt} &= \frac{D\left(\overline{f^b}\, v_B\right)}{Dt} + \overline{\nabla \cdot \left(f \, \mathbf{v}_{A|B}\right)^b} \, v_B, \\
\Leftrightarrow \frac{D\overline{f^a}}{Dt} \, v_A + \overline{f^a} \, \frac{Dv_A}{Dt} &= \frac{D\overline{f^b}}{Dt} \, v_B + \overline{f^b} \, \frac{Dv_B}{Dt} \\
&\quad + \overline{\left(f \, \nabla \cdot \mathbf{v}_{A|B} + \mathbf{v}_{A|B} \cdot \nabla f\right)^b} \, v_B, \\
\Leftrightarrow \frac{D\overline{f^a}}{Dt} + \frac{\overline{f^a}}{v_0} \, \frac{Dv_A}{Dt} &= \frac{D\overline{f^b}}{Dt} + \frac{\overline{f^b}}{v_0} \, \frac{Dv_B}{Dt} \\
&\quad + \overline{\left(f \, \nabla \cdot \mathbf{v}_{A|B}\right)^b} + \overline{\left(\mathbf{v}_{A|B} \cdot \nabla f\right)^b}, \\
\Leftrightarrow \frac{D\overline{f^a}}{Dt} &= \frac{D\overline{f^b}}{Dt} - \frac{\overline{f^o}}{v_0} \left(\frac{Dv_A}{Dt} - \frac{Dv_B}{Dt}\right) \\
&\quad + \overline{f^o} \, \overline{\left(\nabla \cdot \mathbf{v}_{A|B}\right)^b} + \overline{\left(\mathbf{v}_{A|B}\right)^b} \cdot \overline{\nabla f^b}, \\
\Leftrightarrow \frac{D\overline{f^a}}{Dt} &= \frac{D\overline{f^b}}{Dt} + \overline{\left(\mathbf{v}_{A|B}\right)^b} \cdot \overline{\nabla f^b} \\
&\quad - \overline{f^o} \left(\frac{1}{v_0} \, \frac{D\left(v_A - v_B\right)}{Dt} - \overline{\left(\nabla \cdot \mathbf{v}_{A|B}\right)^b}\right), \\
\Leftrightarrow \frac{D\overline{f^a}}{Dt} &= \frac{D\overline{f^b}}{Dt} + \overline{\left(\mathbf{v}_{A|B}\right)^b} \cdot \overline{\nabla f^b},
\end{aligned}$$

using property 14. Note that the average of a product (or sum) is the product (or sum) of the averages. It is also noteworthy that $\forall_{v_A, v_B},\ \overline{f^a}(t_0) = \overline{f^b}(t_0) = \overline{f^o}$. On the other hand,

$$\begin{aligned} \frac{D\overline{f^a}}{Dt} &= \frac{D\overline{f^b}}{Dt} + \overline{\left(\mathbf{v}_{A|B}\right)^b} \cdot \overline{\nabla f^b} \\ \Leftrightarrow \frac{D\left(\overline{f^a} - \overline{f^b}\right)}{Dt} &= \overline{\left(\mathbf{v}_{A|B}\right)^b} \cdot \overline{\nabla f^b} \\ \Leftrightarrow \frac{1}{\overline{f^b}} \frac{D\left(\overline{f^a} - \overline{f^b}\right)}{Dt} &= \overline{\left(\mathbf{v}_{A|B}\right)^b} \cdot \frac{\overline{\nabla f^b}}{\overline{f^b}}. \end{aligned}$$

□

In the particular case when $v_B = v_0$, i.e. when the specific volume is fixed relative to the reference frame, property 15 becomes the classical and very well known material derivative that appears in every textbook of continuum mechanics (Kundu and Cohen, 2002; Gill, 1982):

$$\frac{D\overline{f^a}}{Dt} = \frac{\partial \overline{f^o}}{\partial t} + \overline{\left(\mathbf{v}_{A|0}\right)^o} \cdot \overline{\nabla f^o}. \tag{2.14}$$

Though it is only actually considered a material derivative if the specific volume is a material volume that contains the same mass particles (exempting microscopic particles exchanged by molecular diffusive processes). Otherwise it should be re-named, for semantic purposes, *moving derivative* or *Lagrangian derivative*, since the author who coined the term material derivative doubtfully was considering generic moving specific volumes at all, besides mass-following ones. Classically the material derivative is seen as a bridge between the so-called eulerian and lagrangian reference of frame. In this generalization, it is seen that there it is in fact a special case of transformation of derivative between two different lagrangian reference frames. This new formalism could be potentially interesting in helping calculating schemes in numerical models using two moving reference frames, such as one that follows mass and another that follows moving grid-cells, such as the ones in the work of Martins et al. (1998) and Bleck (2002, 1978). In practice, an equivalent of the extension of the material derivative with a different notation is found in the earlier work of Hassanizadeh and Gray (1990, p. 173) concerning multi-phase flows. However, despite the works of Collado (2007); Hassanizadeh and Gray (1990) that try to import the extension of the Reynolds transport theorem and the material derivative,

respectively, a recent review in multi-phase flow (Balachandar and Eaton, 2010) doesn't integrate these concepts.

This section provides a solid foundation, composed of concepts and of mathematical tools, that will help to define in the next sections, with some rigor, a continuum medium. In particular, equations 2.8 and 2.11 are of paramount importance to build a formalism for the continuum medium. The former is required to relate material -lagrangian- volumes with fixed -eulerian- volumes. The latter is required to relate the fractional rate of change of the specific volume (which is a lagrangian volume) with the divergence of the velocity (i.e. with the divergence of the lagrangian volume's deformation rate of change).

2.2 Continuum medium

It is important to mind that matter, at a microscopic scale, is a rather discontinuous soup of molecules, atoms and quanta. However, the natural anthropologic scale is such that it usually deals with volumes of matter considered rather large when compared to the characteristic lengths of scale of the microscopical constituents, such as the inter-atomic radii or the mean free path of particles in a gas. Thus only the averaged properties of the microscopic constituents are actually measured by a very rich spectrum of tools. Of course, particularly since the early twentieth century, today's modern tools allows us to measure and interact with matter at the smallest scales, up to the scale of the nanometer ($\sim 10^{-9}$ m) and of the picometer ($\sim 10^{-12}$ m), and certainly a new way to describe the physics of fluids and solids will emerge from this past century of experimentation. However, this work deals with continuum media in the classical sense, and the interest lies in describing accurately the mechanics and behavior of fluids and solids from a macroscopical standpoint, while keeping awareness of the inherent limitations of such a description.

Hence, a continuum particle (a curious oxymoron), or macroscopic particle, or material particle, is a particle that contains a significant number, N, of microscopic constituents,

$$N \gg 1,$$

within an infinitesimal volume, which is large enough to contain the N microscopic particles, but which is small enough in order to be unidentifiable by the human eye nor by any pre-twentieth century measurement instrument. This *material particle* possesses several properties, namely its *specific*

volume, v_s, its microscopic particle density, $n \equiv \frac{N}{v_s}$, its density, ρ, which is equal to the microscopic particle density times the effective atomic mass, M, $\rho \equiv n \times M$, its velocity divergence, $\nabla \cdot \mathbf{v}$, its curl, $\nabla \times \mathbf{v}$, etc. Note that the velocity field is a field continuous in space and time that characterizes the motion of the material particles and the deformations they undergo ($\mathbf{v} \equiv \frac{d\mathbf{p}}{dt}$). However the velocity field is assumed to be well-behaved such that, for each material particle, the velocity divergence, the curl or the velocity gradient is unique, such as is the density, or the specific volume. Lavoisier's principle applied to conservation of mass within a closed domain is well accepted. But the continuity hypothesis goes a step further and states that, for each material particle, the specific volume deforms smoothly under the velocity field such that, locally in time, the particles are preserved within the specific volume, in labels and in numbers, excepted for diffusive processes.

2.2.1 The continuity equation

Being m_s the specific mass, defined as the product of the density with the specific volume, $m_s \equiv \rho\, v_s$, the continuity equation yields

$$\begin{aligned}
\frac{Dm_s}{Dt} &= 0 \\
\Leftrightarrow \frac{D\rho\, v_s}{Dt} &= 0 \\
\Leftrightarrow \frac{D\rho}{Dt} v_s + \rho \frac{Dv_s}{Dt} &= 0 \\
\Leftrightarrow \frac{1}{\rho}\frac{D\rho}{Dt} + \frac{1}{v_s}\frac{Dv_s}{Dt} &= 0 \\
\Leftrightarrow \frac{1}{\rho}\frac{D\rho}{Dt} &= -\frac{1}{v_s}\frac{Dv_s}{Dt}.
\end{aligned}$$

By invoking property 14, the above equation yields:

$$\begin{aligned}
\frac{1}{\rho}\frac{D\rho}{Dt} &= -\nabla \cdot \mathbf{v}_{s|0} \\
\Leftrightarrow \frac{D\rho}{Dt} + \rho\, \nabla \cdot \mathbf{v}_{s|0} &= 0. \qquad (2.15)
\end{aligned}$$

Equation 2.15 is known as the lagrangian form of the continuity equation, or

$$\begin{aligned} \frac{D\rho}{Dt} + \rho \nabla \cdot \mathbf{v}_{s|0} &= 0 \\ \Leftrightarrow \frac{\partial \rho}{\partial t} + \mathbf{v}_{s|0} \cdot \nabla \rho + \rho \nabla \cdot \mathbf{v}_{s|0} &= 0 \\ \Leftrightarrow \frac{\partial \rho}{\partial t} + \nabla \cdot \left(\rho \, \mathbf{v}_{s|0} \right) &= 0. \end{aligned} \tag{2.16}$$

Equation 2.16 is known as the convective form of the continuity equation and holds as long as diffusive processes are ignored. It is more useful to represent mass transport in finite volume numerical models. As far as the inclusion of diffusive processes in the continuity equation, probably the work of the eminent Brenner (2005a, 2004, 2005b, 2006) is well worth to be mentioned. He introduces the concept of specific volume transportation, rather than focusing on mass or density transportation.

2.2.2 The advection-diffusion equation

The material specific volume in equation 2.16, however, doesn't take into account any diffusive process. Diffusive processes are an evidence, maybe not of Euler's nor Leibniz's contemporaries, but certainly of the present and past century. Any finite-volume numerical and biological modeling textbook will yield what the author calls the continuum mantra,

$$\begin{aligned} \{\text{Rate of change in time}\} &= \{\text{Ingoing} - \text{Outgoing fluxes}\} \\ &+ \{\text{Created} - \text{Destroyed}\}. \end{aligned} \tag{2.17}$$

which, besides making perfect sense and being a great principle for a conceptual model, is often found in textbooks such as Chapra (1997). Its mathematical formulation, when applied to any continuum property P such as density, temperature or salinity, under the action of an advective field, held within any control volume V_B and moving with any trajectory, would yield,

for all instant t_0:

$$\left.\frac{d\int_{V_B(t)} P(\mathbf{p}(t),\, t)\, dV}{dt}\right|_{t_0} = \underbrace{-\oint_{\partial V_B(t_0)} P\, \mathbf{v}_{A|B}\cdot \mathbf{n}\, dS}_{\text{advection fluxes}} \underbrace{-\oint_{\partial V_B(t_0)} K_P\, \nabla P\cdot \mathbf{n}\, dS}_{\text{diffusive fluxes}} + \underbrace{\int_{V_B(t_0)} Sc - Sk\, dV}_{\text{source and sink terms}}, \tag{2.18}$$

where $\mathbf{v}_{A|B}$ is the advection velocity field relative to the V_B control volume, K_P represents Fick's law diffusion coefficient associated to property P and Sc and Sk represent the source and sink terms respectively. The sign of the internal product with the control volume surface normal, $\mathbf{n}$, indicates whether the fluxes go inward or outward. From property 5, stating in bracket notation that

$$< A \,|\, f \,|\, A >_{t_0} = < B \,|\, f \,|\, B >_{t_0} + [A,\, B]_{f(t_0)}\,,$$

it is seen that there always exists a control volume V_A, diffeomorphic to V_B by means of the vector field $\mathbf{v}_{A|B}$ and coincident at time instant t_0, such that equation 2.18 may write:

$$\left.\frac{d\int_{V_A(t)} P(\mathbf{p}(t),\, t)\, dV}{dt}\right|_{t_0} = \underbrace{-\oint_{\partial V_A(t_0)} K_P\, \nabla P\cdot \mathbf{n}\, dS}_{\text{diffusive fluxes}} + \underbrace{\int_{V_A(t_0)} Sc - Sk\, dV}_{\text{source and sink terms}}.$$

This volume V_A moves, expands and shrink, such that no flow other than the diffusive, flows through its surface. It is not clear, however, if there exists necessarily a control volume V_C that would also "neutralize" the diffusive processes such that

$$\left.\frac{d\int_{V_C(t)} P(\mathbf{p}(t),\, t)\, dV}{dt}\right|_{t_0} = \underbrace{\int_{V_C(t_0)} Sc - Sk\, dV}_{\text{source and sink terms}}.$$

To prove it, it would be necessary to show the existence of such a control volume, one that expands and evolves according to advection and diffusion, and it would be necessary to prove the existence of a diffeomorphism between the original control volume and such special volume. No such special control volume was found to be discussed prior in the literature. It is not of particular interest in this thesis, though the author acknowledges that if such diffeomorphism existed it certainly would prove more general than the bracket notation formalism and should be considered in the scope of a broader formalism of control volumes kinematics for continuum media.

However, when modeling, one often needs to consider the advection-diffusion equation 2.18 with V_B, a control volume with a moving surface boundary, such as the water level surface in the shallow-water equations. An interesting point is that equation 2.18 is in the integral form. To express it in the differential form, though, and to make use of the *Leibniz Integral Rule*, then a third control volume, V_0, completely fixed relative to the reference frame would be required,

$$\begin{aligned} < B \,|\, P \,|\, B >_{t_0} + [A,\, B]_{P(t_0)} &= < 0 \,|\, P \,|\, 0 > + [B,\, 0]_{P(t_0)} \\ &\quad + [A,\, B]_{P(t_0)}\,, \end{aligned}$$

So that equation 2.18 becomes

$$\begin{aligned} < 0 \,|\, P \,|\, 0 > + [A,\, B]_{P(t_0)} + [B,\, 0]_{P(t_0)} &= \underbrace{-\oint_{\partial V_B(t_0)} K_P \,\nabla P \cdot \mathbf{n}\, dS}_{\text{diffusive fluxes}} \\ &\quad + \underbrace{\int_{V_B(t_0)} Sc - Sk\, dV}_{\text{source and sink terms}}, \\ \Leftrightarrow < 0 \,|\, P \,|\, 0 > + [A,\, 0]_{P(t_0)} &= \underbrace{-\oint_{\partial V_0} K_P \,\nabla P \cdot \mathbf{n}\, dS}_{\text{diffusive fluxes}} \\ &\quad + \underbrace{\int_{V_0} Sc - Sk\, dV}_{\text{source and sink terms}}\,. \end{aligned}$$

Re-writing the latter equation in its full explicit integral notation, one gets

$$\int_{V_0} \left(\frac{\partial P}{\partial t} + \nabla \cdot \left(P\, \mathbf{v}_{A|0} \right) + \nabla \cdot \left(K_p \nabla P \right) + Sc - Sk \right) dV = 0,$$

which holds true for all property P, under any advective field $\mathbf{v}_{A|0}$, for all control volume $V_0 \in \mathbb{R}^3$ if, and only if,

$$\frac{\partial P}{\partial t} + \nabla \cdot \left(P \, \mathbf{v}_{A|0} \right) + \nabla \cdot (K_p \nabla P) + Sc - Sk = 0. \tag{2.19}$$

Equation 2.19 is the classic differential advection-diffusion equation, seen in a great many variety of textbooks such as Chapra (1997). If we consider the advection field relative to reference frame $\mathbf{v}_{A|0}$, as the field that deforms, by construction, the material specific volume whose material derivative is noted $\frac{D}{Dt}$, then the material form of equation 2.19 yields:

$$\frac{D\overline{P^a}}{Dt} + P \, \nabla \cdot \mathbf{v}_{A|0} + \nabla \cdot (K_p \nabla P) + Sc - Sk = 0. \tag{2.20}$$

It is relevant to note that the overbar notation is important to remind the reader that the material derivative is taken according to the mono-phase constituted advective field, $\mathbf{v}_{A|0}$. When the continuum medium is mono-phasic, then a single material derivative is required, applied to the flow phase a, defined by $\mathbf{v}_{A|0}$. But if the continuum medium is a Q-phase flow, then a multitude of material derivatives can be defined, such as $\frac{D\overline{P^n}}{Dt}$ where $n \in \{1, 2, ..., Q\}$ and Q is integer, by their multiple counterparts of advective flows $\mathbf{v}_{N|0}$. A practical implementation is found in Collado (2007) for a two-phase flow, but very little other references in the litterature focusing this rather relevant detail was found, to the author's surprise. This fact alone is enough to justify the overbar notation in equation2.20, but also to show the interest of the bracket notation as an adequate formalism to account correctly which lagrangian specific volumes are to be considered and how they are inter-related.

Finally, the already well-known fact that the differential equation 2.19, although correct, is inappropriate to integrate in generic numerical control volumes, unless these are fixed relative to the reference frame (which is, often enough, a too cumbersome constraint), obliges the numerical modellers to think more with finite-volumes rather than to think with finite-differences, and to use the integral equation 2.18 as the standard conceptual model.

This standard conceptual model based on the motto 2.17 and equation 2.18 is generic for all conservative property. In particular, under the presence of an advective field (i.e. a complete set of diffeomorphic volumes), it is generic for every conservative property in a continuum medium and it should be used with density, with momentum, with salinity, with temperature, and with any passive tracer. In fact it should be considered as

the *de facto* continuity equation. Thus, let us apply equation 2.18 to the density and consider a material volume V_A that moves, expands and twists conserving the mass, except for diffusive processes. Thus the advective field is completely absorbed by the moving volume and the resulting candidate to an integral continuity equation yields

$$\begin{aligned}\frac{d\int_{V_A}\rho\,dV}{dt} &= -\oint_{\partial V_A(t_0)} K_\rho\nabla\rho\,dS \\ &\quad + \int_{V_A(t_0)} (Sc - Sk)\;dV.\end{aligned}$$

The differential counterpart, though, needs to consider material specific volume v_A

$$\begin{aligned}\frac{d\left(\overline{\rho^a}\,v_A\right)}{dt} &= -\overline{\nabla\cdot\left(K_\rho\nabla\rho\right)^a}\,v_A + \overline{(Sc-Sk)^a}v_A \\ \Leftrightarrow \frac{D\overline{\rho^a}}{Dt} + \overline{\rho^a}\frac{1}{v_A}\frac{Dv_A}{Dt} &= -\overline{\nabla\cdot\left(K_\rho\nabla\rho\right)^a} + \overline{(Sc-Sk)^a} \\ \Leftrightarrow \frac{D\overline{\rho^a}}{Dt} + \overline{\rho^a}\overline{\left(\nabla\cdot\mathbf{v}_{A|0}\right)^a} &= -\overline{\nabla\cdot\left(K_\rho\nabla\rho\right)^a} + \overline{(Sc-Sk)^a} \\ \Leftrightarrow \frac{\partial\overline{\rho^a}}{\partial t} + \overline{\nabla\cdot\left(\rho\,\mathbf{v}_{A|0}\right)^a} &= -\overline{\nabla\cdot\left(K_\rho\nabla\rho\right)^a} + \overline{(Sc-Sk)^a}.\end{aligned}$$

Thus, comparing the above equation and equation 2.19 one realizes that they're identical except that P is set as ρ. Thus the above equation becomes,

$$\frac{\partial\rho}{\partial t} + \nabla\cdot\left(\rho\,\mathbf{v}_{A|0}\right) = -\nabla\cdot\left(K_\rho\nabla\rho\right) + \left(Sc - Sk\right). \tag{2.21}$$

Equation 2.21 is a good candidate for an extension of the homogeneous differential continuity equation 2.16. This candidate equation considers diffusive processes and source and sinks as natural events in a continuous medium. If the medium is spatially homogeneous, for all time instant, then

$$\nabla\rho = 0,$$

and

$$Sc - Sk = 0,$$

otherwise it couldn't stay homogeneous, thus

$$\frac{\partial\rho}{\partial t} + \rho\;\left(\nabla\cdot\mathbf{v}_{A|0}\right) = 0.$$

If the medium density is stationary, then

$$\frac{\partial \rho}{\partial t} = 0,$$

and

$$Sc - Sk = 0,$$

otherwise it couldn't stay stationary, thus

$$\nabla \cdot \left(\rho \, \mathbf{v}_{A|0} + K_\rho \nabla \rho \right) = 0.$$

If the medium density is both stationary and homogeneous, then, in the context of fluids, the fluid is said to be incompressible, and the continuity equation simply writes

$$\nabla \cdot \mathbf{v}_{A|0} = 0.$$

In the very special case that, $\forall_{t,\mathbf{p}}$,

$$\frac{D\rho}{Dt} = 0,$$

then,

$$\nabla \cdot \mathbf{v}_{A|0} = -\frac{\nabla \cdot (K_\rho \nabla \rho)}{\rho} + \frac{(Sc - Sk)}{\rho}.$$

It is important to note that in the context of geophysical fluids, water and seawater are near-incompressible(Cushman-Roisin and Beckers, 2007; Gill, 1982) in the sense that

$$\frac{\nabla \rho}{\rho} \sim 0.2 - 0.5\%$$

i.e.

$$\frac{\nabla \rho}{\rho} \ll 1$$

and

$$\frac{1}{\rho}\frac{\partial \rho}{\partial t} \ll 1.$$

Thus, in this context, it is fairly reasonable to consider

$$\nabla \cdot \mathbf{v}_{A|0} \simeq 0,$$

which is a part of the Boussinesq approximation(Cushman-Roisin and Beckers, 2007; Gill, 1982).

2.3 Fluid dynamics

Our founding principles lie in Newton's inertia law

$$\frac{D\mathbf{p}}{Dt} = \sum \mathbf{F} \tag{2.22}$$

where $\mathbf{p}$ represents the momentum of a material particle and $\sum \mathbf{F}$ are the sum of all applied forces to the particle in an inertial reference frame. Our physical system is a large ensemble of particles Ω contained within a closed domain $\mathcal{D}$. Our essential restriction is the principle of mass conservation unless the presence of well-defined source or sink terms, S_c or S_k for every closed subset of the domain. Thus, $\forall\, V_0 \in \left\{V :\ V \in \mathcal{D} \ \wedge\ V = \overline{V}\right\}$

$$\frac{dM}{dt} = S_c - S_k \tag{2.23}$$

In a fluid, we usually consider particles as being fluid particles, whose volume size outranges water molecules. Newton's inertia law (equation [2.22]) is applied to these fluid particles. However, these are still microscopical particles from the point of view of the physicist, and thus raises the need to determine macroscopical forces over a *material element*. This material element contains a very great number ($\gg 1$) of fluid particles and the forces acting on it are the sum of all the forces applied to the fluid particles within contained. Furthermore this material element follows all its particles and doesn't acquire any more along its path. Thus it can expands or shrink in volume. Finally, it is adiabatic. In other words (Gill, 1982), for any property γ of this material element

$$\gamma = \gamma\left(x(t),\, y(t),\, z(t)\right) = \gamma\left(\mathbf{x}(t), t\right),$$

where $\mathbf{x}$ is the material element spatial position in function of time, it follows that the rate of change of γ for the material element is given by

$$\frac{d\gamma}{dt} = \frac{\partial\gamma}{\partial t} + \frac{\partial\gamma}{\partial x}\frac{dx}{dt} + \frac{\partial\gamma}{\partial y}\frac{dy}{dt} + \frac{\partial\gamma}{\partial z}\frac{dz}{dt} = \frac{\partial\gamma}{\partial t} + \frac{d\mathbf{x}}{dt}\cdot\nabla\gamma$$

And $\frac{d\mathbf{x}}{dt}$ is the rate of change of the material element in space which is defined by fluid physicists as the macroscopical quantity called fluid velocity (Gill, 1982)

$$\frac{d\mathbf{x}}{dt} \equiv \mathbf{u} \equiv (u,\, v,\, w)\,. \tag{2.24}$$

In the context of fluid dynamics i.e. whenever equation [2.24] applies, we will rephrase the notation of the time derivative (which is coordinates context dependent) $\frac{d}{dt}$ and use the material derivative instead

$$\frac{D}{Dt} \equiv \frac{\partial}{\partial t} + \mathbf{u} \cdot \nabla,$$

which is coordinates independent. Hence the rate of change of the material element property now writes

$$\frac{D\gamma}{Dt} \equiv \frac{\partial \gamma}{\partial t} + \mathbf{u} \cdot \nabla \gamma.,$$

Its utility is straightforward in fluids. For instance, any conserved property such as mass m or salinity S now writes

$$\frac{Dm}{Dt} = 0,$$

$$\frac{DS}{Dt} = 0,$$

if we neglect molecular diffusion. Hence we can now rewrite the mass conservation equation by considering the specific mass m_s of a material element as the product of density ρ by the specific volume v_s,

$$\begin{array}{l} \frac{Dm_s}{Dt} = \frac{D\rho\, v_s}{Dt} = 0 \\ \Leftrightarrow \\ \frac{D\rho}{Dt} + \rho \frac{1}{v_s} \frac{Dv_s}{Dt} = 0, \end{array}$$

Gill (1982) shows that the fractional rate of change of the specific volume is equal to the divergence of the velocity $\nabla \cdot \mathbf{u}$, i.e.,

$$\beta \equiv \frac{1}{v_s} \frac{Dv_s}{Dt} = \nabla \cdot \mathbf{u}. \tag{2.25}$$

Hence using the latter equation in the former we get

$$\begin{array}{l} \frac{D\rho}{Dt} + \rho \nabla \cdot \mathbf{u} = 0 \Leftrightarrow \\ \frac{\partial \rho}{\partial t} + \mathbf{u} \cdot \nabla \rho + \rho \nabla \cdot \mathbf{u} = 0 \\ \Leftrightarrow \end{array}$$

$$\frac{\partial \rho}{\partial t} + \nabla \cdot (\rho \mathbf{u}) = 0, \tag{2.26}$$

which is the mass conservation equation, or, the continuity equation, and is one of the founding equations of fluid mechanics.
In an incompressible fluid, the following statement holds

$$\frac{D\rho}{Dt} = 0,$$

and thus the continuity equation for an incompressible fluid writes

$$\nabla \cdot \mathbf{u} = 0. \tag{2.27}$$

The latter expression means that the fractional rate of change of an incompressible material element specific volume is null - this makes sense.

2.4 Geofluid physics

2.4.1 The Primitive Ocean Equations

In this section we expose the primitive Ocean equations under the hydrostatic, Boussinesq and Reynolds approximation. We follow closely the work of Pietrzak et al. (2002). The equations are written in a Cartesian coordinate system (x, y, z, t). The vertical axis is defined positive going from $-H(x, y)$ the sea-bed up to $\eta(x, y, t)$ the free surface. The continuity equation is given by:

$$\frac{\partial u}{\partial x} + \frac{\partial v}{\partial y} + \frac{\partial w}{\partial z} = 0 \tag{2.28}$$

where (u, v, w) is the velocity coordinate vector. The momentum equations are given by

$$\begin{aligned} &\tfrac{\partial u}{\partial t} + \tfrac{\partial uu}{\partial x} + \tfrac{\partial uv}{\partial y} + \tfrac{\partial uw}{\partial z} - f\,v = \\ &-\tfrac{1}{\rho_0}\,\tfrac{\partial p_{atm}}{\partial x} - g\,\tfrac{\rho(\eta)}{\rho_0}\,\tfrac{\partial \eta}{\partial x} + \textstyle\int_z^\eta \tfrac{\partial b}{\partial x}\,dz' + F_x + \tfrac{\partial\left(\upsilon_t \frac{\partial u}{\partial z}\right)}{\partial z} \end{aligned} \tag{2.29}$$

$$\begin{aligned} &\tfrac{\partial v}{\partial t} + \tfrac{\partial vu}{\partial x} + \tfrac{\partial vv}{\partial y} + \tfrac{\partial vw}{\partial z} + f\,u = \\ &-\tfrac{1}{\rho_0}\,\tfrac{\partial p_{atm}}{\partial y} - g\,\tfrac{\rho(\eta)}{\rho_0}\,\tfrac{\partial \eta}{\partial y} + \textstyle\int_z^\eta \tfrac{\partial b}{\partial y}\,dz' + F_y + \tfrac{\partial\left(\upsilon_t \frac{\partial v}{\partial z}\right)}{\partial z} \end{aligned} \tag{2.30}$$

$$0 = -\tfrac{1}{\rho_0}\tfrac{\partial p}{\partial z} - \tfrac{1}{\rho_0} g\rho \tag{2.31}$$

where b is the buoyancy given by $b = -g(\rho - \rho_0)/\rho_0$, υ_t is the vertical viscosity coefficient, g is the local gravity acceleration, f is the local coriolis acceleration coefficient, ρ and ρ_0 are the local and mean fluid density, p_{atm} is the local atmospheric pressure at the surface and

$$F_x = \left(\upsilon_H \frac{\partial u}{\partial x}\right) + \frac{\partial\left(\upsilon_H u_{,y}\right)}{\partial y} \tag{2.32}$$

$$F_y = \frac{\partial \left(\upsilon_H \frac{\partial v}{\partial x}\right)}{\partial x} + \frac{\partial \left(\upsilon_H \frac{\partial v}{\partial y}\right)}{\partial y} \tag{2.33}$$

where υ_H is the horizontal viscosity coefficient. The conservation equation written for salinity and potential temperature are given by

$$\frac{\partial S}{\partial t} + \frac{\partial S\,u}{\partial x} + \frac{\partial S\,v}{\partial y} + \frac{\partial S\,w}{\partial z} = \frac{\partial \left(K_H \frac{\partial S}{\partial x}\right)}{\partial x} + \frac{\partial \left(K_H \frac{\partial S}{\partial y}\right)}{\partial y} + \frac{\partial \left(K_t \frac{\partial S}{\partial z}\right)}{\partial z} + S_{ss} \tag{2.34}$$

$$\frac{\partial T}{\partial t} + \frac{\partial T\,u}{\partial x} + \frac{\partial T\,v}{\partial y} + \frac{\partial T\,w}{\partial z} = \frac{\partial \left(K_H \frac{\partial T}{\partial x}\right)}{\partial x} + \frac{\partial \left(K_H \frac{\partial T}{\partial y}\right)}{\partial y} + \frac{\partial \left(K_t \frac{\partial T}{\partial x}\right)}{\partial x} + \frac{1}{\rho} Q_H + T_{ss} \tag{2.35}$$

where S_{ss} and T_{ss} are sink and source terms, K_H and K_t are the horizontal and vertical turbulent diffusivity coefficients and Q_H is the heat exchange at the interfaces of the medium. Potential temperature and salinity are the state variables used to compute the density. There are several density state-equations used within MOHID including UNESCO (Millero and Poisson, 1981; Millero et al., 2008) and Jackett and Mcdougall (1995).

$$\rho = \rho(S,\, T\, p)$$

The state-equations are the UNESCO state-equation Millero and Poisson (1981); Millero et al. (2008); Gill (1982) and the Jackett and Mcdougall (1995) state-equation. The boundary kinematic condition at the free surface $z = \eta$ is

$$w = \frac{\partial \eta}{\partial t} + u\frac{\partial \eta}{\partial x} + v\frac{\partial \eta}{\partial y} \tag{2.36}$$

and the sea bed $z = -H$ is

$$w = -u\frac{\partial H}{\partial x} - v\frac{\partial H}{\partial y} \tag{2.37}$$

The normal (and tangential) velocities are set to zero at the side walls. The momentum and tracer boundary conditions at the free surface $z = \eta$ are

$$\upsilon_t \frac{\partial u}{\partial z} = \frac{\tau_s^x}{\rho_0} \tag{2.38}$$

$$\upsilon_t \frac{\partial v}{\partial z} = \frac{\tau_s^y}{\rho_0} \tag{2.39}$$

$$K_t \frac{\partial T}{\partial z} = \frac{Q_T}{\rho_0 \, C_p} \tag{2.40}$$

$$K_t \frac{\partial S}{\partial z} = S_0 \, (evap - prec) \tag{2.41}$$

where the surface wind stress, τ_s^x, τ_s^y is calculated assuming a quadratic friction law, with

$$\tau_s^x = \rho_a \, C_a \, u_{10m} \sqrt{u_{10m}^2 + v_{10m}^2}$$

and

$$\tau_s^y = \rho_a \, C_a \, v_{10m} \sqrt{u_{10m}^2 + v_{10m}^2}.$$

The drag coefficient C_a is a function of wind speed and is calculated according to the Smith and Banke (1975)(Large and Pond, 1981) formulation ρ_a is the density of air taken as 1.25 kg/m^3 and u_{10m} or v_{10m} is the wind speed at 10 m height. Q_T is the heat flux, $evap$ is the evaporation and $prec$ is the precipitation, where evaporation/precipitation denotes the net fresh water surface volume flux rate, and S_0 is the surface salinity. C_p is the heat capacity of sea water, for 35 PSU seawater it has a value of 3986 $J \, kg^{-1} \, K^{-1}$.

At the bed the momentum flux is balanced by quadratic bottom stress computed using the velocity nearest the bottom and a zero flux condition on temperature and salinity is imposed. Therefore the corresponding boundary conditions at the bed $z = -H(x, y)$ are:

$$\upsilon_t \frac{\partial u}{\partial z} = \frac{\tau_b^x}{\rho_0} \tag{2.42}$$

$$\upsilon_t \frac{\partial v}{\partial z} = \frac{\tau_b^y}{\rho_0} \tag{2.43}$$

$$K_t \frac{\partial T}{\partial z} = 0 \tag{2.44}$$

$$K_t \frac{\partial S}{\partial z} = 0 \tag{2.45}$$

where the bottom stress τ_b^x, τ_b^y is calculated from

$$\tau_b^x = \rho_0 \, C_D \, u_b \sqrt{u_b^2 + v_b^2}$$

and

$$\tau_b^y = \rho_0 \, C_D \, v_b \sqrt{u_b^2 + v_b^2}.$$

C_D is a drag coefficient given by

$$C_D = \kappa / \ln \left(\frac{z_b + z_0}{z_0} \right)$$

and u_b and v_b are the corresponding velocities at depth z_b, the depth of the grid point nearest to the bottom, $\kappa = 0.4$ is the von Karman constant, and z_0 m is the roughness length. This formulation is derived assuming a logarithmic velocity profile in the lowest layer and is for the limit of z_b approaching z_0, equivalent to the no-slip boundary condition.

2.4.2 General Vertical coordinates

Standard dimensional analysis of geophysical flows shows that the horizontal length scale has characteristic velocities a thousand-fold higher than vertical motion. Thus, numerical models often opted to deal with the vertical coordinate independently from the horizontal coordinates. Furthermore, the vertical physical processes that occur near the surface or near the thermocline are radically different in nature relatively to those that occur near the bottom. Each physical process requires its own length and time scale. This implies an optimal choice of different resolutions along the vertical axis. Thus the need of describing the equations of motion in a generic vertical coordinate becomes a practical necessity. Furthermore, the classical cartesian reference frame may not be in alignment with the natural tendency of the convective flow, which tend to follow along isopycnals and along isobaths. Diapycnal convection is extremely inhibited and localized, thus diapycnal flow, however small, is best represented by turbulent diffusive processes. Hence a vertical coordinate that follows the topography (or isopycnals) is a pertinent choice (Bleck, 1978) and MOHID in particular presents a wide variety of vertical coordinates varying from cartesian, to generalized vertical, which allow layers of freely varying thickness, to sigma, the classical terrain following coordinates. MOHID even allows an hybrid decomposition of the vertical domain into several sub-domains, each with its own vertical coordinate and each interfacing at the top and at the bottom with the other sub-domains. Thus, a generalized vertical coordinate may be introduced as part of the following transformation of the independent variables (Deleer-

snijder and Ruddick, 1992):

$$\begin{array}{ccccc} \psi & : & \mathbf{R}^4 & \longrightarrow & \mathbf{R}^4 \\ \begin{pmatrix} t \\ x \\ y \\ z \end{pmatrix} & & & \longmapsto & \begin{pmatrix} \tilde{t} \\ \tilde{x} \\ \tilde{y} \\ \tilde{z} \end{pmatrix} = \begin{pmatrix} t \\ x \\ y \\ \tilde{z}\,(t,\,x,\,y,\,z) \end{pmatrix} \end{array} \tag{2.46}$$

Where the $(t,\,x,\,y,\,z)$ notation represent the coordinates of one reference frame, whereas the $(\tilde{t},\,\tilde{x},\,\tilde{y},\,\tilde{z})$ notation represents coordinates in another reference frame. ψ, ψ^* represents the transformation application that maps bijectively one reference frame with another. The reader must beware that herein this section (and the following), the use of the standard Einstein notation to represent sums over space and time coordinates, as well as to represent partial and total derivatives will be adopted for its compactness and elegance. Such notation is common ground and well accepted in General Relativity, but it is also found in Tensorial Mechanics and Thermodynamics. A related work using such a notation applied to Ocean turbulence is the book of Burchard (2002). As we perform the change in the frame of reference the transformation matrix in the dual space is:

$$\begin{array}{ccc} \psi^* & : & \mathbf{R}^{*4} \longrightarrow \mathbf{R}^{*4} \\ \begin{bmatrix} \frac{\partial}{\partial \tilde{t}} \\ \frac{\partial}{\partial \tilde{x}} \\ \frac{\partial}{\partial \tilde{y}} \\ \frac{\partial}{\partial \tilde{z}} \end{bmatrix} & = & \begin{bmatrix} 1 & \cdot & \cdot & z_{,\tilde{t}} \\ \cdot & 1 & \cdot & z_{,\tilde{x}} \\ \cdot & \cdot & 1 & z_{,\tilde{y}} \\ \cdot & \cdot & \cdot & z_{,\tilde{z}} \end{bmatrix} \begin{bmatrix} \frac{\partial}{\partial t} \\ \frac{\partial}{\partial x} \\ \frac{\partial}{\partial y} \\ \frac{\partial}{\partial z} \end{bmatrix} \end{array}$$

and its inverse is:

$$\begin{array}{ccc} (\psi^*)^{-1} & : & \mathbf{R}^{*4} \longrightarrow \mathbf{R}^{*4} \\ \begin{bmatrix} \frac{\partial}{\partial t} \\ \frac{\partial}{\partial x} \\ \frac{\partial}{\partial y} \\ \frac{\partial}{\partial z} \end{bmatrix} & = & \begin{bmatrix} 1 & \cdot & \cdot & \tilde{z}_{,t} \\ \cdot & 1 & \cdot & \tilde{z}_{,x} \\ \cdot & \cdot & 1 & \tilde{z}_{,y} \\ \cdot & \cdot & \cdot & \tilde{z}_{,z} \end{bmatrix} \begin{bmatrix} \frac{\partial}{\partial \tilde{t}} \\ \frac{\partial}{\partial \tilde{x}} \\ \frac{\partial}{\partial \tilde{y}} \\ \frac{\partial}{\partial \tilde{z}} \end{bmatrix} \end{array}$$

A quick check gives us $\psi^*\,(\psi^*)^{-1} = id$ as supposed to be. Notice that derivatives of functions independent of z (or $\tilde{z}$) are independent of the generic vertical coordinate reference frame i.e.

$$\nabla f(t,x,y) = \nabla f(\tilde{t},\tilde{x},\tilde{y}). \tag{2.47}$$

However ψ^* and $(\psi^*)^{-1}$ as they are, do not fully satisfy our needs since the elements of the fourth column are derived according to the transformed

dual-space basis elements and not the pre-image dual-space basis elements. However the quick check gives us a link: let us define $J \equiv z_{,\tilde{z}} = (\tilde{z}_{,z})^{-1}$ and thus $\frac{\partial}{\partial z} = J^{-1}\frac{\partial}{\partial \tilde{z}}$. We can now invert ψ^* using this latter relation and obtain:

$$
\begin{array}{lcl}
(\psi^*)^{-1} & : & \mathbf{R}^{*4} \longrightarrow \mathbf{R}^{*4} \\
\begin{bmatrix} \frac{\partial}{\partial t} \\ \frac{\partial}{\partial x} \\ \frac{\partial}{\partial y} \\ \frac{\partial}{\partial z} \end{bmatrix} & = & \begin{bmatrix} 1 & \cdot & \cdot & -z_{,\tilde{t}}\, J^{-1} \\ \cdot & 1 & \cdot & -z_{,\tilde{x}}\, J^{-1} \\ \cdot & \cdot & 1 & -z_{,\tilde{y}}\, J^{-1} \\ \cdot & \cdot & \cdot & J^{-1} \end{bmatrix} \begin{bmatrix} \frac{\partial}{\partial \tilde{t}} \\ \frac{\partial}{\partial \tilde{x}} \\ \frac{\partial}{\partial \tilde{y}} \\ \frac{\partial}{\partial \tilde{z}} \end{bmatrix}
\end{array}
\tag{2.48}
$$

and from the above transformation we can establish a relation between all the elements of the fourth columns of ψ^* and $(\psi^*)^{-1}$:

$$
\begin{bmatrix} z_{,\tilde{t}} \\ z_{,\tilde{x}} \\ z_{,\tilde{y}} \\ z_{,\tilde{z}} \end{bmatrix} = \begin{bmatrix} -\tilde{z}_{,t}\, J \\ -\tilde{z}_{,x}\, J \\ -\tilde{z}_{,y}\, J \\ J \end{bmatrix}.
$$

Now given any transformation of type ψ (2.46), and once calculated its dual-space basis transformation $(\psi^*)^{-1}$(2.48), the coordinate transformation can occur straightforwardly.

Let us now define a more appropriate velocity vector in sigma (σ) coordinates, one that is similar when defining the total derivative i.e.

$$
\begin{aligned}
\frac{D}{Dt} &= \frac{\partial}{\partial \tilde{t}} + \tilde{u}\frac{\partial}{\partial \tilde{x}} + \tilde{v}\frac{\partial}{\partial \tilde{y}} + \tilde{w}\frac{\partial}{\partial \sigma} \\
&= \frac{\partial}{\partial t} + u\frac{\partial}{\partial x} + v\frac{\partial}{\partial y} + w\frac{\partial}{\partial z} \\
&= \frac{\partial}{\partial \tilde{t}} - z_{,\tilde{t}}\, J^{-1}\frac{\partial}{\partial \sigma} + u\left(\frac{\partial}{\partial \tilde{x}} + z_{,\tilde{x}}\, J^{-1}\frac{\partial}{\partial \sigma}\right) \\
&\quad + v\left(\frac{\partial}{\partial \tilde{y}} + z_{,\tilde{y}}\, J^{-1}\frac{\partial}{\partial \sigma}\right) + wJ^{-1}\frac{\partial}{\partial \sigma} \\
&= \frac{\partial}{\partial \tilde{t}} + u\frac{\partial}{\partial \tilde{x}} + v\frac{\partial}{\partial \tilde{y}} + J^{-1}\left(w - z_{,\tilde{t}} - z_{,\tilde{x}}\, u - z_{,\tilde{y}}\, v\right)\frac{\partial}{\partial \sigma}.
\end{aligned}
\tag{2.49}
$$

If we associate the first and last lines from the latter equation set, we obtain an appropriate sigma velocity vector:

$$
\begin{bmatrix} \tilde{u} \\ \tilde{v} \\ \tilde{w} \end{bmatrix} = \begin{bmatrix} u \\ v \\ J^{-1}\left(w - z_{,\tilde{t}} - z_{,\tilde{x}}\, u - z_{,\tilde{y}}\, v\right) \end{bmatrix}.
\tag{2.50}
$$

Let us now obtain a function integral in the new reference frame

$$\begin{aligned}\int_{z=a}^{z=b} f(z)dz &= \int_{\sigma=\psi(a)}^{\sigma=\psi(b)} f(\psi(z))(z_{,\sigma\ =\psi(z)})d\sigma \\ &= \int_{\sigma=\psi(a)}^{\sigma=\psi(b)} f(\psi(z))J(\psi(z))d\sigma \\ &= \int_{\sigma=\psi(a)}^{\sigma=\psi(b)} f(\psi(z))J(\psi(z))d\sigma\end{aligned}$$

We can now proceed in order to obtain the continuity, momentum and tracer equations in a general vertical coordinate system,

$$\begin{aligned}&Ju_{,x}+Jv_{,y}+Jw_{,z}=0\\ &Ju_{,\tilde{x}}-z_{,\tilde{x}}\,u_{,\sigma}+v_{,\tilde{y}}-z_{,\tilde{y}}\,v_{,\sigma}+w_{,\sigma}=0,\\ &Ju_{,\tilde{x}}+Jv_{,\tilde{y}}+w_{,\sigma}-z_{,\tilde{x}}\,u_{,\sigma}-z_{,\tilde{y}}\,v_{,\sigma}=0,\\ &Ju_{,\tilde{x}}+Jv_{,\tilde{y}}+\left(w-z_{,\tilde{t}}-z_{,\tilde{x}}\,u-z_{,\tilde{y}}\,v\right)_{,\sigma}+z_{,\tilde{t}\sigma}+u\,z_{,\tilde{x}\sigma}+v\,z_{,\tilde{y}\sigma}=0,\\ &Ju_{,\tilde{x}}+Jv_{,\tilde{y}}+(J\tilde{w})_{,\sigma}+z_{,\sigma\tilde{t}}+u\,z_{,\sigma\tilde{x}}+v\,z_{,\sigma\tilde{y}}=0,\\ &Ju_{,\tilde{x}}+Jv_{,\tilde{y}}+(J\tilde{w})_{,\sigma}+J_{,\tilde{t}}+J_{,\tilde{x}}\,u+J_{,\tilde{y}}\,v=0,\\ &J_{,\tilde{t}}+(Ju)_{,\tilde{x}}+(Jv)_{,\tilde{y}}+(J\tilde{w})_{,\sigma}=0,\end{aligned}$$

hence the continuity equation writes

$$J_{,\,\tilde{t}}+(Ju)_{,\,\tilde{x}}+(Jv)_{,\,\tilde{y}}+(J\tilde{w})_{,\,\sigma}=0. \tag{2.51}$$

On the other hand, the momentum equation in the classic cartesian reference frame writes

$$\begin{aligned}u_{,t}=&\\ &-(uu)_{,x}-(vu)_{,y}-(wu)_{,z}+f\,v\\ &-\frac{1}{\rho_0}p_{\mathrm{atm},x}-\frac{\rho(\eta)}{\rho_0}\eta_{,x}+\int_z^{\eta} b_{,x}\,dz'\\ &+F_x+\left(\nu_t u_{,z}\right)_{,z}.\end{aligned}$$

Hence, the momentum equation yields, by means of the transformation of

reference,

$$
\begin{aligned}
Ju_{,\tilde{t}} - z_{,\tilde{t}}\, u_{,\sigma} = \\
&-J(uu)_{,\tilde{x}} + z_{,\tilde{x}}\,(uu)_{,\sigma} \\
&-J(vu)_{,\tilde{y}} + z_{,\tilde{y}}\,(vu)_{,\sigma} \\
&-(wu)_{,\sigma} \\
&+Jf\,v - \frac{1}{\rho_0} J p_{\mathrm{atm},\tilde{x}} + \frac{1}{\rho_0} z_{,\tilde{x}}\, p_{\mathrm{atm},\sigma} \\
&-\frac{\rho(\eta)}{\rho_0} J\eta_{,\tilde{x}} + \frac{\rho(\eta)}{\rho_0} z_{,\tilde{x}}\, \eta_{,\sigma} \\
&+J\int_{\sigma}^{0} \left(b_{,\tilde{x}} - z_{,\,\tilde{x}} J^{-1} b_{,\sigma'} \right) J\, d\sigma' \\
&+JF_x + \left(\nu_t J^{-1} u_{,\sigma} \right)_{,\sigma} ,
\end{aligned}
$$

$$
\begin{aligned}
Ju_{,\tilde{t}} = \\
&-J(uu)_{,\tilde{x}} - J(vu)_{,\tilde{y}} \\
&-\left(wu - z_{,\tilde{t}}\, u + z_{,\tilde{x}}\, uu + z_{,\tilde{y}}\, vu\right)_{,\sigma} \\
&-z_{,\tilde{t}\sigma}\, u - z_{,\tilde{x}\sigma}\, uu - z_{,\tilde{y}\sigma}\, vu \\
&+Jf\,v - \frac{1}{\rho_0} J p_{\mathrm{atm},\tilde{x}} - \frac{\rho(\eta)}{\rho_0} J\eta_{,\tilde{x}} \\
&+J\int_{\sigma}^{0} \left(b_{,\tilde{x}} - z_{,\tilde{x}}\, J^{-1} b_{,\sigma'} \right) J\, d\sigma' \\
&+JF_x + \left(\nu_t J^{-1} u_{,\sigma} \right)_{,\sigma} ,
\end{aligned}
$$

$$
\begin{aligned}
Ju_{,\tilde{t}} = \\
&-J(uu)_{,\tilde{x}} - J(vu)_{,\tilde{y}} - \left(J\tilde{w}\, u\right)_{,\sigma} \\
&-z_{,\sigma\tilde{t}}\, u - z_{,\sigma\tilde{x}}\, uu - z_{,\sigma\tilde{y}}\, vu \\
&+Jf\,v - \frac{1}{\rho_0} J p_{\mathrm{atm},\tilde{x}} - \frac{\rho(\eta)}{\rho_0} J\eta_{,\tilde{x}} \\
&+J\int_{\sigma}^{0} \left(b_{,\tilde{x}} - z_{,\tilde{x}}\, J^{-1} b_{,\sigma'} \right) J\, d\sigma' \\
&+JF_x + \left(\nu_t J^{-1} u_{,\sigma} \right)_{,\sigma} ,
\end{aligned}
$$

$$
\begin{aligned}
Ju_{,\tilde{t}} = & \\
& -J(uu)_{,\tilde{x}} - J(vu)_{,\tilde{y}} - (J\tilde{w}\,u)_{,\sigma} \\
& - J_{,\tilde{t}}\,u - J_{,\tilde{x}}\,uu - J_{,\tilde{y}}\,vu \\
& + Jf\,v - \frac{1}{\rho_0} J p_{\mathrm{atm},\tilde{x}} - \frac{\rho(\eta)}{\rho_0} J\eta_{,\tilde{x}} \\
& + J\int_{\sigma}^{0} \left(b_{,\tilde{x}} - z_{,\tilde{x}}\,J^{-1} b_{,\sigma'}\right) J\,d\sigma' \\
& + JF_x + \left(\nu_t J^{-1} u_{,\sigma}\right)_{,\sigma}\,,
\end{aligned}
$$

$$
\begin{aligned}
(Ju)_{,\tilde{t}} = & \\
& -(Juu)_{,\tilde{x}} - (Jvu)_{,\tilde{y}} - (J\tilde{w}\,u)_{,\sigma} \\
& + Jf\,v - \frac{1}{\rho_0} J p_{\mathrm{atm},\tilde{x}} - \frac{\rho(\eta)}{\rho_0} J\eta_{,\tilde{x}} \\
& + J\int_{\sigma}^{0} \left(b_{,\tilde{x}} - z_{,\tilde{x}}\,J^{-1} b_{,\sigma'}\right) J\,d\sigma' \\
& + JF_x + \left(\nu_t J^{-1} u_{,\sigma}\right)_{,\sigma}\,,
\end{aligned}
$$

thus, we obtain the momentum equations

$$
\begin{aligned}
(Ju)_{,\tilde{t}} = & \\
& -(Juu)_{,\tilde{x}} - (Jvu)_{,\tilde{y}} - (J\tilde{w}\,u)_{,\sigma} \\
& + Jf\,v - \frac{1}{\rho_0} J p_{\mathrm{atm},\tilde{x}} - \frac{\rho(\eta)}{\rho_0} J\eta_{,\tilde{x}} \\
& + J\int_{\sigma}^{0} \left(b_{,\tilde{x}} J - z_{,\tilde{x}}\,b_{,\sigma'}\right)\,d\sigma' \\
& + JF_x + \left(\nu_t J^{-1} u_{,\sigma}\right)_{,\sigma}\,;
\end{aligned}
\tag{2.52}
$$

and

$$
\begin{aligned}
(Jv)_{,\tilde{t}} = & \\
& -(Juv)_{,\tilde{x}} - (Jvv)_{,\tilde{y}} - (J\tilde{w}\,v)_{,\sigma} \\
& - Jf\,u - \frac{1}{\rho_0} J p_{atm,\tilde{y}} - \frac{\rho(\eta)}{\rho_0} J\eta_{,\tilde{y}} \\
& + J\int_{\sigma}^{0} \left(b_{,\tilde{y}} J - z_{,\tilde{y}}\,b_{,\sigma'}\right)\,d\sigma' \\
& + JF_y + \left(\nu_t J^{-1} v_{,\sigma}\right)_{,\sigma}\,;
\end{aligned}
\tag{2.53}
$$

by symmetry.

$$
\begin{aligned}
&S_{,t} = \\
&\quad -(uS)_{,x} - (vS)_{,y} - (wS)_{,z} \\
&\quad F_s + \left(\nu_t u_{,z}\right)_{,z} + S_{ss}, \\
&JS_{,\tilde{t}} - z_{,\tilde{t}}\, S_{,\sigma} = \\
&\quad -J(uS)_{,\tilde{x}} + z_{,\tilde{x}}\,(uS)_{,\sigma} - J(vS)_{,\tilde{y}} + z_{,\tilde{y}}\,(vS)_{,\sigma} - (wS)_{,\sigma} \\
&\quad + JF_S + \left(D_t J^{-1} S_{,\sigma}\right)_{,\sigma} + JS_{ss}, \\
&JS_{,\tilde{t}} = \\
&\quad -J(uS)_{,\tilde{x}} - J(vS)_{,\tilde{y}} - (wS)_{,\sigma} \\
&\quad + z_{,\tilde{t}}\, S_{,\sigma} + z_{,\tilde{x}}\,(uS)_{,\sigma} + z_{,\tilde{y}}\,(vS)_{,\sigma} \\
&\quad + JF_S + \left(D_t J^{-1} S_{,\sigma}\right)_{,\sigma} + JS_{ss}, \\
&JS_{,\tilde{t}} = \\
&\quad -J(uS)_{,\tilde{x}} - J(vS)_{,\tilde{y}} - \left(wS - z_{,\tilde{t}}\, S + z_{,\tilde{x}}\, uS + z_{,\tilde{y}}\, vS\right)_{,\sigma} \\
&\quad - z_{,\tilde{t}\sigma}\, S - z_{,\tilde{x}\sigma}\, uS - z_{,\tilde{y}\sigma}\, vS \\
&\quad JF_S + \left(D_t J^{-1} S_{,\sigma}\right)_{,\sigma} + JS_{ss}, \\
&JS_{,\tilde{t}} = \\
&\quad -J(uS)_{,\tilde{x}} - J(vS)_{,\tilde{y}} - \left(J\tilde{w}S\right)_{,\sigma} \\
&\quad - z_{,\sigma\tilde{t}}\, S - z_{,\sigma\tilde{x}}\, uS - z_{,\sigma\tilde{y}}\, vS \\
&\quad + JF_S + \left(D_t J^{-1} S_{,\sigma}\right)_{,\sigma} + JS_{ss}, \\
&JS_{,\tilde{t}} = \\
&\quad -J(uS)_{,\tilde{x}} - J(vS)_{,\tilde{y}} - \left(J\tilde{w}S\right)_{,\sigma} \\
&\quad - J_{,\tilde{t}}\, S - J_{,\tilde{x}}\, uS - J_{,\tilde{y}}\, vS \\
&\quad + JF_S + \left(D_t J^{-1} S_{,\sigma}\right)_{,\sigma} + JS_{ss}, \\
&(JS)_{,\tilde{t}} = \\
&\quad -(JuS)_{,\tilde{x}} - (JvS)_{,\tilde{y}} - \left(J\tilde{w}S\right)_{,\sigma} \\
&\quad + JF_S + \left(D_t J^{-1} S_{,\sigma}\right)_{,\sigma} + JS_{ss},
\end{aligned}
$$

thus, we obtain the tracer equations

$$
\begin{aligned}
&(JS)_{,\tilde{t}} = \\
&\quad -(JuS)_{,\tilde{x}} - (JvS)_{,\tilde{y}} - (J\tilde{w}S)_{,\sigma} \\
&\quad + JF_S + \left(D_t J^{-1} S_{,\sigma}\right)_{,\sigma} + JS_{ss},
\end{aligned}
\tag{2.54}
$$

and

$$
\begin{aligned}
&(JT)_{,\tilde{t}} = \\
&\quad -(JuT)_{,\tilde{x}} - (JvT)_{,\tilde{y}} - (J\tilde{w}T)_{,\sigma} \\
&\quad +J\,F_T + \left(D_t J^{-1} T_{,\sigma}\right)_{,\sigma} + JT_{ss} + J\,Q_H. \qquad (2.55)
\end{aligned}
$$

Thus equations 2.51, 2.52, 2.53, 2.54, 2.55 combined with the density equation of state form the set known as the Primitive Ocean Equations in a generic vertical coordinate reference frame.

The Sigma coordinate

In the case of the re-known sigma coordinate $\tilde{z}\,(t,\,x,\,y,\,z) \equiv \sigma$

$$
\sigma \equiv \frac{\eta - z}{H + \eta} \qquad (2.56)
$$

The reference frame is centered somewhere in the surface plane and the vertical z-basis vector points towards the stars. The bottom depth is given by $H\,(x,\,y)$ and is assumed not to vary with time, the free surface is given by $\eta\,(t,\,x,\,y)$ and the generic z-coordinate (in cartesian reference frame) is given by z. Let us perform the calculations to obtain $(\psi^*)^{-1}$:

$$
\begin{aligned}
\tilde{z}_{,t} = \frac{\eta - z}{H + \eta}_{,t} &= \eta_{,t} \,/\, (H + \eta) - (\eta - z)\,\frac{(H + \eta)_{,t}}{(H + \eta)^2} \\
&= \eta_{,t} \,/\, (H + \eta) - \eta_{,t}\,\frac{(\eta - z)}{(H + \eta)^2} \\
&= \frac{\eta_{,t}}{H + \eta}\left(1 - \frac{\eta - z}{H + \eta}\right) \\
&= \frac{\eta_{,t}}{H + \eta}\,(1 - \sigma)\,;
\end{aligned}
$$

$$
\begin{aligned}
\tilde{z}_{,x} = \frac{\eta - z}{H + \eta}_{,x} &= \eta_{,x} \,/\, (H + \eta) - (\eta - z)\,\frac{(H + \eta)_{,x}}{(H + \eta)^2} \\
&= \eta_{,x} \,/\, (H + \eta) - (H + \eta)_{,x}\,\frac{(\eta - z)}{(H + \eta)^2} \\
&= \frac{\eta_{,x}\,(1 - \sigma) - H_{,x}\,\sigma}{H + \eta} \\
&= \frac{\eta_{,x} - \sigma\,(H + \eta)_{,x}}{H + \eta};
\end{aligned}
$$

by symmetry, along y, the calculation yields

$$\tilde{z}_{,y} = \frac{\eta_{,y} - \sigma\left(H+\eta\right)_{,y}}{H+\eta};$$

and finally along z

$$\tilde{z}_{,x} = \frac{\eta - z}{H+\eta}_{,z} = -\left(H+\eta\right)^{-1}.$$

Thus the transformation $\left(\psi^*\right)^{-1}$ writes:

$$\left(\psi^*\right)^{-1} = \begin{bmatrix} 1 & \cdot & \cdot & \frac{\eta_{,t}}{H+\eta}\left(1-\sigma\right) \\ \cdot & 1 & \cdot & \frac{\eta_{,x}(1-\sigma)-H_{,x}\sigma}{H+\eta} \\ \cdot & \cdot & 1 & \frac{\eta_{,y}-\sigma(H+\eta)_{,y}}{H+\eta} \\ \cdot & \cdot & \cdot & -\left(H+\eta\right)^{-1} \end{bmatrix} \tag{2.57}$$

If we now want to find ψ^*:

$$\begin{array}{ll} & \sigma = \frac{\eta - z}{H+\eta} \\ \Longleftrightarrow & \left(\eta - z\right) = \sigma\left(H+\eta\right) \\ \Longleftrightarrow & z = \eta - \sigma\left(H+\eta\right); \end{array} \tag{2.58}$$

we can now easily calculate, noting that the base elements are independent in the transformed reference frame

$$\begin{aligned} z_{,\tilde{t}} &= \eta_{,\tilde{t}} - \sigma\left(H+\eta\right)_{,\tilde{t}} \\ &= \eta_{,\tilde{t}} - \sigma\eta_{,\tilde{t}} \\ &= \eta_{,\tilde{t}}\left(1-\sigma\right); \end{aligned}$$

$$\begin{aligned} z_{,\tilde{x}} &= \eta_{,\tilde{x}} - \sigma\left(H+\eta\right)_{,\tilde{x}} \\ &= \eta_{,\tilde{x}}\left(1-\sigma\right) - \sigma H_{,\tilde{x}}; \end{aligned}$$

$$\begin{aligned} z_{,\tilde{y}} &= \eta_{,\tilde{y}} - \sigma\left(H+\eta\right)_{,\tilde{y}} \\ &= \eta_{,\tilde{y}}\left(1-\sigma\right) - \sigma H_{,\tilde{y}}; \end{aligned}$$

$$\begin{aligned} z_{,\sigma} &= -\left(H+\eta\right) \\ &\equiv J \end{aligned}$$

Thus the transformation ψ^* writes:

$$\psi^* = \begin{bmatrix} 1 & \cdot & \cdot & \eta_{,\tilde{t}}\,(1-\sigma) \\ \cdot & 1 & \cdot & \eta_{,\tilde{x}} - (H+\eta)_{,\tilde{x}}\,\sigma \\ \cdot & \cdot & 1 & \eta_{,\tilde{y}} - (H+\eta)_{,\tilde{y}}\,\sigma \\ \cdot & \cdot & \cdot & -(H+\eta) \end{bmatrix}, \tag{2.59}$$

and thus, the transformation matrix (2.48), after computation, is:

$$(\psi^*)^{-1} = \begin{bmatrix} 1 & \cdot & \cdot & \frac{\eta_{,\tilde{t}}}{(H+\eta)}\,(1-\sigma) \\ \cdot & 1 & \cdot & \frac{\eta_{,\tilde{x}} - (H+\eta)_{,\tilde{x}}\sigma}{H+\eta} \\ \cdot & \cdot & 1 & \frac{\eta_{,\tilde{y}} - (H+\eta)_{,\tilde{y}}\sigma}{H+\eta} \\ \cdot & \cdot & \cdot & -(H+\eta)^{-1} \end{bmatrix}. \tag{2.60}$$

Hence, we can now use operators ψ and $(\psi^*)^{-1}$ to transform equations [2.28-2.37] in the sigma reference frame. But before that, let us define a more appropriate velocity vector in sigma coordinates, one that is similar when defining the total derivative i.e.

$$\begin{aligned} \frac{D}{Dt} &= \frac{\partial}{\partial\tilde{t}} + \tilde{u}\frac{\partial}{\partial\tilde{x}} + \tilde{v}\frac{\partial}{\partial\tilde{y}} + \tilde{w}\frac{\partial}{\partial\tilde{z}} \\ &= \frac{\partial}{\partial t} + u\frac{\partial}{\partial x} + v\frac{\partial}{\partial y} + w\frac{\partial}{\partial z} \\ &= \frac{\partial}{\partial\tilde{t}} - \eta_{,\tilde{t}}\,(1-\sigma)\,J^{-1}\frac{\partial}{\partial\tilde{z}} \\ &\quad + u\frac{\partial}{\partial\tilde{x}} - u\left[\eta_{,\tilde{x}} - (H+\eta)_{,\tilde{x}}\,\sigma\right]J^{-1}\frac{\partial}{\partial\tilde{z}} \\ &\quad + v\frac{\partial}{\partial\tilde{y}} - v\left[\eta_{,\tilde{y}} - (H+\eta)_{,\tilde{y}}\,\sigma\right]J^{-1}\frac{\partial}{\partial\tilde{z}} \\ &\quad + wJ^{-1}\frac{\partial}{\partial\tilde{z}} \qquad (2.61) \\ &= \frac{\partial}{\partial\tilde{t}} + u\frac{\partial}{\partial\tilde{x}} + v\frac{\partial}{\partial\tilde{y}} \\ &\quad + \left[w - (\eta_{,\tilde{t}} + \eta_{,\tilde{x}}\,u + \eta_{,\tilde{y}}\,v)\,(1-\sigma) - (-H_{,\tilde{x}}\,u - H_{,\tilde{y}}\,v)\,\sigma\right]J^{-1}\frac{\partial}{\partial\tilde{z}} \\ &= \frac{\partial}{\partial\tilde{t}} + u\frac{\partial}{\partial\tilde{x}} + v\frac{\partial}{\partial\tilde{y}} + \left[w - w_\eta\,(1-\sigma) - w_H\sigma\right]J^{-1}\frac{\partial}{\partial\tilde{z}}\,, \qquad (2.62) \end{aligned}$$

where w_η is the surface vertical velocity and w_H is the bottom vertical velocity, both in the cartesian reference frame. Notice that in the last line

we made use of(2.47). If we associate the first and last lines from the latter equation set, we obtain an appropriate sigma velocity vector:

$$\begin{bmatrix} \tilde{u} \\ \tilde{v} \\ \tilde{w} \end{bmatrix} = \begin{bmatrix} u \\ v \\ (w - w_\eta (1-\sigma) - w_H \sigma) J^{-1} \end{bmatrix}. \tag{2.63}$$

The latter expression is similar to equation(8) from Deleersnijder (1989). Notice how the surface and bottom velocities both form the upslopping term while the sigma velocity itself is the upwelling term.

$$\frac{\partial u}{\partial x} + \frac{\partial v}{\partial y} + \frac{\partial w}{\partial z} = 0 \tag{2.64}$$

2.4.3 Energy equations

All physical quantities must derive from the Primitive Ocean equations (2.28-2.35)] as they are our hypotheses. And so must the energy equations. Hence if we multiply (2.29)

$$\begin{aligned} u_{,t} = & \\ & -(uu)_{,x} - (uv)_{,y} - (uw)_{,x} + f\,v \\ & -\frac{1}{\rho_0} p_{atm,x} - g\,\frac{\rho(\eta)}{\rho_0}\,\eta_{,x} + \int_z^\eta b_{,x}\,dz' \\ & +F_x + (\upsilon_t u_{,z})_{,z}\,, \end{aligned}$$

by $\rho_0 u$

$$\begin{aligned} \rho_0 u u_{,t} = & \\ & -\rho_0 u(uu)_{,x} - \rho_0 u(uv)_{,y} - \rho_0 u(uw)_{,z} + \rho_0 u\,f\,v \\ & -u\,p_{atm,x} - u\,g\,\rho(\eta)\,\eta_{,x} + \rho_0 u \int_z^\eta b_{,x}\,dz' \\ & +\rho_0 u F_x + \rho_0 u\,(\upsilon_t u_{,z})_{,z} \\ (\frac{1}{2}\rho_0 u^2)_{,t} = & \\ & -(\frac{1}{2}\rho_0 u^2 u)_{,x} - (\frac{1}{2}\rho_0 u^2 v)_{,y} - (\frac{1}{2}\rho_0 u^2 w)_{,z} + \rho_0 u\,f\,v \\ & -u\,p_{atm,x} - u\,g\,\rho(\eta)\,\eta_{,x} + \rho_0 u \int_z^\eta b_{,x}\,dz' \\ & +\rho_0 u F_x + \rho_0 u\,(\upsilon_t u_{,z})_{,z}\,, \end{aligned}$$

and if (2.30),

$$
\begin{aligned}
v_{,\,t} = & \\
& -(vu)_{,\,x} - (vv)_{,\,y} - (vw)_{,\,x} - f\,u \\
& -\frac{1}{\rho_0}\,p_{atm,\,y} - g\,\frac{\rho(\eta)}{\rho_0}\,\eta_{,\,y} + \int_z^\eta b_{,\,y}\,dz' \\
& +F_y\, + (v_t v_{,\,z})_{,\,z}\,,
\end{aligned}
$$

is multiplied by $\rho_0 v$,

$$
\begin{aligned}
\rho_0 v v_{,\,t} = & \\
& -\rho_0 v(vu)_{,\,x} - \rho_0 v(vv)_{,\,y} - \rho_0 v(vw)_{,\,z}\, - \rho_0 v\,f\,u \\
& -v\,p_{atm,\,y} - v\,g\,\rho(\eta)\,\eta_{,\,y} + \rho_0 v \int_z^\eta b_{,\,y}\,dz' \\
& +\rho_0 v F_y + \rho_0 v\,(v_t v_{,\,z})_{,\,z}\,, \\
(\frac{1}{2}\rho_0 v^2)_{,\,t} = & \\
& -(\frac{1}{2}\rho_0 v^2 u)_{,\,x} - (\frac{1}{2}\rho_0 v^2 v)_{,\,y} - (\frac{1}{2}\rho_0 v^2 w)_{,\,z}\, - \rho_0 v\,f\,u \\
& -v\,p_{atm,\,y} - v\,g\,\rho(\eta)\,\eta_{,\,y} + \rho_0 v \int_z^\eta b_{,\,y}\,dz' \\
& +\rho_0 v F_y + \rho_0 v\,(v_t v_{,\,z})_{,\,z}\,,
\end{aligned}
$$

and (2.31) by $\rho_0 w$

$$0 = -w p_{,\,z} - w g \rho,$$

and adding them yields

$$
\begin{aligned}
(\frac{1}{2}\rho_0 u^{\hat{k}} u_{\hat{k}})_{,\,t} = & \\
& -(\frac{1}{2}\rho_0 u^{\hat{k}} u_{\hat{k}} u^i)_{,\,i} - w p_{,\,z} - w g \rho \\
& -u^{\hat{k}}\,p_{atm,\,\hat{k}} - u^{\hat{k}}\,g\,\rho(\eta)\,\eta_{,\,\hat{k}} + \rho_0 u^{\hat{k}} \int_z^\eta b_{,\,\hat{k}}\,dz' \\
& +\rho_0 u^{\hat{k}} \left(\upsilon^{ij} u_{\hat{k},\,j}\right)_{,\,i}\,,
\end{aligned}
$$

$$
\begin{aligned}
(\frac{1}{2}\rho_0 u^{\hat{k}} u_{\hat{k}})_{,\,t} = \\
&-(\frac{1}{2}\rho_0 u^{\hat{k}} u_{\hat{k}} u^i)_{,\,i} - w p_{,\,z} - w g \rho \\
&-u^{\hat{k}}\, p_{atm,\,\hat{k}} - u^{\hat{k}}\, g\, \rho(\eta)\, \eta_{,\,\hat{k}} + \rho_0 u^{\hat{k}} \int_z^\eta b_{,\,\hat{k}}\, dz' \\
&+ \left(\upsilon^{ij} \left(\frac{1}{2}\rho_0 u^{\hat{k}} u_{\hat{k}} \right)_{,\,j} \right)_{,\,i} - \left(\rho_0 u^{\hat{k}} \right)_{,\,i} \left(\upsilon^{ij} u_{\hat{k},\,j} \right),
\end{aligned}
$$

$$
\begin{aligned}
(\frac{1}{2}\rho_0 u^{\hat{k}} u_{\hat{k}})_{,\,t} = \\
&-(\frac{1}{2}\rho_0 u^{\hat{k}} u_{\hat{k}} u^i)_{,\,i} - w g \rho \\
&-u^{\hat{k}} \left(p_{atm,\,\hat{k}} + g\, \rho(\eta)\, \eta_{,\,\hat{k}} - \rho_0 \int_z^\eta b_{,\,\hat{k}}\, dz' \right) - w p_{,\,z} \\
&+ \left(\upsilon^{ij} \left(\frac{1}{2}\rho_0 u^{\hat{k}} u_{\hat{k}} \right)_{,\,j} \right)_{,\,i} - \left(\rho_0 u^{\hat{k}} \right)_{,\,i} \left(\upsilon^{ij} u_{\hat{k},\,j} \right),
\end{aligned}
$$

$$
\begin{aligned}
(\frac{1}{2}\rho_0 u^{\hat{k}} u_{\hat{k}})_{,\,t} = \\
&-(\frac{1}{2}\rho_0 u^{\hat{k}} u_{\hat{k}} u^i)_{,\,i} - w g \rho \\
&-u^{\hat{k}} \left(p_{atm,\,\hat{k}} + \left(\int_z^\eta \rho\, g\, dz' \right)_{,\,\hat{k}} \right) - w p_{,\,z} \\
&+ \left(\upsilon^{ij} \left(\frac{1}{2}\rho_0 u^{\hat{k}} u_{\hat{k}} \right)_{,\,j} \right)_{,\,i} - \left(\rho_0 u^{\hat{k}} \right)_{,\,i} \left(\upsilon^{ij} u_{\hat{k},\,j} \right),
\end{aligned}
$$

$$
\begin{aligned}
(\frac{1}{2}\rho_0 u^{\hat{k}} u_{\hat{k}})_{,\,t} = \\
&-(\frac{1}{2}\rho_0 u^{\hat{k}} u_{\hat{k}} u^i)_{,\,i} - w g \rho \\
&-u^i p_{,\,i} \\
&+ \left(\upsilon^{ij} \left(\frac{1}{2}\rho_0 u^{\hat{k}} u_{\hat{k}} \right)_{,\,j} \right)_{,\,i} - \left(\rho_0 u^{\hat{k}} \right)_{,\,i} \left(\upsilon^{ij} u_{\hat{k},\,j} \right),
\end{aligned}
$$

$$
\begin{aligned}
(\frac{1}{2}\rho_0 u^{\hat{k}} u_{\hat{k}})_{,\,t} = \\
&-(\frac{1}{2}\rho_0 u^{\hat{k}} u_{\hat{k}} u^i)_{,\,i} - wg\rho \\
&- \left(u^i p\right)_{,\,i} + u^i_{,\,i} p \\
&+ \left(\upsilon^{ij} \left(\frac{1}{2}\rho_0 u^{\hat{k}} u_{\hat{k}} \right)_{,\,j} \right)_{,\,i} - \left(\rho_0 u^{\hat{k}}\right)_{,\,i} \left(\upsilon^{ij} u_{\hat{k},\,j} \right),
\end{aligned}
$$

$$
\begin{aligned}
(\frac{1}{2}\rho_0 u^{\hat{k}} u_{\hat{k}})_{,\,t} = \\
&-(\frac{1}{2}\rho_0 u^{\hat{k}} u_{\hat{k}} u^i)_{,\,i} - wg\rho \\
&- \left(u^i p\right)_{,\,i} + 0 \\
&+ \left(\upsilon^{ij} \left(\frac{1}{2}\rho_0 u^{\hat{k}} u_{\hat{k}} \right)_{,\,j} \right)_{,\,i} - \left(\rho_0 u^{\hat{k}}\right)_{,\,i} \left(\upsilon^{ij} u_{\hat{k},\,j} \right),
\end{aligned}
$$

where $u^{\hat{k}} \in \{u, v\}$ and $u^i \in \{u, v, w\}$. It is then deduced the transport equation of a conserved quantity κ,

$$\kappa = \frac{1}{2}\rho_0 u^{\hat{k}} u_{\hat{k}}, \tag{2.65}$$

whose closest physical affinity is the kinetic energy of a fluid particle, where $\hat{k}$ is, in this case, a summation over x and y coordinates only, ϵ is the internal dissipation rate of the fluid particle given by

$$\epsilon = \upsilon^{ij} u^{\hat{k}}_{,\,i} u_{\hat{k},\,j}, \tag{2.66}$$

and p is the pressure, obtained by integration of equation [2.31]

$$
\begin{aligned}
p(z) &= p_{atm} + \int_z^\eta \rho g dz', \\
&= p_{atm} + \rho_0 g(\eta - z) - \int_z^\eta \rho_0 b dz'.
\end{aligned}
$$

Thus the quantity defined in equation (2.65) is a conserved quantity, shown in the following equation

$$\kappa_{,\,t} + \left(\kappa u^i - \upsilon^{ij}\kappa_{,\,j} + u^i p\right)_{,\,i} = -\rho g w - \rho_0 \epsilon. \tag{2.67}$$

If we now integrate (2.67) in a closed and sealed volume V, i.e. where $v^i \cdot n_i = 0$ and $v^{ij} = 0$ in its border (n_i being its normal vector), we find (using the divergence theorem)

$$\begin{aligned}
\int_V \kappa_{,\,t}\, dV &= -\int_V \left(\kappa u^i - v^{ij}\kappa_{,\,j} + u^i p\right)_{,\,i}\, dV \\
&\quad -\int_V \rho g w\, dV - \int_V \rho_0 \epsilon\, dV \\
&\Leftrightarrow \\
\int_V \kappa_{,\,t}\, dV &= -\oint_{\partial V} \left(\left(\kappa + p\right) u^i + v^{ij}\kappa_{,\,j}\right) \cdot n_i\, dA \\
&\quad -\int_V \rho g w\, dV - \int_V \rho_0 \epsilon\, dV \\
&\Leftrightarrow
\end{aligned}$$

$$K_{,\,t} = -\int_V \rho g w\, dV - \int_V \rho_0 \epsilon\, dV, \tag{2.68}$$

where K stands for the kinetic energy of the closed volume,

$$K = \int_V \frac{1}{2} \rho_0 u^{\hat{k}} u_{\hat{k}}\, dV.$$

Since the total energy (TE) in V,

$$TE = K + P + I,$$

where P is the potential energy and I is the internal energy, is conserved,

$$TE_{,\,t} = 0,$$

we can easily postulate from (2.68) that

$$P_{,\,t} = \int_V \rho g w\, dV, \tag{2.69}$$

$$I_{,\,t} = \int_V \rho_0 \epsilon\, dV. \tag{2.70}$$

However, we might want to know the rate of change of P and I in any subvolume V_0 of V. Since the potencial energy is the energy stored in the gravitic field, we can stipulate that the specific potential energy π is given by

$$\pi = \rho g z, \tag{2.71}$$

relatively to a zero potential level. This zero-potential level is the equipotential where $g \simeq 9.8$, hence, the approximate involucre of the Earth's surface. The corresponding potential energy in V_0 is

$$P = \int_{V_0} \rho g z \, dV.$$

The transport equation of π is

$$\pi_{,\,t} + u^i \pi_{,\,i} = \rho g w. \tag{2.72}$$

It is only natural that we associate the internal energy (or heat) equation to the temperature (T) equation. And it should be expected that once integrated in an adiabatic volume it yields (2.70). Here we will show how: if we consider the material derivative of specific entropy (μ) of a water parcel (or fluid particle) ($\rho T \frac{D\mu}{Dt}$), then, as it cannot be in isentropic motion, for it is strained to the action of radiative exchange(Gill, 1982) with the surroundings ($\mathbf{F_{rad}}$), heat exchange by molecular conduction ($k\, T_{,\,i}$) and heating due to viscous dissipation, we must equate:

$$\rho T \frac{D\mu}{Dt} = \left(-F^i_{rad} + k\, T^{,\,i}\right)_{,\,i} + \rho\epsilon, \tag{2.73}$$

where k is the thermal conductivity (around $\sim 0.6\ W\ m^{-1}\ K^{-1}$ for water). On the other hand, If we take note on the first law of thermodynamics, we have

$$\frac{De}{Dt} = T \frac{D\mu}{Dt} - p \frac{Dv_s}{Dt}, \tag{2.74}$$

where e is the internal energy per unit mass. Furthermore, Gill (1982) states the following relation between entropy and potential temperature θ (may the reader mind that whenever potential temperature is used instead of temperature, then implicitly, pressure is referred relative to a reference pressure p_r at the surface)

$$\theta \frac{D\mu}{Dt} = c_p(p_r,\, \theta) \frac{D\theta}{Dt}, \tag{2.75}$$

where c_p is the specific heat at constant pressure. Under the Boussinesq approximation (in a near-incompressible fluid we have $\nabla \cdot \mathbf{v} = 0$ i.e. $\frac{1}{v_s}\frac{Dvs}{Dt} = 0$) and considering potential temperature, (2.74) and (2.75) yield the relations

$$\rho_0 \frac{De}{Dt} \Leftrightarrow \rho_0 \theta \frac{D\mu}{Dt} \Leftrightarrow \rho_0 c_p \frac{D\theta}{Dt}. \tag{2.76}$$

Hence internal energy per unit mass is related to potential temperature under the Boussinesq approximation by

$$de = c_p \, d\theta. \tag{2.77}$$

Hence relating (2.76) with (2.73) we get the following equation for the internal energy

$$\begin{aligned} & \rho_0 \frac{De}{Dt} = \left(-F^i_{rad} + k\, T^{,\,i}\right)_{,\,i} + \rho_0 \epsilon \\ \Leftrightarrow \quad & \left(\rho_0 e\right)_{,\,t} + \left(\rho_0 e\, u^i + F^i_{rad} - k\, T^{,\,i}\right)_{,\,i} = \rho_0 \epsilon \\ \Leftrightarrow \quad & \iota_{,\,t} + \left(\iota\, u^i + F^i_{rad} - k\, T^{,\,i}\right)_{,\,i} = \rho_0 \epsilon. \end{aligned} \tag{2.78}$$

Thus the internal energy transport equation (2.78) was obtained, where

$$\iota = \rho_0 e \tag{2.79}$$

is the specific internal energy. Consequently, the internal energy in any given volume V_0 is

$$I = \int_{V_0} \rho_0 e \, dV,$$

and, in the case of an isolated system, integrating (2.78) over the system's volume would yield (2.70), as expected. However, the oceanographer community find a better use for an equivalent expression of (2.78) in terms of potential temperature θ. Furthermore, given the phenomenological nature of Fourier's Law, $-k\, T^{,\,i}$, it is legitimate to argue that one could experimentally validate as well a $-k'\theta^{,\,i}$ law. Thus, relating (2.76) with (2.78), we obtain the following equation set

$$\begin{aligned} & \rho_0\, c_p \frac{D\theta}{Dt} = \left(-F^i_{rad} + k\, \theta^{,\,i}\right)_{,\,i} + \rho_0 \epsilon \\ \Leftrightarrow \quad & \frac{D\theta}{Dt} = \left(-F'^{\,i}_{rad} + k'\, \theta^{,\,i}\right)_{,\,i} - \left(-F^i_{rad} + k\, \theta^{,\,i}\right) \frac{c_{p,\,i}}{\rho_0\, c_p^2} + \frac{\epsilon}{c_p} \\ \Leftrightarrow \quad & \frac{D\theta}{Dt} = \left(-F'^{\,i}_{rad} + k'\, \theta^{,\,i}\right) \left(\frac{\left(-F'^{\,i}_{rad} + k'\, \theta^{,\,i}\right)_{,\,i}}{\left(-F'^{\,i}_{rad} + k'\, \theta^{,\,i}\right)} - \frac{c_{p,\,i}}{c_p} \right) + \frac{\epsilon}{c_p} \\ \Leftrightarrow \quad & \iota_{,\,t} + \left(\iota\, u^i + F^i_{rad} - k\, T^{,\,i}\right)_{,\,i} = \rho_0 \epsilon, \end{aligned} \tag{2.80}$$

The basics for deducing coherent energy equations of motion were laid. The specific kinetic energy is defined in (2.65), the specific potential energy is defined in (2.71) and the specific internal energy is defined in (2.79). Their

respective equations of motion are defined in (2.67), in (2.72) and in (2.80). The specific total energy ϱ is defined by it's sum

$$\varrho \equiv \kappa + \iota + \pi = \frac{1}{2}\rho_0 u^{\hat{k}} u_{\hat{k}} + \rho_0 e + \rho g z, \tag{2.81}$$

and its equation of motion sums up to

$$\varrho_{,\,t} + \left(\varrho\, u^i + F^i\right)_{,\,i} = 0, \tag{2.82}$$

as expected. $\mathbf{F}$ is the sum of the radiative and diffusive fluxes and is defined by

$$F^i = F^i_{rad} - k\, T^{,\,i} - \upsilon^{ij}\kappa_{,\,j} + u^i p. \tag{2.83}$$

A last note reminds that the external heat and kinetic fluxes, namely atmospheric fluxes, are contained within the F^i_{rad} and υ^{ij} terms (refer to (2.38) and (2.39)).

2.4.4 Mixing

Traditionally the mixing issue rises from unresolved time and length scales from the model (Burchard, 2002). Thus parameterizing the unresolved flow becomes a necessity. Thus, traditionally, this section should appear a posteriori regarding the discretized equations of motion. However, we find it interesting to insert the mixing section here, as we can generalize it in order to partitionate the flow length scales in two classes: macro-scale and micro-scale. The first one regards the statistical mean flow which is, in fact, a reference flow; whereas the latter one regards the flow anomaly relative to the reference flow and regards, in fact, a perturbation flow. This partitioning is, in fact, none other than the Reynolds decomposition:

$$x = \overline{x} + x'$$

where $\overline{x}$ is a statistical average of x at a given point in space over an ensemble of system states and x' is the perturbation. Thus this implies that $\overline{x'} = 0$. Other useful relations are $\overline{\overline{x}} = \overline{x}$, $\overline{a\, b} = \overline{a}\,\overline{b}$ and $\overline{\int_a^{b+x'} f(y)\, dy} = \int_a^b \overline{f(y)}\, dy$ if f is symmetric in b along y. Another useful result, given

$$x_{,\,a} = \overline{(x_{,\,a})} + (x_{,\,a})'$$

$$x_{,\,a} = (\overline{x} + x')_{,\,a} = \overline{x}_{,\,a} + x'_{,\,a},$$

is the following

$$\overline{(x_{,\,a})} = \overline{x}_{,\,a}$$

$$(x_{,a})' = x'_{,a}.$$

Now if we apply the Reynolds decomposition to the inertia terms of the momentum equation, i.e. $\frac{dp}{dt} = \frac{d(\overline{p}+p')}{dt}$,

$$\begin{aligned}
&(\overline{u}+u')_{,t} \\
&\quad + \quad ((\overline{u}+u')(\overline{u}+u'))_{,x} + ((\overline{v}+v')(\overline{u}+u'))_{,y} \\
&\quad + \quad ((\overline{w}+w')(\overline{u}+u'))_{,z} - f(\overline{v}+v') \\
\Leftrightarrow& \\
&(\overline{u})_{,t} \\
&\quad + \quad ((\overline{u}+u')(\overline{u}+u'))_{,x} + ((\overline{v}+v')(\overline{u}+u'))_{,y} \\
&\quad + \quad ((\overline{w}+w')(\overline{u}+u'))_{,z} - f(\overline{v}+v')
\end{aligned}$$

Hence the momentum equation with molecular diffusion becomes

$$\begin{aligned}
&(\overline{u})_{,t} - f\overline{v} - fv' = \\
&\quad -((\overline{uu})_{,x} - (\overline{u}u')_{,x} - (u'\overline{u})_{,x} - (u'u')_{,x}) \\
&\quad -((\overline{vu})_{,y} - (\overline{v}u')_{,y} - (v'\overline{u})_{,y} - (v'u')_{,y}) \\
&\quad -((\overline{wu})_{,z} - (\overline{w}u')_{,x} - (w'\overline{u})_{,z} - (w'u')_{,z}) \\
&\quad -\frac{1}{\rho_0}(\overline{p}_{atm,x} - p'_{atm,x}) - g\frac{\rho(\eta)}{\rho_0}\left(\overline{\eta}_{,x} + \eta'_{,x}\right) \\
&\quad + \int_z^{\overline{\eta}} b_{,x}dz' + \int_{\overline{\eta}}^{\overline{\eta}+\eta'} b_{,x}dz' \\
&\quad +(\nu\,\overline{u}_{,x})_{,x} + (\nu\,\overline{u}_{,y})_{,y} + (\nu\,\overline{u}_{,z})_{,z} \\
&\quad +(\nu\,u'_{,x})_{,x} + \left(\nu\,u'_{,y}\right)_{,y} + \left(\nu\,u'_{,z}\right)_{,z}
\end{aligned}$$

where ν is the molecular viscosity tensor. Now, if we average the momentum equation we get

$$\begin{aligned}
&\overline{u}_{,t} = \\
&\quad -(\overline{uu})_{,x} - (\overline{u'u'})_{,x} - (\overline{vu})_{,y} - (\overline{v'u'})_{,y} \\
&\quad -(\overline{wu})_{,z} - (\overline{w'u'})_{,z} + f\overline{v} \\
&\quad -\frac{1}{\rho_0}\overline{p}_{atm,x} - g\overline{\frac{\rho(\eta)}{\rho_0}}\left(\overline{\eta}_{,x}\right) + \int_z^{\overline{\eta}} b_{,x}dz' \\
&\quad +(\nu\,\overline{u}_{,x})_{,x} + (\nu\,\overline{u}_{,y})_{,y} + (\nu\,\overline{u}_{,z})_{,z}
\end{aligned} \tag{2.84}$$

If we average the other primitive ocean equations we obtain the full Reynold's equations:

$$\begin{aligned}\overline{v}_{,t} = \\ &-(\overline{uv})_{,x} - (\overline{u'v'})_{,x} - (\overline{vv})_{,y} - (\overline{v'v'})_{,y} \\ &-(\overline{wv})_{,z} - (\overline{w'v'})_{,z} - f\overline{u} \\ &-\frac{1}{\rho_0}\overline{p}_{atm,y} - g\frac{\overline{\rho(\eta)}}{\rho_0}\left(\overline{\eta}_{,y}\right) + \int_z^{\overline{\eta}} b_{,y}dz' \\ &+(\nu\,\overline{v}_{,x})_{,x} + (\nu\,\overline{v}_{,y})_{,y} + (\nu\,\overline{v}_{,z})_{,z}\end{aligned} \tag{2.85}$$

$$\frac{\partial\overline{u}}{\partial x} + \frac{\partial\overline{v}}{\partial y} + \frac{\partial\overline{w}}{\partial z} = 0 \tag{2.86}$$

$$\begin{aligned}\overline{S}_{,t} = \\ &-(\overline{u}\overline{S})_{,x} - (\overline{u'S'})_{,x} - (\overline{v}\overline{S})_{,y} - (\overline{v'S'})_{,y} - (\overline{w}\overline{S})_{,z} - (\overline{w'S'})_{,z} \\ &+\left(\nu\,\overline{S}_{,x}\right)_{,x} + \left(\nu\,\overline{S}_{,y}\right)_{,y} + \left(\nu\,\overline{S}_{,z}\right)_{,z} + S_{ss}\end{aligned} \tag{2.87}$$

$$\begin{aligned}\overline{T}_{,t} \\ &-(\overline{u}\overline{T})_{,x} - (\overline{u'T'})_{,x} - (\overline{v}\overline{T})_{,y} - (\overline{v'T'})_{,y} - (\overline{w}\overline{T})_{,z} - (\overline{w'T'})_{,z} \\ &+(\nu\,\overline{T}_{,x})_{,x} + \left(\nu\,\overline{T}_{,y}\right)_{,y} + \left(\nu\,\overline{T}_{,z}\right)_{,z} + \frac{1}{\overline{\rho}}\overline{Q}_H + \overline{T}_{ss}.\end{aligned} \tag{2.88}$$

For the density, it is assumed that the Taylor series around (T', S', p') converges fast so the higher terms can be neglected, and thus

$$\overline{\rho} = \rho\left(\overline{T} + T',\, \overline{S} + S',\, \overline{p} + p'\right) \approx \rho\left(\overline{T},\, \overline{S},\, \overline{p}\right). \tag{2.89}$$

As we can see, mixing terms such as $\overline{u'u'}$, $\overline{v'u'}$ and $\overline{w'u'}$ in (2.84) appear in equations (2.84-2.89) from the unresolved turbulent flow. As in general the perturbation velocities are unknown, an adequate parametrization of the mixing terms is required. Based on the assumption that the mixing terms tend to homogenize spatial gradients, a parametrization similar to Fick's law is traditionally adopted where the turbulent viscosity tensor is considered diagonal. Furthermore, the mathematical modelling of the primitive Ocean equations generally lead to give a vertical viscosity and diffusion term and an horizontal viscosity and diffusivity term such as:

$$\overline{u'u'} = -2\nu_H\overline{u}_{,x}$$

$$\overline{v'u'} = -2\nu_H \left(\overline{u}_{,y} + \overline{v}_{,x}\right)$$
$$\overline{w'u'} = -\nu_t \overline{u}_{,z}.$$

Note that $\nu_H \gg \nu$ and $\nu_t \gg \nu$ so the momentum equation usually writes as (2.29) and (2.30).
All of these calculations have been made only for the u-component of the momentum equations. The parametrization and calculation for the v-component of Reynolds equations (2.85-2.88) are performed in a similar manner.

Chapter 3

Discretizing and modeling the physics of fluids

3.1 Implementing a 1D vertical model in MOHID

A correct parametrization of vertical mixing is crucial to adequately reproduce known typical coastal physical ocean processes such as upwelling, internal waves, their propagation, their dissipation and their interaction with the bathymetry. More specifically, vertical diffusive and mixing processes are paramount to correctly represent an adequate vertical profile of the density, also known as the stratification of the water-column, especially near the surface level, where atmospheric forcing affects both the kinetic energy and the internal energy of the water-column. Some key descriptive qualitative concepts that visually render the vertical stratification of the water-column are the mixed layer depth and the thermocline(Gill, 1982). The mixed layer is the surface layer of a pond or of a large waterbody that feels the effect of the wind and atmospheric radiation(Chapra, 1997). As such, it is well mixed and generally warmer than below. Its depth varies seasonally. In the ocean it varies in the range from 30 m to 150 m. The thermocline is a feature displaying a maximum vertical temperature gradient near the depth of the complete aborption of incident solar radiation. Its depth varies seasonally and ranges from 50 m to 300 m in the Ocean (Gill, 1982). Perhaps a more quantitative parameter that accurately describes the water-column stratification is the Brunt-Vaisalla frequency(Brunt, 1927). The higher the frequency of the vertical displacement of water parcels relative to their state of equilibrium, the higher the stratification and the lesser the diapycnal (vertical) diffusion. The vertical mixing process is quite non-linear since. On

one hand, it directly redistributes mass throughout the water-column, thus affecting the density and stratification of the latter but, on the other hand, the vertical diffusivity coefficients values are shown to be directly correlated with the stratification itself(Burchard and Others, 2002). Beyond coastal processes, estuarine flows are also highly dependent on their stratification, especially when one considers tide circulation and the fact that a high salinity gradients co-exist in estuarine environments due to the land-incoming freshwater clashing with the Ocean salty water. Thus vertical mixing is also very important for Regions of freshwater influence (ROFIs). The physics of the circulation become extremely affected by high horizontal and vertical density gradients both on Ocean basin, coastal and estuarine circulation. The hydrodynamic of estuarine nature is also extremely influenced by the density distribution, especially due to the salinity strong uneven distribution that produces superposed layers of freshwater running atop of salty water, both moving on opposite directions. At the front, high stresses inducing a high shear causing massive kinetic energy dissipation and causing high diffusion and mixing. On the Ocean and near the coast, the hydrodynamic is affected by the density-gradient at the time scale of years and decades, when the atmospheric induced circulation is averaged out. This circulation is called thermo-haline due to its nature. Indeed, a state-of-the-art vertical turbulent model is recommended to be used and should be accurately calibrated if the goal is to obtain realistic vertical density profiles exhibiting both realistic seasonal mixed layer depth and seasonal thermocline.

Thus, in order to qualify MOHID as a suitable model to reproduce such realistic vertical density profiles, a test-case was considered that would encompass the following characteristics:

- Null horizontal density gradients
- Low horizontal velocities throughout the year (below 1 cm/s)
- Low wind-stress throughout the year
- Tidal waves of small amplitude
- Yearly available in-situ data

The case-study of choice is found in the GOTM technical manual (Burchard et al., 1999), station PAPA, situated in the middle of the Pacific ocean, where a NOAA buoy coupled with an ADCP and meteorological sensors extracted the precious in-situ data for whole years in a row. The GOTM

technical manual exhibits an astounding conformance in the yearly temperature profile time-serie between the model results and the experimental data. The idea is to guarantee that MOHID results should also exhibit the same conformance. Guaranteeing good results in this test-case proves not only that GOTM was well integrated within MOHID, but also that MOHID is then equipped and capable of generating correct mixed layer depth and seasonal thermocline all year long for the Ocean, given a correct atmospheric forcing.

Firstly, it's important to remind that GOTM is an acronym that stands for General Ocean Turbulence Model, and was devised as a stand-alone one-dimensional vertical model that would implement a suite of state-of-the-art vertical turbulence models(Burchard, 1999; Burchard and Bolding, 2001; Umlauf and Burchard, 2005), such as $k-\epsilon$ and Mellor-Yamada(Mellor and Yamada, 1982) turbulence model. The GOTM code is open-source and was injected as a new module in the MOHID modular architecture(Villarreal, 2000; Braunschweig et al., 2004), thus fully integrating MOHID and generating the vertical turbulent viscosity coefficients from the chosen turbulence closure model. Second, the PAPA station experimental data was obtained from Lars Umlauf's team, the developers of GOTM. Third, MOHID, at the time of the test-case, still had not implemented a pure vertical one-dimensional model. Thus the author implemented the current version of the one-dimensional vertical model for MOHID, which allows a ten-fold increment in speed as it only requires a 3x3xN 3-D matrix and it strips out 90% percent of the code relative to horizontal advection-diffusion. The one-dimensional vertical model in MOHID is chosen in the Hydrodynamic module by defining VERTICAL1D as the option instead of the default SOLVE EQUATIONS option for the EVOLUTION parameter. It's main routine consists of only six calls to already existent subroutines in the Module Hydrodynamic, thus making it the best possible implementation of such a feature in MOHID.

3.1.1 Preliminary results

The models results are expected to reproduce a stably stratified potential temperature and salinity profile and an oscillating Ekman spiral, from the dynamical point of vue. The Ekman spiral is produced by the dynamical combination of the influence of wind stress over the Ekman layer and the Coriolis force(Ekman, 1902; Jenkins and Bye, 2006). At the surface, the wind stress is dominant over the Coriolis force, but at the bottom of the Ekman spiral, the Coriolis force dominates over the influence of wind-stress,

thus the flow direction and intensity evolves vertically in a diminishing spiral from the surface to the bottom of the Ekman layer, known as the Ekman depth. This column of flow spiral oscillates around an equilibrium average with the Earth's inertial frequency. From the mathematical perspective of the Navier-Stokes equations for a near-incompressible fluid (Boussinesq approximation) under the hydrostatic approximation(Roisin, 1994),

$$\begin{cases} \frac{\partial u}{\partial t} + u\frac{\partial u}{\partial x} + v\frac{\partial u}{\partial y} + w\frac{\partial u}{\partial z} - fv = -\frac{1}{\rho_0}\frac{\partial p}{\partial x} + K\left(\frac{\partial^2 u}{\partial x^2} + \frac{\partial^2 u}{\partial y^2} + \frac{\partial^2 u}{\partial z^2}\right) \\ \frac{\partial v}{\partial t} + u\frac{\partial v}{\partial x} + v\frac{\partial v}{\partial y} + w\frac{\partial v}{\partial z} + fu = -\frac{1}{\rho_0}\frac{\partial p}{\partial y} + K\left(\frac{\partial^2 v}{\partial x^2} + \frac{\partial^2 v}{\partial y^2} + \frac{\partial^2 v}{\partial z^2}\right) \\ \frac{\partial w}{\partial t} + u\frac{\partial w}{\partial x} + v\frac{\partial w}{\partial y} + w\frac{\partial w}{\partial z} = -\frac{1}{\rho_0}\frac{\partial p}{\partial z} - \frac{\rho}{\rho_0}g + K\left(\frac{\partial^2 w}{\partial x^2} + \frac{\partial^2 w}{\partial y^2} + \frac{\partial^2 w}{\partial z^2}\right) \end{cases}$$

The continuity hypothesis in incompressible fluid case yield

$$\frac{\partial u}{\partial x} + \frac{\partial v}{\partial y} + \frac{\partial w}{\partial z} = 0.$$

u, v and w are the components of velocity, t, x, y, z are the cartesian coordinates in a non-inertial reference frame; ρ and ρ_0 are the density and average density; p is the pressure; f is the Coriolis frequency and K is the turbulent viscosity coefficient, assumed constant in space and time. It was also assumed that viscous processes were approximated with Fick's law. However, an horizontal null-gradient condition is imposed in the lateral faces of the water column ($\frac{\partial u}{\partial x} = 0 = \frac{\partial v}{\partial y}$ and $\frac{\partial v}{\partial x} = 0 = \frac{\partial u}{\partial y}$). Hence, continuity oblige, $\frac{\partial w}{\partial z} = 0$. Thus, assuming a nil bottom slope, we impose $w = 0$ at the bottom of the column; this implies $w = 0$ for all the points within the water column (ultimately, the water level remains constant in time i.e. $\frac{\partial \eta}{\partial t} = 0$). We now get the simplified Navier-Stokes equations from the above hypothesis:

$$\begin{cases} \frac{\partial u}{\partial t} - fv = -\frac{1}{\rho_0}\frac{\partial p}{\partial x} + K\left(\frac{\partial^2 u}{\partial z^2}\right) \\ \frac{\partial v}{\partial t} + fu = -\frac{1}{\rho_0}\frac{\partial p}{\partial y} + K\left(\frac{\partial^2 v}{\partial z^2}\right) \\ \frac{\partial p}{\partial z} = -\rho g \end{cases}$$

In a steady flow, the equations above become:

$$\begin{cases} -fv = -\frac{1}{\rho_0}\frac{\partial p}{\partial x} + K\left(\frac{\partial^2 u}{\partial z^2}\right) \\ fu = -\frac{1}{\rho_0}\frac{\partial p}{\partial y} + K\left(\frac{\partial^2 v}{\partial z^2}\right) \end{cases}$$

By considering constant density, then, under the hydrostatic approximation, pressure is merely a function of the water level; hence its horizontal variation is constant along the water column. Formalizing the last reasoning we

obtain:

$$p(z) = p_{atm} + \rho_0 g\left(\eta(x,y) - z\right) \Rightarrow \left\{ \begin{array}{l} \frac{1}{\rho_0}\frac{\partial p}{\partial x} = g\frac{\partial \eta}{\partial x}(x,y) \\ \frac{1}{\rho_0}\frac{\partial p}{\partial y} = g\frac{\partial \eta}{\partial y}(x,y) \end{array} \right. = const$$

By defining $f\, v_g \equiv -g\frac{\partial \eta}{\partial x}$ and $f\, u_g \equiv g\frac{\partial \eta}{\partial y}$ we arrive at the following differential equations set:

$$\left\{ \begin{array}{l} -fv = -fv_g + K\left(\frac{\partial^2 u}{\partial z^2}\right) \\ fu = fu_g + K\left(\frac{\partial^2 v}{\partial z^2}\right) \end{array} \right.$$

With boundary conditions given by $u(0) = 0 = v(0)$, and $u(z)\tilde{u}_g \ \wedge \ v(z)\tilde{v}_g$ when $z \to \eta$. Solutions of the above equations can be given by, attending to the boundary conditions:

$$\left\{ \begin{array}{l} u = u_g - e^{-\xi}\left(u_g \cos\xi + v_g \sin\xi\right) \\ v = v_g + e^{-\xi}\left(u_g \sin\xi - v_g \cos\xi\right) \end{array} \right.$$

with

$$\xi = z\sqrt{\frac{f}{2K}} \equiv \frac{z}{D_E}.$$

When equating the wind shear stress with the turbulent viscous term we get

$$\frac{1}{\rho_a}\left(\tau_{0x},\ \tau_{0y}\right) = K\left(\frac{\partial u}{\partial z},\ \frac{\partial v}{\partial z}\right)(0) = \frac{K}{D_E}\left(u_g - v_g,\ u_g + v_g\right)$$

The latter equation shows that the wind stress is northward when the geostrophic component of the current velocity is North-Eastward ($u_g = v_g$).

The results of the vertical 30 m deep model, with 30 one-meter layers, show the Ekman layer effect quite clearly, also the Ekman spiral appears, though it cannot be well represented in the figure below. As it can be seen in figure 3.1.1 the Ekman depth corresponds to about 10 meters which is consistent with the expected theoretical value of $D_E = \sqrt{\frac{2K}{f}}\tilde{1}0\ m$ for values of $K = 0.001$ m^2/s (arbitrary value) and $f = 1.024^{-4}$ Hz (adequate for around 42° Lat). The time serie of the velocity modulus vertical profile is illustrated for three cases: (a) without the coriolis force, (b) with coriolis and constant turbulent viscosity, (c) with Coriolis and the GOTM $k-\epsilon$ model parametrized according to Canuto et al. (2001a). The velocity modulus shows a periodic oscillation of about 17.8 hours, which corresponds to the Coriolis frequency at the studied latitude 42°N. This value is confirmed by the peak of the FFT analysis in figure 3.2. A significant difference is shown between the GOTM turbulence model and the constant vertical viscous coefficients in figure 3.2.

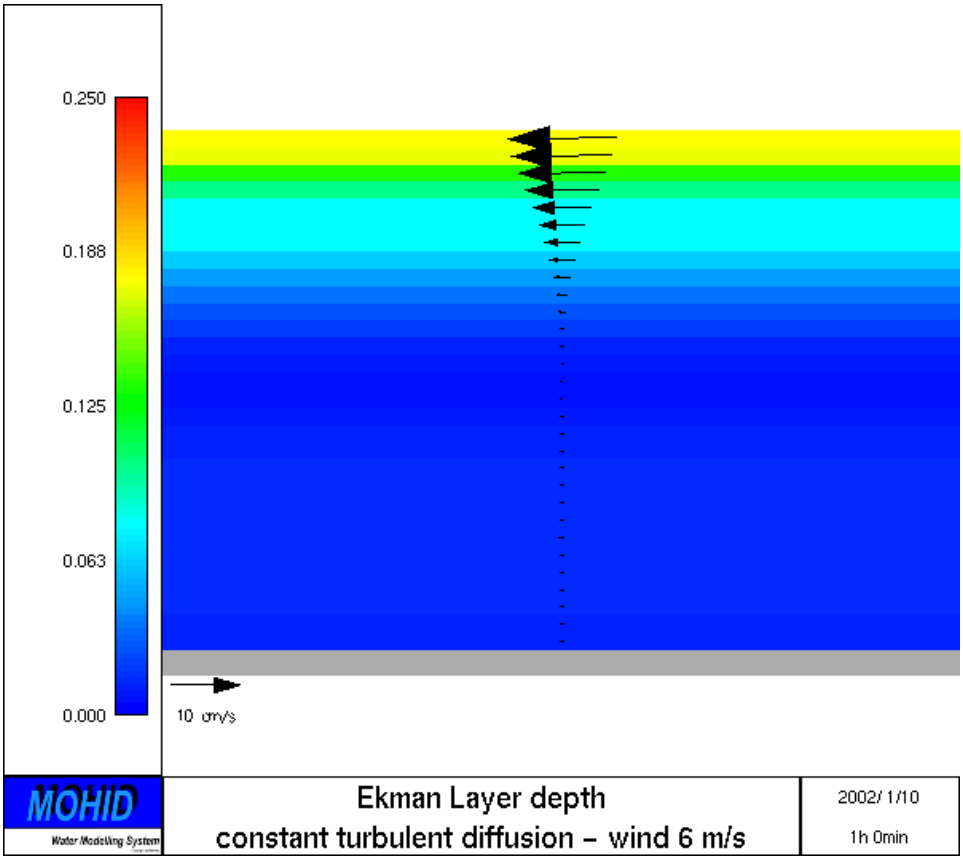

Figure 3.1: Ekman spiral projected along the U-component of velocity, under a constant wind forcing of 6 m/s, in a 30 layers and 30 meters depth domain. The arrows indicate the intensity and direction of the U-component of velocity. The color map indicate the velocity intensity.

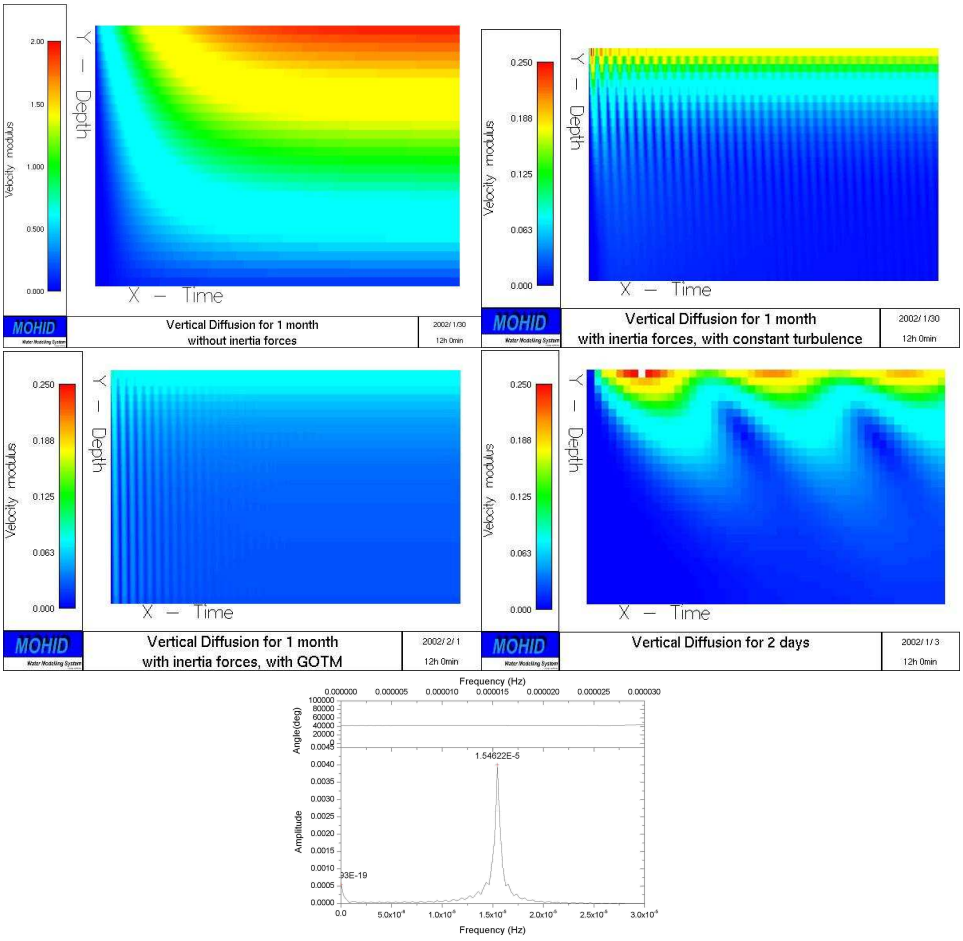

Figure 3.2: The four topmost panels are profile timeseries of the velocity intensity for different test-cases of the same 30 layered model. The top left panel represents a monthly profile timeseries excluding the Coriolis force in the solved equations. The top right panel included the full one-dimensional equation but with constant vertical turbulent viscous coefficients for the same period. The middle left panel shows the same configuration but with the GOTM turbulent model. The middle right panel displays a zoom-in in time of the top-right panel, displaying a 2 day timeserie. The bottom panel displays the timeserie FFT frequency spectrum for the vertical model results with Coriolis force.

3.1.2 Application to a test-case: PAPA station

Station PAPA (145°W, 50°N) is situated in a region where horizontal advection of salt and heat is small. Furthermore, meteorological data of long term observations are available, as well as temperature profiles. Various authors used these data to validate vertical turbulence models, authors such as the makers of the GOTMBurchard et al. (2004). As MOHID uses the GOTM code to calculate both, viscosity and diffusivity coefficients, this test-case tries to reproduce the GOTM results from their experiment applied to the PAPA station, as described in the GOTM manual, as a mean to validate the vertical model. What was meant in the beginning, (to validate, by direct comparison, one model with the other), turned out, in the end, to become the exposure of an interesting feature known as the pressure correction effect in the Brunt-Vaisalla frequency (Brunt, 1927) in the first hundred meters of a stratified water column. This correction to the equation of state of sea-density affects the Brunt-Vaisalla frequency enough to give rise to several degrees of difference in the SST in this test-case. This is due to the fact that the turbulence closure schemes employed by the GOTM make use of the local stratification frequency in order to calculate the vertical viscous coefficients. From the GOTM site (www.gotm.net) the required data for the experiment was retrieved: the salinity and temperature profiles for the initial conditions; the wind stress, the surface radiation, the latent heat, the sensible heat and the infrared radiation for the surface forcing. We also defined the same bottom and surface rugosity values, as well as the light extinction coefficients for turbid waters of type II first described by Jerlov (1968). As MOHID is intrinsically a tri-dimensional model, horizontal null-gradients for all properties were imposed. As the bottom slope is null, by continuity, there is no vertical advection during the experiment. In parallel, the latest version of GOTM is compiled and is run with this test-case configuration, to obtain results, exactly comparable with the MOHID results. For both models are used a k-e model for the turbulent kinetic energy, with stability functions described in Canuto et al. (2001a); the length scale is calculated with a dynamic dissipation rate equation and no internal wave parameterization was used. The preliminary results, with pressure correction in both models, for SST and temperature profile with time are found to be quite different than expected, as can be seen in figure 3.3. These results clearly show an abnormal difference between the MOHID and GOTM's runs: accumulated heat in the upper layers in MOHID (lower left panel of figure3.4) give a rise in the SST of nearly 3 degrees during summer (lower right panel of figure3.4). Why is that so? In some references(Chapra, 1997),

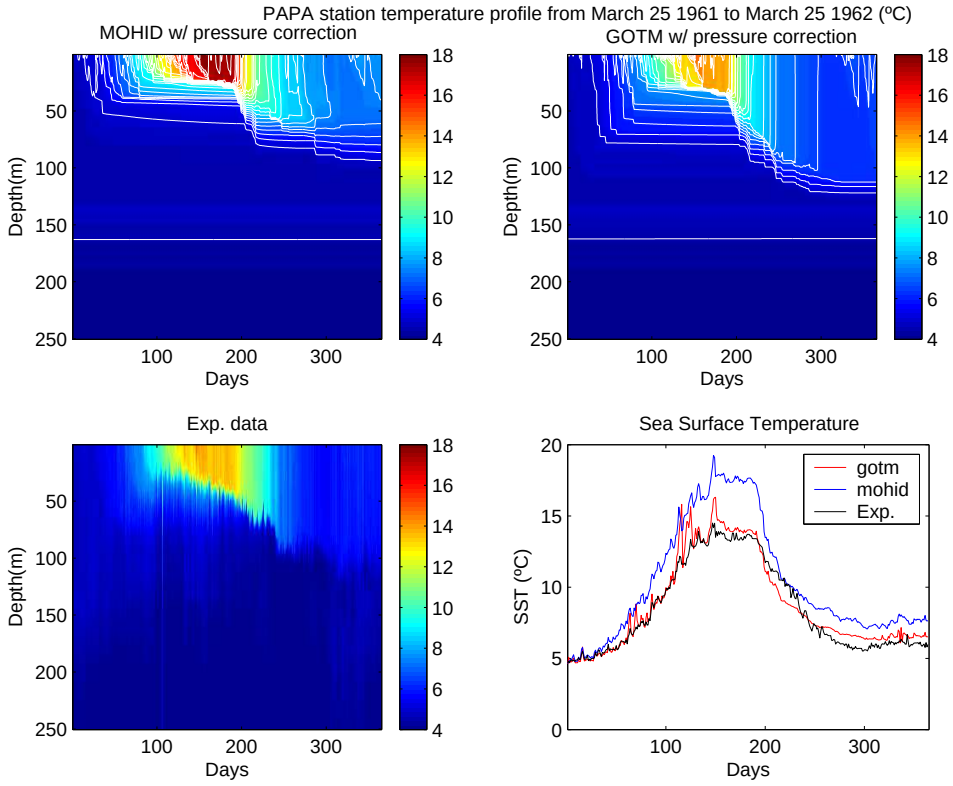

Figure 3.3: In the upper left panel: the temperature profile given by MOHID with pressure correction. In the upper right panel: the temperature profile given by GOTM v3 with pressure correction. In the lower left panel: the experimental data temperature profile. In the lower right panel: the SST given by GOTM, MOHID and in-situ data. All the isopleth are spaced of a half degree between the extrema of the color scale.

temperate lakes are defined as those with temperature above 4°C in winter, thermal gradients large, two circulation periods in spring and late autumn. This describes the PAPA station situation; furthermore it is stated that the thermal regime of those water columns is primarily the result of the interplay of two processes: (1) heat and momentum transfer across the water's surface and (2) the force of gravity acting on density differences within the water column. Thus, the wind tends to mix the water column, but buoyancy effects tend to inhibit such mixing. Hence, the difference between both models results could be explained, whether from heat or momentum transferred at the surface, whether from buoyancy effects. To confirm the heat fluxes balance and to test if both models were conservative, the heat in the water column was integrated for both models and was compared to the surface heat exchange. The results are shown in figure 3.4 and they show that GOTM is clearly conservative, whereas MOHID is nearly conservative (upper right panel of figure 3.4) with a slight gain in heat increasing up to 5 : 1000 at the end of the year (lower right panel of figure 3.4). The conservativity issue has to be investigated within MOHID, however we can still conclude that, for the duration of the experiment, both models are conservative as regards accumulation of heat without biasing the final conclusions. Since the conservation of heat is confirmed for both models, the main hypotheses that are left to explain the differences, are those of the conservation of momentum and of the buoyancy effects. The buoyancy gradient is also known as the square of the Brunt-Vaisalla frequency. If we look at the evolution of the Brunt-Vaisalla frequency in MOHID and in GOTM (figure 3.5) we do find relevant differences. For instance we get exceeding buoyancy gradients in the upper layers for the MOHID model compared to GOTM. This is a major hint explaining the difference of the results shown in figure 3.3. Exceeding buoyancy gradients in the upper layers in MOHID would inhibit the mixing in the vertical columns while deficient buoyancy gradients below the upper layers would increase the mixing. And these are the results from the upper left panel of figure 3.3: an excess of temperature in the upper layers of MOHID (possibly due to a deficient mixing) and, below, a negative difference in temperature (possibly due to an excessive mixing). But how can this be, if both models use the same UNESCO equation of state for density $\rho = \rho(S, T, p)$(Millero and Poisson, 1981; Millero et al., 2008)? Furthermore, when both models are run with the UNESCO equation of state $\rho = \rho(S, T)$, without the pressure correction, the obtained results are presented in figure 3.6. The results are basically very similar. They show differences (lower left panel of figure 3.6) along the region of the thermocline, where the gradients in temperature are sharper. Also differ-

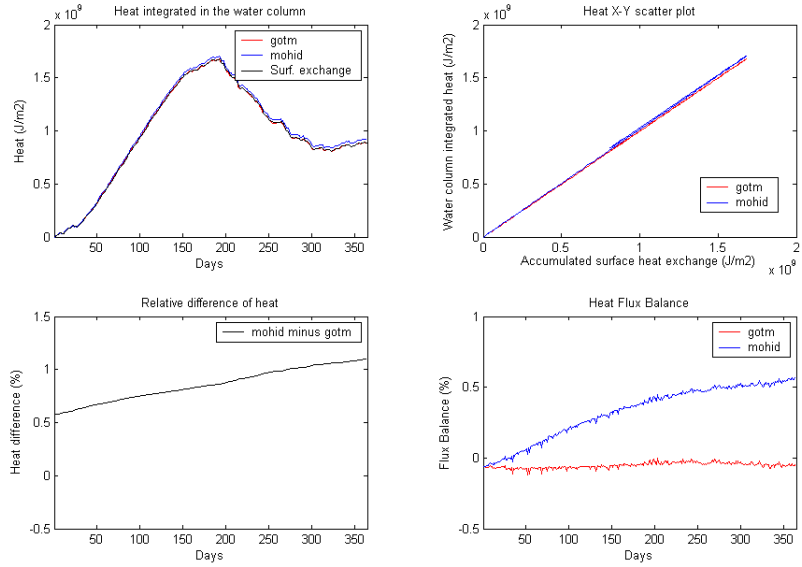

Figure 3.4: In the upper left panel: the accumulated heat integrated in the water column and the accumulation of heat exchanged at the surface. In the upper right panel: the X-Y scatter plots of accumulated heat of GOTM and MOHID versus the accumulation of heat exchanged at the surface. In the lower left panel: the relative difference in heat between MOHID and GOTM. In the lower right panel: the relative difference in heat of MOHID and GOTM with the surface exchange.

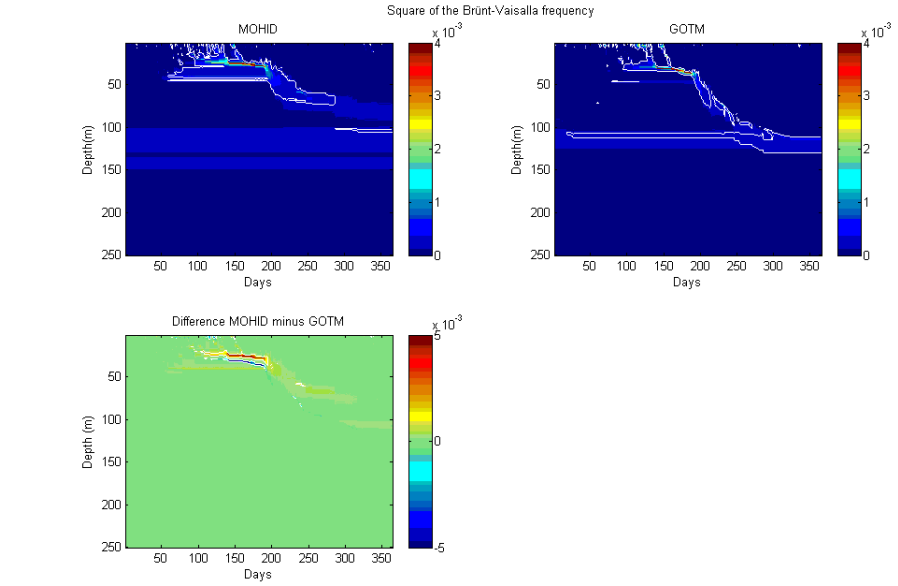

Figure 3.5: Evolution of the square of the Brünt-Vaisalla frequency in depth over time. Upper left panel: results from MOHID. Upper right panel: results from GOTM. Lower left panel: Differences of MOHID related to GOTM. In all the panels, the extrema values are beyond the range of the color scale. This is so in order to put in evidence the differences of patterns between the results. Extrema values are (0, ¿0.01) for the upper left panel; (-0.002, ¿0.008) in the upper right panel and (-0.01, ¿0.01) for the lower panel. The isopleth of the upper panels is set to 2E-4 s-2 and the isopleths of the lower panel are set to -8E-4 and 8E-4.

ences are found in the SST where the GOTM tends to point out some sharp peaks that MOHID smoothes out, but that is all. In sum both models give very similar results. When figure 3.6 is compared to figuree 3.3, the most striking observation is that MOHID shows a high sensitivity to the pressure correction factor, while GOTM doesn't. Figure 3.7 shows the correspondent buoyancy gradient of figure 3.6 results. Both buoyancy gradients are very similar. What is the influence of the pressure correction in the buoyancy gradient (i.e. the Brunt-Vaisalla frequency)? Is it relevant, like tends to be pointed out by MOHID? Or is it irrelevant like shows GOTM? The square of the buoyancy gradient is usually given by

$$\begin{cases} N^2(S,T,p) = \frac{g}{\rho_0}\frac{\partial\rho(S,T,p)}{\partial z} \\ N^2(S,T) = \frac{g}{\rho_0}\frac{\partial\rho(S,T)}{\partial z} \end{cases}$$

as seen in Cushman-RoisinRoisin (1994), depending if the equation of state (EOS) depends on pressure (depth) or not. Now, if we compare MOHID results with the experimental data from the PAPA station, as can be seen in figures 3.3 and 3.6, only the non-pressure correction model run gives realistic results; particularly in the SST of figure 3.6, where the fit is more accurate than for GOTM's results, as the sharp peaks that appear for GOTM vanish in the experimental data. As pointed out in GOTM's manual, the sea surface temperature maximum is exceeded by over 2°C for all parameterizations except when using the Kantha and Clayson (1994) internal wave parameterization. This is the case of the upper panel of figure 3.6. This overestimation was estimated to be due to the numerical scheme characteristics as pointed out in the GOTM manual. It was also suggested by Large et al. (1994) that a change from turbid waters of type II to type Ia could cause a change of about 1°C in the maximum SST. After day 230, the SST is decreasing much more slowly in both models. This was already pointed out in the GOTM manual. This discrepancy is due to the winter advection in the seasonal thermocline and its subsequent mixing into the mixed layer as discussed by Large et al. (1994).

A note about the GOTM coding for the Brunt-Vaisalla frequencyBrunt (1927): when discretizing equation (3.1) the GOTM code performs

$$\frac{b(S_{i+1},T_{i+1},p_{i+1}) - b(S_i,T_i,p_{i+1})}{\Delta z_{i+1}}$$

where b is the buoyancy. Clearly, the pressure correction effect in the buoyancy is, thus, nullified. This explains the results: the pressure correction

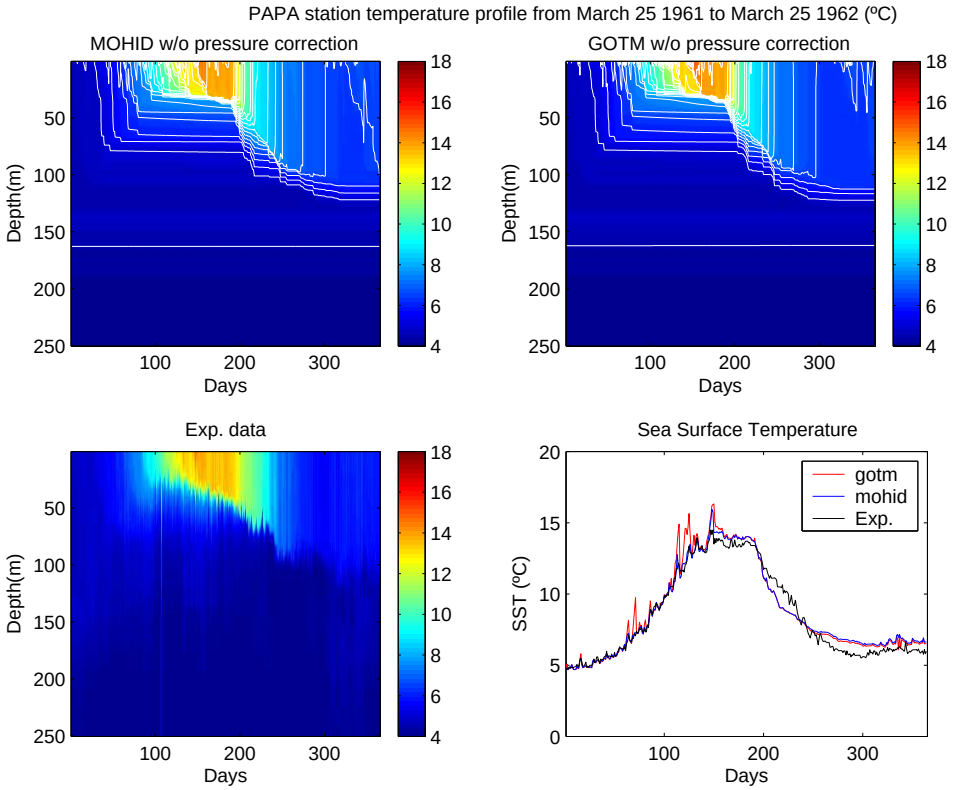

Figure 3.6: In the upper left panel: the temperature profile of MOHID without the pressure correction. In the upper right panel: the temperature profile of GOTM without the pressure correction. In the lower left panel: the temperature profile of in-situ data. In the lower right panel: the Sea Surface Temperature of MOHID, GOTM without the pressure correction and in-situ data. All isopleths spaced of half degree between the extrema of the color scale.

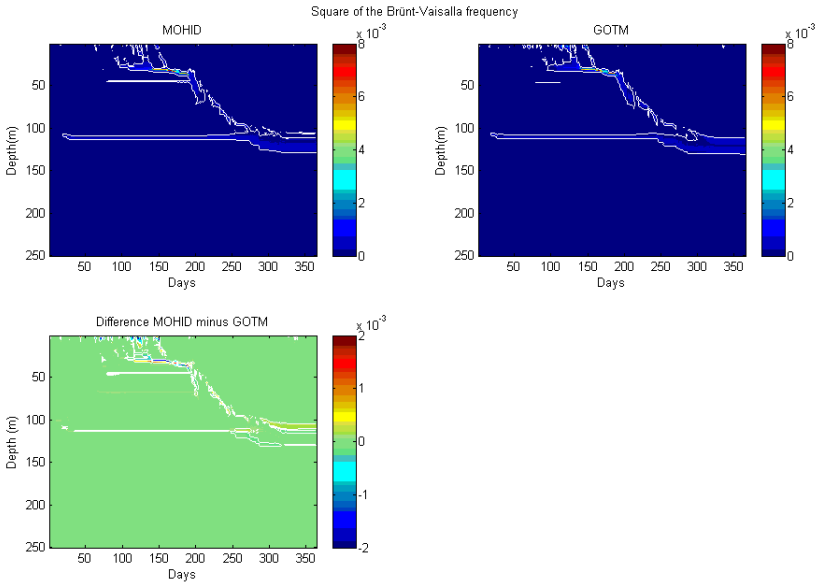

Figure 3.7: The square of the Brünt-Vaisalla frequency. In the upper left panel: the result of MOHID without the pressure correction. In the upper right panel: the result of GOTM without the pressure correction. The isopleth is of 2E-4 s-2. In the lower panel: the differences between MOHID and GOTM with isopleths of -1E-4 and 1E-4 s-2.

becomes thus essentially nullified once the buoyancy of a water parcel following its lagrangian perturbatory trajectory is considered sufficiently slow, relatively to pressure waves, so that it's inner temperature and salinity remain constant. Thus, it's temperature and salinity remain the same, but it adjusts its pressure to the surrounding pressure (adiabatically). Historically, the parameterizations for the turbulence models were made with simpler and linearized density equations, subsequent changes and corrections were added to the state equation. Hence what, then, would provide good results, now, gives poor results as the pressure correction was added in the state equation. The conclusions of this test-case in trying to reproduce the results from GOTM applied to the PAPA station are essentially: (1) The MOHID vertical 1D model reproduces well the GOTM results without pressure correction, it reproduces even better than GOTM the SST when comparing with the experimental data as some noisy peaks appearing in GOTM clear out with the MOHID model. However, the MOHID model shows a slight tendency in gaining heat ($5 : 1000$ at end of the run). It would be best to investigate further the heat gain. (2) The pressure correction turns out to represent a relevant correction for mixing issues as the heat distribution during the run is clearly different. This is because the buoyancy gradient was wrongly calculated:

$$\frac{b(S_{i+1}, T_{i+1}, p_{i+1}) - b(S_i, T_i, p_i)}{\Delta z_{i+1}}.$$

This is the direct implementation of the Roisin (1994) buoyancy gradient equations, and it's conceptually wrong.

Problem with the stratification frequency

While trying to reproduce the PAPA station test-case GOTM results with MOHID, we tumbled into a different conception of the Brunt-Vaisalla frequency when using the pressure correction to the UNESCO (Millero and Poisson, 1981; Millero et al., 2008) density EOS (Roisin, 1994). The original version in MOHID was

$$N^2 = -\frac{g}{\rho_0}\frac{\partial \rho}{\partial z} \tag{3.1}$$

which is the same formula stated in Roisin (1994) It worked fine without the pressure correction on the EOS. However, turning the pressure on caused an extra stratification leading to differences over 3 degrees in the SST of the PAPA station test-case. This work pin-points exactly why. Furthermore,

this work suggests that different stratification frequencies exist, one for each fluid present within the medium. This has direct implications in the evaluation of the stratification frequencies for tracers other than temperature.

3.1.3 Review of the state-of-the-art on static stability

Mellor (1996) introduces a new density gradient "suitable" for static stability i.e a "suitable" Brunt-Vaisalla frequency:

$$\frac{\partial \tilde{\rho}}{\partial z} \equiv \frac{\partial \rho}{\partial S}\frac{\partial S}{\partial z} + \frac{\partial \rho}{\partial \Theta}\frac{\partial \Theta}{\partial z} \tag{3.2}$$

$$N^2 \equiv -\frac{g}{\rho}\frac{\partial \tilde{\rho}}{\partial z} \tag{3.3}$$

where the term $\frac{\partial \rho}{\partial p}\frac{\partial p}{\partial z}$ in eq. (3.2) is excluded because

> *Physically one excludes the change in density a particule undergoes by an adiabatic change in depth and pressure; it is only non-adiabatic differences that are important to stability. G.M. (Mellor, 1996)*

If we use the hydrostatic approximation $\frac{\partial p}{\partial z} = -\rho g$ and if we set $\frac{\partial \rho}{\partial p} = c^{-2}$ where c is speed of sound in the medium, then we obtain $\frac{\partial \rho}{\partial p}\frac{\partial p}{\partial z} = -\frac{\rho g}{c^2}$.

$$\frac{\partial \rho}{\partial z} = \frac{\partial \rho}{\partial S}\frac{\partial S}{\partial z} + \frac{\partial \rho}{\partial \Theta}\frac{\partial \Theta}{\partial z} + \frac{\partial \rho}{\partial p}\frac{\partial p}{\partial z} = \frac{\partial \tilde{\rho}}{\partial z} - \frac{\rho g}{c^2} \tag{3.4}$$

Thus the Brunt-Vaisalla frequency becomes, according to G. Mellor

$$N^2 \equiv -\frac{g}{\rho}\frac{\partial \tilde{\rho}}{\partial z} = -\frac{g}{\rho}\left(\frac{\partial \rho}{\partial z} + \frac{\rho g}{c^2}\right) = -\frac{g}{\rho}\frac{\partial \rho}{\partial z} + \frac{g^2}{c^2} \tag{3.5}$$

He also states that

> *Another good approximation is $\frac{\partial \tilde{\rho}}{\partial z} = \frac{\partial \rho_\Theta}{\partial z}$. Thus the potential density function can be used to determine horizontal density gradients which drive horizontal motions and vertical density gradients which govern vertical mixing. (Mellor, 1996)*

where $\rho_\Theta \equiv \rho(S, \Theta)$. POM uses eq. (3.5) to calculate its N^2.
Hallberg (2005) defines

$$N^2 = -\frac{g^2}{\alpha^2}\left(\frac{d\alpha}{dp} - \left.\frac{\partial \alpha}{\partial p}\right|_{\Theta, S}\right) \tag{3.6}$$

where α is the specific volume or thermal expansion coefficient.
Kantha and Clayson (2000) define:

$$N^2 = g\alpha\left(\Gamma + \frac{dT}{dz}\right) - g\beta\frac{dS}{dz} \tag{3.7}$$

where $\alpha \equiv \frac{1}{\rho}\left.\frac{\partial\rho}{\partial T}\right|_{p,\,S}$, $\beta \equiv \frac{1}{\rho}\left.\frac{\partial\rho}{\partial S}\right|_{p,\,T}$ are the thermal expansion and haline contraction coefficients and where

$$\Gamma \equiv -\left.\frac{dT}{dz}\right|_{\sigma} = g\,v_s\,T/c_p \tag{3.8}$$

is the adiabatic lapse rate, v_s being the specific volume (Mcdougall and Feistel, 2003).
The latter expression is equivalent to the following one, in terms of potential temperature

$$N^2 = g\left(\alpha\frac{d\Theta}{dz} - \beta\frac{dS}{dz}\right) \tag{3.9}$$

as was suggested by Eden and Willebrand (1999) or by Mcdougall et al. (2003). MOM4 uses the Accurate and computationally efficient algorithms of Mcdougall et al. (2003). ROMS uses the Jackett and Mcdougall (1995) EOS algorithm. It seems relevant to use potential temperature to calculate buoyancy effects in the stratification since it includes the adiabatic lapse rate effect.

3.1.4 The principle of Archimedes

It will be shown that equations (3.5), (3.6), (3.7) and (3.9) under the hydrostatic approximation, are equivalent, within a certain approximation, to a more generic and physically simpler to understand definition of static stability. It relies solely on the principle of Archimedes when small disturbances are applied to a Test Material Volume (TMV) at rest in a stably stratified fluid. The system and its axis is represented in figure 3.8.
The principle of archimedes states that the buoyant restoration force is equal to the weight of the dislocated volume of the surrounding environment. Hence if a TMV is dislocated from rest along the vertical in a stably stratified fluid, it will feel the buoyant restoration force driving him back towards his rest position. Putting it in equations this gives:

$$\begin{aligned}
\tilde{\rho}\,\ddot{z} &= -\tilde{\rho}\,g + \rho\,g, \\
\ddot{z} &= g\,\frac{\rho - \tilde{\rho}}{\tilde{\rho}}, && (3.10)\\
\ddot{z} &= -g', && (3.11)
\end{aligned}$$

where the ˜ stands for the TMV state variables, thus $\tilde{\rho}$ is the TMV's density, ρ is the fluid's density, g is the local gravity acceleration, $g' \equiv g\frac{\tilde{\rho}-\rho}{\tilde{\rho}}$ is the reduced gravity, z is the TMV vertical position coordinate and $\ddot{z}$ is the TMV local vertical acceleration. Thus equation 3.10 gives the perturbation motion of any TMV at rest, embedded in any stably stratified environment, according to the principle of Archimedes. Depending on the composition of the constituents of the TMV and of the enviroment, the perturbation motion can quite complex as the evolution of the thermodynamic properties of the constituents can be highly non-linear. Nevertheless, a sound physical intuition would yield, to a first order of approximation, that the motion due to small perturbations around the rest position would be oscillatory, similar to the harmonic oscillator motion. The differential equation of the oscillatory motion is linear, and is given by Hooke's law

$$\ddot{z} = -\omega^2 z, \tag{3.12}$$

where $\frac{\omega}{2\pi}$ is the oscillation frequency (in Hz). Hence, the square of the angular oscillation frequency is found by taking the vertical derivative of equation 3.12 at the rest position, i.e.

$$\omega^2 = -\frac{d\ddot{z}}{dz}. \tag{3.13}$$

Hence, approximating the motion of the TMV perturbed from its rest position given in equation 3.10 to Hooke's law in equation 3.12 yields

$$\begin{aligned} \omega^2 &= -g\frac{d}{dz}\left(\frac{\rho-\tilde{\rho}}{\tilde{\rho}}\right) \\ &= -\frac{g}{\tilde{\rho}}\frac{d\rho}{dz} + \frac{g\,\rho}{\tilde{\rho}^2}\frac{d\tilde{\rho}}{dz} \\ &= -\frac{g}{\rho}\frac{d\,(\rho-\tilde{\rho})}{dz}, \end{aligned} \tag{3.14}$$

which is a generic frequency of oscillation. It must be noted that the derivative was taken at the position of rest where $\tilde{\rho} = \rho$. A particular case of equation 3.14, envolving air parcels and water parcels disturbed from rest, was first considered by Brunt (1927) and its frequency was called the Brunt-Vaisalla frequency.

The TMV could be any material where the thermodynamic's laws are valid. Let us undertake the following mental experience: consider a cork of density higher than surface seawater at rest in a stable stratified water column. Now consider a small vertical disturbance of it's mean rest state. Clearly,

the restoring buoyant force will be equal to the balance between the cork and the displaced water weights (or densities) i.e. $Fb = \Delta\rho g$. Since the cork's density is the same of the surrounding medium when at rest, we can state that buoyancy is proportional to the density's vertical gradient and that that a normalized measure of the effect of buoyancy is

$$\frac{1}{\rho_0}\frac{\partial\rho}{\partial z} \tag{3.15}$$

where ρ is the medium's density and ρ_0 a reference density (e.g. the cork's density). This leads to equation (3.1).
However, when considering displacements of water parcels, these parcels no longer behave like a cork. They undergo expansion and contractions of their volume or they could exchange mass, heat etc... Thus, when applying a disturbance to a generic TMV, one has to enter into consideration its own density variations (albeit adiabatic and isentropic - i.e. reversible), $D\tilde{\rho}$. This wasn't required for the cork, because the cork had not any density variations. This is not the case for a generic TMV embedded in a given medium. The principle of Archimedes remains unchanged, and the generic measure of the buoyancy effect in a stably stratified fluid, called the square of the Brunt-Vaisalla angular frequency, is written as

$$N^2 = -\frac{g}{\rho_0}\left(\frac{d\rho}{dz} - \frac{d\tilde{\rho}}{dz}\right), \tag{3.16}$$

following equation 3.14. Equation (3.16) is completely generic, has no approximations, is original, should be considered as the de facto adequate squared stratification frequency and yields the following discretization:

$$N_i^2 = -\frac{g}{\rho_0}\left(\frac{\rho\left(\Theta_{i+1}, S_{i+1}, p_{i+1}\right) - \rho\left(\Theta_i, S_i, p_i\right)}{z_{i+1} - z_i}\right. \tag{3.17}$$

$$\left. - \frac{\tilde{\rho}\left(\tilde{\Theta}_i, \tilde{S}_i, \tilde{p}_{i+1}\right) - \tilde{\rho}\left(\tilde{\Theta}_i, \tilde{S}_i, \tilde{p}_i\right)}{z_{i+1} - z_i}\right) \tag{3.18}$$

where i, indexes the state of rest and $i+1$, the perturbated state. If the TMV is incompressible and has no material variation of its density (like a cork), then equation (3.16) reduces to the original equation (3.1). We still need to relate, somehow, the TMV's density with the exterior density in order to make some use of eqs.(3.16) and (3.17). Figure (3.8) illustrates the perturbation applied to a seawater TMV initially at rest. It undergoes an adiabatic transformation and conserves its mass, hence only the pressure

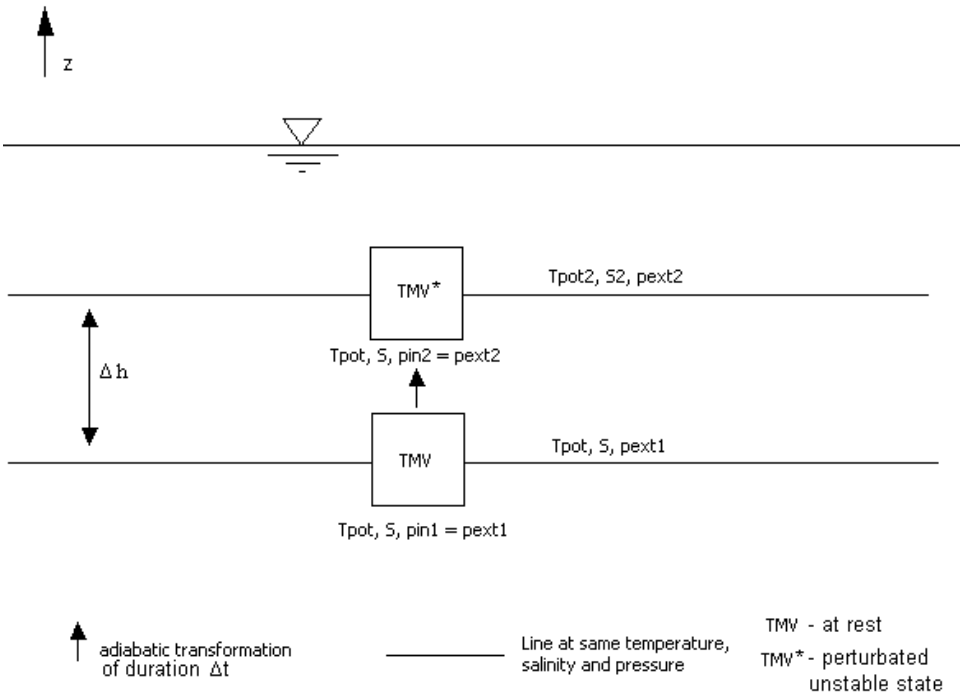

Figure 3.8: Illustration of an adiabatic and isohaline transformation of a seawater TMV, from a state of rest, to a perturbated state, away from equilibrium. The transformation is slow enough, so that compression forces have time to restore the pressure inside the TMV along the way.

changes. How does the pressure changes? Well, it changes between its original value and the exterior value, it can even fluctuate in time. Thus we need another assumption:

$$\frac{\Delta h}{\Delta t} \ll c_s. \tag{3.19}$$

where c_s is the sound of speed. This allows the TMV to adiabatically adjust its inner pressure to the surrounding pressure as the speed of sound is far greater than the speed of the transformation. Hence, under this assumption, $\tilde{p} = p$ all along the transformation (see figure 3.8). Furthermore, if it's a seawater TMV, then $\tilde{\Theta}_i = \Theta_i$, $\tilde{S}_i = S_i$ and the discretized eq.(3.16) simplifies to

$$N_i^2 = -\frac{g}{\rho_0}\left(\frac{\rho\left(\Theta_{i+1}, S_{i+1}, p_{i+1}\right)}{z_{i+1} - z_i} - \frac{\rho\left(\Theta_i, S_i, p_{i+1}\right)}{z_{i+1} - z_i}\right). \tag{3.20}$$

This discretization is equivalent to the one used in GOTM, and, now, in MOHID. Also, in the absence of pressure correction, (3.20) reduces to the discretized form of (3.1).

3.1.5 The equivalence of the interpretation

Let us show the equivalence between this interpretation of the Brunt-Vaisalla frequency and Mellor's:
The variation of $\tilde{\rho} = \tilde{\rho}\left(\tilde{\Theta},\, \tilde{S},\, \tilde{p}\right)$ along a path s parameterized by t is stated in the material derivative

$$\frac{D\tilde{\rho}}{Dt} = \frac{\partial\tilde{\rho}}{\partial\tilde{\Theta}}\frac{D\tilde{\Theta}}{Dt} + \frac{\partial\tilde{\rho}}{\partial\tilde{S}}\frac{D\tilde{S}}{Dt} + \frac{\partial\tilde{\rho}}{\partial\tilde{p}}\frac{D\tilde{p}}{Dt} \tag{3.21}$$

$$= \frac{d\tilde{\rho}}{ds}\frac{ds}{dt} \tag{3.22}$$

The line path is vertical, the thermodynamical process is adiabatic ($d\tilde{\sigma} = 0$) and mass conservative ($D\tilde{S} = 0$). Consequently, $D\tilde{\Theta} = 0$. Thus equation (3.21) simplifies and writes

$$\frac{d\tilde{\rho}}{dz} = \frac{\partial\tilde{\rho}}{\partial\tilde{p}}\frac{D\tilde{p}}{Dt}\left(\frac{dz}{dt}\right)^{-1} \tag{3.23}$$

The variation of the residual scalar field $\rho = \rho\left(\Theta,\, S,\, p\right)$ along a path s per line element ds, is stated as

$$\frac{d\rho}{ds} = \frac{\partial\rho}{\partial\Theta}\frac{d\Theta}{ds} + \frac{\partial\rho}{\partial S}\frac{dS}{ds} + \frac{\partial\rho}{\partial p}\frac{dp}{ds}. \tag{3.24}$$

In this case, it rephrases as

$$\frac{d\rho}{dz} = \frac{\partial\rho}{\partial\Theta}\frac{d\Theta}{dz} + \frac{\partial\rho}{\partial S}\frac{dS}{dz} + \frac{\partial\rho}{\partial p}\frac{dp}{dz}. \tag{3.25}$$

Equations (3.21), (3.23) and (3.25) give the correct Brunt-Vaisalla frequency stated in eq.(3.16). If we choose the adiabatic path, slow enough compared to compressibility forces ($\frac{dz}{dt} << c_s$, where c_s is the medium's sound speed), such that the inner pressure from the TMV always balances the medium's pressure, then $\frac{D\tilde{p}}{Dt} = \frac{dp}{dt}$ would hold, and eq.(3.23) would simplify under the hydrostatic approximation to

$$\frac{d\tilde{\rho}}{dz} = \frac{\partial\tilde{\rho}}{\partial p}\frac{dp}{dz} = -\frac{\rho g}{c_s^2} \tag{3.26}$$

where c_s is the speed of sound in the TMV. It is, approximately, the speed of sound in the medium.
The Brunt-Vaisalla frequency then writes

$$N^2 = -\frac{g}{\rho}\frac{\partial\rho}{\partial z} + \frac{g^2}{c_s^2} \tag{3.27}$$

which is the same as equation (3.5). Q.E.D.
An alternative demonstration was already described by Mellor in the appendix of *POM user's guide* (Mellor, 1992).

3.1.6 Discussion

The assumptions are the Archimedes principle and the adiabatic, isohaline perturbation with pressure equilibrium along its path. The concept is clear and simple. It clearly implies that *in-situ* temperatures need to be corrected for potential ones, because of the adiabatic lapse rate effect. Also the use of the potential density without pressure correction seems indeed a very good approximation, as was already pointed out by Mellor. Of all the codes available for the calculation of the Brunt-Vaisalla frequency (GOTM, ROMS, POM, MOM4, MOHID), the GOTM's approach seems the more direct-to-the-physics. Because it is so simple it is probably the one that introduces less round off errors. The others relate to the alternate equations reviewed in this work. The GOTM implementation of the Brunt-Vaisalla frequency has been since successfully implemented in MOHID. Now, since 2005, the GOTM and the MOHID results of the PAPA station case-study are nearly identical, both with use of correction of pressure or without.

3.2 The freshwater cylinder test-case

3.2.1 Objectives

To assess the reliability of Mohid in coastal simulations, we performed a classic well-known and well-described numerical experiment: the rotating freshwater cylinder experiment. We used the conditions of the Tartinville et al. (1998) experiment. We studied the formation of fronts, barotropic and baroclinic instabilities, the evolution of energy and of enstrophy of the system.

3.2.2 Description

The physical system to simulate is a square basin of constant depth with salty water under rotation. In the middle of the basin there is a cylindrical volume of less haline water.

The forces that apply to this cylindrical volume of water are: the buoyancy, a vertical force applied to the cylinder of lesser dense water which results of the balance from the gravity force and the vertical pressure gradient; and the horizontal pressure gradient due to the horizontal variation of density.

$$\int \frac{d\left(\rho\,\vec{v}\right)}{dt} dV = \sum \vec{F}$$

$$\sum \vec{F} = \int \left(\rho\,\vec{g}\right)\, dV + \int \left(-\vec{\nabla} p\right)\, dV + \ \ldots$$

Under these forces alone, the cylinder would simply emerge and spread over to the surface. The horizontal pressure gradient term separates itself into two modes: the external mode (giving birth to the barotropic force) and the internal mode (giving birth to the baroclinic force),

$$-p(z) = \int_{z'=z}^{\eta} \left(\rho - \rho_0\right) g\, dz' + \rho_0\, g\, \left(\eta - z\right)$$

$$-\frac{\partial p}{\partial x}(z) = \underbrace{\frac{\partial}{\partial x}\left(\int_{z'=z}^{\eta} \left(\rho - \rho_0\right) g\, dz'\right)}_{baroclinic\ force} + \underbrace{\rho_0\, g\, \frac{\partial \eta}{\partial x}}_{barotropic\ force}$$

An analysis of the initial condition of the system tells us that the density gradient has an inwards azimuthal symmetry, where the azimuthal axe is the

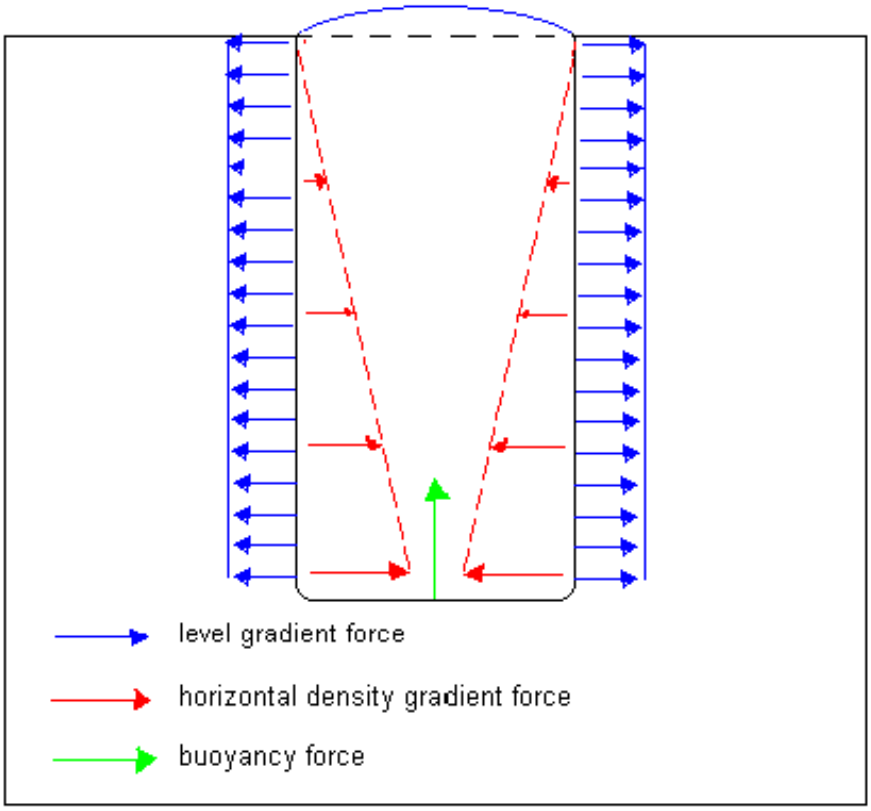

Figure 3.9: freshwater cylinder, pressure gradient and gravity forces.

cylinder's. The baroclinic force is nil at the surface and grows with depth as a result of the vertical integration. On the other hand, the level gradient is constant throughout the water column. Hence, if we release the system, the freshwater cylinder's bottom will be compressed inwards and pushed upwards by the baroclinic force and impulsion; this will immediately raise the water level of the freshwater cylinder, which in turn, will create an outwards barotropic force. The barotropic force will find herself unbalanced near the surface and will start spreading radially the freshwater. Near the bottom of the cylinder, where the baroclinic force is higher, the latter will overcome of the former and continue compressing inwards the freshwater cylinder (see figure 3.9). On top of that, a Coriolis acceleration exists due to the system's rotation which is perpendicular to the fluid flow. This tends

to create vortices.

$$\ldots + 2\,\vec{\Omega} \times \vec{v} = \int (\rho\,\vec{g})\; dV + \int \left(-\vec{\nabla} p\right)\; dV + \ldots$$

The experiment neglects surface or bottom stresses. It also neglects viscous terms, though it is present in the form of numerical diffusion.

Since the flow is divergent at the surface, the vortices will be anti-cyclonic; conversely, since the flow is convergent at the base of the cylinder, the vortices will be cyclonic.

The convergent/divergent structure creates an upward flow. The whole process will oscillate around geostrophic balance.

Co-rotating and counter-rotating vortices will appear around the central eddy produced by barotropic or baroclinic instabilities. These instabilities result from sheared currents near the density front and energy transfers from the average kinetic energy ($\overline{KE}$) to the perturbation kinetic energy (KE') and from the average available potential energy (Lorenz, 1955) ($\overline{APE}$) to KE' for barotropic and baroclinic instabilities, respectively, where $KE = \overline{KE} + KE'$ and $APE = \overline{APE} + APE'$ (i.e. both kinetic and available potential energy are separated in geostrophic and perturbed components).

In short, the barotropic process will generate a clockwise central eddy and anti-clockwise co-rotating eddies; while the baroclinic process will generate an anti-clockwise central eddy with clockwise co-rotating eddies(Tartinville et al., 1998). As a result, a mix of barotropic and baroclinic instabilities appears at all depths, while the central eddy remains barotropic at the surface and baroclinic at the bottom of cylinder.

Laboratory setups of this experiment show that 2nd order baroclinic and barotropic instabilities occur (2 secondary vortices around the center) and tend to grow. Pedlosky (1969) conjectured a law based upon the internal Rossby radius of deformation and the ratio of the cylinder radius with its depth that predicted the creation of baroclinic instabilities. It states that baroclinic instabilities should arise whenever the squared ratio of the cylinder radius versus the internal Rossby radius is higher than $\sqrt{2}$. This is the case in this experiment.

Pedlosky (1967, 1969) also suggests that, since the vortices are equally distributed around the cylinder's perimeter, the radius of the vortices produced times their order scales with the cylinder's radius. I.e:

$$R - fwc \propto n\,R - v$$

Tartinville et al. (1998) advances that the order of the baroclinic instabilities

should scale with the inverse of the Froude number:

$$n \propto \frac{\sqrt{g'\,h'}}{U},$$

where g' is the reduced gravity, h' is the freshwater cylinder depth and U is the characteristic intensity of flow velocity.

Roisin (1994) demonstrates that $\theta \equiv \frac{\overline{KE}}{\overline{APE}}$, the ratio of kinetic energy versus available potential energy in geostrophic balance, is proportional to the squared Froude number:

$$\theta \propto \frac{U^2}{g'\,h'}$$

Hence the order of the instability is related with θ by:

$$n \propto \theta^{-1/2} \tag{3.28}$$

Tartinville et al. (1998) also shows that the growth rate of the most unstable baroclinic mode in geostrophic balance is proportional to the Froude number:

$$\omega \propto \sqrt{\theta} \tag{3.29}$$

Equation (3.28) and equation (3.29) were developed in order to explain Tartinville et al. (1998) results based on the geostrophic kinetic and potential energy. It is the scope of this report to use these equations to predict qualitative results and, thus, to assess the validity of the former.

3.2.3 Model setup

The setup of the Tartinville et al. (1998) experiment is identical to the one tested with MOHID (table 3.2.3).

Exactly the same setup than Tartinville et al. (1998) was used.

3.2.4 Battery tests

The experience will be conducted in two main steps:

- The first step consists in assessing the optimal missing parameters.
- The second step consists in testing the several advection schemes using the optimal parameters determined in the first step.

The following methodology was adopted:

Table 3.1: Description of the model setup

Domain		
Parameter	Value	Observations
Depth	20 m	
Size	30 x 30 km	without relaxation zone
latitude	52°N	
Coriolis	1.15×10^{-4} s-1	
hor. res.	1 km	
layers	20 levels	
Cylinder		
Depth	10 m	
Radius	3 km	
Initial condition		
Salinity	$S = 1.1 * (d/3)8 + 33.75$	d is the cylinder radius.
Temperature	20°C	Constant.
Equation of state		
linear	$\rho = 1025 + 0.78 * (S - 33.75)$	
Simulation time		
Duration	6 days	
Vertical boundaries		
Bottom stress	none	
Surface stress	none	
Viscosity and diffusivity		
Vertical	none or minimal	
Horizontal	none or minimal	
Open boundary		
Momentum	null-gradient	
Water-level	four-points-wide relaxation to zero	coefficients of 1, 0.5625, 0.25, 0.0625
Salinity	four-points-wide relaxation to 34.85	coefficients of 1, 0.5625, 0.25, 0.0625

Table 3.2: Battery of time increment tests

Run ID	Time step (s)	Observations
1	600	Unstable
2	300	Good
3	150	Good
4	60	Good

1. First, the time increment below which there are no significant variations of the system was determined using a total variation diminishing (TVD) advection scheme.

2. Double precision was enforced so that it would increase the accuracy of the results when compared to single precision.

3. Several vertical coordinates available by Mohid were used (Cartesian, Sigma and Lagrangean) to determine which one minimizes numerical diffusion whilst not introducing too many errors.

4. Flather (1976) level radiation scheme alone was tested as an alternative to the use of flow relaxation schemes (FRS)(Martinsen and Engedahl, 1987) to see if it improves the quality of the results from the best configuration taken from above.

5. Finally, from the best configuration above, several methods for the calculation of the baroclinic force were tested. The best method is the one that minimizes the pressure gradient error (Beckmann and Haidvogel, 1993). The pressure gradient error is known to generate spurious vertical velocities in terrain following grids (Beckmann and Haidvogel, 1993).

The time increment was chosen accordingly to the computing available resources while the outputs yield stable results. The open boundary conditions are fully compliant so that the experiment may be compared with the Tartinville et al. (1998) benchmark. The second step is taken and a battery of the available advection schemes was tested (table 3.2.4). Some of them are similar to those employed in the models tested by Tartinville et al. (1998) (table 3.2.4).

Table 3.3: Battery of precision tests

Run ID	Precision
single	Single precision
double	Double precision

Table 3.4: Battery of vertical discretizations tests

Run ID	Vertical coordinate
cartesian	Cartesian
sigma	Sigma
Lagrangean	Lagrangean

Table 3.5: Battery of pressure gradient error tests (Sigma mesh only)

Run ID	Baroclinic force method
uniform	Uniform
linear	Linear
leibniz	Leibniz
leibniz2	Leibniz2

Table 3.6: Battery of advection schemes tests. The first number is the advection scheme ID. The second number (optional) is the ID of the TVD type of scheme. Both numbers seen in table 3.2.4

Run ID	Momentum		Salinity	
	horizontal	vertical	horizontal	vertical
1	1	1	1	1
2	2	4/4	2	4/4
3	3	4/4	3	4/4
4	4/4	4/4	4/4	4/4
5 MU	1	1	4/4	4/4
6 DE	2	5	3	1
7 CL	5	1	5	1

Table 3.7: ID numbers of advection schemes and of TVD schemes (variants of the TVD).

Advection	ID	TVD	ID
Upwind	1	MinMod	1
Upwind2	2	VanLeer	2
Upwind3	3	Muscl	3
CentralDif	4	SuperBee	4
TVD	5	PDM	5

Table 3.8: Numerical models and their advection schemes, as tested by Tartinville et al. (1998).

Models	Momentum		Salinity	
	Horizontal	Vertical	Horizontal	Vertical
CL	SAHS	Upwind	SAHS	Upwind
DE	SI	Upwind 2nd	SI	Upwind
IF	Quickest	Quickest	Quickest	Quickest
MU	Upwind	Upwind	TVD	TVD
PO	PPM	PPM	PPM	PPM

3.2.5 Results

The results from the runs will mainly be the volume integrated conserved quantities such as energy and enstrophy, and the surface section with horizontal currents and with isohalines. The former type of results will allow us to stipulate if the model is stable and conservative, while the latter type will allow a more visual interpretation of the simulated process concerning the vortices formations and the influence of the open boundaries.

Opimizing numerical parameters

As can be seen from the results (figure 3.2.5 and 3.2.5) the system doesn't show sensitivity to time increment. The changes for KE, PE and Enstrophy are inferior to 1The changes in the UV current field at the surface at 144 h are more intense currents at the surface for the highest time resolution, while the lowest time-resolution shows currents less intense. Since the KE is the same for both time increments, this means that speed is differently distributed throughout the volume. This difference in distribution is a result of lower numerical diffusion for higher time-resolution schemes. However the

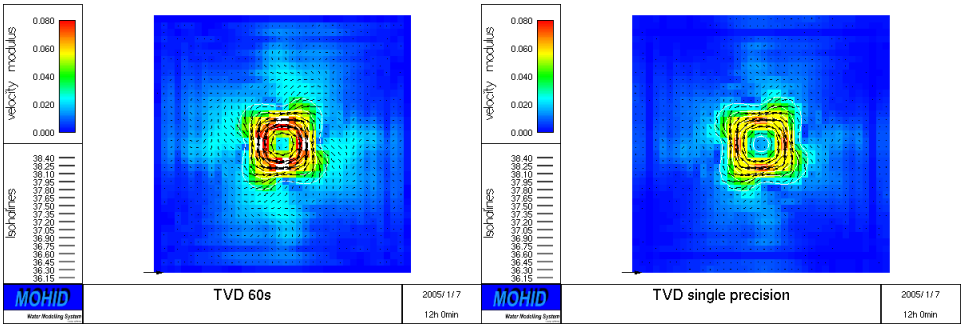

Figure 3.10: Model results after 6 days run. The color scale represents the velocity intensity and the isohalines are spaced by 0.15. On the left panel is the test result with a time-step of 60s. On the right panel is the test result with a time-step of 300s.

difference isn't significant as it doesn't changes the order of the instabilities. Hence, the lowest time resolution is chosen, as it is the less machine-time consuming: 300 s.

Using single or double precision does give some difference in the volume integrated properties (figures 3.2.5 and 3.2.5). However, in the currents field at 144 h, no sensitivity to precision was found. Sensitivity in precision means, sensitivity to round-off errors during numerical calculations. Obviously, the numerical calculations during an integral calculus cumulates the round-off errors, thus the difference shows more in the integrated properties. Indeed these are less than 10% of the maximum variability of the integrated properties and less than 0.1% when compared to referenced values. These are nonetheless low differences and are irrelevant for the general behaviour of the system. In particular, the models of Tartinville et al. (1998) yield higher differences than those found between the single precision tests and the double precision tests. Hence, for the sake of resource management, the single precision was adopted.

Three types of vertical coordinates were tested: Z-level, Sigma and Lagrangean coordinates. The z-level (generalized cartesian) and the sigma coordinates are classic and well described(Semtner, 1974; Cox and Bryan, 1984; Haidvogel and Beckmann, 1999). The Lagrangean coordinate delimits the layers with isobaric surfaces and, thus, evolve with time. A description can be found in the thesis of Martins et al. (1998). The terrain-following coordinate (sigma) give results identical to the geopotential following coor-

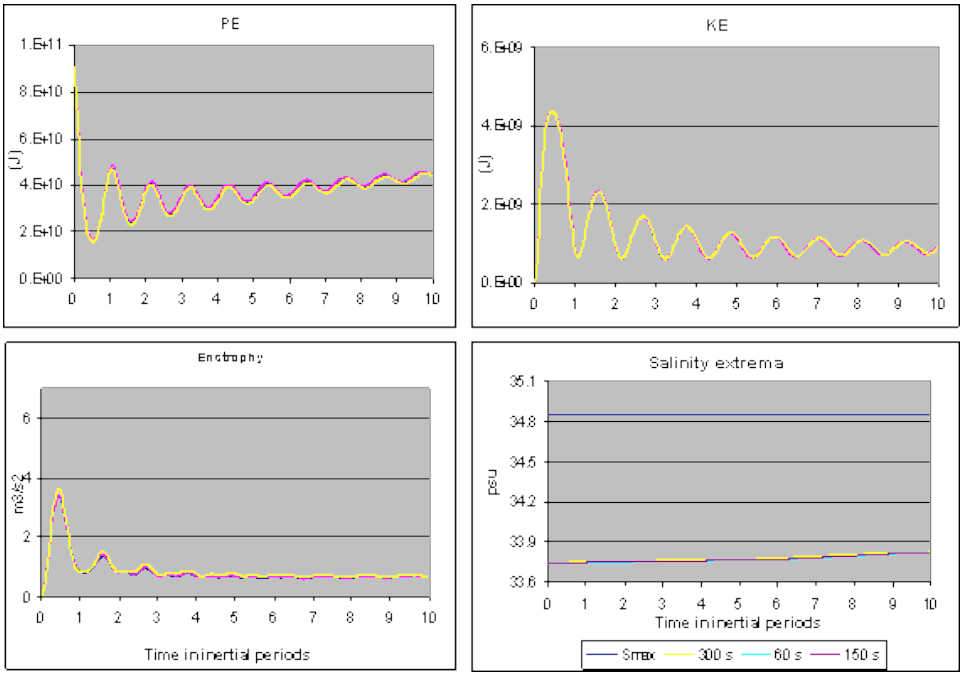

Figure 3.11: Potential Energy, Kinetic Energy, Enstrophy and Salinity extrema for runs with several time increments of 60s, 150s and 300s.

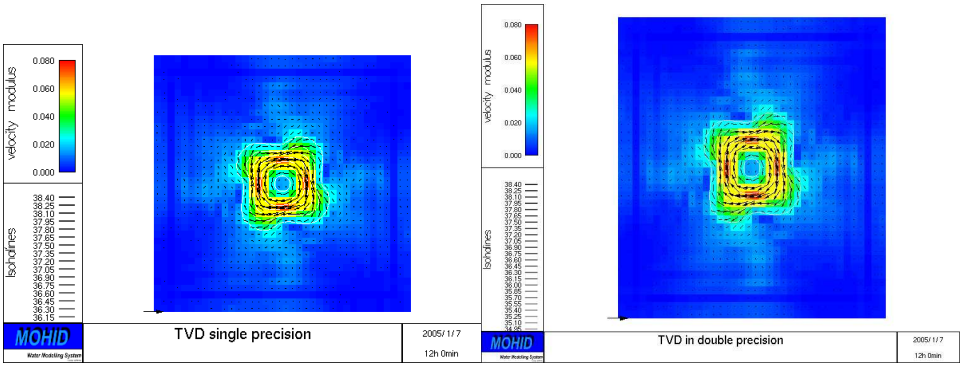

Figure 3.12: Surface currents after 6 days of simulation. The colour scale maps velocity intensity. The vector field represents the velocity field. On the left panel, single precision results. On the right panel, double precision results.

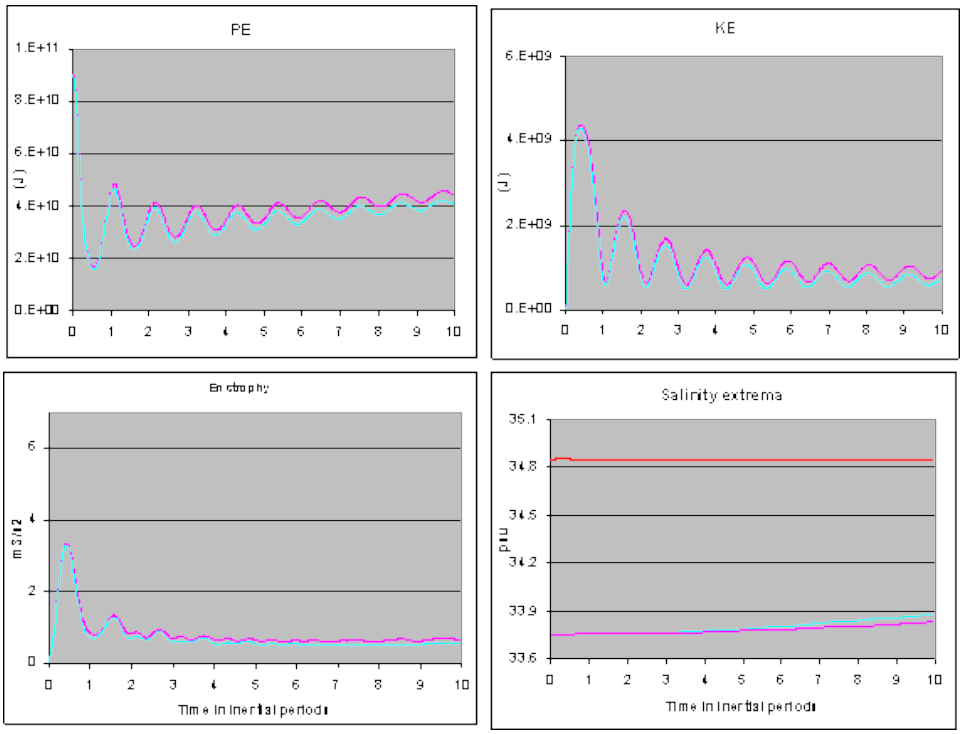

Figure 3.13: Potential Energy, Kinetic Energy, Enstrophy and Salinity extrema for runs with single (pink) and double (blue) precision.

dinate (cartesian). This is expected since there are no bottom topographical gradients. However the Lagrangean coordinate does present better defined salinity lobes and better developed vortices at the end of the simulation (144 h).

Two runs were performed for the Lagrangean coordinate: one with a FRS at the boundaries and the other with level radiation instead. The Lagrangean run gives different results than non-Lagrangean runs in terms of salinity lobes and surface vortices: they are sharper and better developed. This is explained because the Lagrangean coordinate follows level variations and, hence, inhibits numerical diffusion. Unfortunately, the Lagrangean scheme is not mass nor volume conservative and a bias trendline appears in Mass, Volume and Level evolutions for the two types of border conditions which are not acceptable for the sake of realism. Hence, since the Lagrangean scheme also fails in showing other orders of instabilities, the choice relies between sigma and cartesian.

An interesting remark from these results regarding the differences between radiation and relaxation schemes: relaxation requires longer time of spin-up before the model stabilizes in terms of conserved quantities such as Mass, Volume or Level, while radiation condition makes the run converge a lot sooner; however, regardless of the methods, the run stabilizes to the same values of Mass, Volume and Level. For the Lagrangean coordinate, the KE and the Enstrophy tend to grow at the end of the run. The growth is higher for the relaxation condition. This is a typical path to instability. Hence, we can assume for this experiment that the radiation condition is more robust than the relaxation condition in terms of stability.

As for the choice between Z-level and Sigma coordinates, both coordinates are nearly identical, but in the integrated properties, Sigma appears as the less diffusive coordinate because it yields a higher Enstrophy, a lower salinity minimum and a higher KE. Hence the choice goes to sigma.

We tested four ways to calculate the baroclinic force. The four ways are Linear, Uniform, Leibniz and Leibniz2. From the currents figures, no visual changes appear. The KE however does show a higher variation for the Uniform and Linear methods, although it isn't of relevance for the qualitative dynamical results. In this experiment clearly the methods seem identical (except for the KE) hence the standard method, Leibniz2, was chosen.

Fixing the missing parameter's values according to table 8, the runs defined in table 3.2.4 were made, thus testing the several available advection schemes. The results of surface currents and isohalines, and of volume integrated KE, PE, Enstrophy and salinity maxima are displayed in figures 3.2.5 to 3.2.5. The Tartinville et al. (1998) results of integrated quantities are dis-

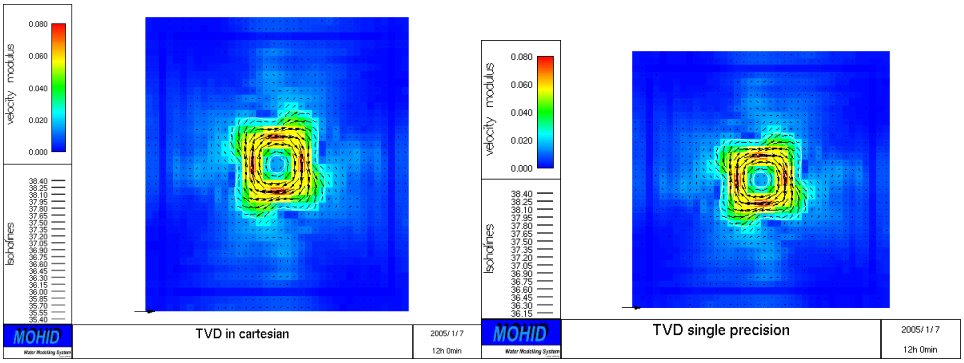

Figure 3.14: Surface currents after 6 days. Cartesian coordinates in the left panel and sigma coordinates in the right panel.

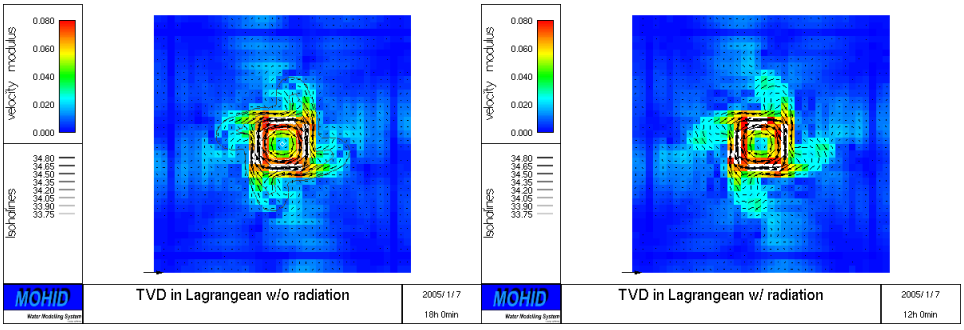

Figure 3.15: Surface currents after 6 days. No level radiation was implemented in the left panel. Flather level radiation was implemented in the right panel.

Table 3.9: Optimal numerical parameters summary

Parameter	Optimal value
Time-step	300 s
Precision	Single
Vertical coordinate	Sigma
Baroclinic force	Default

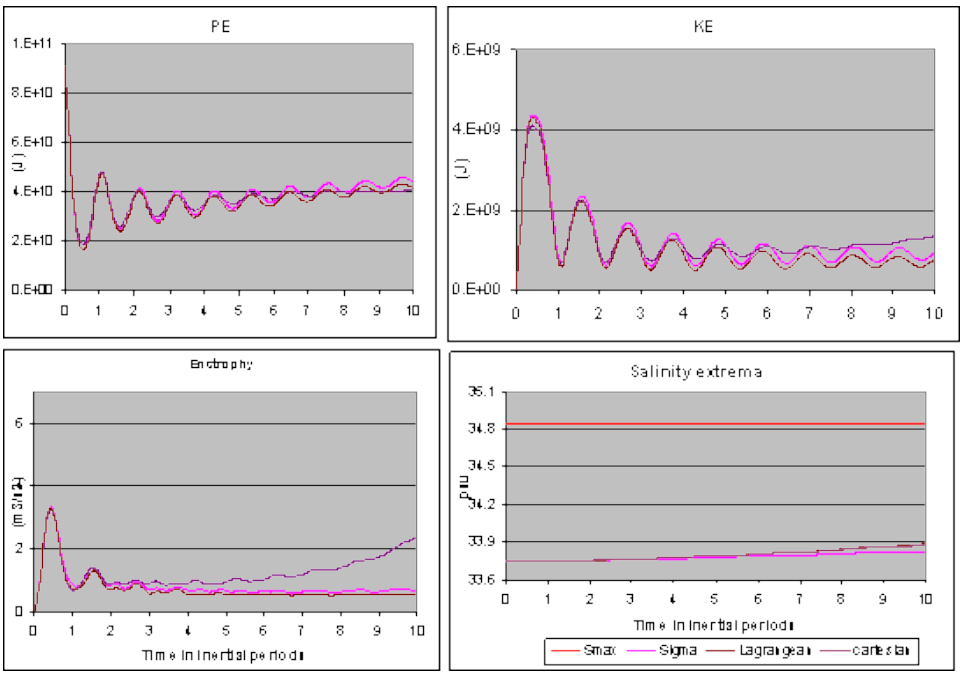

Figure 3.16: Potential Energy, Kinetic Energy, Enstrophy and Salinity extrema for runs with Cartesian, Sigma and Lagrangean w/o radiation coordinates.

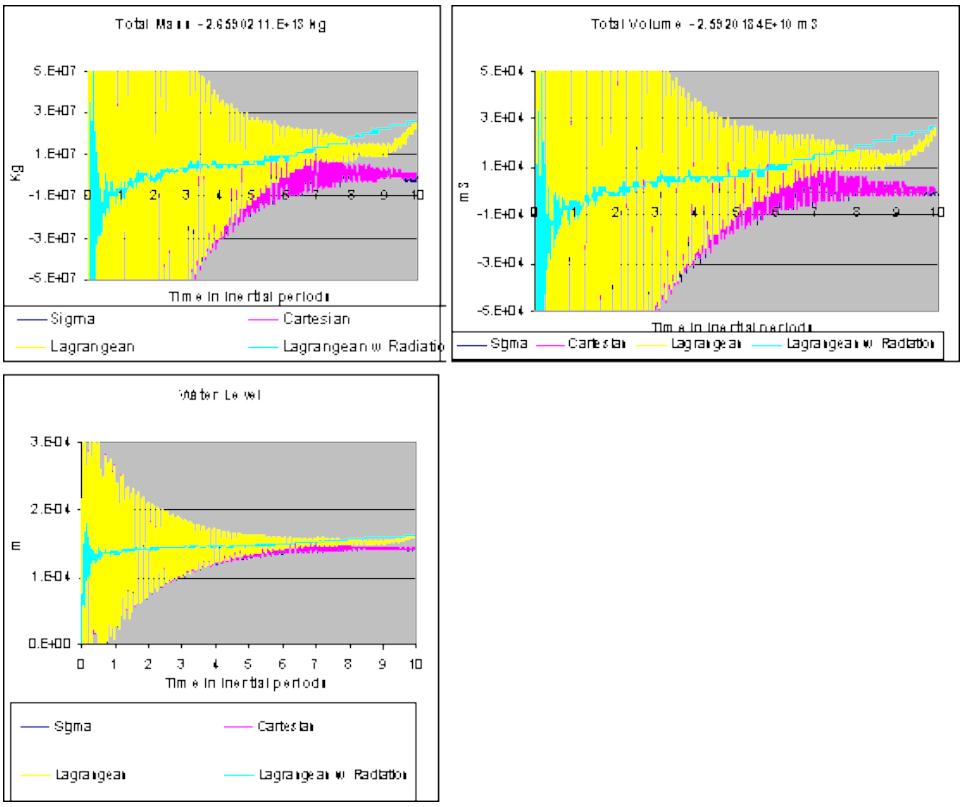

Figure 3.17: Timeserie of the perturbation of initial mass, volume and level for runs with Cartesian, Sigma, Lagrangean (w/ FRS) and Lagrangean (w/ radiation) coordinates.

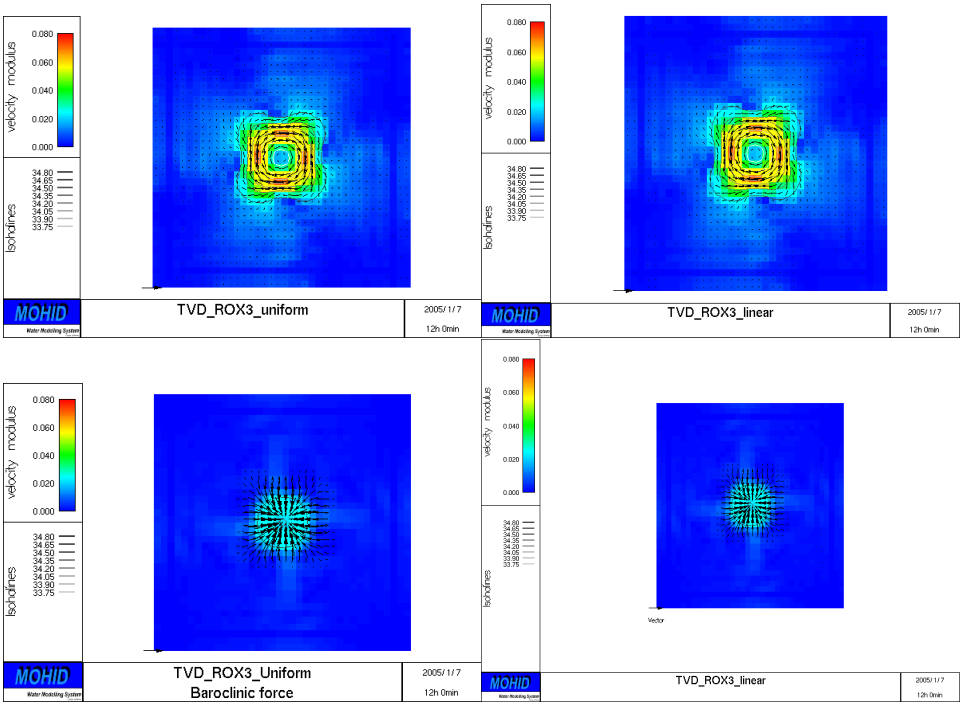

Figure 3.18: The top panels are showing surface currents. The bottom panels are showing 10 m depth currents. All results are shown after 6 days of simulation. The left panels display the uniform method to calculate the baroclinic force. The right panels display the linear method.

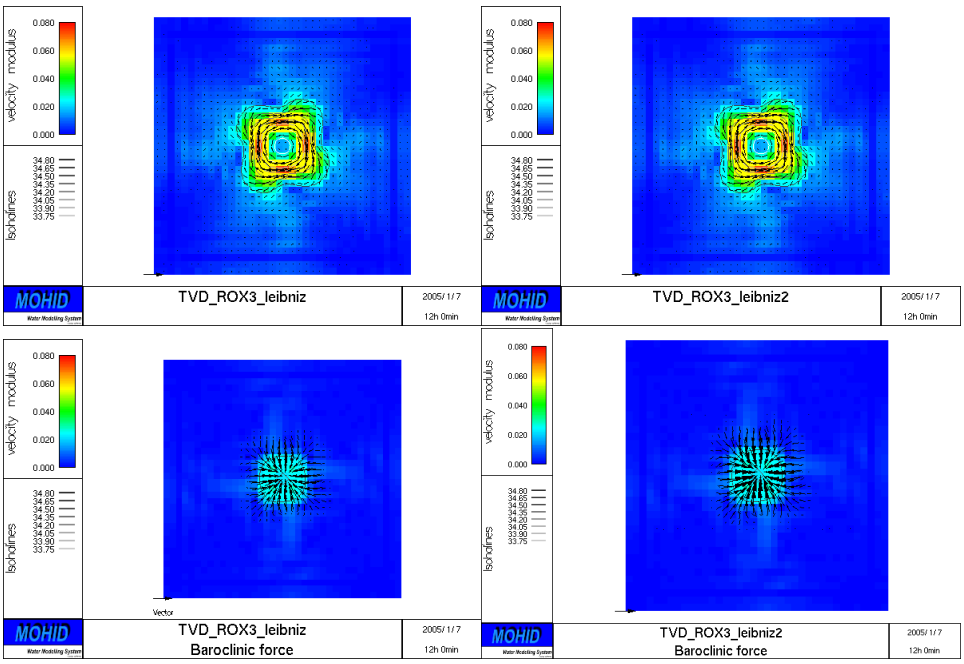

Figure 3.19: The top panels are showing surface currents. The bottom panels are showing 10 m depth currents. All results are shown after 6 days of simulation. The left panels display the Leibniz method to calculate the baroclinic force. The right panels display the Leibniz2 method.

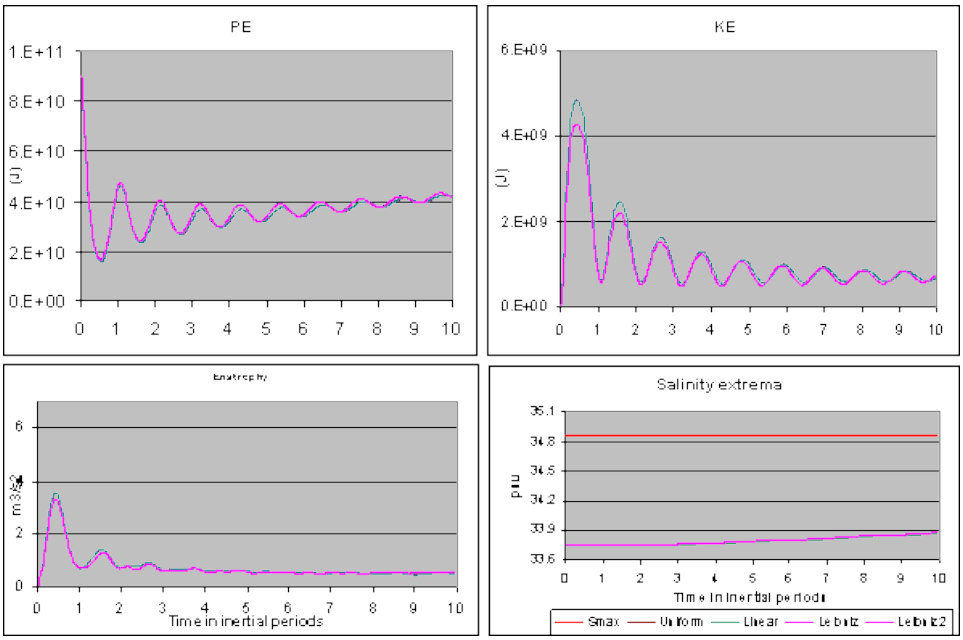

Figure 3.20: Potential Energy, Kinetic Energy, Enstrophy and Salinity extrema for runs with uniform, linear, Leibniz or Leibniz 2 methods for calculating the horizontal density gradient.

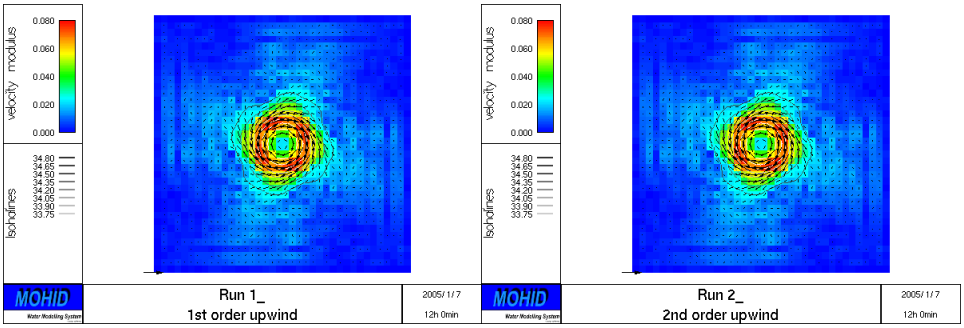

Figure 3.21: Surface currents and isohalines after 6 days run. Left panel, upwind first order scheme, right panel, upwind 2nd order scheme.

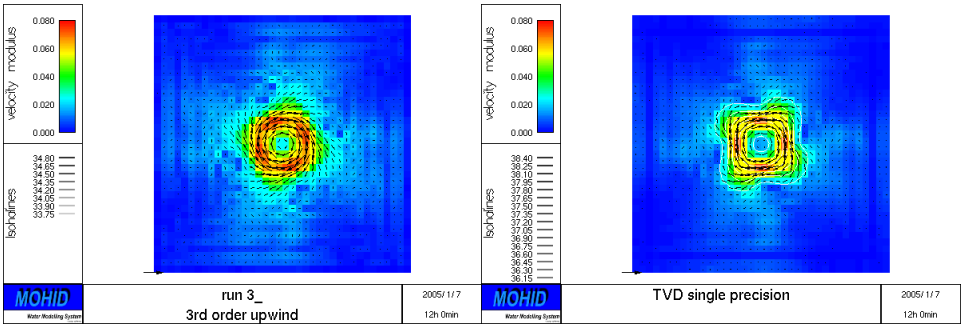

Figure 3.22: Surface currents and isohalines after 6 days run. Left panel, upwind third order scheme, right panel, TVD superbee scheme.

played in figure 3.2.5 in order to compare them directly with our model's results.

All advection schemes yielded 4th order instabilities, while they were supposed to yield 2nd order as shown by real experiments(James, 1996). This is a numerical problem. Tartinville et al. (1998) and Burchard (1999) also had 4th order instabilities. Burchard (1999), that mounted a similar experiment as Tartinville et al. (1998) and that even refined the grid, suggests that it is the square grid that triggers the 4th order instabilities. Tartinville et al. (1998), who developed a more profound study on the cause of the instabilities order, state that the difference of number, growth rate and type of instabilities between models rely on the influence of the numerical methods on the energy budget i.e. the transfer of to and from to for

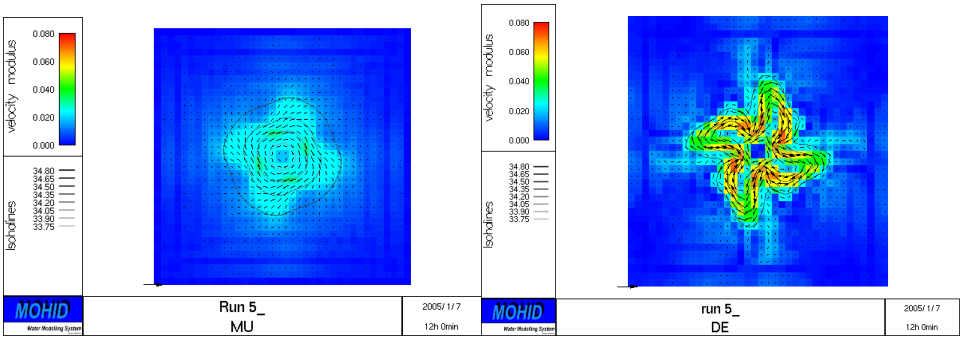

Figure 3.23: Surface currents and isohalines after 6 days run. Left panel, scheme equivalent to MU in Tartinville et al. (1998), right panel, scheme equivalent to DE in Tartinville et al. (1998).

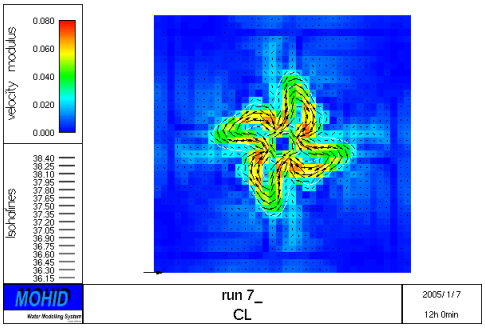

Figure 3.24: Surface currents and isohalines after 6 days run with a scheme equivalent to CL in Tartinville et al. (1998).

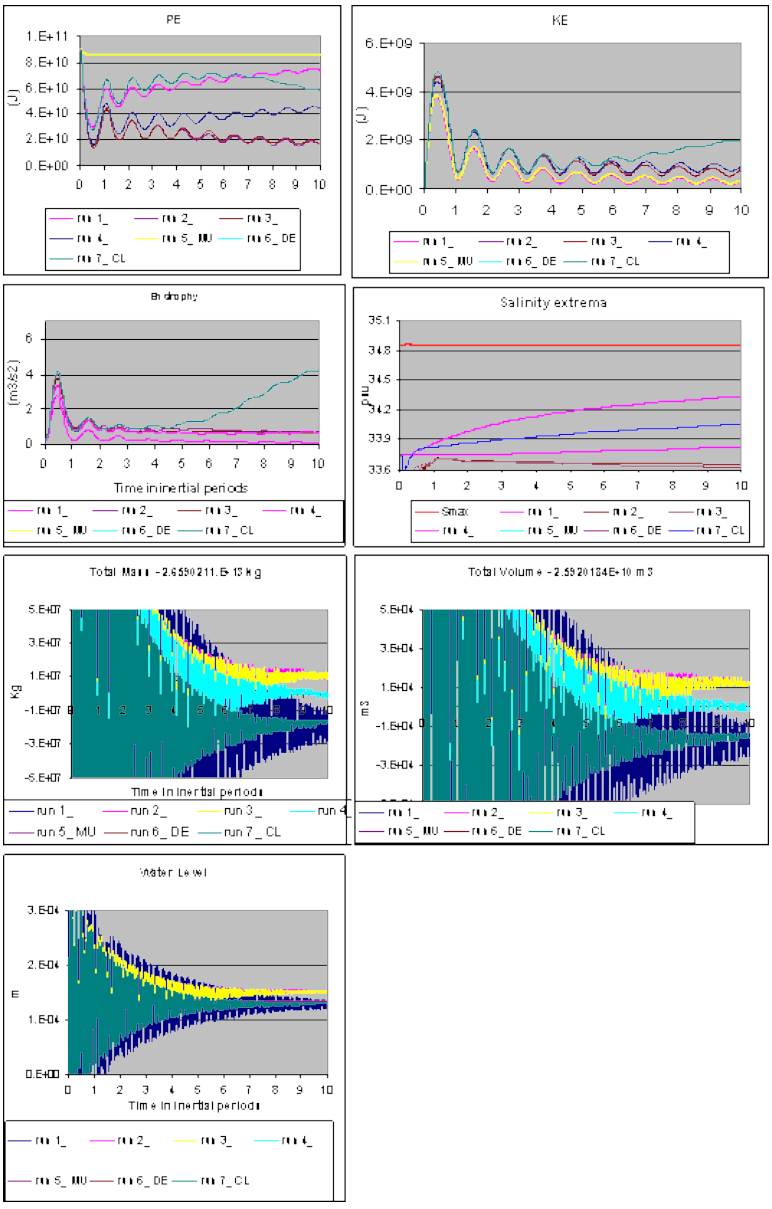

Figure 3.25: Potential Energy, Kinetic Energy, Enstrophy, Salinity extrema, total mass, total volume and level for runs of ID 1, 2, 3, 4, 5, 6 and 7 as described in table 3.2.4.

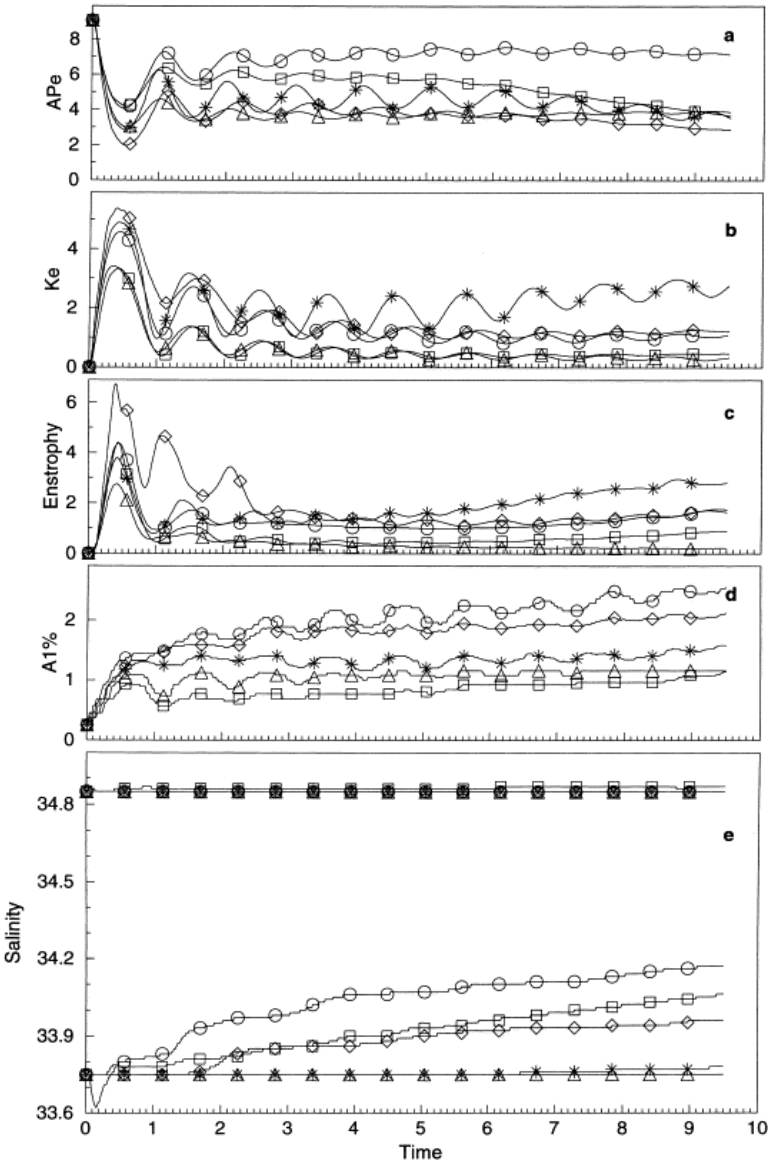

Figure 3.26: Potential Energy (in 10^9 J), Kinetic Energy (in 10^9 J), Enstrophy (in m^3/s^2), surface area with one percent less salinity than ambient value (in 10^8 m^2) and Salinity extrema (in psu). CL gets a circle; DE gets a square; IF gets a diamond; MU gets a triangle and PO gets a star. Courtesy of Tartinville et al. (1998)

barotropic and baroclinic instabilities, respectively. Tartinville et al. (1998) enumerates four possibilities to such cause: the grid staggering, the open boundary conditions, the salinity advection scheme and the horizontal momentum scheme. But his conclusions are that the horizontal momentum advection scheme is the factor of influence on the number of the instabilities while other factors such as staggering and salinity advection can affect the energy ratio and hence influence the growth rate and the type of instabilities. In this work, it is seen that the vertical coordinate is another candidate to create differences in the growth rate. From the analysis of the figures of the different advection schemes (figures 3.2.5 to 3.2.5), although they all show fourth-order baroclinic instabilities, different shapes and growth of vortices appear as well as isohaline lobes. The upwind schemes show the less developed vortices and the less developed isohaline lobes (figures 3.2.5 and 3.2.5). The TVD based schemes tend to produce better developed vortices and lobes (figure 3.2.5). The DE and CL schemes (figures 3.2.5 and 3.2.5) show the best developed vortices, and isohalines lobes; but the less defined central eddy. The most diffusive schemes, such as in run 1 and run 5-MU (figures 3.2.5 and 3.2.5), yield the lowest KE and Enstrophy and the highest APE, as seen in figure 3.2.5. This is expected since numerical diffusion smoothes the momentum and the density gradients which in turn yield a lesser KE and Enstrophy; while the artificial excessive horizontal diffusion of salinity relatively to higher order schemes tends to diminish the effect of the buoyant force such that it increases the equilibrium final APE. The vortices become sharper and better developed with TVD or Centred Differences schemes than with upwind momentum advection schemes as can be seen from runs 4, 6 and 7 (figures 3.2.5, 3.2.5 and 3.2.5 respectively) compared to runs 1, 2 and 3 (figures 3.2.5 and 3.2.5). The salinity lobes become sharper and better developed when TVD salinity advection schemes are employed instead of first order upwind (a clear case is run 4 and run 5-MU in figures 3.2.5 and 3.2.5, respectively, where the only difference is the salinity advection scheme. There, the momentum advection scheme is the same and the vortices are nearly equally developed). The previous remarks really tend to confirm the importance of numerical diffusion both for salinity and momentum advection. Runs 6 and 7 (figures 3.2.5 and 3.2.5) show the best developed vortices and salinity lobes; the central eddy is nearly vanished, which seems totally unrealistic. Apparently there is a very high transfer from APE into KE as shown in the energy graphs, and also, near the end, a large increase of Enstrophy appears. Energetically speaking, this could be a normal thing to happen. However the size of the external vortices compared to the cylinder perimeter violates the hypothesis seen in Pedlosky

(1967, 1969) that the surrounding vortices should have a smaller diameter than the central vortice: $R_{fwc} \propto n\, R_v$. Indeed, from real experiments, the constant of proportionality measured was superior to 1 while in run 6 and 7 the proportionality constant is inferior to 1/4 as each baroclinic vortice has a larger radius than the central eddy. Hence the results from the run 6 and 7 are unrealistic (figures 3.2.5 and 3.2.5). Thus, the better advection scheme is the TVD superbee run 4 (figure 3.2.5) which has a good compromise of developed vortices and isohaline lobes, showing a higher KE and Enstrophy and lower APE relative to other schemes (except to runs 6 and 7). All methods with the sigma coordinate conserve mass, volume and level. However they present enormous oscillations. This is a characteristic side-effect of using a FRS at the open boundary. One can see that radiation in figure 3.2.5 doesn't present such oscillations of these quantities. We stick to FRS as this is the indication given from Tartinville et al. (1998). But, given that mass, volume and level wouldn't oscillate so much, radiating level with a Flather (1976) scheme is believed to be the best choice. When compared to Tartinville et al. (1998) results, in figure 3.2.5, ours are exactly within the same margin of values and exhibit the same behaviour. Particularly, run 5 (figure 3.2.5), which is similar to the run MU (the triangle in figure 3.2.5) in Tartinville et al. (1998), shows very close results with the latter in all figures. Finally, in table 3.2.5 we estimate the geostrophic KE and PE from a time average over the last two-hundred iterations and, thus, try to verify equations (3.29) and (3.28) as regards the growth rate ω and order of instability n. Indeed, the highest values of ω correspond to the fastest growing vortices and salinity lobes (run 6 and 7) and the lowest values of ω correspond to the least expanded vortices and salinity lobes (run 1 and 5). However the order of the instability is clearly erroneous as seen in real experiments (James, 1996).

Conclusions

This work compares several advection schemes available within MOHID and intercompares them with similar already made and acknowledged experiments (Tartinville et al., 1998; James, 1996). We obtain very similar results to Tartinville et al. (1998). Fourth order baroclinic vortices are developed. Real experience should yield second order barotropic/baroclinic instabilities; but this is a numerical problem that seems to affect most standard models such as GETM (Burchard et al., 2004) and is probably due to the symmetry of the horizontal grid and the performance of the advection scheme in transferring KE into KE' and average APE into KE'. The best advection

Table 3.10: Integrated quantities averaged in time over the last two-hundred iterations with a time-step of 300 s.

Run ID	KE (J)	APE (J)	θ	ω	n
1	2.93E+08	7.32E+09	0.04	0.20	5.00
2	6.88E+08	1.79E+09	0.39	0.62	1.61
3	6.91E+08	1.89E+09	0.37	0.60	1.66
4	8.71E+08	4.33E+09	0.20	0.45	2.23
5 MU	3.33E+08	8.57E+09	0.04	0.20	5.07
6 DE	1.84E+09	6.16E+09	0.30	0.55	1.83
7 CL	1.84E+09	6.16E+09	0.30	0.55	1.83

scheme available within the Tartinville et al. (1998) experimental frame is the full-TVD superbee (Tartinville et al., 1998). However the best model setup would seem to use instead a Lagrangean coordinate with radiative boundary condition, though caution should be taken, as the Lagrangean coordinate tends to deviate from mass and volume conservation. The importance of this study in coastal application relies on the liability of the model to show realistic meandering of river plume fronts, coastal currents and baroclinic instabilities in oceanic frontal systems. In such case, further development of the model should be made in order to obtain second order instabilities. It must be noted however that for symmetry reasons, it is impossible that a correctly implemented numerical scheme could yield any other than result than bi-axial symmetry along north-south and east-west axis. Furthermore, members of the Mercator-Océan team tried to reproduce the Tartinville et al. (1998) experiment with the NEMO-OPA model and obtained exactly the same fourth-order instability. They used a Quick and Quickest scheme for the advection-diffusion of both momentum and salinity.

Chapter 4

Proposing a scalar to assess the influence of the open boundary condition

4.1 The scalar of Okubo-Weiss

4.1.1 A conserved quantity coined by Rossby as potential vorticity

We follow Gill (1982) to derive a conserved quantity called potential vorticity from the inviscid, incompressible shallow-water equations. It consists mainly by taking the curl of the Euler equations in a rotating reference frame and combine it with the continuity equation. The Euler equations in rotating reference frame write as

$$\begin{aligned} \frac{Du}{Dt} - f\,v &= -\frac{\partial p}{\partial x}, \\ \frac{Dv}{Dt} + f\,u &= -\frac{\partial p}{\partial y}, \end{aligned} \tag{4.1}$$

where u and v are the fluid horizontal velocity, f is the rotating frequency and p is the pressure. The continuity equation writes as

$$\frac{\partial \eta}{\partial t} + \frac{\partial H\,u}{\partial x} + \frac{\partial H\,v}{\partial y} = 0, \tag{4.2}$$

where η is the water elevation, $H = \eta + d$ is the full water depth and d is the water depth from the rest surface level.

Lagrange in 1781 was the first to write down the following useful relation:

$$\mathbf{v} \cdot \nabla \mathbf{v} = (\nabla \times \mathbf{v}) \times \mathbf{v} + \nabla \left(\frac{1}{2} \mathbf{v} \cdot \mathbf{v} \right). \tag{4.3}$$

We start by defining the quantity ζ as the curl of the velocity, $\zeta \equiv \nabla \times \mathbf{v}$ and by rewriting equation 4.1 as a function of ζ. Considering that $\mathbf{v} = (u,\, v,\, 0)$ and, thus, that $\zeta = (0,\, 0,\, \zeta) = (0,\, 0,\, \frac{\partial v}{\partial x} - \frac{\partial u}{\partial y})$, since u and v are depth-independent, equation 4.1 may be rewritten, by making use of equation 4.3, as

$$\begin{aligned} \frac{\partial u}{\partial t} - (\zeta + f)\, v &= -\frac{\partial \left(p + \frac{1}{2} \mathbf{v} \cdot \mathbf{v} \right)}{\partial x}, \\ \frac{\partial v}{\partial t} + (\zeta + f)\, u &= -\frac{\partial \left(p + \frac{1}{2} \mathbf{v} \cdot \mathbf{v} \right)}{\partial y}, \end{aligned} \tag{4.4}$$

so that, if we take the curl of equation 4.4 we get

$$\frac{\partial \zeta}{\partial t} + \frac{\partial (\zeta + f)\, u}{\partial x} + \frac{\partial (\zeta + f)\, v}{\partial y} = 0.$$

Developing, we get

$$\frac{\partial \zeta}{\partial t} + \frac{\partial (\zeta + f)}{\partial x} u + \frac{\partial (\zeta + f)}{\partial y} v + (\zeta + f) \left(\frac{\partial u}{\partial x} + \frac{\partial v}{\partial y} \right) = 0.$$

Furthermore, if we note that $\frac{\partial f}{\partial t} = 0$, we can finally write

$$\frac{D (\zeta + f)}{Dt} + (\zeta + f) \left(\frac{\partial u}{\partial x} + \frac{\partial v}{\partial y} \right) = 0. \tag{4.5}$$

Furthermore, the continuity equation, equation 4.2, can be invoked with some prior work-out,

$$\frac{\partial \eta}{\partial t} + \frac{\partial H}{\partial x} u + \frac{\partial H}{\partial y} v + H \left(\frac{\partial u}{\partial x} + \frac{\partial u}{\partial y} \right) = 0,$$

$$\frac{DH}{Dt} + H \left(\frac{\partial u}{\partial x} + \frac{\partial u}{\partial y} \right) = 0. \tag{4.6}$$

Equation 4.5 and equation 4.6 yield

$$\frac{1}{(\zeta + f)} \frac{D (\zeta + f)}{Dt} = \frac{1}{H} \frac{DH}{Dt}, \tag{4.7}$$

which integrates into

$$\begin{aligned} \ln(\zeta + f) &= \ln H + C, \\ \ln \frac{\zeta + f}{H} &= C, \\ \frac{\zeta + f}{H} &= e^C, \end{aligned}$$

which derivates to finally yield

$$\frac{DQ}{Dt} = 0. \tag{4.8}$$

Hence, $Q \equiv \frac{\zeta+f}{H}$ is a lagrangian conserved quantity, in a non-local manner, in the incompressible, inviscid two-dimensional flow, named potential vorticity. The term potential vorticity was coined by Rossby around 1940.

4.1.2 Quantitative flow characterization

In a two-dimensional incompressible flow, the curl of the velocity may be seen as the spinning rate of a material particle. However, the motion of a water particle and of any continuum medium particle, has more to it than just spinning. Any volume invariant material particle may be translated, rotated, stretched, sheared and expanded, as sketched in the figure 4.1.2.

The rotation and the translation of a cartesian element of volume preserves both the angles and the width ratio. However, the streching and the shearing respectively change the width ratio and the angles. Of course, the translation is measured directly from the intensity of the velocity components of the advecting field. The other deforming rates, however, would be given by

$$\begin{cases} \frac{\partial v}{\partial x} - \frac{\partial u}{\partial y}, & \text{spin} \\ \frac{\partial u}{\partial x} - \frac{\partial v}{\partial y}, & \text{stretch} \\ \frac{\partial v}{\partial x} + \frac{\partial u}{\partial y}, & \text{shear} \\ \frac{\partial u}{\partial x} + \frac{\partial v}{\partial y}, & \text{growth} \end{cases} . \tag{4.9}$$

These diagnostic quantities, that characterize the advecting field, can be of extreme usefulness to identify the type of motion that a material particle may undergo. Previous studies already identified some of these quantities (Weiss, 1991) and used them to identify areas of the domain where the flow was predominantly hyperbolic or elliptic. In particular, Arakawa (1966) used some of these quantities to determine numerical schemes that

were more robust. Finally, the *spin* and *shear* are often referred in fluid mechanic textbooks (Kundu and Cohen, 2002) as the equivalent shear strain rate tensor and rotation tensor, respectively

$$e_{ij} \equiv \frac{1}{2}\left(\frac{\partial u_j}{\partial x_i} + \frac{\partial u_i}{\partial x_j}\right)$$

and

$$r_{ij} \equiv \left(\frac{\partial u_j}{\partial x_i} - \frac{\partial u_i}{\partial x_j}\right).$$

However these same textbooks fail to explore the usefulness and the physical meaning of the *stretch* and *growth* tensor counterparts.

Part of the usefulness of the *spin*, *stretch*, *shear* and *growth* is the fact that they comply to the Stokes theorem and, thus, that they're all equivalent to a circulation integral over the boundary of any given control volume. Thus they have a very natural numerical implementation, for instance, in an Arakawa C-grid. Hence they're easy to compute diagnostic variables in numerical, hence they should be exploited thoroughly in order to analyse the numerical results of a fluid flow problem.

The other fundamental part of their usefulness is how they have powerful relations with the geometry of the domain. For instance, if we consider equation 4.6, we can see how the eulerian *growth* rate is related with the depth and height of a two-dimensional lagrangian particle,

$$\frac{1}{H}\frac{DH}{Dt} = -\left(\frac{\partial u}{\partial x} + \frac{\partial u}{\partial y}\right). \tag{4.10}$$

Equation 4.10 yields that the relative rate of change of the height of a lagrangian particle is equivalent to minus the horizontal divergence (*shrink* rate) of the eulerian flow. Thus, if a lagrangian particle should decrease its height, it will grow horizontally and, conversely, if the velocity field should shrink horizontally the particle, then the particle will alter its height so as to preserve its volume. Naturally, one can expect a high correlation between strong horizontal velocity divergence and steep topographic gradients. Furthermore, equation 4.10 is an equivalent form of the continuity equation, but with the added value that it links a lagrangian property, the height, to eulerian properties, the flow. Finally, this process of preserving volume for two-dimensional properties has an important implication to rotating fluids, first discovered by Rossby, and that is that potential vorticity must be preserved (in equation 4.8) and thus that the relative rate of change of height of a lagrangian vortex is equal to the relative rate of change of its vorticity.

Thus, when vortex tubes strech vertically, they tend to increase their rotating frequency, whereas when vortex tubes compress vertically, they tend to decrease their rotating frequency. Equation 4.10 reminds us also, though, that the vortex tubes must enlarge or shrink horizontally so as to preserve their volume. Ultimately, another way of expressing the potential vorticity principle, in terms of rates of motion of the flow, would be

$$\frac{1}{\text{spin}}\frac{D\,\text{spin}}{Dt} = -\,\text{growth}, \tag{4.11}$$

if the spin factor is allowed to be rewritten as

$$\text{spin} \equiv \frac{\partial v}{\partial x} - \frac{\partial u}{\partial y} + f.$$

The preceding equation simply considers the spin tensor from the point of view of an observer in a non-rotating inertia reference frame, looking at a fluid rotating on a table with frequency f.

4.1.3 Qualitative flow characterization

A 1981 pre-print of a study by Weiss (1991) showed that in the regions where the flow was dominantly hyperbolic, the gradients of vorticity would grow exponentially, while in the regions where the flow was dominantly elliptic, the gradients of vorticity would present a periodic behavior. He related this by comparing the squared rate of strain with the squared rate of rotation of the fluid. The identity he derives, also presented by Arakawa (1966) fifteen years earlier, is equivalent to

$$\frac{\text{shear}^2 + \text{stretch}^2 - \text{spin}^2}{2} = 2\,\frac{\partial v}{\partial x}\frac{\partial u}{\partial y} - \frac{\partial u}{\partial x}\frac{\partial v}{\partial y} \tag{4.12}$$

The rate of rotation is identified with vorticity, and its square is identified with enstrophy. Basically, in the regions of the flow where the rate of strain (shear and stress) is dominant, the vorticity is sheared by the hyperbolic flow, while in the regions of the flow where the rate of vorticity is dominant, the vorticity is smoothly advected. Thus the hyperbolic flow is responsible for the growth of the gradients of vorticity. Furthermore, Weiss (1991) demonstrated, based on a work by Bourguignon and Brezis (1974), that the nature of the flow (elliptic or hyperbolic) is largely influenced by the domain boundary, probably as a consequence that the boundary topology reflects on the Gaussian curvature of the flow's stream function, which Weiss shows

to be none other than the rate of strain squared minus the rate of rotation squared (i.e. vorticity squared i.e. enstrophy).

In particular, Weiss demonstrated that for smooth convex boundaries (i.e. the tangent plane to the boundary of the domain D, ∂D, is interior to D at all points on ∂D), the flow is predominantly hyperbolic, while for concave boundaries (i.e. the tangent plane to ∂D is exterior to D i.e. closed domains, bathtubs, pools, etc) the flow is predominantly elliptic in nature, as most classical boundary valued problems (BVPs) are.

These relationships that indicate the influence of the geometry on the flow, and vice-versa, are recurrent and very powerful. Equation 4.7 and equation 4.10 are other examples of how the *spin* rate and *growth* rate of a two-dimensional incompressible flow are steered, partly at least, by topography.

Hua and Klein (1998) later showed how the Okubo-Weiss parameter is none other than the eigenvalue of the velocity gradient. He also discussed some of its limitations and proposed a study on the eigenvalues of the pressure gradient for the Euler equations, which would return the OW eigenvalues added with a correction factor.

$$w = \frac{\partial v}{\partial x} - \frac{\partial u}{\partial y} \tag{4.13}$$

$$\sigma_n = \frac{\partial u}{\partial x} - \frac{\partial v}{\partial y} \tag{4.14}$$

$$\sigma_s = \frac{\partial v}{\partial x} + \frac{\partial u}{\partial y} \tag{4.15}$$

$$W = \sigma_n^2 + \sigma_s^2 - w^2 \tag{4.16}$$

4.2 Developing a shallow waters model in MATLAB

4.2.1 From the continuum to the discrete

After discretizing a domain with a set of finite volumes, and averaging the continuous momentum equations over the finite volumes, a correct evaluation of the applied forces is still required. The difficulty in such a task, is that there is a degenerescence of solutions when coming from the continuous

equations of momentum - under Newton's infinitesimal calculus formalism, which assumes regular cartesian infinitesimal elements of volume, whose limit is very near the null volume - to the discretized equations of momentum. This degenerescence can be exposed, in particular, in the multiple available definitions of discrete derivatives, such as the forward, the backward or the mid-point discrete derivative. Once the infinitesimal limit tends to zero, in the continuous approach, all discrete derivatives yield the same result.

$$\begin{aligned}\left.\frac{df}{dx}\right|_x &= \lim_{h\to 0}\frac{f(x+h)-f(x)}{h}\\ &= \lim_{h\to 0}\frac{f(x)-f(x-h)}{h}\\ &= \lim_{h\to 0}\frac{f(x+h)-f(x-h)}{2h}.\end{aligned}$$

However, when the infinitesimal limit is non-zero, say, due to computational restrictions, the discrete derivative will yield in fact different results, each with a different error and with a different order of the error (the backward and forward discrete derivatives yield a first-order truncature error, while the mid-point discrete derivative yields a second-order truncature error).

In particular, when dealing with problems involving partial differential equations (PDE), a finite difference (FD) approach is often undertaken to obtain a realistic physical solution. Such approach is often described on a regular mesh (Courant et al., 1928) which, by using a Taylor series expansion of f, yields the exact order of the error of truncature. However, hardly ever anyone re-did explicitly the calculations for non-regular meshes. But, still often, the computational limits oblige the numerician to rethink the discretized derivative in a non-regular mesh in a geometry imposed by its set of finite volume and their inherent geometry. Thus, the infinitesimal width of the finite volume h is no longer a constant and the mid-point derivative, for example, needs to be rewritten as:

$$\left.\frac{df}{dx}\right|_x = \lim_{h^-,h,h^+\to 0}\frac{\frac{h\,f(x+(h+h^+)/2)+h^+\,f(x)}{h+h^+}-\frac{h^-\,f(x)+h\,f(x-(h^-+h)/2)}{h^-+h}}{h},$$

where h^-, h and h^+ represent the backward volume, the central volume and the forward volume infinitesimal width, respectively. Notice how the latter equation reduces to the regular mesh mid-point derivative when $h^- \to h$ and when $h^+ \to h$.

Hence, the above example is enough to demonstrate that beyond the PDE, the initial condition (IC) and the boundary condition (BC), which are usually given care when dealing with PDE problems, the geometry of the mesh is also of paramount importance in order to properly solve the problem, when resorting to FD methods in real-case applications.

Now, although there is enough room and interest to perform a full review of the FD methods within the bounds of non-standard analysis (Robinson, 1974), which is, in the author's opinion, the natural framework to deal with FD solvers of PDE, the objective of this work is to properly calculate the incompressible pressure force acting over a set of finite volumes that compose a 1D channel while using the concept of Newton's or Leibniz's infinitesimals. This pressure force, correctly calculated, will be included in a FD solver of the 1D shallow water equations (SWE). An added interest of this solution, is that it improves the available documentation of the barotropic force calculation in the MOHID hydrodynamic modeling system.

4.2.2 Calculating the barotropic force

One of the major breakthroughs of Arakawa (1966) was to impose the conservation of squared quantities such as the total energy, or the potencial enstrophy, as a means to smooth out growing instabilities during long time integrations. He discovered ideal families of schemes that followed these constraints, but of higher-order than first or second-order FD schemes. To correctly impose these restrictions, Arakawa realized that the mesh needed to be clearly defined. Thus, he resorted to define staggered grids, such as the Arakawa A, B or C grid. For this work, the most natural choice is the Arakawa C grid which in the unidimensional case proposes two colocated types of cells: the T-cells and the U-cells. At the geometric center of the T-cell type are evaluated the water level, η, the cell depth, h, and the cell widths, Δx and Δy. At the center of the T-cell faces is the evaluated average of momentum, ρu over a U-cell volume. The U-cell volume has its faces crossing the T-cells geometric center, thus forming a staggered grid composed of T-cells and U-cells. This structure, thus defined, is of paramount relevance if we are to actually compute the barotropic force. In this case, we can only compute the barotropic force in such a structure. Any other mesh or structure would yield different calculations, but the original generic concept remains the same: the barotropic force is the vectorial sum of the pressure over any given finite volume's surface or, by virtue of the divergence theorem (see section A.1.1), the barotropic force is the sum of the pressure

gradient over any finite volume.

$$F_p = \int_V \nabla p \, dV$$

$$F_p = \oint_{\partial V} p \, \mathbf{n} dS. \tag{4.17}$$

F_p is the pressure force, p is the pressure, V is volume, ∂V is the volume's surface and $\mathbf{n}$ is the volume's surface normal vector. We will show that the former is the most natural way to compute it in Arakawa C grid. The pressure force, in an unconstrained volume submitted to a volumic force such as the Earth's surface under the gravitational field, is roughly the weight per unit area of the infinite column above any given point, plus the inertial weight due to the acceleration of the column. This column follows the local vertical up to the faraway stars. It comprises the weight of the air column, which by sea-level, equals roughly to one atmosphere, summed to the weight of the water column, should the point be underwater, where one meter depth sums up a pressure of one atmosphere; plus, the inertial weight due to the vertical acceleration of the column. By "inertial weight", we mean the difference that a weight-scale would measure between an elephant at rest and a falling elephant landing on it, at the instant of impact. Often, in the case of the atmosphere, or of the Ocean, we neglect the inertial weight term since the atmosphere is roughly static along the vertical compared to its weight, as well as is the Ocean. This neglection is called the hydrostatic approximation and the pressure is thus only the sum of the weight of the column above a given point. Gill (1982) often states a more subtil physical interpretation of the hydrostatic approximation, and that is that the vertical motions are small relative to the horizontal motions. The pressure under the hydrostatic approximation is given by

$$\frac{\partial p}{\partial z} = -\rho \, g \tag{4.18}$$

where z is the upward local vertical coordinate, ρ is the medium density and g is the local gravitational acceleration. It follows that:

$$p(z') = \int_{z'}^{+\infty} \rho \, g \, dz \tag{4.19}$$

where z' is the value of the height of the point where the pressure is being measured. Typically the hydrostatic pressure force acting on a free-surface watercolumn, doted of a water elevation η, is calculated by splitting the

pressure of the atmospheric column body from the whole column body (watercolumn plus the atmospheric column),

$$\begin{aligned} p(z') &= \int_{z'}^{\eta} \rho\, g\, dz + \int_{\eta}^{\infty} \rho\, g\, dz, \\ &= \int_{z'}^{\eta} \rho\, g\, dz + p_{\mathrm{atm}}. \end{aligned}$$

Then, as the horizontal gradient of the hydrostatic pressure is calculated, it is split into the barotropic and baroclinic components by means of the extended Leibniz integration rule (see equation 2.5),

$$\begin{aligned} \frac{\partial p}{\partial x} &= \frac{\partial p_{\mathrm{atm}}}{\partial x} + \frac{\partial}{\partial x}\left(\int_{z'}^{\eta} \rho\, g\, dz\right) \\ &= \frac{\partial p_{\mathrm{atm}}}{\partial x} + \int_{z'}^{\eta} \frac{\partial \rho}{\partial x}\, g\, dz + \frac{\partial \eta}{\partial x}\, \rho(\eta)\, g. \end{aligned} \tag{4.20}$$

The last two terms of the RHS of the above equation are, respectively, the baroclinic force and the barotropic force. Alternatively, a reference density ρ_0 may be defined, and the static pressure gradient would then yield

$$\begin{aligned} \frac{\partial p}{\partial x} &= \frac{\partial p_{\mathrm{atm}}}{\partial x} + \frac{\partial}{\partial x}\left(\int_{z'}^{\eta} (\rho - \rho_0)\, g\, dz + \int_{z'}^{\eta} \rho_0\, g\, dz\right) \\ &= \frac{\partial p_{\mathrm{atm}}}{\partial x} + \frac{\partial}{\partial x}\left(\int_{z'}^{\eta} (\rho - \rho_0)\, g\, dz\right) + \frac{\partial \eta}{\partial x}\, \rho_0\, g. \end{aligned}$$

The latter alternative splitting of the pressure gradient does not correspond to the classic barotropic and baroclinic forces, although it is very similar for practical purposes. Nevertheless, it suffices to choose a ρ_0 very different from the surface density to see that the pseudo-barotropic term loses all its physical meaning by an amount of the same difference. By the way, the barotropic force is supposed to return the bulk of the force felt through the whole of the watercolumn body by the motion of the water level alone.

Equation (4.20) returns the pressure gradient valid for a solid point of the fluid in a water body. But what if the pressure gradient force would be calculated for a whole control volume embedded in an incompressible fluid? What would yield the result? This question is of practical necessity to numerical modelers as they have only needs of pressure gradient forces integrated within discrete control volumes, not points. Now if equation 4.17 were calculated along the x direction, applied to a U-cell control volume

as shown in figure 4.2, clockwise in the $x\,z$ plan, using equation 4.19 to determine the pressure, we'd have:

$$\begin{aligned} F_{p\,i+1/2} = \Delta y \quad (& \\ & -H_i \tfrac{p(\eta_i)+p(h_i)}{2} \\ & +|\eta_{i+1}-\eta_i|\,\tfrac{p(\eta_{i+1})+p(\eta_i)}{2} \\ & +H_{i+1}\tfrac{p(\eta_{i+1})+p(h_{i+1})}{2} \\ & +(h_{i+1}-h_i)\,\tfrac{p(h_{i+1})+p(h_i)}{2} \\ ) & \end{aligned}$$

where $p(\eta) = p_{atm}$ and p_{atm} is the pressure of the weight of the air column at rest, $H \equiv \eta - h$ and $p(h) = \rho\,g\,H + p_{atm}$ where $p(h)$ is the sum of the pressure weight of the air column and of the water column at depth h, both at rest, for an incompressible fluid. As the reference pressure level is set at the surface, we have $p_{atm} = 0$. Thus,

$$F_{p\,i+1/2} = \frac{\Delta y\,\rho\,g}{2}\left(H_{i+1}^2 - H_i^2 + (h_{i+1}-h_i)\,(H_{i+1}+H_i)\right).$$

If we use the relation $a^2 - b^2 = (a-b)\,(a+b)$ and if we consider that $H_{i+1/2} \equiv \frac{H_{i+1}+H_i}{2}$, then we get:

$$F_{p\,i+1/2} = \Delta y\,\rho\,g\,H_{i+1/2}\,(H_{i+1} - H_i + h_{i+1} - h_i),$$

or, putting it more simply,

$$F_{p\,i+1/2} = \Delta y\,\rho\,g\,H_{i+1/2}\,(\eta_{i+1} - \eta_i). \tag{4.21}$$

It immediately strikes that, inverting the discretization process, the barotropic pressure term can be written as

$$\frac{\partial p}{\partial x} = \rho\,g\frac{\partial \eta}{\partial x} \tag{4.22}$$

where $V = \Delta y\,\Delta x\,H_{i+1/2}$ is the volume value. Note that all calculations on pressure we made with the incompressible fluid case in mind. Equation 4.22 is classic; it can be deduced directly from equation 4.19 and can be seen written out in many references (Gill, 1982),(Cushman-Roisin and Beckers, 2007). It states that the barotropic hydrostatic pressure gradient depends only on the surface gradient. The bottom gradient is irrelevant and is cancelled by the bottom equal and opposite reaction to the water bottom pressure. The air at the surface, however, cannot react to the water surface pressure gradient creating thus an imbalance in the forces. This imbalance yields a force that is uniform throughout the water column, or independent of depth.

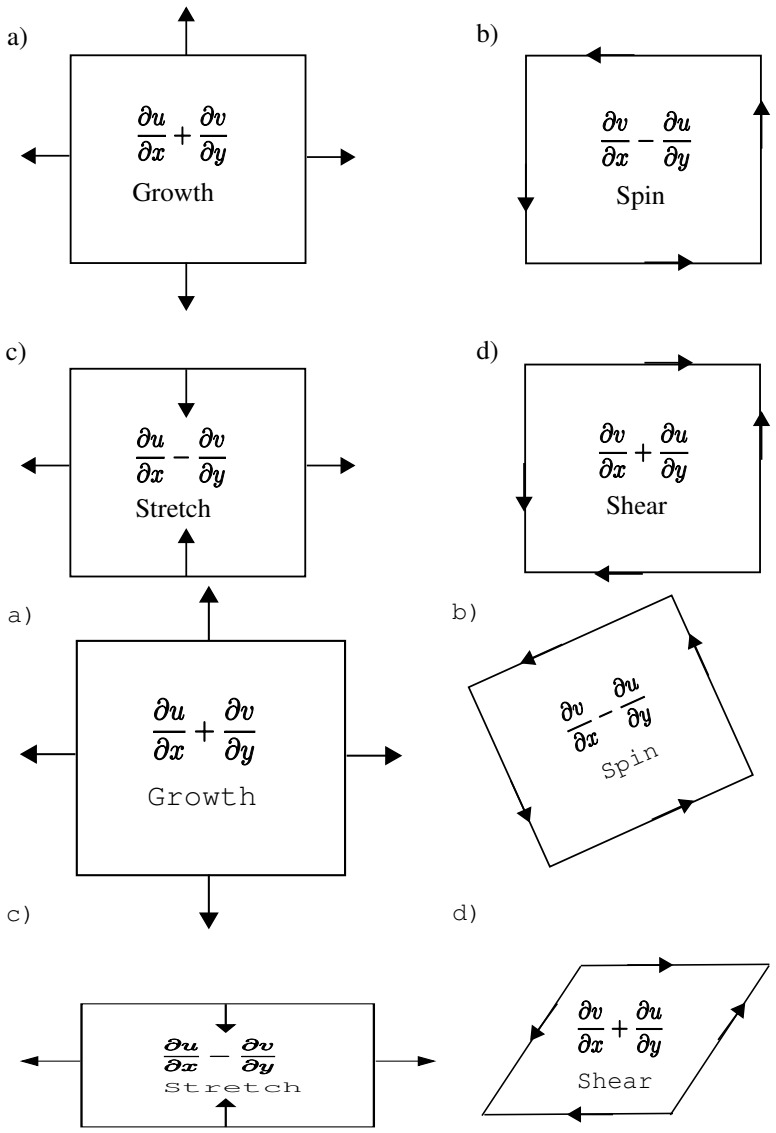

Figure 4.1: Bi-dimensional cartesian elements of volume representing geometrical distortion through a) growth, b) spin, c) stretch and d) shear operations. The geometrical operation is performed by computing the integral circulation of the scalar product of the vector field (u, v) with the unit vectors represented in the figure. The Kelvin-Stokes theorem and the divergence theorem are easily derived in the particular respective cases of spin and growth.

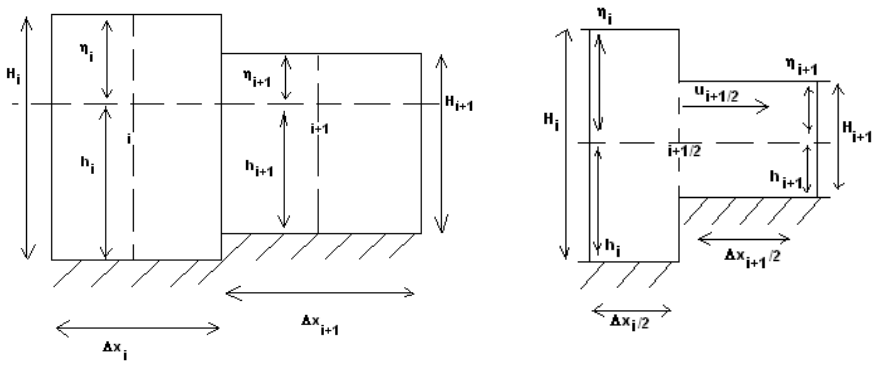

Figure 4.2: Unidimensional equivalent of the Arakawa C staggered grid. Two T-cells on the left panel. One U-cell on the right panel.

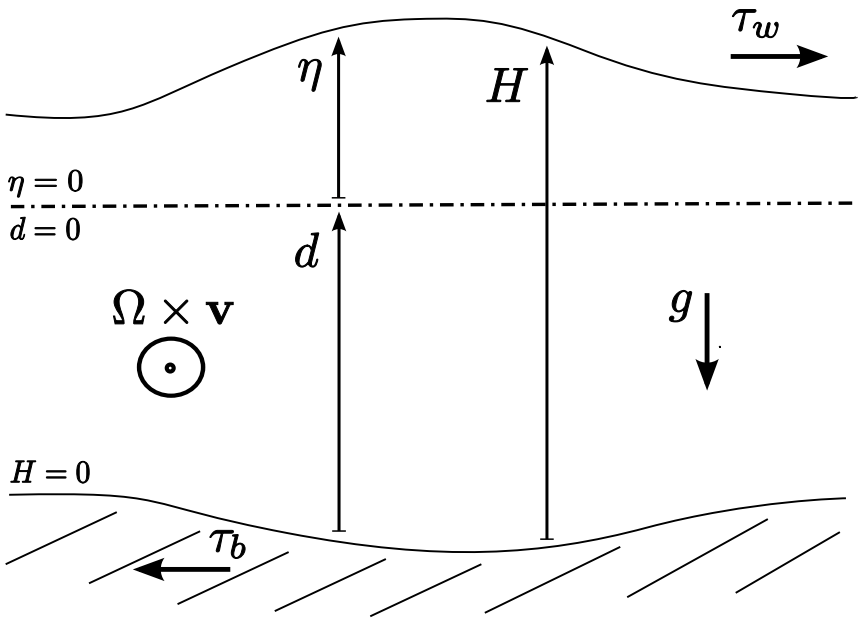

Figure 4.3: System depicted by the mathematical model. The reference level is indicated by a dash-dotted line. η is the water elevation from the reference level, d is the depth from the reference level and H is the total depth. The forces acting on the system are illustrated by vector arrows. g is the gravitational acceleration, τ_w is the wind stress, τ_b is the bottom stress and $\Omega \times \mathbf{v}$ is the Coriolis acceleration.

4.2.3 The mathematical model

The shallow waters equations (SWE) describe the 2D barotropic motion of water masses. The system and its forcings are illustrated in figure 4.3. The SWE are widely described throughout the literature; for example, they are given in Kantha and Clayson (2000) as

$$\begin{cases} \frac{\partial Hu}{\partial t} + \frac{\partial Huu}{\partial x} + \frac{\partial Huv}{\partial y} - fHv = & \nu\left(\frac{\partial}{\partial x}\left(H\frac{\partial u}{\partial x}\right) + \frac{\partial}{\partial y}\left(H\frac{\partial u}{\partial y}\right)\right) \\ & -gH\frac{\partial \eta}{\partial x} + \frac{\tau_u^w}{\rho_0} - \frac{\tau_u^b}{\rho_0} \\ \frac{\partial Hv}{\partial t} + \frac{\partial Hvu}{\partial x} + \frac{\partial Hvv}{\partial y} + fHu = & \nu\left(\frac{\partial}{\partial x}\left(H\frac{\partial v}{\partial x}\right) + \frac{\partial}{\partial y}\left(H\frac{\partial v}{\partial y}\right)\right) \\ & -gH\frac{\partial \eta}{\partial y} + \frac{\tau_v^w}{\rho_0} - \frac{\tau_v^b}{\rho_0} \\ \frac{\partial \eta}{\partial t} + \frac{\partial Hu}{\partial x} + \frac{\partial Hv}{\partial y} = 0 \end{cases} \tag{4.23}$$

where H is the depth from the surface level to the bottom, u and v are the zonal and meridional components of velocity, x, y and z are the zonal, meridional and depth positions respectively. $f = 1.01 \times 10^{-4}$ rad/s is the Coriolis frequency at 42^o of latitude, ν is the horizontal turbulent viscosity, $g = 9.8$ m^2/s is the gravity acceleration, $\rho_0 = 1033$ kg/m^3 is the water mean density and eta is the water level relative to rest. τ_u^b is the bottom stress zonal component, τ_u^w is the wind stress zonal component. The bottomstress (Pietrzak et al., 2002) is given by

$$\tau_u^b = \rho_0 C_D u_b \sqrt{u_b^2 + v_b^2}$$

where C_D is the bottom drag coefficient and u_b and v_b are the zonal and meridional velocity bottom velocity components. The bottom drag coefficient (Leitão, 2003b) is given by

$$C_D = \left(k / \ln \left(\frac{z_D + z_0}{z_0} \right) \right)^2$$

where z_D is the distance to the bottom , $z_0 = 0.002$ m is a typical roughness length (Leitão, 2003b) and the Von Karman constant (Leitão, 2003b) is set to

$$k = 0.4.$$

The wind stress (Pietrzak et al., 2002) is given by

$$\tau_u^w = \rho_a C_a u_{10} \sqrt{u_{10}^2 + v_{10}^2}$$

where $\rho_a = 1.25$ kg/m3 is the air density, C_a is an air drag coefficient whose values can be found in Pietrzak et al. (2002) and u_{10} and v_{10} is the air speed at 10m height.

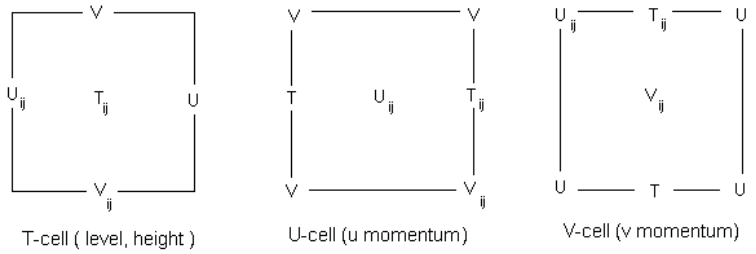

Figure 4.4: Arakawa C staggered grid patterns. From left to right: the T-cell, where η and H are evaluated at the centres, and u and v are evaluated at the eastern, western faces and southern, northern faces respectively. The U-cell where u is evaluated at the centre, η and H are evaluated at the eastern, western faces, and v is evaluated at the corners. The V-cell, where v is evaluated at the centre, η and H are evaluated at the southern, northern faces, and u is evaluated at the corners. The distance between two consecutive cells of the same type is Δx, zonally, and Δy, meridionally. The indices i and j correspond to the i-th zonal cell and the j-th meridional cell counted in the South-North direction and in the West-East direction respectively.

4.2.4 The mesh

The mesh in use is an Arakawa Staggered regular C-grid(Arakawa, 1966) as illustrated in figure 4.4. It is composed of three distinct cells: the U-cell, the V-cell, and the T-cell, where are, respectively, at the centres the u, the v and the η variables of equations 4.23. The C-grid provides better precision for the non-linear advecting terms than the B-grid, however it looses precision when evaluating the Coriolis term in equations 4.23 (Arakawa, 1966). For simplicity, the mesh will have constant step-sizes Δx and Δy. The indices i and j as shown in figure 4.4 and in figure 4.5 correspond to the i-th zonal cell and the j-th meridional cell counted in the South-North direction and in the West-East direction respectively.

4.2.5 Boundary conditions

Currently, only Dirichelet conditions are implemented at the boundaries. Indeed, if the T-cells domain has $M \times N$ nodes then the U-cells have $M \times (N+1)$ nodes and the V-cells have $(M+1) \times N$ nodes. η is calculated within $\{2, ..., (M-1)\} \times \{2, ..., (N-1)\}$ and u and v are calculated within $\{2, ..., (M-1)\} \times \{2, ..., N\}$ and $\{2, ..., M\} \times \{2, ..., (N-1)\}$.

Null-flux

A land mask, m_T, for the T-cells mesh is introduced. The goal is to impose a null-flux boundary condition surrounding any land cell, i.e.

$$\vec{v} \cdot \vec{n} = 0.$$

It returns 1 if the cell is filled with water and 0 if the cell is land. This implies the definition of appropriate null-fluxes masks, m_U and m_V, for the U and V-cells. Thus, for every i, j such that $m_T = 0$, it is required that $m_U = 0$, $m_{U\,i+1} = 0$, $m_V = 0$ and $m_{V\,j+1} = 0$. Everywhere else the value of the masks is 1. The T, U and V masks are to be applied in the numerical scheme to the T-cell properties, the U-cell properties and the V-cell properties, respectively.

No-slip

The optional no-slip boundary condition (Pedlosky, 1987, p.194) consists of both null-flux and null-tangential velocities at the vertical walls of the domain, i.e.

$$\vec{v} \cdot \vec{n} = 0,$$

and

$$\vec{v} \perp \vec{n} = 0.$$

Thus, for every i, j such that $m_T = 0$, it is required, additionaly to the defined above null-flux condition, that $m_{U\,i,\,j+1} = 0$, $m_{U\,i+1,\,j+1} = 0$, $m_{U\,i,\,j-1} = 0$ and $m_{U\,i+1,\,j-1} = 0$ and that $m_{V\,i-1,\,j} = 0$, $m_{V\,i+1,\,j} = 0$, $m_{V\,i-1,\,j+1} = 0$ and $m_{V\,i+1,\,j+1} = 0$. One interesting aspect of the no-slip boundary condition is that it necessarily requires a global zero-curl for closed domains,

$$\oint \vec{v} \cdot d\vec{S} = 0.$$

Hence, using the Kelvin-Stokes theorem, the no-slip boundary condition is an interesting configuration to test the correct implementation of the model:

the curl within the domain must sum up to zero. Nevertheless, the no-slip boundary condition is a very strong constraint that acts on the kinematics and not on the dynamics of the motion per se (it is independent of the equation of motion).

Radiative boundary conditions

When no wall is to be considered at the boundaries, then all perturbation generated inside the domain eventually needs to go out of the domain. Furthermore, it could be interesting to propagate perturbations and information coming from outside of the domain. To this purpose are considered the broad class of open boundary conditions (OBC). The OBC are classified into two functional groups: the passive boundary conditions and the active boundary conditions. The passive boundary condition are designed to let information generated inside the domain to leave the domain, whereas the active boundary conditions try to propagate information from outside into the domain. Most regional oceanic modellers desire both aspects, of letting information out of and into the domain, which is considered a challenge. For very good reviews on OBC for regional ocean models, refer to Blayo and Debreu (2005) and Herzfeld (2009). For more recent types of radiative boundary conditions suitable for internal waves as well as the external mode, see Marsaleix et al. (2009). Radiative boundary conditions are passive boundary conditions (designed to let perturbations go out of the boundary) and usually consider the linearized hyperbolic version of equations 4.23 along the normal axis relatively to the open boundary. In this work, the gravity wave radiative method (also known as Sommerfeld radiative method) was implemented for the water elevation, η, and for the velocity tangential to the open boundary,

$$\frac{\partial \Phi}{\partial t} t + \mathbf{c} \cdot \mathbf{n} \frac{\partial \Phi}{\partial x} = 0, \tag{4.24}$$

where Φ is either the water elevation or the tangential velocity, $\mathbf{n}$ is the external normal vector to the open boundary and $\mathbf{c}$ is the phase wave celerity vector. In every occurence, the normal celerity wave intensity is considered to be $\mathbf{c} \cdot \mathbf{n} = \sqrt{g\,H}$. The passive Flather (1976) radiation method was implemented for the velocity normal to the open boundary,

$$H\,\mathbf{v} \cdot \mathbf{n} = \eta\,\mathbf{c} \cdot \mathbf{n}, \tag{4.25}$$

where $\mathbf{v}$ is the flow velocity vector. Both methods are implemented with the normal velocity outside of the elevation node (NVOE) (Herzfeld, 2009). The NVOE indicates how the radiative condition is implemented in the

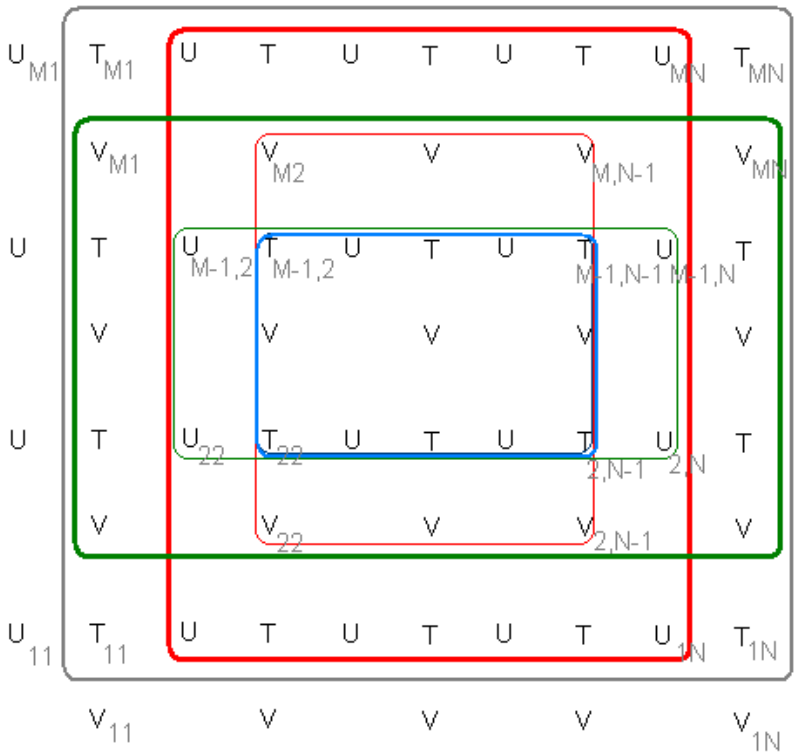

Figure 4.5: Detailed mesh emphasizing the boundaries. Composite of T, U and V-cells, the mesh illustrates the zone of integration of each type of cell: the blue rectangle contains the T-cells computed nodes, the thin green rectangle contains the U-cells computed nodes, the thin red rectangle contains the V-cells computed nodes. The thick green and red rectangles, however, delimit respectively the faces of the U and V-cells computed nodes.

numerical scheme and it is dependent on the design of the grid and of the boundaries by the modeller. The configuration with the normal velocity inside the elevation node (NVIE) is not considered in this work, though it is thought to be relatively easier to adapt it from a NVOE configuration, rather than the other way around (Herzfeld, 2009). Finally, the NVIE was seen to return poorer results in some basic experiments (Herzfeld, 2009). The NVIE-NVOE dichotomy is pertinent as each implementation will affect differently each term of the SWE equations 4.23. Herzfeld (2009) reported some very interesting tables describing which terms of the SWE equations 4.23 are affected by the NVIE and NVOE implementations.

4.2.6 The numerical scheme

For simplicity in the notation, the indices i and j will be omitted by default. The spatial finite difference numerical scheme is centered in time and centered in time (CTCS) described in Kantha and Clayson (2000):
For the zonal momentum (U-Cell), the first-order spatial discretization writes:

$$\begin{aligned}
\frac{\partial Hu}{\partial t} &= -\left((Huu)_{i+1/2} - (Huu)_{i-1/2}\right)/\Delta x \\
&\quad -\left((Huv)_{j+1/2} - (Huv)_{j-1/2}\right)/\Delta y \\
&\quad +f\,(Hv) \\
&\quad +\nu\left(\left(H\frac{\partial u}{\partial x}\right)_{i+1/2} - \left(H\frac{\partial u}{\partial x}\right)_{i-1/2}\right)/\Delta x \\
&\quad +\nu\left(\left(H\frac{\partial u}{\partial y}\right)_{j+1/2} - \left(H\frac{\partial u}{\partial y}\right)_{j-1/2}\right)/\Delta y \\
&\quad -gH\left(\eta_{i+1/2} - \eta_{i-1/2}\right)/\Delta x \\
&\quad +\frac{\rho_a}{\rho_0}C_a u_{10}\sqrt{u_{10}^2 + v_{10}^2} \\
&\quad -C_D u_b \sqrt{u_b^2 + v_b^2} \\
&\quad \equiv Ru
\end{aligned}$$

where the halved indices correspond to fluxes at the U-cells' faces. Thus, the CTCS fluxes write:

$$\begin{aligned}
(Huu)_{i+1/2} &= m_{U\,i+1}\,H\left(u_{i+1}+u\right)^2/2^2, \\
(Huu)_{i-1/2} &= m_{U\,i-1}\,H_{i-1}\left(u+u_{i-1}\right)^2/2^2, \\
(Huv)_{j+1/2} &= m_{U\,j+1}\left(H_{i-1}+H_i+H_{i-1,j+1}+H_{i,j+1}\right) \\
&\quad \times\left(u_{j+1}+u\right)\left(v_{i-1,j+1}+v_{i,j+1}\right)/16, \\
(Huv)_{j-1/2} &= m_{U\,j-1}\left(H_{i-1}+H_i+H_{i-1,j-1}+H_{i,j-1}\right) \\
&\quad \times\left(u+u_{j-1}\right)\left(v_{i-1}+v\right)/16, \\
f\,(Hv) &= f\left(H+H_{i-1}\right)/2 \\
&\quad \times\frac{\left(m_V\,v\right)_{i-1}+m_V\,v+\left(m_V\,v\right)_{j+1}+\left(m_V\,v\right)_{i-1,j+1}}{m_{V\,i-1}+m_V+m_{V\,j+1}+m_{V\,i-1,j+1}},
\end{aligned}$$

$$\nu\left(\left(H\frac{\partial u}{\partial x}\right)_{i+1/2}-\left(H\frac{\partial u}{\partial x}\right)_{i-1/2}\right)=$$
$$\nu\left(m_{U\,i+1}H\frac{u_{i+1}-u}{\Delta x}-m_{U\,i-1}H_{i-1}\frac{u-u_{i-1}}{\Delta x}\right),$$
$$\nu\left(\left(H\frac{\partial u}{\partial y}\right)_{j+1/2}-\left(H\frac{\partial u}{\partial y}\right)_{j-1/2}\right)=$$
$$\nu\left(m_{U\,j+1}H\frac{u_{j+1}-u}{\Delta y}-m_{U\,j-1}H_{j-1}\frac{u-u_{j-1}}{\Delta y}\right),$$
$$gH\left(\eta_{i+1/2}-\eta_{i-1/2}\right)=$$
$$g\left(H+H_{i-1}\right)/2\left(\eta-\eta_{i-1}\right),$$
$$C_D u\sqrt{u^2+v^2}=$$
$$C_D u\sqrt{u^2+\left(\frac{(m_V\,v)_{i-1}+m_V\,v+(m_V\,v)_{j+1}+(m_V\,v)_{i-1,j+1}}{m_{V\,i-1}+m_V+m_{V\,j+1}+m_{V\,i-1,j+1}}\right)^2}.$$

Notice how the $(Huu)_{j+1/2}$, $(Huv)_{j-1/2}$, $f\,(Hv)$ and $C_D u\sqrt{u^2+v^2}$ terms, loose significant precision over the other terms, due to their 4 terms averaging.
Hence, rewriting the full momentum CTCS spatial scheme we get:

$$
\begin{aligned}
&\frac{\partial Hu}{\partial t} = \\
&\quad -\left(m_{U\,i+1} H \left(u_{i+1}+u\right)^2/2^2 - m_{U\,i-1} H_{i-1} \left(u+u_{i-1}\right)^2/2^2\right)/\Delta x \\
&\quad -\left(\begin{array}{l} m_{U\,j+1}\ \left(H_{i-1}+H_i+H_{i-1,j+1}+H_{i,j+1}\right) \\ \times \left(u_{j+1}+u\right)\left(v_{i-1,j+1}+v_{i,j+1}\right)/16 \\ -m_{U\,j-1}\ \left(H_{i-1}+H_i+H_{i-1,j-1}+H_{i,j-1}\right) \\ \times \left(u+u_{j-1}\right)\left(v_{i-1}+v\right)/16 \end{array}\right)/\Delta y \\
&\quad +f\left(H+H_{i-1}\right)/2 \\
&\quad \times \frac{\left(m_V\, v\right)_{i-1} + m_V\, v + \left(m_V\, v\right)_{j+1} + \left(m_V\, v\right)_{i-1,j+1}}{m_{V\,i-1} + m_V + m_{V\,j+1} + m_{V\,i-1,j+1}} \\
&\quad +\nu\left(m_{U\,i+1} H \frac{u_{i+1}-u}{\Delta x} - m_{U\,i-1} H_{i-1} \frac{u-u_{i-1}}{\Delta x}\right)/\Delta x \\
&\quad +\nu\left(m_{U\,j+1} H \frac{u_{j+1}-u}{\Delta y} - m_{U\,j-1} H_{j-1} \frac{u-u_{j-1}}{\Delta y}\right)/\Delta y \\
&\quad -g\left(H+H_{i-1}\right)/2\left(\eta-\eta_{i-1}\right)/\Delta x \\
&\quad +\frac{\rho_a}{\rho_0} C_a u_{10} \sqrt{u_{10}^2+v_{10}^2} \\
&\quad -C_D u \\
&\quad \times \sqrt{u^2 + \left(\frac{\left(m_V\, v\right)_{i-1} + m_V\, v + \left(m_V\, v\right)_{j+1} + \left(m_V\, v\right)_{i-1,j+1}}{m_{V\,i-1} + m_V + m_{V\,j+1} + m_{V\,i-1,j+1}}\right)^2} \\
&\quad \equiv Ru
\end{aligned}
\tag{4.26}
$$

For the meridional spatial momentum scheme in the V-Cells, clever symmetry one-to-one relations with zonal momentum scheme in the U-cells are used:

- switch Δx and Δy: $\Delta x \leftrightarrow \Delta y$,
- switch i and j: $i \leftrightarrow j$,
- switch u and v: $u \leftrightarrow v$,
- switch signal of the Coriolis term: $(+ \leftrightarrow -)$.
- switch M and N: $M \leftrightarrow N$,

The finite-difference first-order numerical scheme for the waterlevel (T-Cell) writes out:

$$\begin{aligned}\frac{\partial \eta}{\partial t} &= -\left((Hu)_{i+1/2} - (Hu)_{i-1/2}\right)/\Delta x \\ &\quad -\left((Hv)_{j+1/2} - (Hv)_{j-1/2}\right)/\Delta y \\ &\equiv R\eta\end{aligned}$$

and each face's CTCS flux term writes down:

$$\begin{aligned}(Hu)_{i+1/2} &= m_{T\,i+1}\,(H + H_{i+1})/2\,u_{i+1}, \\ (Hu)_{i-1/2} &= m_{T\,i-1}\,(H_{i-1} + H)/2\,u, \\ (Hv)_{j+1/2} &= m_{T\,j+1}\,(H + H_{j+1})/2\,v_{j+1}, \\ (Hv)_{j-1/2} &= m_{T\,j-1}\,(H_{j-1} + H)/2\,v.\end{aligned}$$

Thus, the full waterlevel CTCS numerical scheme is:

$$\begin{aligned}\frac{\partial \eta}{\partial t} &= -\left(m_{T\,i+1}\,(H + H_{i+1})/2\,u_{i+1} - m_{T\,i-1}\,(H_{i-1} + H)/2\,u\right)/\Delta x \\ &\quad -m_{T\,j+1}\left((H + H_{j+1})/2\,v_{j+1} - m_{T\,j-1}\,(H_{j-1} + H)/2\,v\right)/\Delta y \\ &\quad \equiv R\eta\end{aligned}$$

The time scheme used is the Leapfrog as described in Kantha and Clayson (2000):

$$\begin{aligned}\eta^{l+1} &= \eta^{l-1} + 2\Delta t\,\{R\eta\}, \\ H^{l+1} &= \eta^{l+1} + d, \\ u^{l+1} &= \left(u^{l-1}\left(H^{l-1} + H_{i-1}^{l-1}\right) + 4\Delta t\,\{Ru\}\right)/\left(H^{l+1} + H_{i-1}^{l+1}\right), \\ v^{l+1} &= \left(v^{l-1}\left(H^{l-1} + H_{j-1}^{l-1}\right) + 4\Delta t\,\{Rv\}\right)/\left(H^{l+1} + H_{j-1}^{l+1}\right).\end{aligned}$$

Notice how the leapfrog time scheme obliges two initial conditions at t_0 and at t_1. Hence, in order to avoid mode decoupling, a Robert-Asselin filter (Asselin, 1972) for u, v, η at each integration time-step is used, as suggested by Kantha and Clayson (2000):

$$P^l = P^l + \gamma\left(P^{l-1} - 2P^l + P^{l+1}\right),$$

where γ is a parameter set to 0.1 (Kantha and Clayson, 2000). The Robert-Asselin provides a good coupling between the two initial conditions, at the expense of some loss in precision (Asselin, 1972).
The radiative scheme implemented follows a NVOE stencil on a C grid (Herzfeld, 2009). The *western* boundary radiative condition is defined, for the elevation and the component of velocity perpendicular to the boundary, by

$$\begin{aligned} \eta_{1,\,j}^{l+1} &= \eta_{1,\,j} - 2\frac{\Delta t}{\Delta x}\sqrt{g\,H_{1,\,j}}\,\left(\eta_{1,\,j} - \eta_{2,\,j}\right), \\ u_{1,\,j}^{l+1} &= -\sqrt{\frac{g}{H_{1,\,j}^{l+1}}}\,\eta_{1,\,j}^{l+1}, \end{aligned}$$

for $j = 1, ..., N$, and is defined by, for the velocity component tangent to the boundary,

$$v_{1,\,j}^{l+1} = \left(\begin{array}{l} v_{1,\,j}\,\left(H_{1,\,j} + H_{1,\,j-1}\right) \\ -2\,\frac{\Delta t}{\Delta x}\sqrt{g\,\frac{H_{1,\,j}+H_{1,\,j-1}}{2}}\,\left(v_{1,\,j} - v_{2,\,j}\right) \end{array} \right) / \left(H_{1,\,j}^{l+1} + H_{1,\,j-1}^{l+1}\right),$$

for $j = 2, ..., N$.
For the *eastern* boundary, the radiation boundary condition writes,

$$\begin{aligned} \eta_{M,\,j}^{l+1} &= \eta_{M,\,j} - 2\frac{\Delta t}{\Delta x}\sqrt{g\,H_{M,\,j}}\,\left(\eta_{M,\,j} - \eta_{M-1,\,j}\right), \\ u_{M+1,\,j}^{l+1} &= -\sqrt{\frac{g}{H_{M,\,j}^{l+1}}}\,\eta_{M,\,j}^{l+1}, \end{aligned}$$

for $j = 1, ..., N$, and is defined by, for the velocity component tangent to the boundary,

$$v_{M,\,j}^{l+1} = \left(\begin{array}{l} v_{M,\,j}\,\left(H_{M,\,j} + H_{M,\,j-1}\right) \\ -2\,\frac{\Delta t}{\Delta x}\sqrt{g\,\frac{H_{M,\,j}+H_{M,\,j-1}}{2}}\,\left(v_{M,\,j} - v_{M-1,\,j}\right) \end{array} \right) / \left(H_{M,\,j}^{l+1} + H_{M,\,j-1}^{l+1}\right),$$

for $j = 2, ..., N$. Note that the Flather (1976) radiation condition applied to the normal component of velocity to the boundary can be replaced with a simple null-gradient and yield similar results,

$$u_{1,\,j}^{l+1} = u_{2,\,j}^{l+1},$$

for $i = 1$, and

$$u_{m+1,\,j}^{l+1} = u_{m,\,j}^{l+1},$$

for $i = m + 1$.
Once more, to derive an adequate scheme for the *southern* and *northern* boundary conditions, simply follow the symmetrical rules below and apply them to the preceding equations

- switch i and j: $i \leftrightarrow j$,
- switch u and v: $u \leftrightarrow v$,
- switch M and N: $M \leftrightarrow N$,
- switch Δx and Δy: $\Delta x \leftrightarrow \Delta y$,
- switch (*West*, *East*) with (*South*, *North*).

The stability criterion is the Courant-Friedrich-Levy criterion (Courant et al., 1959)(CFL) described in Kantha and Clayson (2000):

$$\Delta t \left(\sqrt{gH} + V_{max} \right) \left(\frac{1}{\Delta x} + \frac{1}{\Delta y} \right) < 1.0$$

where V_{max} is the maximum advection field intensity in m/s. Note that for stability reasons, in the momentum equations, the friction terms are evaluated at time $l - 1$.

4.2.7 Validation

The interest of a gaussian level initial condition is that one can test adjustment under gravity of a non-rotating fluid under the hydrostatic approximation, much like the exercise on Gill (1982, p. 110). The hydrostatic approximation simply neglects the vertical velocity and acceleration of the particles to calculate the local pressure. Later on, the Coriolis acceleration can be added, and the flow adjustment under gravity of a rotating fluid can take place, again, much like the exercise on Gill (1982, p. 199). Some basic simulations are set to test the conservation of volume, momentum and vorticity. Even though energy should be conserved when considering the Euler equations, in practice, the numerical viscosity in the model ensures the maintenance of a good rate of dissipation of energy. The interesting thing to test then, is to estimate the rate of energy dissipation based on equation 2.66. More on that later.

Gaussian bell-shaped geometry

The other interesting aspect of the gaussian level initial condition, is that its volume is easily integrable, and its initial potential energy is also easily integrable. Indeed, the gaussian water elevation is given by expression

$$\eta_{\sigma_x\,\sigma_y}(x,y) = \frac{V}{\sigma_x\sigma_y\pi} e^{-\left(\frac{(x-x_0)^2}{\sigma_x^2}+\frac{(y-y_0)^2}{\sigma_y^2}\right)} \tag{4.27}$$

where σ_x, σ_y is the gaussian bell width along the x-axis and the y-axis, x_0, y_0 are the coordinates of the gaussian bell centre. The integral of equation 4.27 over an infinite domain is classical[1] and yields exactly V

$$\int \eta_{\sigma_x\,\sigma_y}\,dx\,dy = V.$$

Another way of writing equation 4.27 in terms of the gaussian bell-shaped surface height, $h_0 \equiv \eta_{\sigma_x\,\sigma_y}(x_0,\,y_0)$, is

$$\eta_{\sigma_x\,\sigma_y}(x,y) = h_0\, e^{-\left(\frac{(x-x_0)^2}{\sigma_x^2}+\frac{(y-y_0)^2}{\sigma_y^2}\right)}, \tag{4.28}$$

which makes

$$V = \pi\,\sigma_x\,\sigma_y\,h_0. \tag{4.29}$$

[1] $\int_{-\infty}^{\infty} e^{-x^2}\,dx = \sqrt{\pi}$

Equation 4.29 is quite plausible since when considering $\sigma_x = \sigma_y$, the volume V is equivalent to that of a cylinder of radius σ and height h_0. However, to make things further interesting, integrating the square of the gaussian bell-shaped surface would lead in determining the initial total energy of the system. Thus, a general relationship between power orders of $\eta_{\sigma_x,\,\sigma_y}$ would be mighty useful. In fact, it can be easily deduced as follows, for the volume:

$$\begin{aligned} V_{\frac{\sigma_x}{\sqrt{n}},\,\frac{\sigma_y}{\sqrt{n}}} &= \pi \frac{\sigma_x}{\sqrt{n}}\,\frac{\sigma_y}{\sqrt{n}}\,h_0 \\ &= \frac{V}{n}, \end{aligned} \tag{4.30}$$

and for the water level:

$$\begin{aligned} \eta^n_{\sigma_x\,\sigma_y} &= \left(\frac{V}{\sigma_x\,\sigma_y\,\pi}\right)^n e^{-n\left(\frac{(x-x_0)^2}{\sigma_x^2}+\frac{(y-y_0)^2}{\sigma_y^2}\right)} \\ &= \left(\frac{V}{\sigma_x\,\sigma_y\,\pi}\right)^{n-1} \left(\frac{\frac{V}{n}}{\frac{\sigma_x}{\sqrt{n}}\,\frac{\sigma_y}{\sqrt{n}}\,\pi}\right) e^{-\left(\frac{(x-x_0)^2}{\left(\frac{\sigma_x}{\sqrt{n}}\right)^2}+\frac{(y-y_0)^2}{\left(\frac{\sigma_y}{\sqrt{n}}\right)^2}\right)} \\ &= \left(\frac{V}{\sigma_x\,\sigma_y\,\pi}\right)^{n-1} \eta_{\frac{\sigma_x}{\sqrt{n}}\,\frac{\sigma_y}{\sqrt{n}}}. \end{aligned} \tag{4.31}$$

Hence for $n = 2$,

$$\eta^2_{\sigma_x\,\sigma_y} = \left(\frac{V}{\sigma_x\,\sigma_y\,\pi}\right) \eta_{\frac{\sigma_x}{\sqrt{2}}\,\frac{\sigma_y}{\sqrt{2}}}. \tag{4.32}$$

Equation 4.32 will be very useful, calculate the exact initial total energy of a gaussian bell-shaped system released under a local gravitacional acceleration.

Energy

The kinetic energy, KE is given by

$$KE = \int \frac{1}{2}\rho\,(u^2 + v^2)\,H\,dA, \tag{4.33}$$

where dA is an elementary surface area. The available potential energy, (or perturbation potential energy (Gill, 1982, p. 111)), APE is given by

$$APE = \int \frac{1}{2}\rho\,g\,\eta^2\,dA. \tag{4.34}$$

The total energy is the sum TE = KE + APE.
The APE in equation 4.34 of a gaussian bell-shaped surface water elevation described by equation 4.27 is easily calculated considering equation 4.32 and is equal to

$$\begin{aligned}
APE_{0,\,h_0,\,\sigma_x,\,\sigma_y} &= \int \frac{1}{2}\rho\,g\,\eta^2_{\sigma_x,\,\sigma_y}\,dA \\
&= \int \frac{1}{2}\rho\,g\,\frac{V}{\sigma_x\,\sigma_y\,\pi}\,\eta_{\frac{\sigma_x}{\sqrt{2}},\,\frac{\sigma_y}{\sqrt{2}}}\,dA \\
&= \frac{1}{2}\rho\,g\,\frac{V}{\sigma_x\,\sigma_y\,\pi}\int \eta_{\frac{\sigma_x}{\sqrt{2}},\,\frac{\sigma_y}{\sqrt{2}}}\,dA \\
&= \frac{1}{2}\rho\,g\,\frac{V}{\sigma_x\,\sigma_y\,\pi}\,\frac{V}{2} \\
&= \frac{\rho\,g}{4\pi}\,\frac{V^2}{\sigma_x\,\sigma_y} \\
&= \frac{\rho\,g}{4}\,V\,h_0 \\
&= \frac{\rho\,g}{4}\,\pi\,\sigma_x\,\sigma_y\,h_0^2.
\end{aligned} \tag{4.35}$$

Hence equation 4.35 gives the approximate initial TE of a square domain, so long as the length of the domain equals several times the gaussian bell width σ.

Geometric and similitude considerations

The volume of the gaussian bell surface is geometrically determined by equation 4.29 and maintains itself constant throughout the wave dispersion, even if the wave gets reflects by walls or by a bumpy bathymetry.
Beyond simple geometrical relationships, the most interesting relationships are given by adimensional numbers and by characteristic quantities of space, time and velocity. The celerity of gravity waves, c, is given, in the shallow water approximation, by (Kundu and Cohen, 2002)

$$c = \sqrt{g\,H}. \tag{4.36}$$

The characteristic speed of the flow, U, in the gaussian bump initialization, is zero everywhere, except at the wave front, where the characteristic velocity can be estimated by geometrical considerations from equation 4.33 and from equation 4.35.

$$\frac{1}{2}\,\rho\,U_0^2\,H\,\pi\,\sigma^2 \sim \frac{TE_0}{2}, \tag{4.37}$$

where U_0 is the initial velocity, TE_0 is the initial total energy and $\sigma \equiv \sigma_x = \sigma_y$. By replacing TE_0 with equation 4.35,

$$\begin{aligned} U_0 &\sim \sqrt{\frac{TE_0}{\rho\,H\,\pi\,\sigma^2}} \\ &\sim \sqrt{\frac{\frac{\rho\,g}{4}\,\pi\,\sigma^2\,h_0^2}{\rho\,H\,\pi\,\sigma^2}} \\ &\sim \frac{h_0}{2}\sqrt{\frac{g}{H}}. \end{aligned} \tag{4.38}$$

The estimated characteristic velocity of the flow near the wave front in equation 4.38, in the vicinity of the instant of release, is quite plausible since the similar exercise in Gill (1982, p. 110) yields a perfectly analogous result. Hence, the external mode celerity is defined by the total depth H, and the barotropic flow intensity is defined by half of the height between the crest and the trough, $\frac{h}{2}$ and modulated total depth. Analogously to similitude theory, one may expect, as an hypothesis, qualitatively similar dynamical behavior for fluids maintaining the same ratio between phase wave speed and flow velocity near the wave front. Such ratio is known since classical hydraulics as being the Froude number, Fr, as seen in equation 4.39,

$$\mathrm{Fr} \sim \frac{U}{c}. \tag{4.39}$$

The Froude number, in hydraulic pipes, characterizes slow, rapid and critical flows according if the number is below, above or equal to unity. Each type of flow has distinct topological properties. Particularly in their locus of control, leewards (slow) or upwards (rapid). In the wave motion propagation, it also makes sense to characterize the ratio between the phase wave celerity and the flow created by its propagation in its wake. Concretely speaking, the flow corresponds to the oscillatory motion that undergo the surface particles, the time period being that of the phase wave period, T, and the radius of oscillation simply being the half of the height between a crest and a trough, as illustrated in figure 4.6. In the particular case of the gaussian bump, the Froude number is deduced by taking the ratio between equations 4.38 and 4.36, and yields

$$\mathrm{Fr} \sim \frac{h_0}{2\,H}. \tag{4.40}$$

Equation 4.38 indicates that the flow velocity in the wake of the wave grows with the initial elevation, which is rather intuitive, but also indicates that the flow velocity reduces as the depth grows, which is rather counter-intuitive. Hence, the faster the gravity wave celerity ,the slower the flow velocity in its wake and the smaller the Froude number. Conversely, the upper limit of the Froude number relating a gravity wave and the flow in its wake is determined (noting that $H = h_0 + d$) when considering

$$h_0 \gg d,$$

yielding

$$\mathrm{Fr} \overset{h_0 \gg d}{\longrightarrow} \frac{1}{2}. \tag{4.41}$$

Equation 4.41 is an extreme condition that reminds us that the gravity wave celerity is, at least, twice as fast the velocity of the flow in its wake, for a two-dimensional wave propagating with a radial symmetry. This limit, in practice is never met by the shallow waters equations numerical implementation, because the hydrostatic approximation, which relies on the

$$h \ll H$$

assumption, is violated long before.
It would be interesting, beyond estimating the initial mechanical energy, TE_0, to estimate the integrated time evolution of the mechanical energy, specifically for the gaussian water elevation. The integrated equation of

motion for the total mechanic energy in a closed domain is given after integration of the summed equations 2.67 and 2.72, yielding,

$$TE_{,t} = -\int_V \rho\,\epsilon\,dV, \tag{4.42}$$

where ϵ is the dissipation rate originally seen in equation 2.66, which yields for the shallow waters equation of motion,

$$\epsilon = \nu\left(\left(\frac{\partial u}{\partial x}\right)^2 + \left(\frac{\partial u}{\partial y}\right)^2 + \left(\frac{\partial v}{\partial x}\right)^2 + \left(\frac{\partial v}{\partial y}\right)^2\right). \tag{4.43}$$

Considering that the viscous dissipation is a simple turbulence model, then one can infer that the integrated turbulent kinetic energy (TKE) production rate is given by the kinetic energy viscous dissipation rate but with an opposite sign,

$$TKE_{,t} = \int_V \rho\,\epsilon\,dV. \tag{4.44}$$

In the particular geometry of the gaussian elevation, it would be interesting to estimate an analytical approximation of the viscous dissipation rate. To do so, an over-estimation of the velocity gradient comes in need. The initial characteristic flow velocity in the wake of the gaussian bump wave is deduced from the initial energy,

$$KE_0 = \frac{1}{2}\,TE_0,$$

Hence

$$\frac{1}{2}\,\rho\,U_0^2\,\pi\,\sigma_x\,\sigma_y\,H = \frac{1}{2}\,TE_0,$$

which yields

$$U_0^2 = \frac{TE_0}{\rho\,\pi\,\sigma_x\,\sigma_y\,H}, \tag{4.45}$$

as the squared characteristic velocity in the wake of the gaussian elevation wave front. An estimative of the width of the gaussian bump wave front is simply given by $\sigma = \frac{\sigma_x+\sigma_y}{2}$. Thus, a plausible estimative of the viscous dissipation coefficient for a gaussian bump initial elevation, shortly the initial instant is

$$\epsilon_\sigma(x,\,y,\,t_0) = \begin{cases} \nu\,\left(\frac{U_0}{\sigma}\right)^2, & \text{if } x^2+y^2 < \sigma \\ 0, & \text{if not.} \end{cases} \tag{4.46}$$

Integrating equation 4.42 near instant t_0 and using equation 4.46 gives

$$\begin{aligned} TE_{,t} &= -\rho\,\epsilon_\sigma\,\pi\,\sigma^2\,H \\ &= -\frac{\nu}{\sigma^2}\,TE_0. \end{aligned} \tag{4.47}$$

Hence the linear approximation of the time evolution of the adimensionalized mechanical energy can be estimated by,

$$\frac{TE}{TE_0}(t) = -\frac{\nu}{\sigma^2}\, t + 1. \tag{4.48}$$

Equation 4.48, which satisfies the condition

$$TE(0) = TE_0,$$

is very interesting because it allows to postulate a characteristic time of dissipation, T_σ, of the mechanical energy of the system (a gaussian bump) given by

$$T_\sigma = \frac{\sigma^2}{\nu}. \tag{4.49}$$

This characateristic time should yield the order of magnitude of the time taken for the gaussian bump to dissipate a substancial amount of its initial energy, after being released. It is interesting to notice that it is independent of the gravitic acceleration. A full adimensionalization of the total energy equation is now possible:

$$t^\star \equiv \frac{t}{T_\sigma},$$

and

$$\frac{TE}{TE_0}(t^\star) = -t^\star + 1. \tag{4.50}$$

Equation 4.50 seems like a good candidate for a linear fully-adimensional approximation near the instant of release of the gaussian bump, t_0, of the time evolution of the mechanical energy of the system. Further below in section 4.2.7, it will be seen with a numerical experiment that the proposed model of the adimensional equation 4.50 shows an accurate characteristic time, T_σ, and an accurate dependency with the inverse of σ^2. However, it fails to show a dependency with ν.

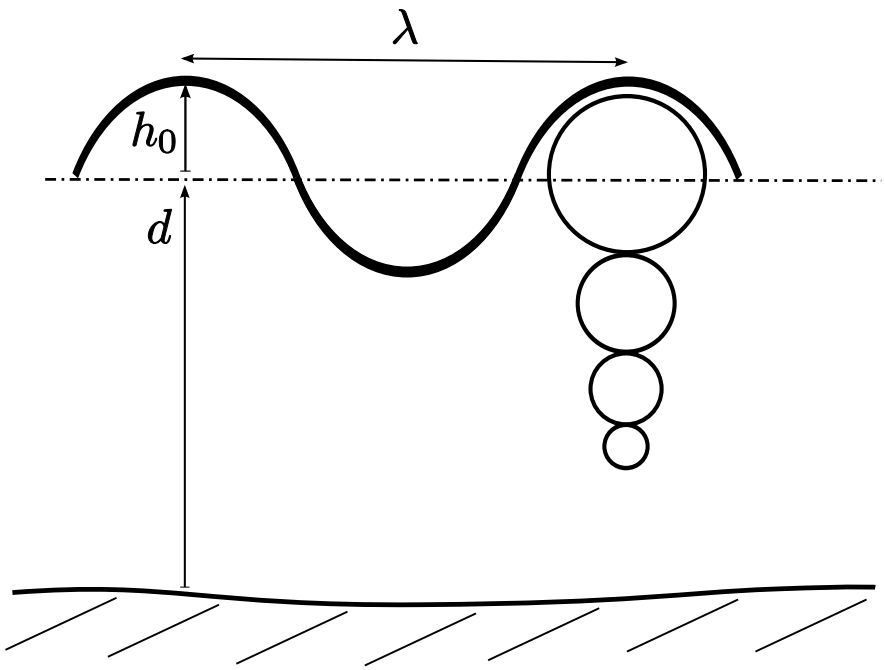

Figure 4.6: The oscillatory motion of particles caused by wave propagation is characterized by the wave amplitude, h_0, and time period, $T = \frac{\lambda}{\sqrt{g\,(h_0+d)}}$. Their mean linear velocity is estimated to be $U = \frac{2\,\pi\,h_0}{T} = \frac{2\,\pi\,h_0\,\sqrt{g\,(h_0+d)}}{\lambda}$.

Table 4.1: Configuration of the model for a non-rotating fluid with a gaussian initial elevation.

Parameter	Value
H	10 m
h_0	1 cm
σ_x	6×10^4 m
ν	0 m^2 s^{-1}
$M \times N$	37×37
Duration	1.8×10^5 s
dx	2×10^4 m
dt	500 s
TE_0	2.86×10^9 J
U_0	$\sim 5 \times 10^{-3}$ m s^{-1}
c	~ 10 m s^{-1}
Fr	$\sim 5 \times 10^{-4}$
Boundary	Closed
Volume	1.13×10^8 m^3

Basic results

Figure 4.7 shows the gaussian bump at initial instant for the configuration described in table 4.1. In the configuration described by table 4.1, the geometry of the system is bi-axially symmetric along the x-axis and along the y-axis. The grid is square and with an uneven number of cells along each axis. The gaussian bump described in equation 4.27 and configured as shown in table 4.1 has radial symmetry and its barycentre is located exactly at the central grid-cell of the square domain. The momentum and continuity equations 4.23 also display radial symmetry. Hence, the expected solution should display a symmetry equal to the composition of the symmetries contained by the geometry, the initial condition and the PDE. In this case, it should display a perfectly bi-axial symmetry, along the x-axis and along the y-axis. Figure 4.8 and figure 4.9 show the state of the waterlevel and the flow of the velocity field after 1.8×10^5 s of simulation. The axial symmetry of the waterlevel and of the velocity field is one of the attributes that advocates in favor of a correct implementation of the numerical scheme. If any mistake was made in the terms of the continuity equation or in the terms of the momentum equation (it could be a sign error or an index attribution error in the numerical scheme), then it would probably break the symmetry of the results. In the present test-case, the conservation of vol-

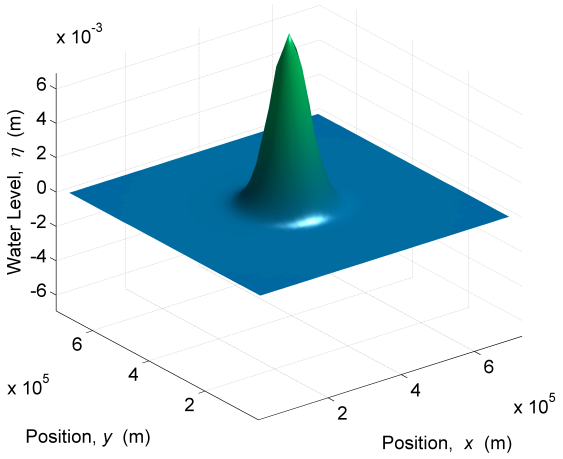

Figure 4.7: Gaussian elevation test-case energy time evolution in inviscid, frictionless conditions at initial instant.

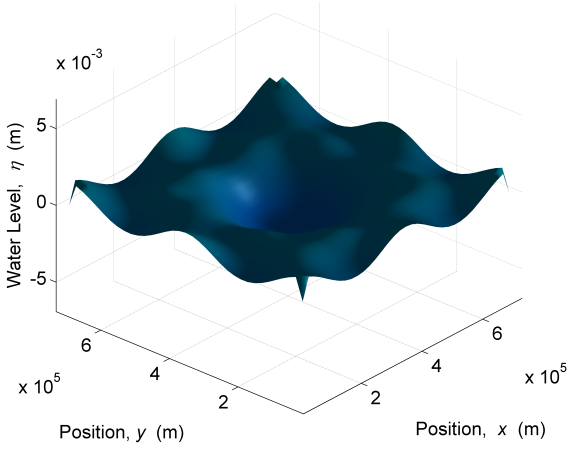

Figure 4.8: Gaussian elevation test-case in inviscid, frictionless conditions at time instant 1.8×10^5 s.

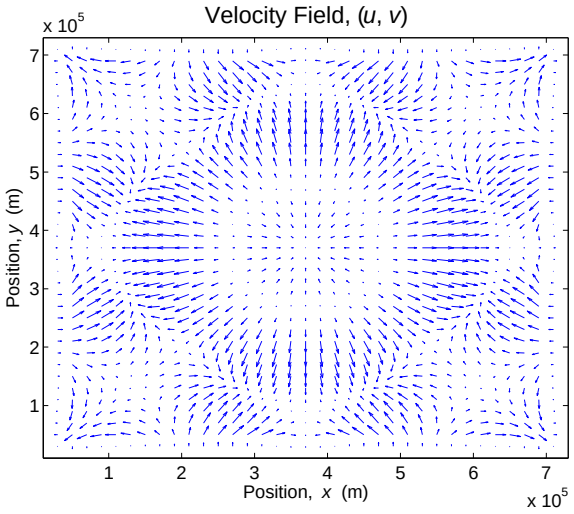

Figure 4.9: Gaussian level velocity field in inviscid, frictionless conditions at time instant 1.8×10^5 s.

ume, vorticity and momentum are expected. The conservation of energy is not expected due to the artificial numerical viscosity inherent in this type of finite-diferencing technique. Figure 4.10 shows the time evolution of the volume. The total volume is conserved as expected both from the continuity equation condition and from the conservative nature of the finite-volume CTCS diferencing technique applied to regularly-spaced grid cells. Figures 4.11 and 4.12 display the vertical curl field,

$$\zeta = \frac{\partial v}{\partial x} - \frac{\partial u}{\partial y},$$

at the end of simulation, at time instant 1.8×10^5 s, and the integrated curl field along the time. The local curl field is zero everywhere except close to the boundaries. Nevertheless, the circulation along the boundaries still yields zero, as attests figure 4.12. Arakawa (1966) has an insightful discussion examining several jacobian discretization operators that allow the conservation of energy, vorticity, or both for the vorticity equation of motion. It is not a trivial task to ensure conservation of both energy and vorticity. Conservation of vorticity was ensured with this rather simple and economic scheme. The partial time derivative of the momentum equations in the the shallow-water equations 4.23, after integration in a closed domain,

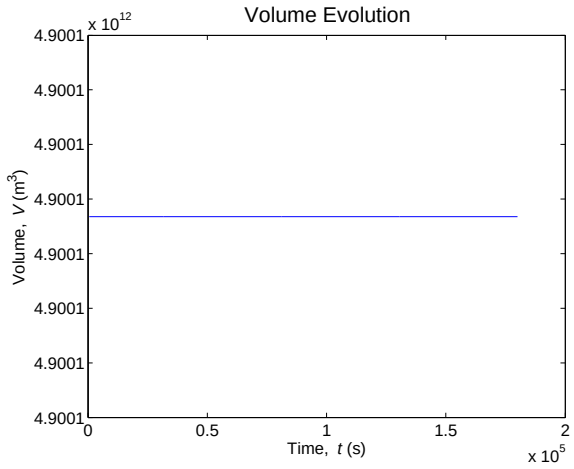

Figure 4.10: Time evolution of the volume. The boundaries are closed and the volume is conserved at 4.9×10^12 m^3.

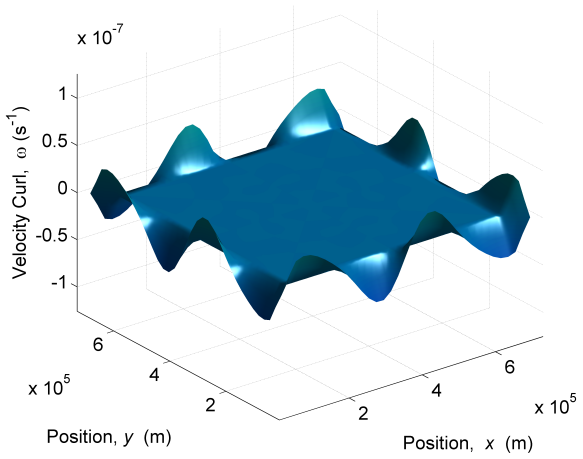

Figure 4.11: Curl at instant 1.8×10^5 s. The order of magnitude of the extrema is roughly 10^{-7} s^{-1}. The curl is locally zero everywhere, except in a line near the boundary. Its integration yields zero nonetheless, as is confirmed by the global curl results.

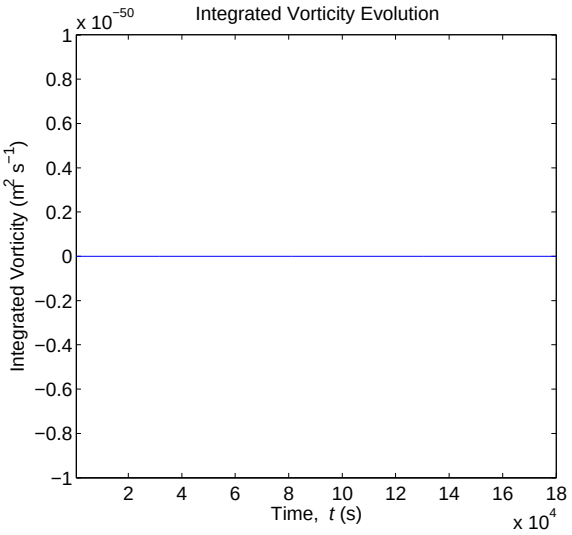

Figure 4.12: Evolution with time of the global curl. Global curl is conserved, as expected.

Ω, yields zero in the absence of friction terms (source and sink terms),

$$\int_{\Omega} \frac{\partial u}{\partial t}\, dA = 0.$$

This latter result was calculated making use of the fundamental theorem of Calculus as described in equation 2.1. In figure 4.15, the time evolution of the integrated velocity associated to the u and v components is shown. The expected result is zero but in fact, the model returns a result in the order of 10^{-7} m^4 s^{-1}. This discrepancy is mainly due to numerical error that arises when subtracting two large but very similar numbers using digital computers. Consider n the order of magnitude of the large, yet similar, subtracted numbers. The exact floating-point operation should return nearly zero. However, the 14 decimal digit number returned by the numerical calculation, yields the correct result only up to $10^{-14} \times 10^{n}$ of precision. To simplify, and as an example, the following calculation

$$1.12345678901234E-2 \;-\; 1.12345678901233E-2$$

which should return exactly

$$1.000000000000000E-16,$$

instead, returns in MATLAB,

$$9.88792381306780E-17.$$

As can be seen from the above example, the MATLAB returns an unacceptably low number of accurate (significant) digits. This numerical phenomenon is known as loss of significance. Hence, all the significant algarisms are sheer noise and the result is only valid within 10^{-14} times the order of magnitude of the maximum number of the subtraction, i.e. in our example, within $10^{-2-14} = 10^{-16}$. This same numerical error is at the basis of the pressure-gradient error (Beckmann and Haidvogel, 1993) in topographical following coordinate models. Thus, when integrating the axisymmetrical u and v velocity fields, it is fairly reasonable to expect that they add up to zero, but only to the limit of their numerical precision given the maximum characteristic velocity allowed times 10^{-14}, hence the white noise error err is estimated as

$$\begin{aligned} err &\sim U_0\, A\, H \times 10^{-14} \\ &\sim 2 \times 10^{-3}\, 5 \times 10^{11} \times 10 \times 10^{-14} \\ &\sim 10^{-4}. \end{aligned} \tag{4.51}$$

Thus, any value similar or below the error, $err \sim 10^{-4}$, as regards the integration of any scalar field of velocities, is as close to zero as it gets. Hence, the signal in the time evolution of the integrated velocities in the domain should be considered white noise. Consequently, as far numerical computing goes, the momentum is conserved by the implemented numerical scheme.
Figure 4.16 shows the evolution of the total, kinetic and potential energy of the gaussian elevation test case in inviscid, frictionless conditions. The initial energy is in very good agreement with the theoretical estimate of 2.89×10^9 J, calculated via equation 4.35, and its decay is strictly due to numerical diffusion, since the closed boundary conditions allow no energy flux through the boundary (radiation) and there are no source nor sink terms. The leapfrog+CS scheme is only second-order accurate in time and space, and is known for its rather high numerical diffusion. If the modeled domain had its walls pushed back to infinity, then the KE and the APE would each be exactly half the TE (Gill, 1982). In this case, the walls reflect the waves back and forth within the domain. At each reflection, a major energy transfer occurs from KE to PE, resulting in a peak in PE and a low in KE, which is visible in the waterlevel by an elevation at the boundary when the transfer occurs. The term that allows this energy transfer is the source and

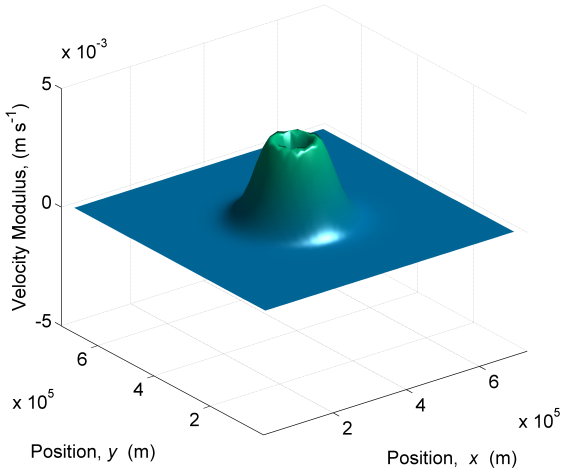

Figure 4.13: Velocity modulus at instant 3500 s. The maximum velocity is estimated to be around 2×10^{-3} m s^{-1}.

sink term $\rho\, g\, w$ as seen in the, previously deduced, energy equations of motion for kinetic energy, equation 2.67, and for potential energy, equation 2.72. Mind however that this energy transfer is fully reversible and doesn't have a direct implication in the, so-called, energy cascade process (Burchard and Others, 2002). During this process no dissipation of energy is considered in the energy equations 2.67. Hence, in order to completely explain the time evolution behaviour of energy, it would be very interesting to estimate the energy decay rate. Another very interesting question would be to determine in which conditions does the energy decay returned by the numerical model is driven by physical viscosity instead of numerical viscosity. In this case, for instance, the energy dissipation is driven by numerical viscosity since it has zero physical viscosity.

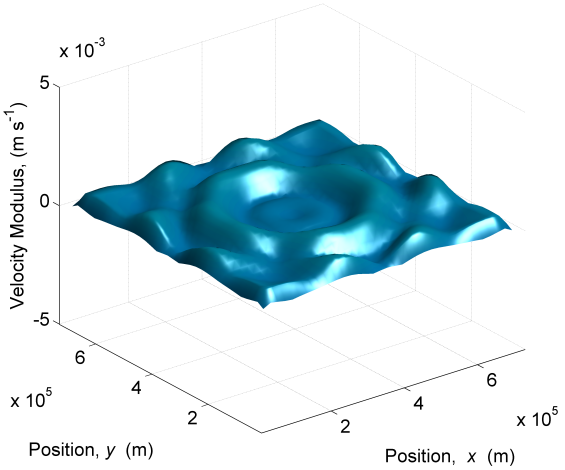

Figure 4.14: Velocity modulus at instant 180000 s. The maximum velocity is estimated to be around 1×10^{-3} m s^{-1}.

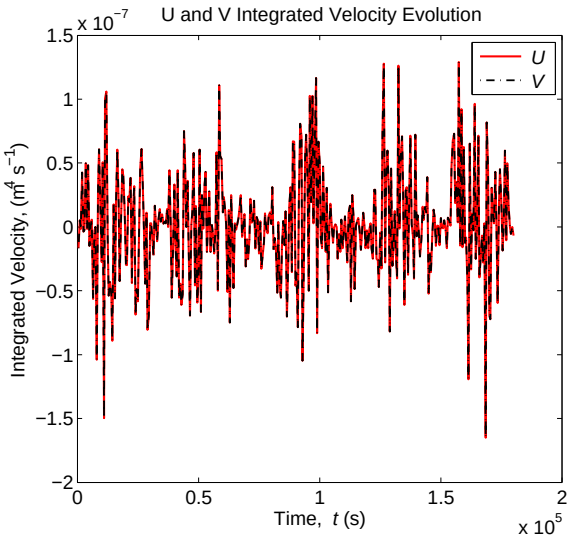

Figure 4.15: Time evolution of the the u and v components of velocity integrated in the whole domain. The erratic behavior ranging 10^{-7} m^4 s^{-1} is strictly due to numerical errors.

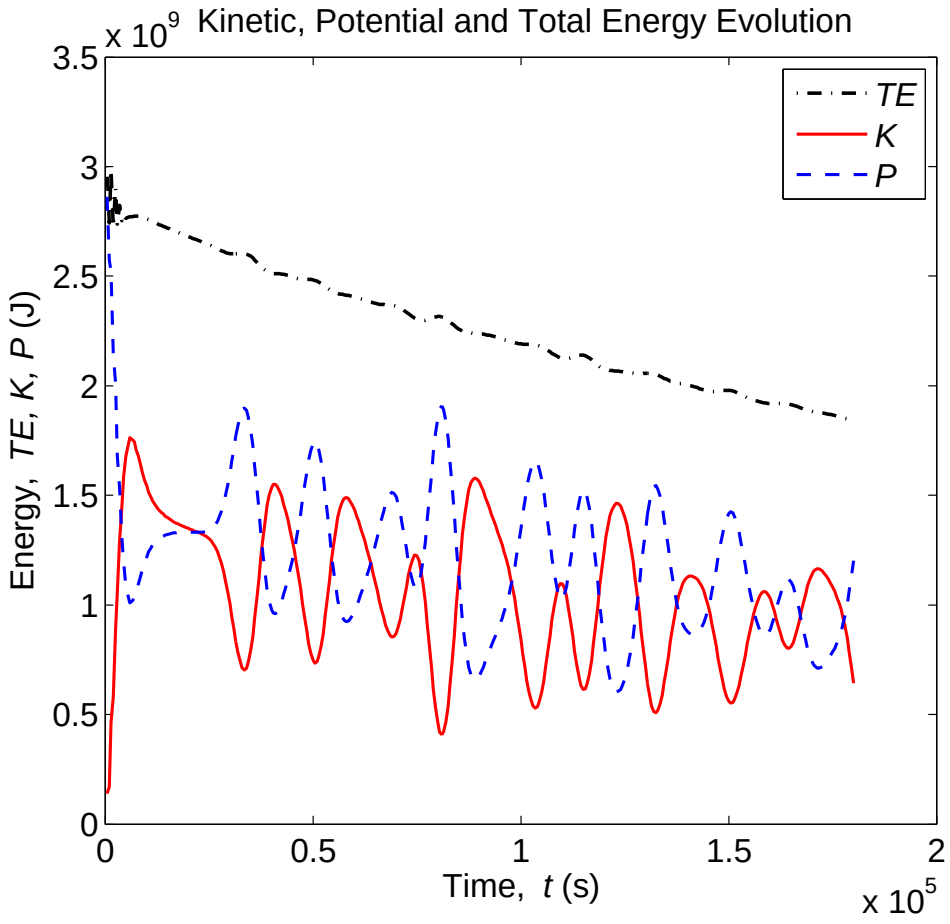

Figure 4.16: Gaussian elevation test-case energy time evolution in inviscid, frictionless conditions for a 180000 s run. The energy decay is strictly due to numerical diffusion.

Energy decay study

In order to answer the last question of the previous paragraph, a study with the same model configuration described in table 4.1 was undertaken, and several runs were made, each with a different viscosities. The energy decay is expected to increase with physical viscosity, however, both physical and numerical viscosity coexist. Numerical viscosity is caused by advection, and since the advective part of the momentum equations 4.23 remain unchanged by the varying viscosity, the numerical viscosity is expected to have exactly the same influence on the energy decay in the different runs. Figure 4.17 displays the results for different viscosities, ν, ranging from 0 to 5×10^4 $m^2\ s^{-1}$. Though figure 4.17 confirms the fact that energy decay increases

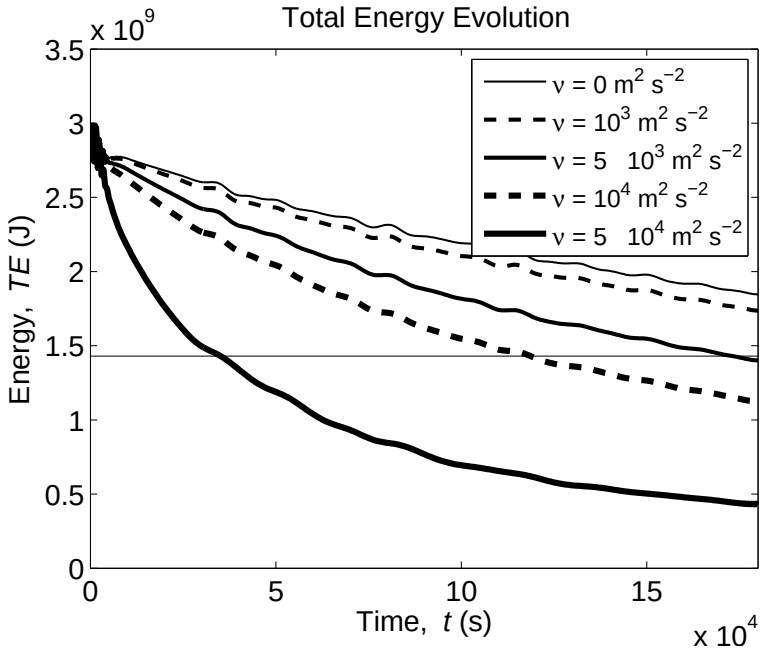

Figure 4.17: TE decay with time for several viscosities, ν, ranging from 0 to 5×10^4 $m^2\ s^{-1}$. The horizontal line represents exactly one half of the initial energy.

with viscosity, it actually yields little added value on *how* does energy decays with viscosity. Thus a different approach is needed. A technique often used among particle physicists that need to study the rate of decay of unstable atom isotopes is to look at the half-life, $\tau_{1/2}$, of the particles. The half-life is the time duration for a physical quantity to decay half of its orig-

inal value. In this case-study, its the time duration that the system takes to dissipate half of its initial total energy. Figure 4.18 shows a plot of the TE half-life of the system for different viscosities. The plot shows three regions, the low viscosity region for $0 < \nu < 2 \times 10^2$ m^2 s^{-1}, the transition region for $2 \times 10^2 < \nu < 2 \times 10^3$ m^2 s^{-1}, and the high viscosity region for $2 \times 10^3 < \nu < 10^5$ m^2 s^{-1}. For viscosities higher than 10^5 m^2 s^{-1} the system, described in table 4.1, reaches the limits of its numerical stability. In the low viscosity region there is no dependence of the TE half-life with viscosity, showing a half-life of 3×10^5 s. This is probably due to numerical viscosity which prevails over the physical viscosity. The transition region shows a balance between the numerical viscosity and the physical viscosity whereas in the high viscosity region, the TE half-life is dominated by physical viscosity, displaying a linear dependence. Therefore, the system can be studied with the aid of numerical experimentation for low Reynolds number, which corresponds to the high viscosity region. Since numerical viscosity is present in every numerical modeling experiment, the TE half-life dependence with viscosity is a very useful tool to quantify the behaviour of any system as regards its energy dissipation. Furthermore, it allows to determine the range of viscosities where energy dissipation is dominated by physical viscosity. Finally, it allows to estimate what is the effective viscosity equivalent to the numerical viscosity. In this case, described by table 4.1, the numerical viscosity has an effective viscosity of about 200 m^2 s^{-1}, as indicated by figure 4.18. Although figure 4.18 proposes an experimental technique to determine the viscosity equivalent to numerical viscosity, in practice, depending on the modelled system, it can be lengthy to make all the required runs. Thus it would be interesting to find an analytical method that would estimate the range of viscosities corresponding to the transition region in figure 4.18. Analyzing schematically the numerical scheme for advection and diffusion in equation 4.26 (face-centred), the main terms in the x-direction yield

$$\left(\frac{U\,\Delta t}{2\,\Delta x} + \frac{\nu\,\Delta t}{\Delta x^2}\right) u_{i+1} + 2\,\frac{\nu\,\Delta t}{\Delta x^2}\,u_i + \left(-\frac{U\,\Delta t}{2\,\Delta x} + \frac{\nu\,\Delta t}{\Delta x^2}\right) u_{i-1}, \qquad (4.52)$$

where U is the characteristic velocity. Viscous diffusion is due to the $\frac{\nu\,\Delta t}{\Delta x^2}$ term while advection and numerical diffusion is due to the $\frac{U\,\Delta t}{2\,\Delta x}$ term. Thus, to ensure that viscous diffusion dominates the numerical one is equivalent to ensure that

$$\frac{U\,\Delta t}{2\,\Delta x} \ll \frac{\nu\,\Delta t}{\Delta x^2},$$

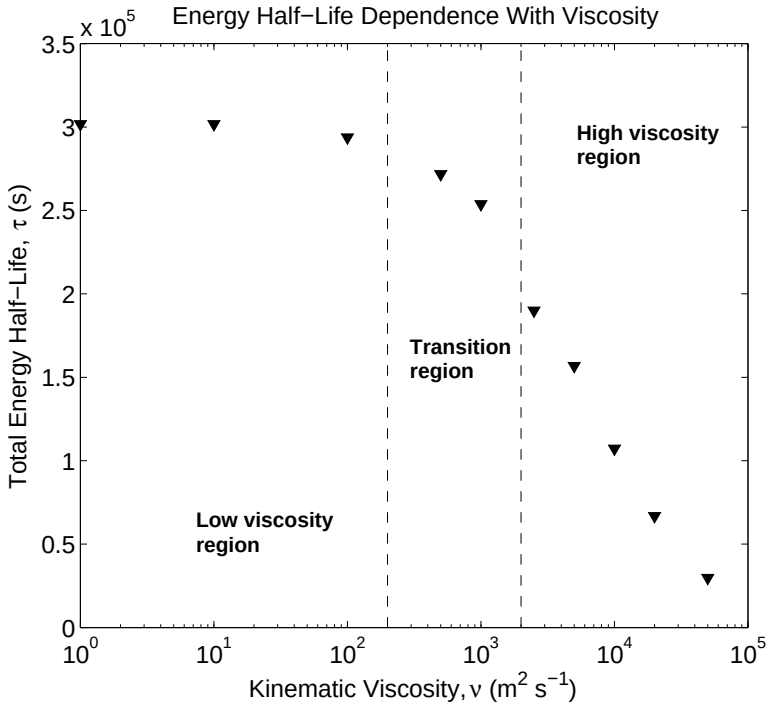

Figure 4.18: Dependence of the total energy half-life with viscosity. The viscosity axis is logarithmic. The initial energy of the gaussian bump was 2.86×10^9 J. Three regions are separated by the vertical dashed lines: the low viscosity region for $0 < \nu < 2 \times 10^2$ m^2 s^{-1}, the transition region for $2 \times 10^2 < \nu < 2 \times 10^3$ m^2 s^{-1} and the high viscosity region for $2 \times 10^3 < \nu < 10^5$ m^2 s^{-1}.

which is equivalent to consider a very small numerical Reynolds number (or numerical Péclet number) as seen in equation 4.53,

$$\frac{U\,\Delta x}{2\,\nu} \ll 1. \tag{4.53}$$

Using the parameters in the model setup defined in table 4.1, we get

$$\nu \gg 50 \text{ m}^2\text{s}^{-1},$$

which means that viscosities around 50 m^2 s^{-1} are well within the low viscosity region, viscosities around 500 m^2 s^{-1} should be around the transition region, and viscosities around 5000 m^2 s^{-1} should be well within the high

viscosity region. The numerical experimentation results shown in figure 4.18 corroborates the hypothesis that physical viscosity is dominant in numerical models when the condition seen in equation 4.53 is satisfied. Figure 4.18 displays a low viscosity region where numerical diffusion is dominant, for $\nu = 50$ m^2 s^{-1}, a transition region, for $\nu = 500$ m^2 s^{-1}, and a high viscosity region where physical viscosity is dominant, for $\nu = 5000$ m^2 s^{-1}. The interesting and counter-intuitive aspect about the condition in equation 4.53 is that it has not a dependency on the time-step. If the criterion in equation 4.53 is not met then energy dissipation is driven by numerical diffusion alone, which is undesired for a proper study on energy cascade or turbulence in general.
Figure 4.19 displays the time evolution of $\frac{TE}{TE_0}(t^\star)$ for $\nu = 5000$ m^2 s^{-1} in adimensional units of T_σ for several values of σ. The multiple plots show a perfect overlap, indicating that the linearized adimensional equation 4.50 is plausible. Furthermore, the adimensional time unit of T_σ, given in equation 4.49, corresponds roughly to the energy half-life of the system, which is exactly what a characteristic energy dissipation time is expected to yield. Finally, and to finish the study on the energy dissipation, figure 4.20 shows the mechanical energy and its sum with the turbulent kinetic energy, calculated accordingly with the proposed model in equations 4.44 and 4.43. The expected result

$$TE + TKE = TE_0$$

is nearly obtained. The slight linear loss can be due to the impact of numerical diffusion and to a consistent cumulative error while averaging the crossed derivative terms in equation 4.43. Hence the energy analytical diagnostic models deduced from the simple geometry and symmetry provided by the gaussian bump show good agreement. This seems to show that the gaussian bump is a very interesting academic test-case to verify the correct implementation of numerical schemes of the shallow waters equations.

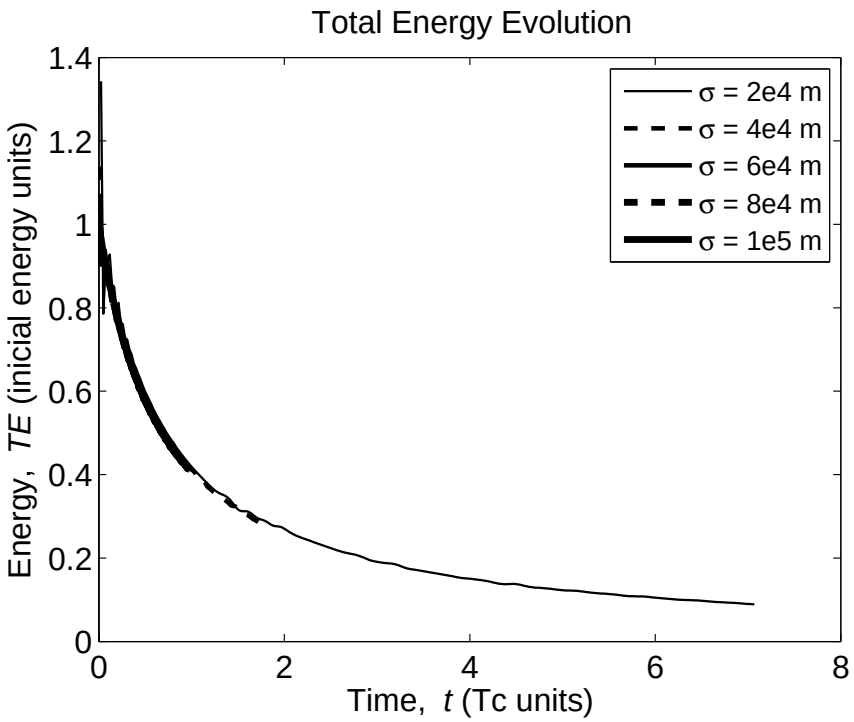

Figure 4.19: Evolution of $\frac{TE}{TE_0}$ with $t^\star$ for several values of σ and for a value of $\nu = 5000$ m^2 s^{-1}. The several time-series with the same ν show a perfect overlap. $t^\star = 1$ is equal to T_σ, the characteristic time of dissipation proposed in equation 4.49.

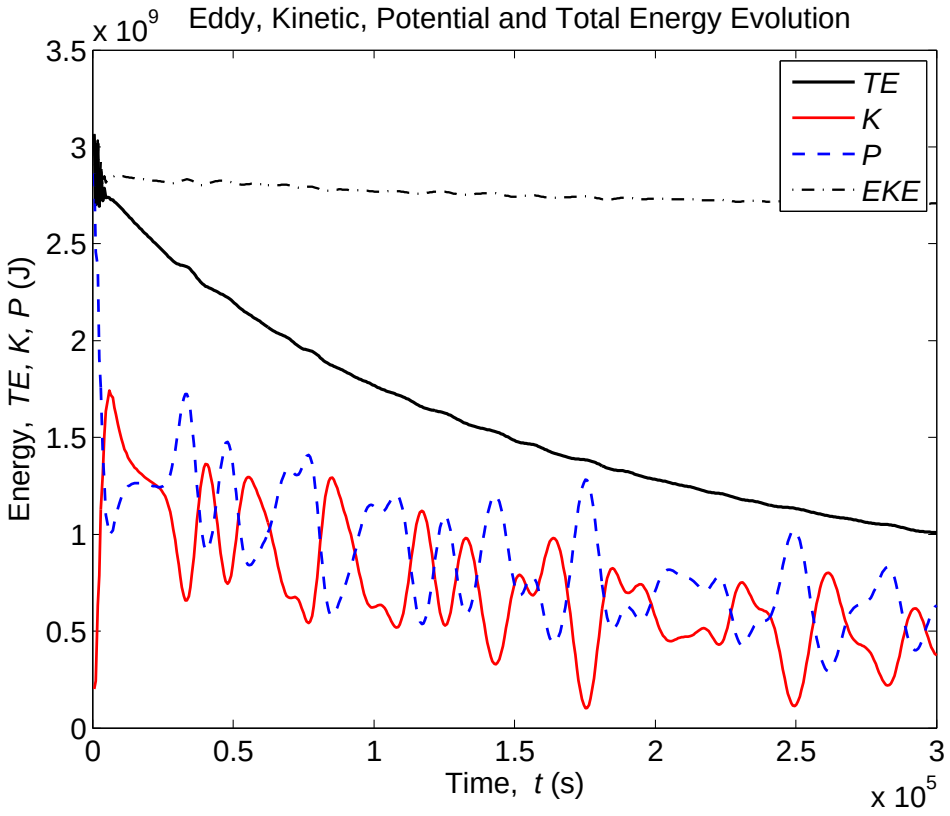

Figure 4.20: Gaussian elevation test-case energy time evolution with $\sigma = 60$ km and with $\nu = 5000$ m^2 s^{-1}. The TKE summed with the TE returns a near constant value as expected, proving that the TKE model accurately reproduces the loss in KE by viscous forces.

Table 4.2: Configuration of the model for a non-rotating fluid with a gaussian initial elevation and with open boundaries.

Parameter	Value
H	10 m
h_0	1 cm
σ_x	6×10^4 m
ν	5×3 m^2 s^{-1}
$M \times N$	37×37
Duration	1.8×10^5 s
dx	2×10^4 m
dt	500 s
TE_0	2.86×10^9 J
U_0	$\sim 5 \times 10^{-3}$ m s^{-1}
c	~ 10 m s^{-1}
Fr	$\sim 5 \times 10^{-4}$
Boundary	GWE+FLA
Volume	1.13×10^8 m^3

Radiation boundary condition

The former set of experiences was achieved with closed walls at the boundaries. The followig set of experiences aims at validating and assessing the performance of the simple gravity wave explicit (GWE) radiation condition for the water elevation and for the tangential velocity, and the Flather (1976) (FLA) radiation condition for the normal velocity. Table 4.4 contains the new configuration of the numerical experiment.

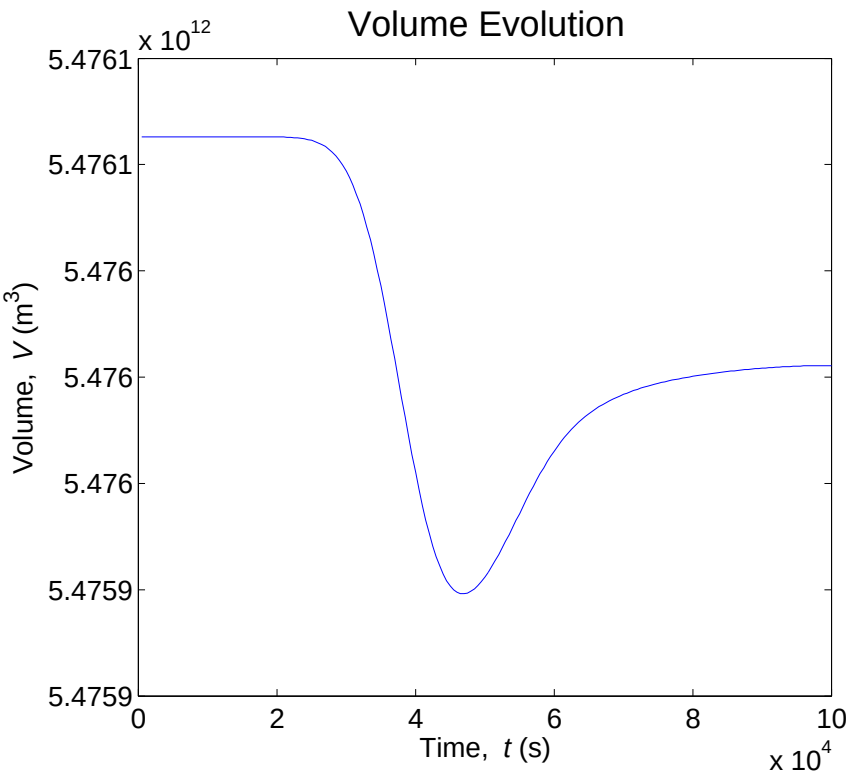

Figure 4.21: Domain volume evolution in time. The transient perturbation in the volume occurs when the gravity wave reaches the OB while making its exit. The final volume is slightly less than the original volume, as the gaussian bump exits the domain. The volume difference is roughly of the order of $\sim 10^8$ m^3.

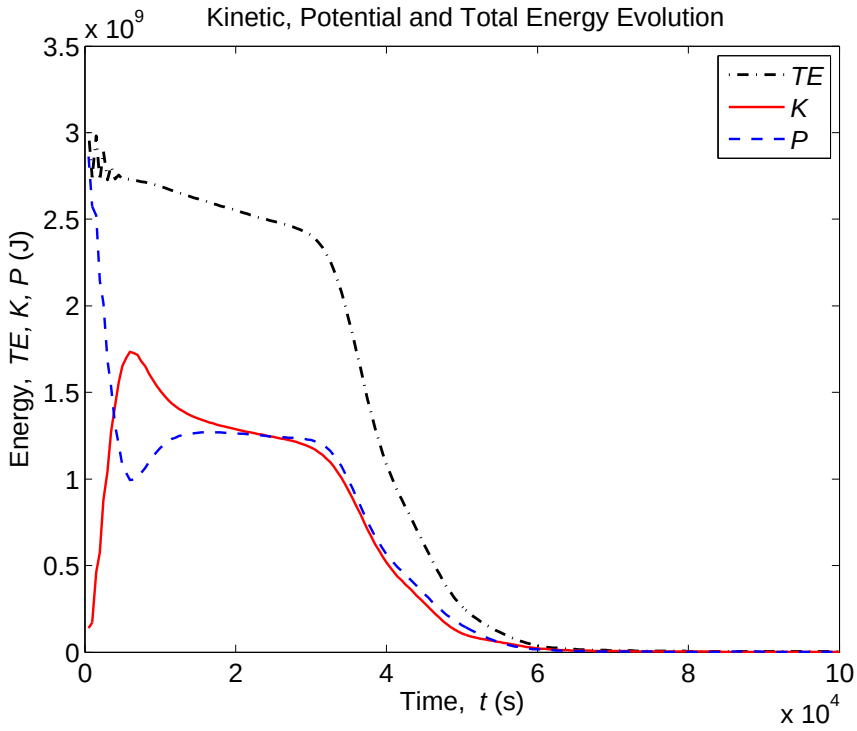

Figure 4.22: Mechanical, kinetic and potential energy evolution with time. When the gravity wave reaches the boundary, the energy, which was concentrated in the wave wake, exits the domain.

Geostrophic equilibrium

The steady-state solution where the Coriolis force balances the pressure gradient in a domain writes

$$\begin{cases} f\, v_g = g\, \frac{\partial \eta_g}{\partial x} \\ f\, u_g = -g\, \frac{\partial \eta_g}{\partial y} \end{cases}, \tag{4.54}$$

By applying the first derivatives along y and x to the first and second differential equation respectively, and assuming that the Coriolis frequency is constant throughout the domain, the result yields:

$$\begin{cases} \frac{\partial v_g}{\partial x} = \frac{g}{f} \frac{\partial^2 \eta_g}{\partial x^2} \\ \frac{\partial u_g}{\partial y} = -\frac{g}{f} \frac{\partial \eta_g}{\partial y^2} \end{cases} \Rightarrow \frac{\partial^2 \eta_g}{\partial x^2} + \frac{\partial^2 \eta_g}{\partial y^2} = \frac{f}{g} \left(\frac{\partial v_g}{\partial x} - \frac{\partial u_g}{\partial y} \right) = \frac{f}{g} \zeta_g. \tag{4.55}$$

ζ_g is the vertical component of relative vorticity in geostrophical equilibrium. Remembering the conservation of potential vorcitity, defined in equation 4.8,

$$\begin{aligned} Q &= \frac{\zeta + f}{H} = const \\ \Rightarrow \frac{\zeta_g + f}{H_g} &= \frac{\zeta_0 + f}{H_0} \\ \Rightarrow \zeta_g &= \frac{H_g}{H_0} (\zeta_0 + f) - f = \left(\frac{H_g}{H_0} - 1 \right) f + \zeta_0 \\ \Leftrightarrow \zeta_g &= \frac{\eta_g - \eta_0}{H_0} f + \zeta_0. \end{aligned} \tag{4.56}$$

The g, 0 subscript notation means, respectively, geostrophical equilibrium and initial instant; furthermore, $H \equiv d + \eta$, where d is the depth relative to a reference geopotential and eta is the surface elevation from a reference geopotential. Inserting the property found in equation 4.56 into equation 4.55 yields

$$\begin{aligned} \frac{\partial^2 \eta_g}{\partial x^2} + \frac{\partial^2 \eta_g}{\partial y^2} &= \frac{f^2}{g\, H_0} (\eta_g - \eta_0) + \frac{f}{g} \zeta_0 \\ &= \frac{f^2}{c^2} (\eta_g - \eta_0) + \frac{f}{g} \zeta_0 \end{aligned} \tag{4.57}$$

where $c_0^2 \equiv g\, H_0$ and where it is considered that $\eta \ll d$, so that $c_0 \approx c$. When the solution has radial symmetry and the initial vorticity is null, equation 4.57 writes

$$\frac{\partial^2 \eta}{\partial r^2} = \frac{f^2}{c^2} (\eta_g - \eta_0), \tag{4.58}$$

Table 4.3: Configuration of the model for a rotating fluid with a gaussian initial elevation and with open boundaries.

Parameter	Value
H	10 m
h_0	1 cm
σ_x	6×10^4 m
ν	5×3 m^2 s^{-1}
$M \times N$	37×37
Duration	1.8×10^5 s
dx	2×10^4 m
dt	500 s
TE_0	2.86×10^9 J
U_0	$\sim 5 \times 10^{-3}$ m s^{-1}
c	~ 10 m s^{-1}
Fr	$\sim 5 \times 10^{-4}$
Boundary	GWE+FLA
Volume	1.13×10^8 m^3

which is a non-homogeneous second-order linear differential equation, where $r^2 \equiv x^2 + y^2$. Depending on the value of η_0, an analytical solution of equation 4.58 can be easily found, in perfect analogy with the example shown in Gill (1982).

Table 4.3 indicates the configuration of the experiment consisting in the release of a gaussian bump elevation in a rotating fluid (with the Earth Coriolis rotation frequency equal to 43^o N). Figure 4.23 shows the total volume evolution with time of the experiment described in table 4.3. This time, the final volume gains a small increase relative to its original value. This is theoretically deducible with the principe of conservation of the initial potential vorticity, Q, given by, according to Gill (1982, p. 192),

$$Q(t) = \frac{\zeta - f\,\frac{\eta}{H}}{H}. \tag{4.59}$$

Finally, contrarily to the non-rotating case, after the gravity wave is radiated out of the domain, a significant amount of energy is retained within the geostrophic balance as seen in figure 4.24, about a third of the initial TE, half of which is composed by potential energy coming from the elevation solution at rest and another half which is composed by the geostrophic flow velocity field. The Okubo-Weiss parameter was already applied to identify vortex

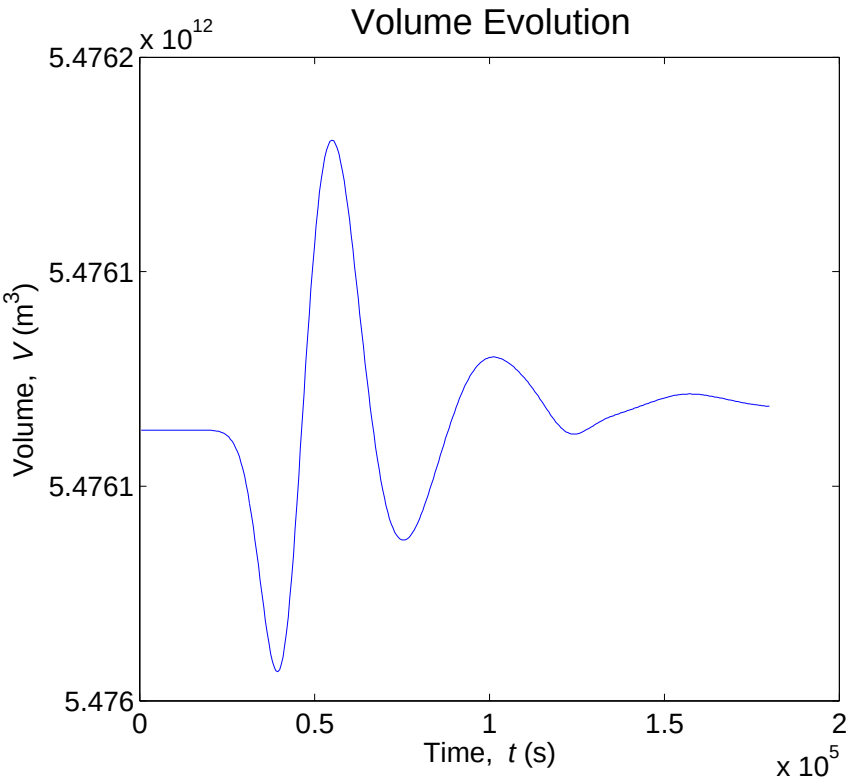

Figure 4.23: Domain volume evolution in time. The transient perturbation in the volume occurs when the gravity wave reaches the OB while making its exit. The final volume oscillates and is slightly above the original volume, as the gaussian bump exits the domain. The volume difference is roughly of the order of $\sim 10^7$ m^3.

structures from satelite SST and SSH shots over the mediterranean (Isern-Fontanet et al., 2004). In this case study there is a central barotropic eddy in the centre of the domain. Figure 4.25 shows, as described by Isern-Fontanet et al. (2004), the center of the eddy clearly dominated by enstrophy, as is seen by the negative values of OW at the centre of the domain, and near the edges of the eddy, a strain stress dominated field, where most of the TKE production occurs. The sequence of panels in figure 4.26 illustrate the geostrophic adjustement of the gaussian bump after release in three stages: a) before the gravity wave front arrives at the boundary, b) during the boundary crossing of the gravity wave and c), after the gravity wave front passed and a geostrophic balance remains.

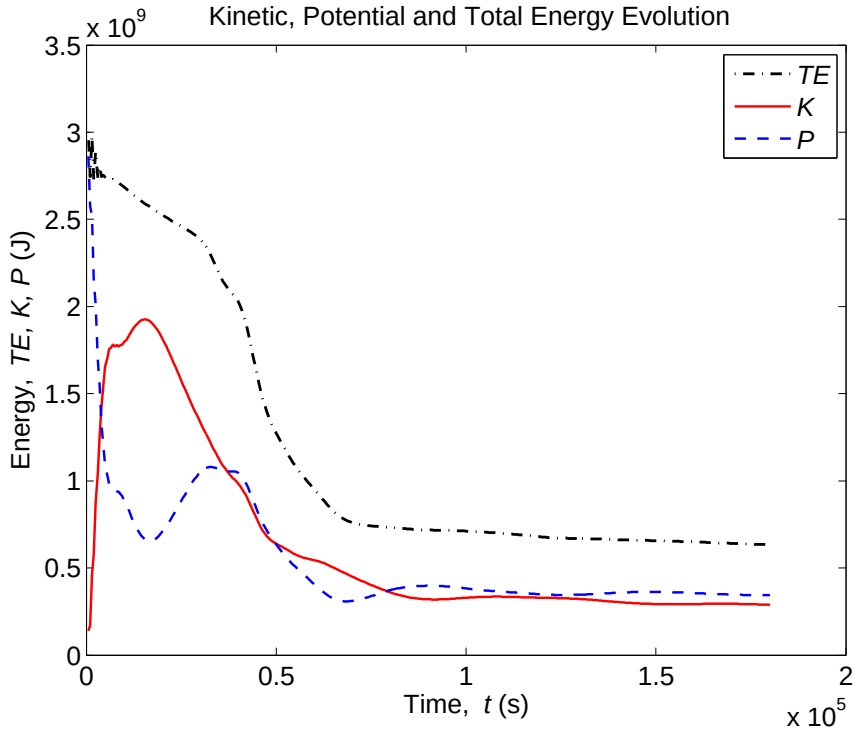

Figure 4.24: Mechanical, kinetic and potential energy evolution with time. When the gravity wave reaches the boundary, part of the total energy, (the part concentrated in the wave wake,) exits the domain. The remnant part is distributed half in potential energy and half in kinetic energy to form the geostrophic (stationary) equilibrium of water elevation with currents.

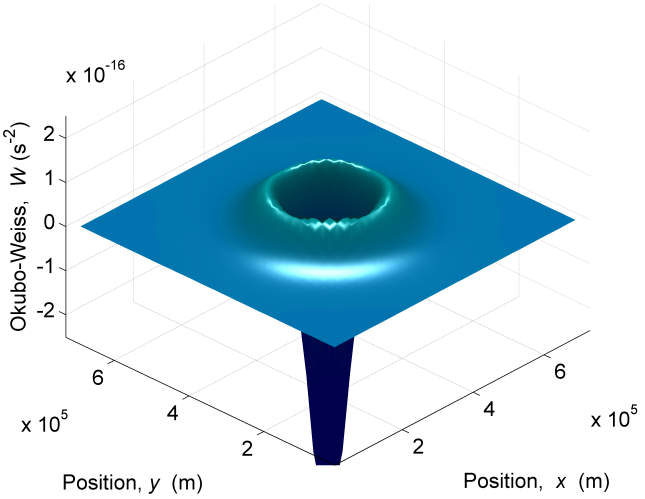

Figure 4.25: Okubo-Weiss field of the geostrophic balance, after the gravity wave exited the domain. The central eddy signature is defined by the negative OW, surrounded by positive OW at the edges.

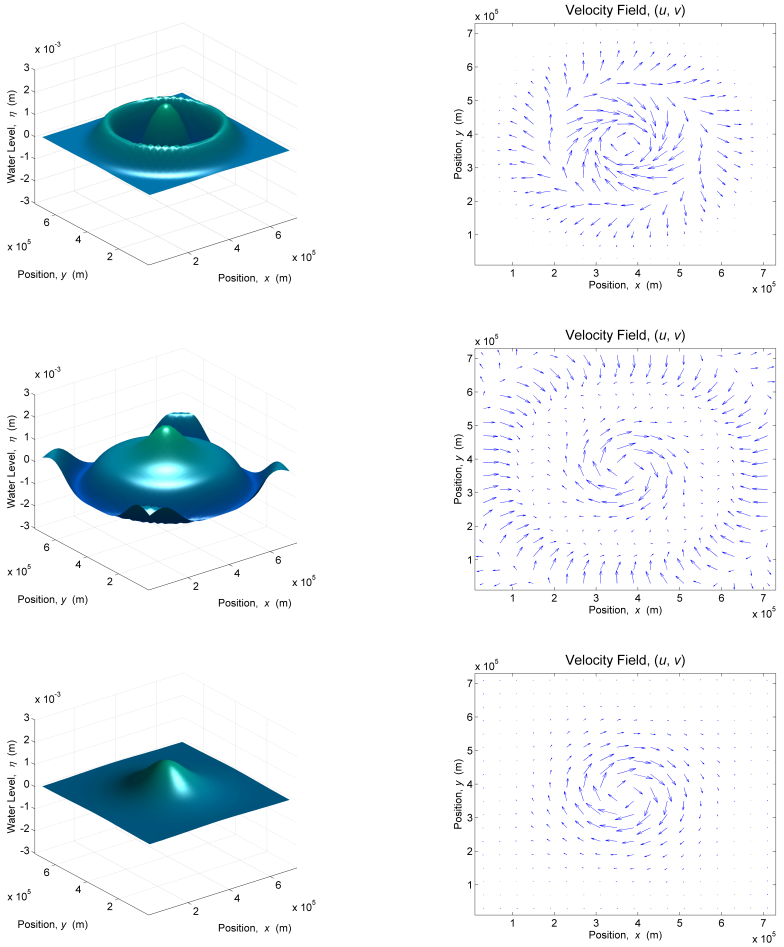

Figure 4.26: Adjustement of a gaussian elevation in a rotating domain. Left panels display the gravity wave elevation and right panels display the flow velocity field. a) The top panels show the transient state of the system shortly after the initial gaussian elevation was released and before the gravity wave front arrive at the boundaries. b) The middle panels show the gravity wave front crossing the boundaries and the instauration of the central eddy evolving towards geostrophic equilibrium. c) The bottom panels show the geostrophic equilibrium, well after the gravity wave front was radiated at the boundaries.

4.2.8 Appying the Okubo-Weiss scalar to assess the open-boundary condition

Besides being an effective tool at identifying eddies, the Okubo-Weiss scalar is fundamentally an objective tool capable of identifying hyperbolic regions of the flow, (dominated by the strain rate tensor, yielding positive values), from elliptic regions of the flow (dominated by vorticity, yielding negative values). The theory goes that solid boundaries (regions of null-flux) influence locally towards an elliptic flow (Weiss, 1991). The idea is check wether the gravity wave radiative boundary condition influence what otherwise should have been a perfectly hyperbolic flow (i.e. OW < 0). A numerical experiment was setup with two models releasing exactly the same gaussian elevation at their centre. One of the models has the boundaries farther away, thus doubling its grid-cells per dimension. The duration of 80000 s was chosen so that the gravity wave front passed through the smaller domain boundaries but barely reached the larger domain boundaries. The idea is to compare the Okubo-Weiss parameter in the common region of both domains at the same instant of 80000 s. Differences in the nature of the flow should be attributed to the existence of a boundary. Different implementations of boundary conditions should yield differences as well. The goal is to find the best open boundary radiative scheme, thus the goal is to find the boundary condition which yields the most similar OW map with the one from the large domain near the boundaries. The contour plot in figure 4.27, on the left panel, displays a radial and all positive Okubo-Weiss scalar field with an order of magnitude of about $\sim 10^{-21}$ for the large domain. It means that the flow is purely hyperbolic and has little intensity when compared to the velocity in the wake of the wave front. On the right panel, the OW contour plot in the smaller domain shows an elliptic boundary layer, due to the partial reflection of the gravity wave. The hyperbolic flow on the domain interior reaches $\sim 10^{-19}$, i.e. two orders of magnitude above the flow on the interior of the large domain. This means that the hyperbolic flow of the gravity waves was partially reflected back into the interior of the domain. Objectively, a better radiative boundary condition would minimize or even remove the elliptic boundary layer present in the small domain shown by the Okubo-Weiss parameter.

Table 4.4: Configuration of the models for a non-rotating fluid with a gaussian initial elevation and with open boundaries.

Parameter	Value
H	10 m
h_0	1 cm
σ_x	6×10^4 m
ν	5×10^3 m^2 s^{-1}
$M \times N$ small model	37×37
$M \times N$ large model	73×73
Duration	8×10^4 s
dx	2×10^4 m
dt	500 s
TE_0	2.86×10^9 J
U_0	$\sim 5 \times 10^{-3}$ m s^{-1}
c	~ 10 m s^{-1}
Fr	$\sim 5 \times 10^{-4}$
Boundary	GWE
Volume	1.13×10^8 m^3

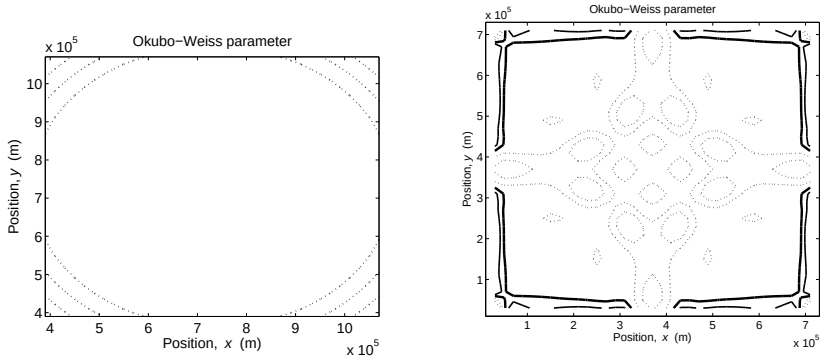

Figure 4.27: Contour plots of the Okubo-Weiss scalar for the same region. On the left panel, the large domains result. On the right panel, the small domain results. Positive OW contours are dashed and represent hyperbolic flow. Negative OW contours are solid and represent elliptic flow. The null-OW contour is the thick solid line and marks the transition from hyperbolic to elliptic flow.

4.2.9 Conclusions

Here lies the shallow-water equations numerical model as described in Kantha and Clayson (2000) with the same numerical scheme. It currently only has the Dirichelet boundary conditions and the gravity wave explicit radiation scheme added of a null-gradient or Flather for the normal velocity. This means that, in the former case, all surface waves bounce back at the boundary and and give rise to a cascade of multiple linear superpositions leading to a path of unavoidable numerical instability. In the latter case, the solution radiates any level perturbation (gravitic waves) at the open boundaries (Orlanski, 1976; Shchepetkin, 2003). It is important to note that the geometric considerations of the gaussian bump elevation at the instant of release were crucial in order to estimate matching predictions of energy partitioning and production of TKE. In particular, it was found that the relative production rate of TKE varies with viscosity and σ alone, and is independent of the Froude number associated with the gaussian gravity wave. Further work involves implementing relaxing conditions at the boundaries, variable coriolis force, cyclic boundary conditions. Ultimately, using a sponge layer near the boundaries is considered (Martinsen and Engedahl, 1987; Shchepetkin, 2003; Pietrzak et al., 2002), as well as developing the recent works of Blayo and Debreu (2005) with incoming characteristics and of Lavelle and Thacker (2008) with the PML conditions.

Chapter 5

Application and assessment to real-world case studies

5.1 The continental Portuguese coast operational model

5.1.1 Introduction

A three-level nested tridimensional hydrodynamic model was applied for the west Iberia coast and refined near the Estremadura promontory using MOHID. Realistic forcing was used provided by the large-scale North-Atlantic Mercator-Océan(Drillet et al., 2005) oceanic solution and by the atmospheric MM5 model run at meteo-IST(Domingos and Trancoso, 2005). Tide is forced using the FES2004 solution(Lyard et al., 2006). The Psy2v2R1 Mercator-Océan solution consists of a weekly 14 day forecast and a last 7 day reanalysis. The meteo-IST solution consists in a 7 day atmospheric forecast. A pre-operational system was mounted at Maretec-IST that pre-processes the forcing solutions, runs the hydrodynamical model and serves every monday nowcasts and forecasts until thursday of the general circulation off west Iberia. The results are stored in netcdf files and served by a LAS and an Opendap(Doty et al., 2001) server.

While the work of Coelho et al. (2002) focused more on the study of the upwelling process, the poleward current and the Portugal Current system, the current work aims at investigating the model's capability of reproducing accurately the known processes near the Gulf of Cádiz up to the Estremadura promontory in forecast mode. Namely the Mediterranean outflow spreading pathway and the ENACW entrainment near the gulf of Cádiz. To do so,

results from the model starting in mid-November 2006 up to mid-February 2007 were analysed.

5.1.2 Downscaling

The MOHID hydrodynamical numerical model solves the Navier-Stokes equations of a rotating fluid in a β plane. The geophysical fluid is constrained to the hydrostatic and the Boussinesq approximations, as a practical result of a dimensional analysis(Bryan, 1969).
The numerical solver uses a finite-volumes approach(Martins et al., 2000) similar to the one described by Chu and Chenwu (2002).
MOHID solves also a seawater density non-linear state equation depending on pressure, salinity and potential temperature originally proposed by Millero and Poisson (1981).
Finally, to calculate the turbulent vertical mixing coefficient, MOHID embeds GOTM(Umlauf and Burchard, 2005; Burchard and Others, 2002). The mixing-length scale parametrization proposed by Canuto et al. (2001a) is used.
The horizontal discretization is an Arakawa C grid(Arakawa, 1966). The vertical coordinate is hybrid and generic, allowing to choose between z-level, sigma and lagrangian coordinates(Martins et al., 1998).
The baroclinic pressure gradient term is always calculated using a z-level approach, with a linear interpolation, in order to minimize spurious pressure-gradient errors that induce unrealistic vertical velocities(Beckmann and Haidvogel, 1993; Shchepetkin, 2003; Kliem and Pietrzak, 1999).
In this application, the 2D model uses a sigma coordinate, and the tridimensional models use a lagrangian vertical coordinate with shaved-cells at the bottom(Adcroft et al., 1997) and a z-level initial condition.
The temporal numerical scheme is an alternate direction semi-implicit (ADI) method(Leendertse, 1967). The spatial discretization numerical scheme is a total variation diminishing (TVD) scheme(Fletcher and Srinivas, 1991).
The modelled domains description and configuration follows in the next subsections. Tables 5.1 and 5.2 summarize the initial conditions and the boundary conditions. In order to obtain coherent open boundary conditions (OBC), a good reference solution is mandatory(Blayo and Debreu, 2005). The high resolution solution of the Northern Atlantic and the Mediterranean basin provided by Mercator-Océan, **PSY2v2r1**, is likely to be a reliable solution available(Drillet et al., 2005; Bahurel et al., 2001) that reproduces realistically the Northern Atlantic circulation and in particular the western Iberian coastal circulation and the Gulf of Cadiz circulation. While assimi-

Table 5.1: Nested models boundary conditions. The abbreviations definitions are: Zonal and meridional velocity components (U, V), potential temperature (T) and salinity (S), water level relative to a reference level (η), flow relaxation scheme (FRS), Mercator-Océan solution(M-O), western Iberia barotropic model (WI), portuguese Iberian coastal model(P), Estremadura promontory model (C).

Boundary conditions	
Surface	**models**
Wind stress forcing from MM5 winds through equation 5.1.	P, C
Interpolated heat fluxes from MM5 data.	P and C
Open Boundary Conditions	**models**
FRS(Martinsen and Engedahl, 1987) of the M-O solution for U, V, T and S.	P and C
Interpolation of η, U, V, T and S from M-O.	P and C
Barotropic mode *Blumberg* radiation(Blumberg and Kantha, 1985).	WI
Barotropic mode *Flather* radiation(Flather, 1976).	P and C
Sponge layer.	P and C
Land boundary	**models**
Freshwater discharges.	P and C
Null fluxes of (U,V).	WI, P and C
Bottom boundary	**models**
Bottom stress forcing according to equation 5.8.	WI, P and C

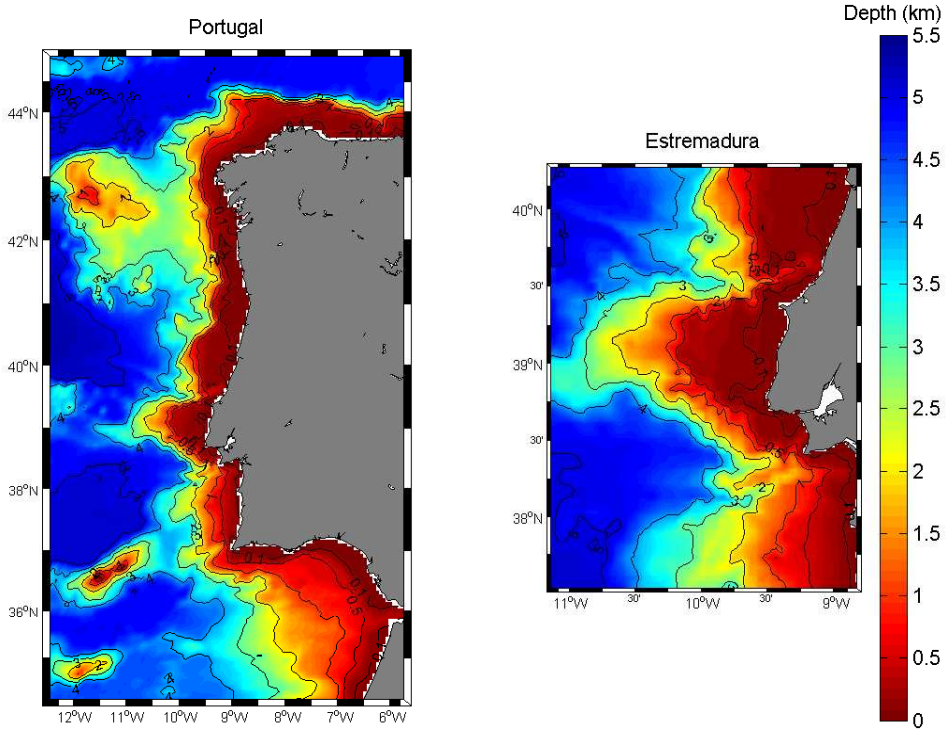

Figure 5.1: On the left panel, the Western Iberia coast baroclinic model bathymetry. The domain is labeled *P*. Bounded by $[-12.6^\circ\ -5.5^\circ]$ W $\times$ $[34.4^\circ\ 45.0^\circ]$N. 0.06° spatial resolution. On the right panel, Portugal continental central regional coastal model bathymetry, labeled *C*. Bounded by $[-11.2^\circ\ -8.8^\circ]$W $\times$ $[40.3^\circ\ 37.5^\circ]$N. 0.02° spatial resolution. Baseline data from ETOPO $2'$(Etopo, 1988) on both panels.

Table 5.2: Nested models' initial conditions, assimilations and spin-up. The abbreviations definitions are: Zonal and meridional velocity components (U, V), potential temperature (T) and salinity (S), water level relative to a reference level (η), flow relaxation scheme (FRS), modèles de Mercator-Océan (M-O), western Iberia barotropic model (WI), portuguese Iberian coastal model(P), Estremadura promontory model (C).

Initial conditions	
U, V, S and T are interpolated from the M-O solution.	P and C
η is initialized to a reference level.	WI, P and C
Assimilation	
U, V, T and S FRS according to equation 5.5.	P and C
Spin up	
Baroclinic force and wind forcing ignition over 10 inertial periods.	P
FRS and *Flather* radiation ignition over 10 inertial periods.	P

lating *in-situ* data, remote sensed sea level anomaly (SLA) and sea surface temperature (SST), as well as atmospheric forecasts fed by the European Centre for Medium Range Weather Forecast (ECMWF), the Mercator solution reproduces accurately the main characteristics of the circulation off western Iberia peninsula. Namely, it reproduces the Mediterranean Outflow (MO), several downstream Mediterranean veins(Ambar et al., 2002; Bower et al., 2002; Iorga and Lozier, 1999) and also the formation of meddies near Cape St.Vincent and over the Estremadura bank(Pichevin and Nof, 1996; Bower et al., 2002). However, the number of meddies formed by the model at St.Vincent Cape is inferior relatively to the observations. According to Drillet et al. (2005), this is probably due to the z-level vertical coordinate choice. Indeed, such a choice of coordinates is seemed to underestimate the dense water sinking downstream of the Gibraltar strait because of the intense nature of the MO near the Gibraltar strait. This problem was coped by Drillet et al. (2005) with a stronger relaxation towards Reynaud et al. (1998)'s climatology downstream of the Gibraltar strait(Drillet et al., 2005). Unfortunately, the bias of the results in Reynaud's climatology are propagated and an inferior temperature and salinity of about $0.75°C$ and 0.15 psu, respectively, is obtained(Drillet et al., 2005) when compared with known

measurements such as in the works of Iorga and Lozier (1999). This said, Mercator's solution is likely to be a good candidate as a reference solution capable of forcing a model operationally. The Mercator solution extraction domain ranges approximately from $24.5°W$, $28°N$ to $4°W$, $51°N$. The Mercator solution is interpolated to the MOHID meshes in two steps:

1. An interpolation using a triangulation method is used for each bidimensional layer. It produces an auxiliary field with the same horizontal mesh than the MOHID model.

2. A linear interpolation of each vertical column of the auxiliary field to the MOHID columns is applied. This step will produce a field consistent with the MOHID mesh.

The Mercator solution is labeled herein *M-O*. The model is coupled with MM5 (Grell et al., 1995) atmospheric model from IST in *offline* mode. The three-level nested atmospheric model is forced with the Global Forecasting System (GFS)7 day forecast over the region bounded by $20°W$, $28°N$ and $5°W$, $50°N$. The nested models resolution are 81, 27 and 9 km and are composed of 25 vertical layers. It simulates winds, sensible heat, latent heat, solar radiation, precipitation, evaporation, specific humidity, cloud cover and atmospheric pressure.The Finite Element Solutions (FES) are tidal atlases released nearly every two years, being the latest one of them the FES2004(Lyard et al., 2006). These tidal atlases result from model computation in unstructured meshes with spectral element methods(CEFMO and MOG2D-G code) applied to the nearly-linearized shallow water equations. The FES model assimilates remote-sensing data (Topex/Poseidon, ERS1 and ERS2 satellite altimetric data assimilated with the CADOR code), in-situ tidal gauges measurements, and tide atmospheric forcing (ECMWF). Being a state-of-the-art atlas, it is recommended for tidal applications(Lyard et al., 2006).
The surface fluxes of the MOHID models are composed of momentum (induced by wind stress and calculated by a diffusive term), sensible heat, latent heat, evaporation, precipitation and infrared radiation. The latter term is the system's response to the solar radiative forcing discussed further below. Wind forcing is calculated(Pietrzak et al., 2002) according to equation 5.1

$$\tau_w^u = \rho_a C_a u_{10} \sqrt{u_{10}^2 + v_{10}^2} \tag{5.1}$$

where τ_w^u is the surface stress induced by wind, $\rho_a = 1.25$ kg/m^3 is air density, C_a is a drag coefficient whose range is described in Leitão (2003b),

finally u_{10} and v_{10} are the horizontal components of air speed at 10 m of height above the sea surface.
The solar radiation term is decomposed into the long wave and short wave penetration into the water column. It's physically modelled by a penetrating heat source term at the surface and decaying along the water column. The decay constants are two-fold and depend on the type of waters and the type of wave-lengths. The system's physical response to this radiative forcing is the infrared radiation, modelled as an outwards surface flux.
Two methods of open boundary conditions (OBC) are frequently used: radiative methods, based on the Sommerfeld condition,

$$\frac{\partial \Phi}{\partial t} + \mathbf{c} \cdot \mathbf{n} \frac{\partial \Phi}{\partial x} = 0 \tag{5.2}$$

and nudging (or relaxation) methods. For an interesting review on the main OBC methods see Blayo and Debreu (2005). According to his work, the Flather radiation method(Flather, 1976), consisting of the Sommerfeld condition combined with the continuity equation, is best for radiating the water level. However, it requires an external water level and an external barotropic flux to be known in order to be used. Indeed the Flather radiation method may be equated at the model's open boundaries in the following way:

$$(\mathbf{q} - \mathbf{q}_{ref}) \cdot \mathbf{n} = (\eta - \eta_{ref}) (\mathbf{c} \cdot \mathbf{n}) . \tag{5.3}$$

where $\mathbf{q}$ and $\mathbf{q}_{ref}$ are the model's and the external solution's barotropic flux, respectively; $\mathbf{n}$ is the external open boundary normal vector; η and η_{ref} are the model's and the external solution's water level. $\mathbf{c}$ is the surface gravity wave's celerity, approximated by $\sqrt{g\,H}\,\overrightarrow{r}$, where $\overrightarrow{r}$ is the propagation direction unit vector. When only the external water level is known, then the Blumberg method(Blumberg and Kantha, 1985), consisting of a combination between a nudging term and the Sommerfeld condition, may be used as an alternative:

$$\frac{\partial \eta}{\partial t} + \mathbf{c} \cdot \mathbf{n}\, \nabla \eta = -\frac{\eta - \eta_{ref}}{T_{lag}} \tag{5.4}$$

η is the water level, η_{ref} is the reference water level, $\mathbf{c}$ is the external wave celerity, $\|\mathbf{c}\|$ is estimated to be $\sqrt{g\,H}$, $\mathbf{n}$ is open boundary external normal vector, g is the local gravity acceleration, H is the depth and T_{lag} is the relaxation decay time. The Blumberg method relaxation decay time ranges from a shorter 200 s in deep waters to a longer 2000 s in coastal shallow waters. For the other variables, where no accurate estimation of their celerity

is available, another class of OBC method is used: the relaxation method. It consists on a looser approach to the clamped (Dirichelet) conditions on the open boundary Γ of the domain Ω(Blayo and Debreu, 2005), where a relaxation decay time is introduced and an additional domain is created Ω_s, 10 cells wide, which interfaces between $\partial\Omega \equiv \Omega \cap \Omega_s$ and Γ. This approach is commonly regarded as a Flow Relaxation Scheme (FRS)(Martinsen and Engedahl, 1987). The relaxation term writes

$$\frac{\partial \Phi}{\partial t} = -\frac{\Phi - \Phi_{ref}}{\tau}. \tag{5.5}$$

where Φ is the relaxed variable, Φ_{ref} is the reference solution and τ relaxation time decay constant. The time decay varies from 3×10^4 s on Γ to 1×10^9 s on $\partial\Omega$, 10 cells to the interior. Thus the computed domain becomes $\Omega \cup \Omega_s$. Following Martinsen and Engedahl (1987), the FRS approach is used as the main downscalling technique for S, T, u and v, respectively the salinity, the potential temperature, the zonal velocity component, and the meridional velocity component. Additionally, in order to smooth out the nudging at Ω_s, a sponge layer, consisting of a high viscosity layer, is implemented. The viscosity terms range, inside Ω_s, from 1.8×10^4 m^2/s at Γ to 10 m^2/s on $\partial\Omega$. In Ω, the horizontal viscosity is considered constant at 10 m^2/s. Finally, in order to filter out the high frequency noise generated by resonant open boundary spurious reflections, a laplacian biharmonic filter is implemented in the primitive equations. Typical values of the biharmonic filter coefficient may vary between 1×10^{10} m^4/s and 1×10^9 m^4/s.A null mass and momentum flux is imposed at the lateral land boundary:

$$\mathbf{v} \cdot \mathbf{n} = 0 \tag{5.6}$$

where $\mathbf{v}$ is the velocity vector and $\mathbf{n}$ is the normal vector at the land-water interface. A freshwater discharge with daily values is imposed near the Tagus area for both models. The data source comes from the publicly available *INAG* (*Instituto da Água*) web-site[1] and, in this application, spans the 2004-2006 period. The 2006 year is replicated and used in 2007 simulations as an estimative of realistic daily freshwater discharges. The bottom stress is given by Pietrzak et al. (2002)

$$\tau_b^u = \rho_0 \, C_D \, u_b \sqrt{u_b^2 + v_b^2} \tag{5.7}$$

where τ_b^u is the bottom stress, u_b and v_b are the near-bottom velocity horizontal componentes, ρ_0 is the reference density. The drag coefficient is given

[1] http://snirh.pt/

byLeitão (2003b),

$$C_D = k/\ln\left(\frac{z_D + z_0}{z_0}\right)^2 \tag{5.8}$$

where z_D is the bottom height and z_0 is the roughness length. The Von Karman constant is set to(Leitão, 2003b) $k = 0.4$. The bottom roughness length is set to $z_0 = 0.0025\ m$ for all models.

Barotropic model *WI*

Since the Mercator solution is rigid-lid and doesn't takes into account the tide effect correctly, the idea came that a tidal reference solution should be built and linearly superposed to the Mercator reference solution in order to force coastal models with oceanic and tidal effects. Thus, a barotropic model model of western Iberia was created named *WI*, forced only with the FES2004 tidal atlas solution. The atmospheric forcing from the MM5 model was not be included, but the S1 and S2 components of the FES2004 solution already take into account the atmospheric tide forcing(Lyard et al., 2006). The bathymetry baseline data is taken from the ETOPO $2'$(Etopo, 1988). The domain has $0.06°$ horizontal and $180\,s$ temporal resolution and is bounded within the interval $[-13.7°\ -5.3°]\ W\ \times\ [33.5°\ 46.1°]\ N$. The water level reference solution is computed from the FES2004 tidal harmonic components. The Blumberg radiative condition(Blumberg and Kantha, 1985)(eq. 5.4) is applied at the open boundaries. A biharmonic filter is implemented in the domain to filter out high-frequency noise and has a $10^9\ m^4/s$ coefficient. The barotropic force is gradually connected over 10 inertia periods.

Portuguese coastal model *P*

A tridimensional baroclinic model is nested to the latter. It may be viewed as the enhanced version relative to Coelho et al. (2002). Composed by 42 vertical layers, it possesses a $0.06°$ horizontal resolution and a $180\,s$ temporal resolution (Coelho only had 18 layers and 8.5 km of resolution). Bounded by $[-12.6°\ -5.5°]\ W\ \times\ [34.4°\ 45.0°]\ N$ the model's forced with the MM5 atmospheric forcing reference solution at the surface, and by the barotropic model *WI* and the Mercator model reference solutions *M-O* at the open boundaries. The atmospheric forcing is slowly started over 10 inertia periods. The level is radiated by a Flather radiation method(Flather, 1976) whose barotropic flux and level reference solution, q_{ref} and η_{ref}, are given

by the linear superposition of the barotropic fluxes and water levels of *WI* and *M-O* respectively, $q_{ref} = q_{WI} + q_{M-O}$ and $\eta_{ref} = \eta_{WI} + \eta_{M-O}$. Also, the Flather radiation method is slowly activated over 10 inertia periods. Furthermore, a FRS(Martinsen and Engedahl, 1987) is applied to S, T, u and v. The baroclinic force is slowly activated over 10 inertia periods. The biharmonic filter coefficient is set to $1 \times 10^{10}\ m^4/s$. Turbulent horizontal viscosity is estimated roughly to $10\ m^2/s$ inside the domain, but a sponge layer is applied at the open boundaries, ten cells wide. The sponge layer evolves gradually from a viscosity of $10^2\ m^2/s$ inside of the domain, up to $1.8 \times 10^4\ m^2/s$ at the boundary. The modelled domain is labeled P and its bathymetry is shown in figure 5.1.

Estremadura model *E*

The Estremadura bank regional model, bounded by $[-11.2^\circ\ -8.8^\circ]\ W\ \times$ $[40.3^\circ\ 37.5^\circ]\ N$, differs from P in the horizontal spatial resolution and in the temporal resolution, respectively of 0.02° and $90\ s$. It also differs from P in the Flather radiation (eq. 5.3) where the reference level and the barotropic flux come only from the P model. This model should be able to reproduce the evolution of finer-scale physical processes. In particular those associated to the Rossby baroclinic radius of deformation who, near the western Iberia zone, should have approximately a $25km$ radius (Chelton et al., 1998). Stevens (1990) suggests that a resolution ten times higher than the first baroclinic Rossby radius of deformation (i.e. circa $2.5\,km$) is required in order to resolve the associated finer scale physical processes. In the western Iberia region, 0.06° of horizontal resolution doesn't meets the latter requirement but 0.02° does. It is, thus, expectable that finer-scale processes should appear in this model. These processes are filtered out by the rougher resolution in the P model. This model is labelled C (as in Centre), and its bathymetry (interpolated from ETOPO $2'$(Etopo, 1988)) is illustrated in figure 5.1.

5.1.3 Results

There are two modes of forcing:

- The analysis mode, where the oceanic forcing uses the analyzed *M-O* solution.
- The forecast mode, where the oceanic forcing uses the prediction mode *M-O* solution.

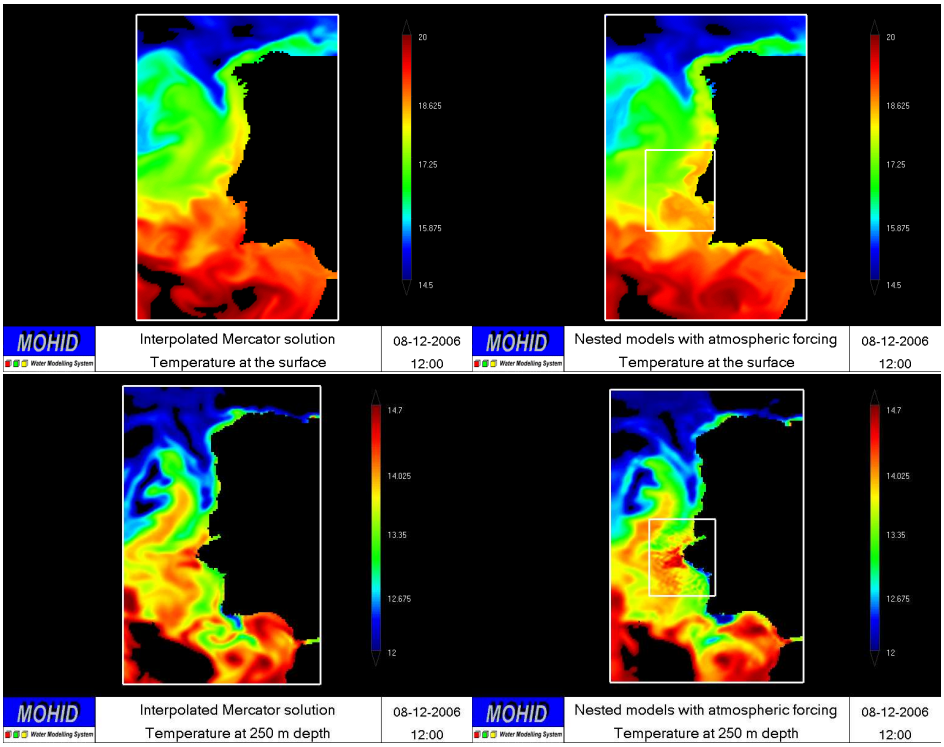

Figure 5.2: To the left, the interpolated temperature fields of the *M-O* solution. To the right, the superposition of the temperature fields of the C model over the P model. The temperature scale's interval is [14.5 20.0]$^{\circ}C$ at the surface (top) and [12.0 14.7]$^{\circ}C$ at 250 m (bottom). The graphical tool is Mohid GIS.

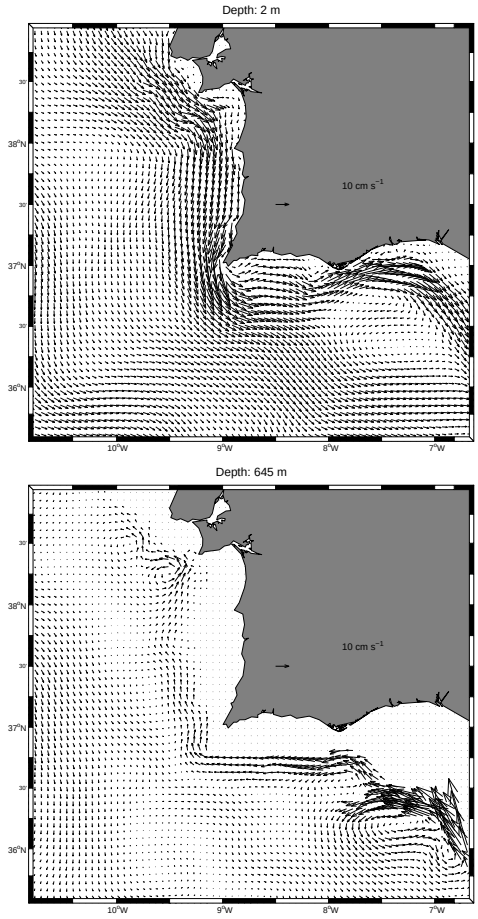

Figure 5.3: Horizontal distribution of velocity ensemble average at 2 m depth for the top panel and 645 m depth for the bottom panel. Two main branches of the MW spreading pathways are well pronounced in the bottom panel: the poleward slope current branch, and the cyclonic recirculation flowing southward.

Either way, the atmospheric forcing always used the *MM5-IST* 7 day forecasting solution. This provided less reliable results for the analysis mode runs. It is an issue to be addressed in the near future. The models are scheduled to run the past 7 days in analysis mode and the next 7 days in forecasting mode. The 14 day run requires 48 hours to finish, thus giving in the end, 5 days of ocean forecasts. The time to complete the runs can be optimized, perhaps reducing to a 40 hours run. The first 7 days run is the model's spin-up, allowing it to slowly activate the wind-forcing, the baroclinic forces and the radiative methods while it adjusts a velocity field to the initial density field. An alternate method consisting of performing a calculus continuation from the end of the last analysis is considered. However, for initialization purposes, performing a 7 day spin-up every week is thought to be numerically more robust than undertaking a hot start, since the latter method would induce a lot of high-frequency noise in the η, u and v terms. Two common approaches are used to tackle inconsistent current and level initial fields: one is based in an inverse model method which consists of analyzing previously the initial fields and, by means of adequate constraints, to generate a physically consistent initial velocity and level fields. But this method is generally quite slow to implement and demands robust computerized resources (for example the VIFOP tool (Auclair et al., 2000)). Another approach is to create a digital filter by means of an adequate convolution product with a high-frequency cut-off distribution (Lynch and Huang, 1992). A third method is to use proven consistent velocity and level fields to start with, such as the null velocity and constant reference level fields. This work undertook the latter method. A comparison between the Mohid results and the Mercator solution is undertaken. The first increment of the comparison is the visual inspection. Results of the temperature and salinity fields of the Mercator solution can be visually inspected against results of the Mohid solution in figure 5.2 for a 2006 mid-December day. The C model results are superimposed over the P model results. We can observe a general gain in the spatial variability of fronts forming in the C domain, for all depths and all variables (not shown). This was expected due to the finer resolution of the C domain. At the depth of the thermocline over the Estremadura bank, at the C domain at 250 m depth, internal waves interference patterns can be observed in figure 5.2 due to reflections at the domain's boundaries. These interferences occur during the model's spin-up (starting about the 3rd day) and are rapidly dissipated (by the 7th day). They appear near the thermocline depth, which is where the vertical density gradient is steeper, and which is where the number of vertical layers is higher. An alternative hypothesis is that these internal waves were produced at different generation

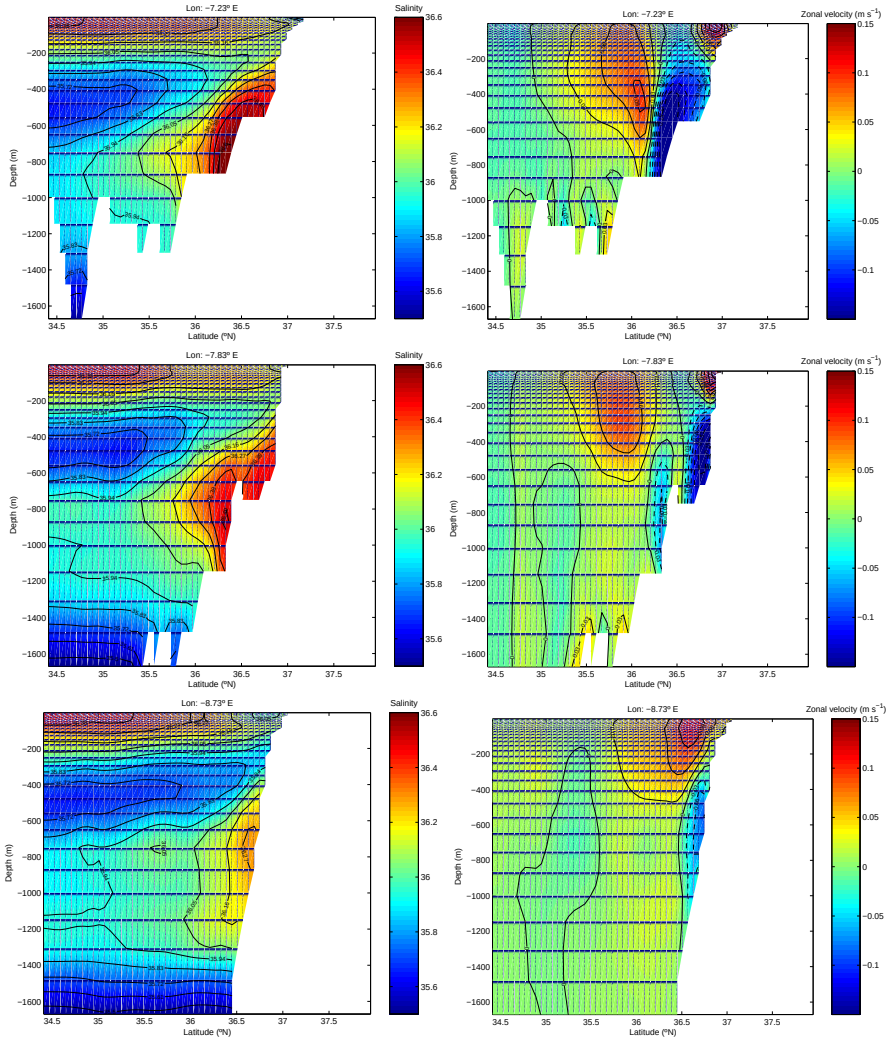

Figure 5.4: On the left panel, ensemble averages of salinity contours of [35.5, 35.52, 35.83, 35.94, 36.05, 36.16, 36.27, 36.38, 36.49, 36.6] and color maps in the interval [35.5 36.6]. On the right panel, ensemble averages of zonal velocity contours of [-.15, -.12, -.09, -.06, -.03, .0, .03, .06, .09, .12, .15] m s^{-1} and color maps in the interval [-.15 .15] m s^{-1}. The plots are meridional sections in the Gulf of Cádiz at longitudes $7.23\,^{\circ}W$, $7.83\,^{\circ}W$ and $8.73\,^{\circ}W$ from top to bottom, respectively. They show how the MO shifts from a bottom current to a buoyancy driven intermediate depth jet current.

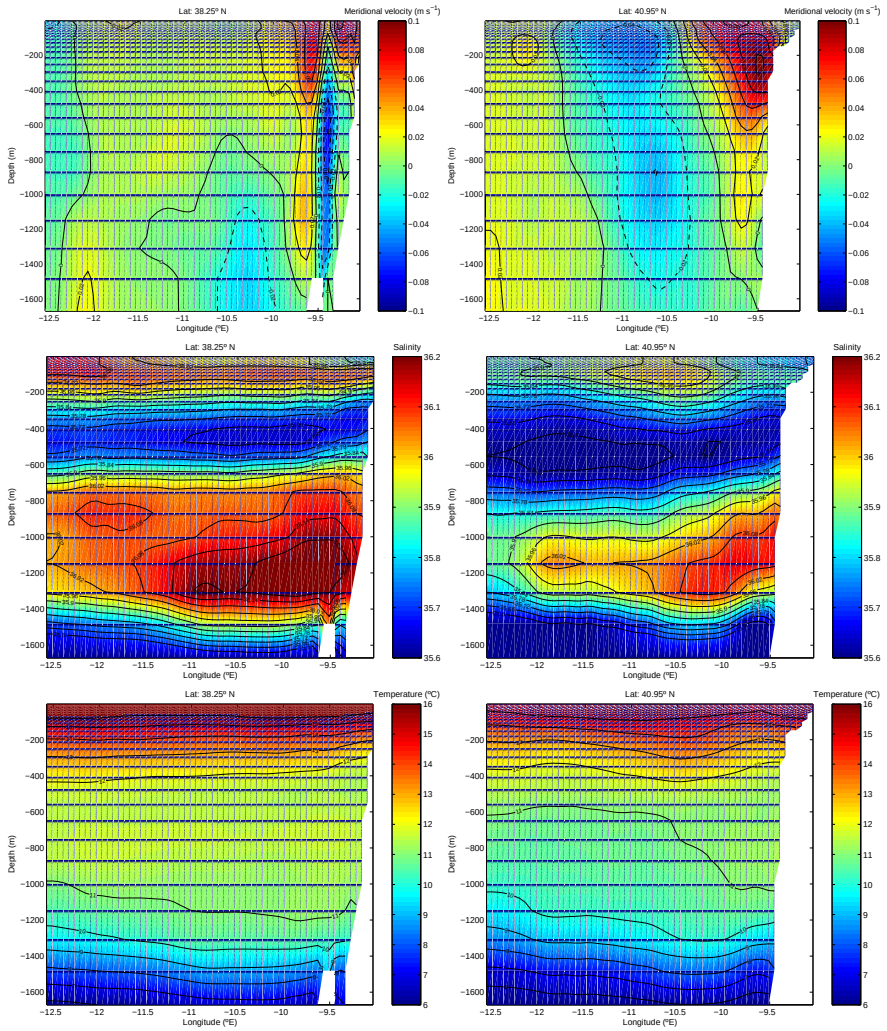

Figure 5.5: On the top panels, ensemble averages of meridional velocity contours of 0.1 $m\,s^{-1}$ apart and color maps in the interval $[-.1\,.1]$ $m\,s^{-1}$ are shown. Positive velocities are equatorward and negative velocities are poleward. On the middle panels, ensemble averages of salinity contours of [35.6, 35.66, 35.72, 35.78, 35.84, 35.90, 35.96, 36.02, 36.08, 36.14, 36.2] and color maps in the interval [35.6 36.2] are shown. On the bottom panels, ensemble averages of temperature isocontours of $1°C$ apart and color maps in the interval $[6\ 16]°C$ are shown. The plots are zonal sections off the Portuguese coast at latitudes $38.25\,°N$, for the left panel; and $40.95\,°N$, for the right panel.

points in the Estremadura promontory, and that their interaction yields the interference pattern. This shows that the C domain is able to generate internal waves. This type of internal wave interference pattern doesn't appear in the P domain. This is probably due to an insufficient horizontal resolution, or simply because the domain's characteristic length and time period isn't compatible with the formation of internal waves. Near the Iberian coastal area, the characteristic length of internal waves is estimated to vary between $20 - 30\ km$ (close to the the first baroclinic Rossby radius of deformation). According to Stevens et al. (2000), a tenfold resolution is required in order to accurately reproduce frontogenesis and baroclinic instabilities, i.e. a $2km$ resolution in the West-Iberia coastal area. Hence, the latter argument sustains the hypothesis that the P domain has a non-permitting baroclinic instability resolution. The work of Drillet et al. (2005) validates the capability of the Mercator solution of accurately reproducing the meddies life-cycle (since their genesis near Cape São Vicente or over the Estremadura bank to their dissolution in Atlantic waters) as well as the characteristic Mediterranean veins of the area. Nonetheless, as we initialize each time with a null velocity and level field, a 14 day run isn't sufficient for our model to generate fully developed meddies as these yield characteristic times of formation of at least 80 days(Papadakis et al., 2003). Thus, by these standards, the model is de-facto non-meddy permitting. This problem is expected to be solved with longer runs or with calculus continuation from the last analysis run. However, the salinity and temperature profiles and the qualitative aspect of the density-driven currents can be analyzed and expected to yield realistic results. Thus each 14 day run was integrated in time, and the ensemble mean of these averages spanning from mid-november 2006 to mid-february 2007 was calculated. Given an ensemble of fields $\left\{\psi^1, \psi^2, ..., \psi^N\right\}$ that evolve over a period of time T, we can split their time average

$$\overline{\psi^i} \equiv \frac{\int_0^T \psi^i(t)\, dt}{T} \tag{5.9}$$

into the spin-up characteristic time τ component, $\psi^{i\prime}$, (described in the used methodology) and the rest, $\widehat{\psi^i}$, i.e.

$$\overline{\psi^i} = \frac{\int_0^\tau \psi^i(t)\, dt}{\tau + (T-\tau)} + \frac{\int_\tau^T \psi^i(t)\, dt}{\tau + (T-\tau)} \equiv \frac{\overline{\psi^{i\prime}}\,\tau}{T} + \frac{\overline{\widehat{\psi^i}}\ (T-\tau)}{T}. \tag{5.10}$$

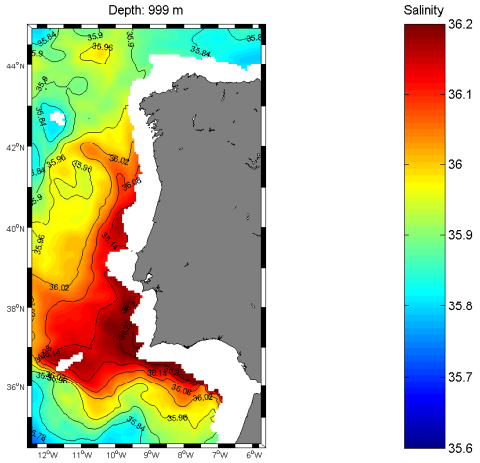

Figure 5.6: Color map and contours of salinity distribution ensemble average at 1000 m depth ranging in interval [35.6 36.2] showing the spreading pathway of the MO off western Iberia. Contour lines are valued [35.6, 35.78, 35.84, 35.9, 35.96, 36.02, 36.08, 36.14, 36.2].

Hence their ensemble average can write

$$\begin{aligned} \left\langle \overline{\psi} \right\rangle &\equiv \sum_{i}^{N} \overline{\psi^i}/N \\ &= \sum_{i}^{N} \frac{a\,\overline{\psi^{i\prime}} + b\,\overline{\widehat{\psi}^i}}{N} \\ &= a\left\langle \overline{\psi'} \right\rangle + b\left\langle \overline{\widehat{\psi}} \right\rangle, \end{aligned} \tag{5.11}$$

where $a = \tau/T$ and $b = (T-\tau)/T$. Thus, in our case, it is a reasonable assumption to state that

$$|\left\langle \overline{\psi'} \right\rangle| < |\left\langle \overline{\widehat{\psi}} \right\rangle|, \tag{5.12}$$

as regards the η, u and v fields; since all start with null values and since tide, windstress and density gradient forces are gradually connected during the spin-up period time, τ. Hence, minding the Schwarz inequality,

$$\begin{aligned} |a\left\langle \overline{\psi'} \right\rangle + b\left\langle \overline{\widehat{\psi}} \right\rangle| &< a\,|\left\langle \overline{\psi'} \right\rangle| + b\,|\left\langle \overline{\widehat{\psi}} \right\rangle| \\ &< a\,|\left\langle \overline{\widehat{\psi}} \right\rangle| + b\,|\left\langle \overline{\widehat{\psi}} \right\rangle|, \end{aligned} \tag{5.13}$$

thus, from equation 5.11 and since $a + b = 1$, the latter inequality is equivalent to

$$|\langle\overline{\psi}\rangle| < |\left\langle\widehat{\overline{\psi}}\right\rangle|. \tag{5.14}$$

Inequality 5.14 has a strong physical meaning, assuming that equation 5.12 holds. It means that the ensemble average properties for η, u and v are probably underestimated and that this should be minded when looking at $\langle\overline{\eta}\rangle$, $\langle\overline{u}\rangle$ and $\langle\overline{v}\rangle$ results. Figure 5.3 shows the ensemble average according to equation 5.11 of the horizontal velocity near the surface and 645 m deep. At the surface a wind-driven equatorward flow evolves whereas at the subsurface an intermediate depth MW undercurrent evolves and branches. Two main branches are depicted by the model's results: a poleward slope current branch that flows leaned against the Portuguese shelf whereas, south of the Strait of Gibraltar, another branch is formed showing a cyclonic recirculation southward that will feed the Canary currents system. This MW spreading pathways scenario is consistent with the ones evidenced in the works of Bower et al. (2002) and Iorga and Lozier (1999). Figure 5.4 is a series of meridional cross sections of ensemble averages according to equation 5.11 of salinity and zonal velocity in the Gulf of Cádiz at longitudes $7.23\,^{\circ}W$, $7.83\,^{\circ}W$ and $8.73\,^{\circ}W$. The cross sections show the formation of deep Mediterranean Water flowing past the Gibraltar Strait into the Atlantic, forming the Mediterranean salt tongue(Bower et al., 2002). The overflow of denser Mediterranean waters entrains at the Gibraltar Strait under the less dense North Atlantic Central Water (NACW) and downslopes(Deleersnijder, 1989) along the continental slope on the northern margin, south of Algarve as a density-driven current. As it flows westwards, at about 8° W, it reaches neutral buoyancy and detaches from the bottom near 700 m depth and continues as a boundary undercurrent, then it descends down to 1000 m depth(Bower et al., 2002) near 8.5° W (fig.5.4) where it seems to attain hydrostatic equilibrium. The Mediterranean salt tongue turns northward past Cape São Vicente and probably continues flowing northward to as far as Porcupine bank (50° N)(Iorga and Lozier, 1999). Figure 5.5 is a series of zonal vertical cross sections of ensemble averages of salinity, temperature and meridional velocity of western Iberia at $38.25\,^{\circ}N$ and $40.95\,^{\circ}N$. Figures 5.4 and 5.5 evidence the main Mediterranean vein by the anomalous salinity maximum. The depth of salinity maxima varies between the 800 m and 1200 m depth. The number of salinity maxima varies from one to two, sometimes three. It is interesting to see how the boundary driven main Mediterranean veins follow the poleward undercurrent by

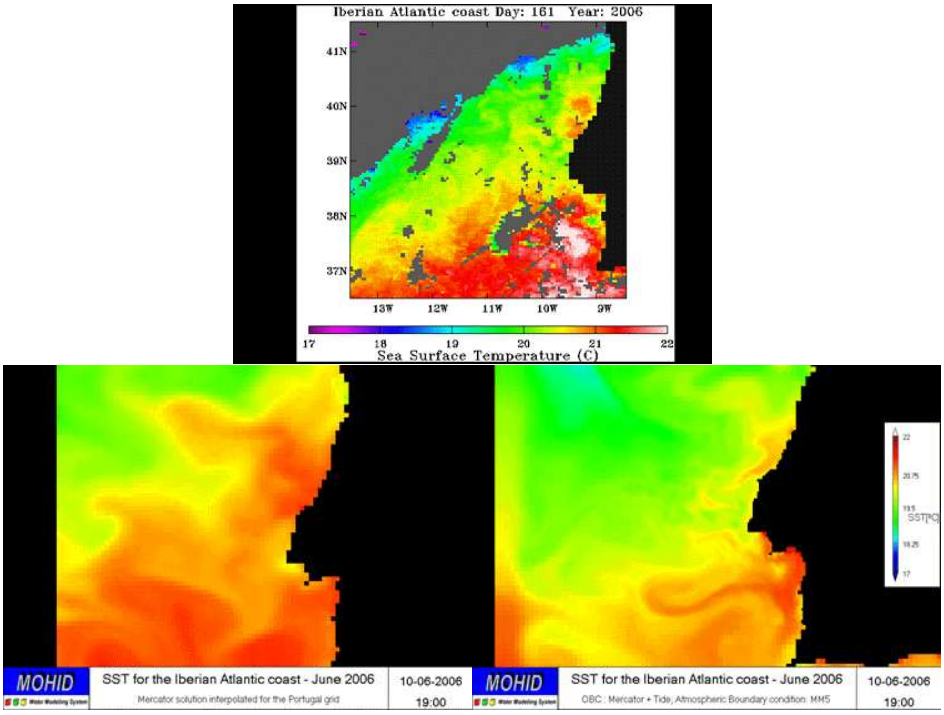

Figure 5.7: The Mercator solution sea surface temperature daily average on the September 9th 2006, at the bottom left. A NOAA sea surface temperature satellite image taken during the same day, at the top. At the bottom right, the Mohid instantaneous solution taken the same day at 19h00 hours. The temperature scale is set to $[17°C\ 22°C]$. However, the color palettes differs between the satellite images and the model's fields. The graphical tool used is *Mohid GIS*.

inspecting the number of salinity maxima, each maximum corresponding to one MW vein. Figure 5.6 shows the ensemble average of salinity off western Iberia at 1000 m depth. It shows clearly the spreading extension of the Mediterranean tongue with a similar signature as that evidenced in the works of Drillet et al. (2005); Papadakis et al. (2003); Coelho et al. (2002). Figure 5.7 compares results from the Mercator solution interpolated over the P domain and the results from the P and C models and a NOAA satellite sea surface temperature (SST) image. All results are for the same day. Mercator results are daily average, MOHID results are instantaneous at 12h00 and the satellite image was taken during the mid-afternoon. Though it's hard to analyze the results, the MOHID finer resolution model has a higher

spatial variability and is likely to resemble more the satellite SST.

5.1.4 Conclusions

A three-level nested tridimensional hydrodynamical model was implemented for the Portuguese coast with MOHID. It is forced with realistic ocean (Mercator, FES2004) and atmospheric (Meteo-IST) forecasts. The system is pre-operational as its results are published via an opendap server weekly since November 2006. It can provide realistic OBC to finer scale regional and local models in realtime or in offline (such as the Oil Observer). There is evidence that the finer-resolution E domain is internal-wave-permitting in contrast to its upper-scale models P model and M-O model. The model's MW spreading pathways scenario is realistic when compared to other works observations and analysis(Iorga and Lozier, 1999; Bower et al., 2002; Drillet et al., 2005; Coelho et al., 2002). The results show a shift in the MO from a bottom current to an intermediate depth buoyancy driven current near $8\,^{\circ}W$ in concordance with observations(Bower et al., 2002; Iorga and Lozier, 1999). Also the salinity maxima observations show a realistic entrainment from the NACW in the Gulf of Cádiz. The model's ensemble average of the salinity signature at $1000\,m$ depth occured by non-meddy MW spreading is consistent with the works of Drillet et al. (2005); Coelho et al. (2002).

5.2 The bay of Biscay inter-comparison

5.2.1 Circulation and processes in the Bay of Biscay

The Bay of Biscay in the North Atlantic Ocean

The Atlantic general circulation of the northern hemisphere, illustrated in figure 5.2.1, is commonly illustrated by two cells: the anti-cyclonic sub-tropical gyre, intensified on the American continent coast (the Gulf Stream: intense surface and warm current), and the sub-polar cyclonic gyre. The borderline between these two gyres is roughly situated at 45°N. The Gulf Stream branches at about 42°N. One of the branches derives south-eastward, crosses the Atlantic ridge, south of the Azores archipelago (between 32°N and 37°N) and enters the eastern basin thus forming the Azores Current (AzC). The other branch moves north-eastward, forming the North-Atlantic Drift (NAD). At the level of the Charlie-Gibbs fracture situated at 52°N and 26°W, a NAD branch forms the less intense South-Eastward Portugal Current (PC). The PC will eventually merge more to the South with the AzC. Both currents will then delimit the eastern Subtropical Gyre.

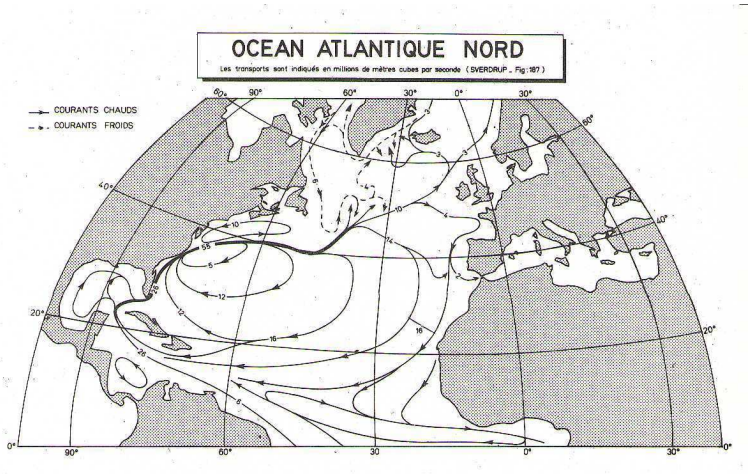

Figure 5.8: Proposed circulation pattern of the Atlantic Ocean in the northern hemisphere of the earth. The circle represents the Bay of Biscay region.

The region that includes the Bay of Biscay, delimited by the NAD, the AzC and the Eastern borders (Portuguese, Spanish, French and United-Kingdom coasts) is atypical in the sense that it presents particularities that are unique when compared with other regions of the Eastern Ocean coast. It can be split into three distinct areas: the abyssal plain, the continental slope, and the continental shelf. The circulation that develops in these areas is well characterized and systematic, while presenting seasonal and inter-annual variability.

The most important aspect that drives the North-Atlantic circulation is the distribution of the different water masses; it is thus relevant to characterize them as well in this study.

North-Atlantic and Bay of Biscay Waters Description

Water masses are formed at the surface in precise regions of the Ocean. They are then transported to different regions and to different depths. Water masses tend to preserve in time their characteristics in potential temperature and salinity, and usually represent an important volume. In table 5.2.1 are described the water masses found in the North-East Atlantic Ocean, and, more particularly, in the vicinity of the Bay of Biscay. They are referenced and quantitavely described in the works of Ambar (1983); Van Aken and Becker (1996); Ambar and Howe (1979); Rios et al. (1992); Pollard et al. (1996). The Eastern North Atlantic Central Water (ENACW) are

Table 5.3: Water masses in the North-eastern Atlantic Ocean.

Water masses	Depth (m)	T (°C)	S	σ (kg.m^{-3})
ENACW (subtropical branch)	< 300	> 12.5	> 35.75	< 27.05
ENACW (subpolar branch)	< 400	$10.5 - 12.5$	$35.6 - 35.7$	$27.1 - 27.2$
ENACW (Bay of Biscay)	< 600	$10.5 - 11.5$	$35.6 - 35.6$	$27.2 - 27.3$
MW (surface core)	$400 - 700$	$11.8 - 12.2$	$35.8 - 35.9$	$27.2 - 27.3$
MW (upper core)	$700 - 900$	$10.5 - 13.5$	$35.8 - 36.8$	$27.4 - 27.7$
MW (lower core)	$1000 - 1500$	$9.5 - 12.5$	$35.8 - 37.5$	$27.7 - 27.9$
EASAIW	$500 - 1500$	$6.0 - 9.0$	$35.1 - 35.3$	$27.4 - 27.6$
LSW	$1500 - 3000$	$3.4 - 4.0$	$34.9 - 35.0$	$27.7 - 27.8$
LDW	> 3000	< 3.3	$34.9 - 35.0$	> 27.8

sub-surface waters characterized by high temperatures; the Mediterranean Waters (MW) are characterized by high salinity cores at 1000 m depth; the Eastern Atlantic Sub-Arctic Intermediate Water (EASAIW) possess low temperature and moderate salinity up to 1500 m depth; the Labrador Sea Water (LSW) presents high depth, very low temperature and low salinity; finally the Lower Deep Water are very deep currents with extremely low temperatures and low salinity.

Water masses in upper layers

The ENACW are produced in the surface in the North-East Atlantic during periods of convections and winter mixing. During summer, they are protected from the surface by stratification. The ENACW can be found as deep as 600 m depth. A subpolar branch of the ENACW is formed southward of the NAD, and roams South-Eastwards (Pollard et al., 1996). A subtropical branch of the ENACW, to the North of the AzC, roams North-Eastwards towards the Spanish coast (Pingree, 1997). The abyssal plain region off the Bay of Biscay is a zone of strong winter convection, where the ENACW are also formed (Fraga, 1981).

Water masses in intermediate Ocean layers

The Mediterranean Waters (MW) are salty dense waters that enter the Atlantic Ocean in the bottom of the Gibraltar straight. The outflow downslopes and is entrained by the ENACW in the Gulf of Cadiz until it reaches hydrostatic equilibrium. Two cores are usually formed and measured, one that contains a maximum of salinity (upper core), and another that contains a maximum of temperature (lower core). A third core more near the surface is also formed in the western part of the Gulf of Cadiz, but is identifiable only along the Western Iberia coasts (Ambar, 1983).

Water masses in deep Ocean layers

The Labrador Sea Water (LSW) and the Lower Deep Water (LDW) are cool and fresh waters found in the bottom layers of the ocean. The LDW are a composition of the North Atlantic Deep Waters (NADW) and of the Antactic Bottom Waters (ABW).

The abyssal plain

The general circulation in the first hundreds meters isn't too intense as it is characterized by the anti-cyclonic Portugal Current (PC). At a lower scale, essentially anti-cyclonic eddies are frequently observed with a typical diameter ranging from 50 to 100 km. The abyssal plain is separated from the continental shelf by the shelf-slope, along which a strong slope current develops showing strong seasonal and inter-annual variability.

The continental slope

The large scale meridional surface density gradient generates an Eastward flow. The consequent volume accumulation near the coast on the shelf creates a level gradient that generates a Northward geostrophic current along the shelf slope, thus separating the shelf dynamics, from the deep Ocean's. The slope current is coupled with a downwelling motion that lowers the isopycnals. The slope current is highly baroclinic and its direction may inverse with depth.

The zonal wind is another driver of the circulation. During summer, the Azores anti-cyclone is centred on the North-Atlantic. On Europe's western coast, Northerly winds are predominant. This causes an offshore water transportation resulting in upwelling events and a diminution in intensity of the slope current. During winter, the Azores anti-cyclone moves southward,

and thus the Westerly winds become predominant in Europe's western coast. The slope current is thus intensified and propagates northward penetrating into the Bay of Biscay as the Navidad current. Its width is around 40 km, its depth goes down to 200 m and typical currents reach 10 - 20 cms-1.

The Navidad current shows a very strong seasonal and inter-annual variability that seems to correlate well with the North-Atlantic Oscillation (NAO) index. Changing winds and bathymetry accidents, such as canyons, can easily cause this current to disperse and generate eddies called SWODDIES (Slope Water Oceanic eDDIES), because they trap warm and salty surface waters and transports them to the center of the Bay of Biscay (Garcia-Soto et al., 2002).

The continental shelf

The Bay of Biscay comprises a large French continental shelf oriented in the North-South direction, and a narrower Spanish continental shelf oriented in the East-West directions. The French continental shelf size ranges from 300 km over the Armorican region, down to 50 km in the Aquitan region. The Spanish continental shelf is the narrowest, with only 30 to 40 km wide. The circulation over the shelf is highly influenced by physical processes such as tide, wind and river discharges.

Tidal currents Tidal currents intensity depends largely on the water column depth: deeper water column will yield a less intense tidal current, whereas shallower water columns will yield more intense currents. This is a consequence of the momentum conservation principle. Also, refraction and other non-linear couplings may occur due to irregularities in the bathymetry.

The tide-driven current intensity ranges from a few centimetres per second to nearly a meter per second (near Ushant). But in the southern part of the Bay of Biscay, velocities are nearly zero.

Tide driven currents are more intense over the shelf, and the shear stress induced introduces strong vertical mixing between surface waters and bottom waters.

Internal waves Internal waves are reputed to contribute to the general Ocean mixing and to the equilibrium of the thermohaline circulation (Munk and Wunsch, 1998). The interaction of internal waves with topography can induce energy transfers, instability development and internal waves breaking (Wunsch and Ferrari, 2004). Baines (1982)

shows that the continental slope in the Bay of Biscay is the area where the M2 internal wave's generation is more intense. However the M4 non-linear wave is also relevant for generating internal waves over the continental slope. Internal waves are also known to be dependent on the horizontal density gradient, besides the vertical stratification. Variations of density gradients would induce a change in the internal waves rays slope.

River plumes River plumes are an important feature of the shelf circulation. Unfortunately, the MOHID model wasn't setup to properly handle the river plume simulation. The main rivers are the Loire, the Gironde and the Adour, with a mean flow of 900 $m^3\,s^{-1}$. Freshwater over the shelf are transported by winds and geostrophy currents formed by the intense surface density gradients. Their transport is seasonal, either Northward, during winter, up to the British channel, either Southward of the Bay of Biscay, during spring.

The Ushant front The Ushant front is a result of the interaction between topography and tidal currents, which are very intense near Ushant (Mariette and Le Cann, 1985). In this shallow water area, the bottom friction homogenizes the water column and avoids the forming of a seasonal thermocline, whereas, westwards, the water column is deeper, and the bottom friction isn't enough to homogenize, and a seasonal thermocline is formed. Thus, during summer, an intense horizontal density gradient is formed and is called the Ushant front. The front is dynamically unstable as wind and topography may interact with it. Near the coast, the tidal currents are less intense, and the seasonal thermocline appears, thus forming an internal front. The Ushant front is characterized by a 1 to 2 K / km thermal gradient, and the temperature difference between the cold water and the warm water can reach over 5 K.

Seasonal stratification Over the continental shelf, seasonal stratification is rather common. Tidal currents however, tend to homogenize the stratification and form complex hydrological structures, such as the Ushant front. The inter-annual stratification variability depends on the interaction of several processes such as the heat balance at the surface interface, the river plumes and the general circulation over the shelf (Puillat et al., 2004).

Upwelling The upwellings are characterized by an offshore transport of

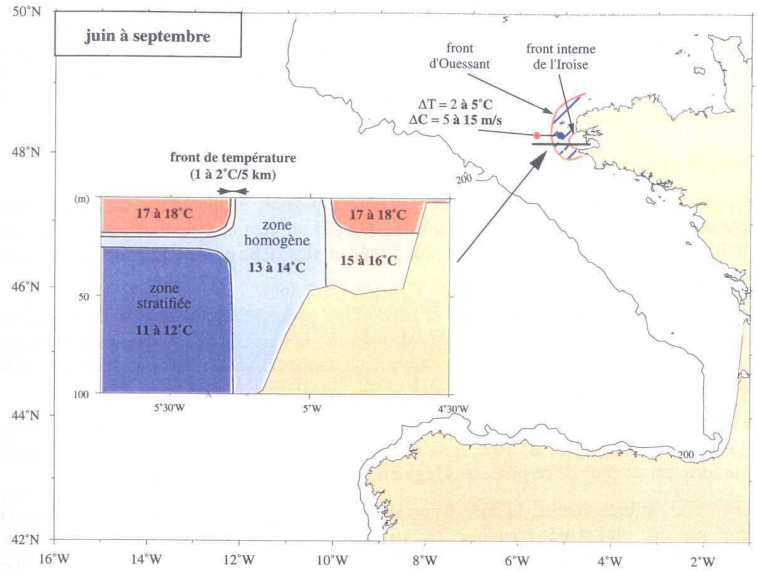

Figure 5.9: The Ushant front as described in the literature. A homogeneous water column (in light blue) separating, at the surface, stratified warmer waters in the inner shelf and in the outer-shelf (red).

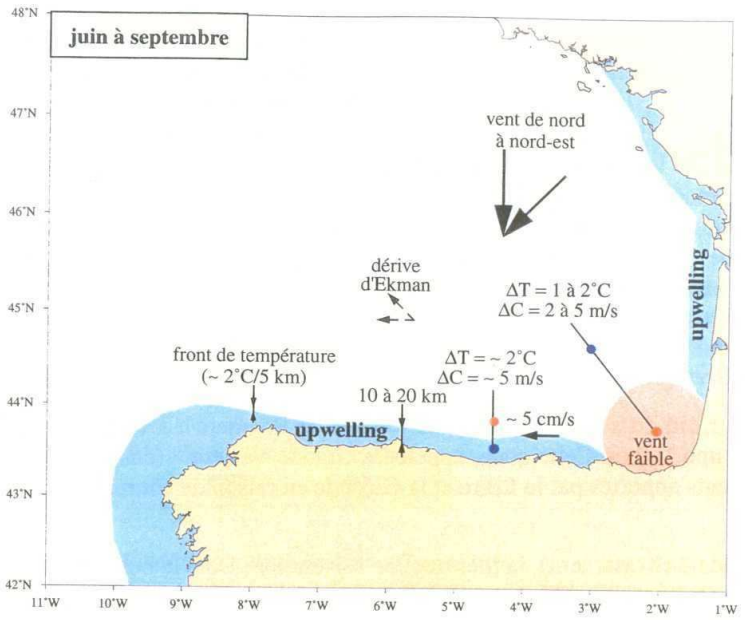

Figure 5.10: Upwelling regions in the Bay of Biscay in blue. Warmpool region, with weak winds, in red.

surface waters, leading to an upwelling of subsurface colder waters to the surface. This produces a front separating warmer waters offshore and cooler waters near-shore. This offshore transport occurs, when Northerly winds blows, and a balance between the wind stress and the Coriolis force establishes whose resultant surface stress is westward and offshore. Upwellings are predominant in summer, when the Azores anti-cyclone is positioned for maximum northerly winds on Western Europe. Western Iberian coast and in the French Lands are have more intense upwellings, while Northern Iberian coast and Southern Brittany have less intense upwellings (see figure 5.2.1). When well established, it is represented by 2 K colder surface waters over 10 to 20 km of width on the near-shore.

The trapped cold water mass The trapped cold water mass is a cold water mass (¡ 12 °C), positioned over the continental shelf and trapped below the seasonal thermocline, that doesn't change its hydrological characteristics all year long. During summer, the seasonal thermocline isolates it from the surface. During winter, the river halocline isolates

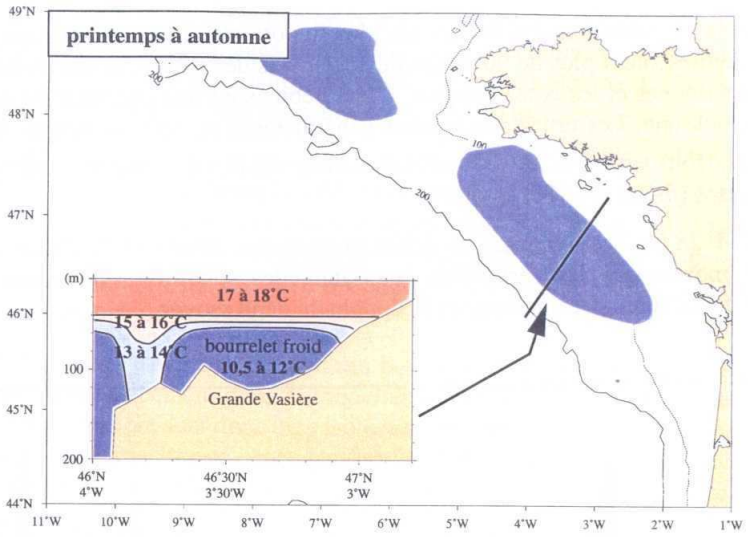

Figure 5.11: The cold water mass in the Bay of Biscay in deep blue. Seasonal stratified surface waters in red. Well mixed water column in light blue.

the cold "bourrelet" from the surface. Near the continental slope, a dropping of the isopycnals (as seen in figure 5.2.1), isolates the cold "bourrelet" from the deep waters area.

Warmpool During summer, in the South-Eastern corner of the Bay of Biscay, the solar flux is more intense and winds are weak. This conjuncture tends to create a 20 m depth thin, stratified thermocline, 1-2 K warmer than its offshore counterpart. Seasonal autumn winds disperse the warm water northwards, although this northward transportation is highly sensitive to wind conditions.

5.2.2 Modelling strategies

Description of the models MOHID and NEMO-OPA

MOHID Based on a standard finite-volume approach of the Ocean Primitive Equations, using a generic combination of sigma and/or cartesian vertical coordinates with an ADI semi-implicit scheme for the horizontal advection-diffusion numerical schemes, as well as possessing a complete suite of modern and standard OBC, the MOHID model is comparable in its specifications to ROMS or NEMO-OPA. Thus it was

for the MOHID team a great opportunity to participate in this inter-comparison exercise on a real-life case-study: the Biscay area. Some literature that best describes MOHID, besides the PhD thesis of Martins et al. (1998); Leitão (2003a), would be Coelho et al. (2001); Leitão et al. (2005); Riflet et al. (2007b).

NEMO-OPA NEMO(Nucleus for European Modelling of the Ocean) is a state-of-the-art modeling framework for oceanographic research and operational oceanography. While OPA is an Ocean Parallel model. It allows several ocean related components of the earth system to work together or separately. This framework is intended to be interfaced with the remaining component of the earth system (atmosphere, land surfaces, ...) via the OASIS coupler.

NEMO is distributed under CeCILL license. In order to define and organize human expertise and financial ressources, the major partners are organized within the NEMO Consortium, including CNRS, Mercator-Ocean, UKMO and NERC.

NEMO is an ocean modelling framework which is composed of "engines" nested in an "environment". The "engines" provide numerical solutions of ocean, sea-ice, tracers and biochemistry equations and their related physics. The "environment" consists of the pre- and post-processing tools, the interface to the other components of the Earth System, the user interface, the computer dependent functions and the documentation of the system.

MOHID and NEMO-OPA description are presented in table 5.2.2 below.

It must be noted that the models can only be compared if the horizontal grid and the forcings are the same.

Forcings

The best ocean forcing data available was found to be the Mercator-Océan PSY2V1 system for the 2004 period, while the atmospheric forcing is defined by the Aladdin model. Realistic freshwater river discharges are provided for the main rivers in the region.

Bathymetry and horizontal grid

The bathymetry used for the intercomparison is from SHOM(Service Hydrographique et Océanographique de la Marine) and ETOPO5'(Electronic

Table 5.4: Description of the models used in the intercomparison

	NEMO-OPA	MOHID
Free Surface	Time-spliting linear free surface	Time-coupled free surface, ADI semi-implicit (Leendertse and Liu, 1977)
Vertical coordinate	Cartesian + partial-step (the bottom layer adapts itself to the bathymetry), 49 levels	Cartesian + partial-step cells(Adcroft et al., 1997) (minimum is 5% of the layer thickness), 43 levels
Advection tracer	QUICKEST + ULTIMATE (Leonard, 1979, 1991)	TVD scheme (explicit in horizontal and implicit in vertical)
Horizontal Diffusion	constant	constant
Corrections to advection scheme	Preserves the energy and the enstrophy	-
Corrections to turbulent diffusion scheme	Biharmonic -5.10^8 m^4 s^{-1}	Biharmonic 10^9 m^4 s^{-1}(Delhez and Deleersnijder, 2007)
Vertical turbulent diffusion scheme	Blanke and Delecluse (1993)	Canuto et al. (2001b)
Surface forcing	BULK formula (Large et al., 1994)	BULK formula (Kraus and Businger, 1994; Jerlov, 1968; Chapra, 1997)
Barotropic timestep	4s	90 s
Baroclinic timestep	240s	90 s

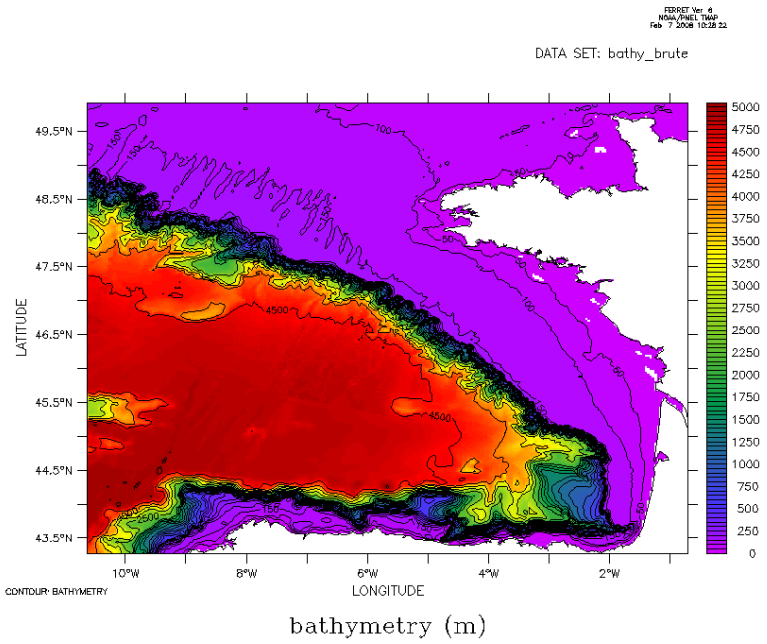

Figure 5.12: Original bathymetry used for the intercomparison.

Table 5.5: Bathymetry filtering method for NEMO-OPA and MOHID

Model	Bathymetry processing	Reason
NEMO-OPA	Minimum depth of 5.75 m	To avoid having too few layers in shallow water areas.
MOHID	Filtering high gradient areas.	MOHID runs a tool that checks every cell of the bottom layer and assures that a minimum thickness ratio with adjacent cells is guaranteed.

TOPOgraphic maps) and presents an initial resolution of 1´. The regular horizontal grid has a resolution of 3 km (1/36°).

Atmospheric fields

The Météo-France ALADIN(Aire Limitée Adaptation Dynamique Développement International) yearly model fields (Courtier and Geleyn, 1988) were used with a 0.1° resolution and a 3 h timestep. Its data would include dayly fields:

- Surface atmospheric pressure,
- Specific humidity at 2 m,
- Air temperature at 2 m,
- Zonal wind speed at 10 m,
- Meridional wind speed at 10 m.

Integrated fields:

- Zonal wind stress,

- Meridional wind stress,
- Precipitation,
- Brut solar flux,
- IR flux.

Tide

The model MOG2D(2D gravity waves model) (Lyard et al., 2006; Pairaud et al., 2008) provides fields for the M2, N2, K2, S2, K1, O1, P1, Q1 and M4 components:

- Water level,
- Barotropic transport,
- Charge.

Open Boundary (OB) fields

The problem of dealing with open boundary conditions (OBC) is the most common in coastal modelling. It's also the hardest to solve.

The mathematical algorithm used at the OB must allow the incoming of external information while letting the model's solution evolve freely. Outgoing perturbations generated inside the model must travel outside the domain and must not be reflected at the boundaries.

There are a great number of OBC numerical schemes to let radiate the barotropic mode, the baroclinic mode and scalar quantities (Palma and Matano, 1998, 2001; Marchesiello et al., 2001).

A maximum three-fold resolution ratio is recommended when applying a reference solution at the OB. Moreover, an intermediate model should be nested between the reference solution and the inner model, in order to stay below the three-fold resolution ratio. Also, it is necessary to have a good knowledge of the water masses presented in the reference solution. If the water masses are not correctly initialized in the model, then no correct solution is bound to be found.

Water masses are generated by the thermohaline circulation of the global ocean, and their genesis requires a very large time scale (millenniums)(Emery and Meincke, 1986). Thus, regional models cannot reproduce these water masses. The water masses need to be present in the initial condition and at the OB: in this case, they are present in the PSY2V1 thermohaline solution.

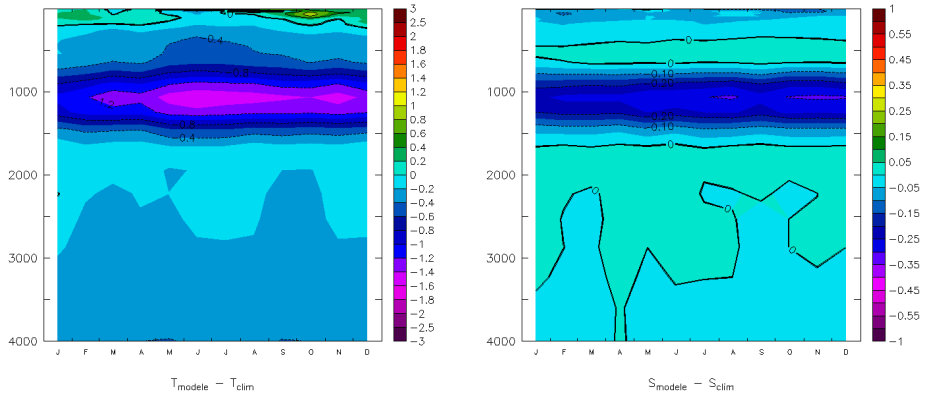

Figure 5.13: Bias of temperature (left panel) and salinity (right panels) profiles between PSY2V1 and IFREMER climatology, during 2004.

Figure 5.2.2 shows the evolution of the monthly and horizontally averaged temperature and salinity, between the PSY2V1 model and a climatology (from IFREMER), during year 2004. Besides differences in surface temperatures, ranging up to 0.8°C, mainly due to the absence of tidal mixing in PSY2V1, the most remarkable biases in temperature and salinity are relative to the Mediterranean Waters (MW) centred on the 1000 m depth (the differences reach negative 1°C and negative 0.25).

Figure 5.2.2 represents the TS diagram of PSY2V1 model, in each grid point off the shelf (> 200 m depth). Left panel represents the TS diagram of the initial condition (01/01/2004) and the right panel represents the annual mean. Surface warmer waters have a high variability in time, thus the main difference between the initial condition and the annual average. Water masses are globally well represented, albeit the PSY2V1 MW are less pronounced, with a lower than expectable salinity maximum; even if the MW are within the climatology interval bounded in red in the figure. However, the MW signal is even less pronounced in the annual mean TS diagram, which could indicate an advection problem in the PSY2V1 model in the Bay of Biscay region. This characteristic is also present in figure 5.2.2, with average biases that tend to grow in time.

Hence, the PSY2V1 thermohaline solution in the bay of Biscay is good enough to be used as initial condition and as lateral boundary condition. However, a less good representation of the MW must be considered when

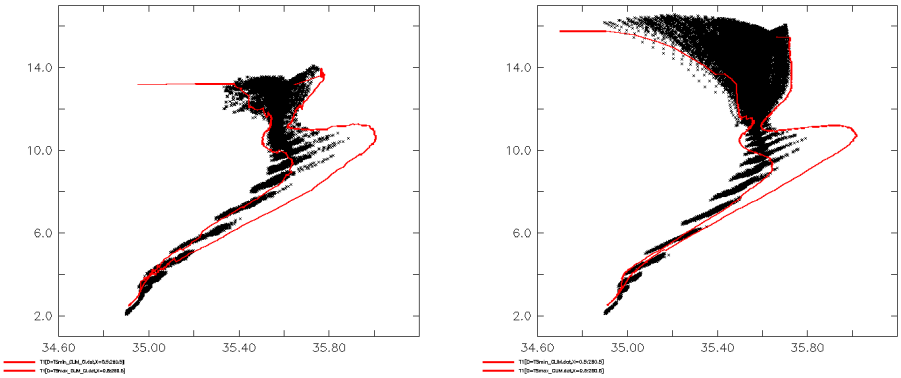

Figure 5.14: PSY2V1 TS diagram in the Bay of Biscay. Left, 01/01/2004 diagram (initial condition for the regional models). Right, 2004 annual mean diagram. The red curves represent the climatology minima and maxima.

comparing results with real data. Thus, this problem will also affect all the regional models.

The used algorithms for the OBC are displayed in table 5.2.2

Rivers

For this study, only the three main french rivers were considered: The Loire, the Garonne and the Adour. The daily runoffs are represented in figure 5.2.2. The Loire and the Garonne flow are more oust han the Adour flow, by at least a ten-fold factor.

Unfortunately, no river discharges were considered during the MOHID simulation. This means the shelf results will not be comparable at all. However, water masses and large scale currents are well comparable.

Initialization

Initialization is equally a critical point in coastal modelling. There are several methods available according to the nature of the study, but in most cases, the initial fields come from the OGCM. A simple interpolation/extrapolation procedure of the OGCM fields will generate small perturbations that will manifest as spurious high-frequency gravity waves and high vertical velocities. An adjustment time is required to radiate the initial

Table 5.6: Numerical OBC schemes.

	NEMO-OPA	MOHID (Leitão et al., 2005)
Barotropic OBC	Flather (1976) (η, u, v)	Flather (1976)
Baroclinic OBC	specified at the boundary	flow relaxation scheme u, v (Martinsen and Engedahl, 1987) + viscosity sponge (Delhez and Deleersnijder, 2007)
Tracer OBC	specified at the boundary	flow relaxation scheme S, T (Martinsen and Engedahl, 1987)
Relaxation zone	15 grid-cells wide in space and one day duration (for T and S only)	30 grid-cells wide in space and one third of day duration for u, v, S and T. Exponencial decay in space directed away from the relaxation zone.
Frequency	daily	daily

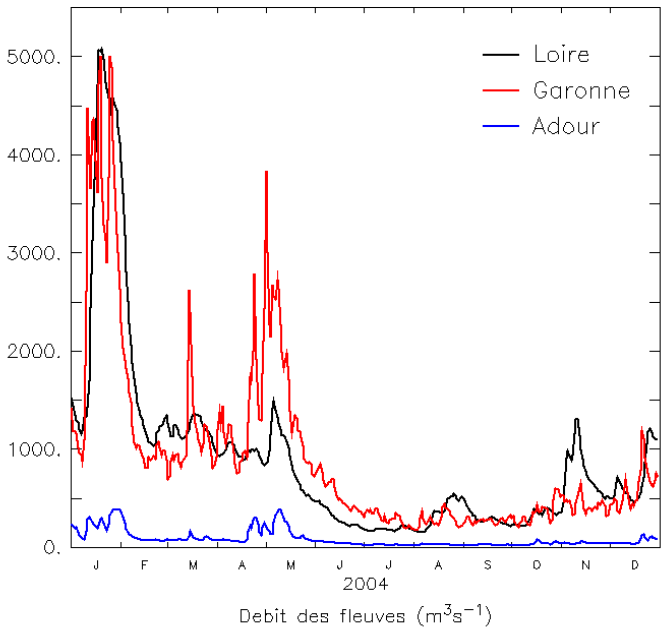

Figure 5.15: Adour, Loire and Garonne rivers daily flow used to simulate year 2004.

Table 5.7: Initialization methods used in NEMO-OPA and in MOHID.

Model	initialization
NEMO-OPA	S and T initialization. The model then adjusts with these fields to the bathymetry.
MOHID	Horizontal interpolation and vertical re-interpolation. S and T initialization. The model then adjusts with these fields to the bathymetry.

perturbations, defined as the spin-up time. There are several initialization methods that allow to reduce or even to nullify this spin-up (Palma and Matano, 2001; Leitão et al., 2005). The different initialization methods chosen by each team are shown in table 5.2.2.

Computation time

The NEMO-OPA simulation lasted roughly 3 days on a 12 CPUs Fujtsu/Siemens cluster. Each CPU is an AMD Opteron dual-core 64 bits between 2 and 2.2 GHz.

The MOHID simulation lasted around 37 days (using only a single core) Intel Core 2 Extreme X9650 3 GHz, 8 GB RAM.

In-situ data inventory

Climatology Climatology from IFREMER. 0.4^o resolution and 261 layers.

Satellite imagery
- Daily, weekly, monthly and yearly MODIS SST,
- Hourly or daily SEVIRI SST,
- Daily NAR satellite imagery,

Time series
- 8 SST buoys (as seen in figure 5.2.3, left panel),
- 18 tidal stations (as seen in figure 5.2.3, right panel),

In-situ profiles
- PELGAS campaign 28-04-2004 to 23-05-2004. 75 S, T profiles.
- EVHOE campaign 29-10-2004 to 12-12-2004. 101 S, T profiles.

5.2.3 Results comparison, validation and analysis

Water masses evolution and biases

Before undergoing a showdown of each models result to each of the identified physical processes described in section 5.2.1, it is important to show the global consistency of the coastal model relatively to the reference solution, as initial and lateral boundary conditions.

Water masses evolution, bias relatively to the PSY2V1 reference

The water masses in solution PSY2V1 were presented, as well as the temperature and salinity biases relative to the IFREMER climatology. It is important to follow the evolution of these water masses introduced by the initialization method, and maintained by the open boundary conditions and vertical physics. For each month was calculated an average profile of the difference between the model and the PSY2V1 reference solution. The resulting biases are presented in figure 5.2.3.

Globally, the water masses characteristics are preserved by the NEMO-OPA model, even if the model stocks excessive heat and salt around 1000 m depth, particularly during summer. The biases tend towards zero by the end of the simulation.

MOHID, however, although starting from a near null bias with the reference solution, quickly presents, after the first month, a dipolar bias in temperature and salinity that grows in time and that strengthens the MW signal. There are several hypotheses that can explain this anomaly relative to the reference solution. On one hand, the PSY2V1 reference solution may have higher vertical diffusion than MOHID. On the other hand, little differences in the density state-equation would change the equilibrium depth of water parcels, thus presenting a systematic dipolar-like bias between model and reference. Finally, there's also the hypothesis that this could indicate some problem with the vertical mixing or with the advection.

In figure 5.2.3 are traced the TS diagrams of the abyssal plain ($>$ 200 m depth) for the initial conditions and the annual mean for each model. Also, the maxima and minima TS contours of the PSY2V1 reference solution are superimposed in red (from figure 5.2.2). The results obtained with NEMO-OPA and MOHID are well inside the PSY2V1 reference solution contour. However the surface waters don't reproduce the river plumes accurately. This is expected in MOHID, as the river plumes aren't modelled at all. As for NEMO-OPA, the river plumes are detailed in detail in the main body of this report.

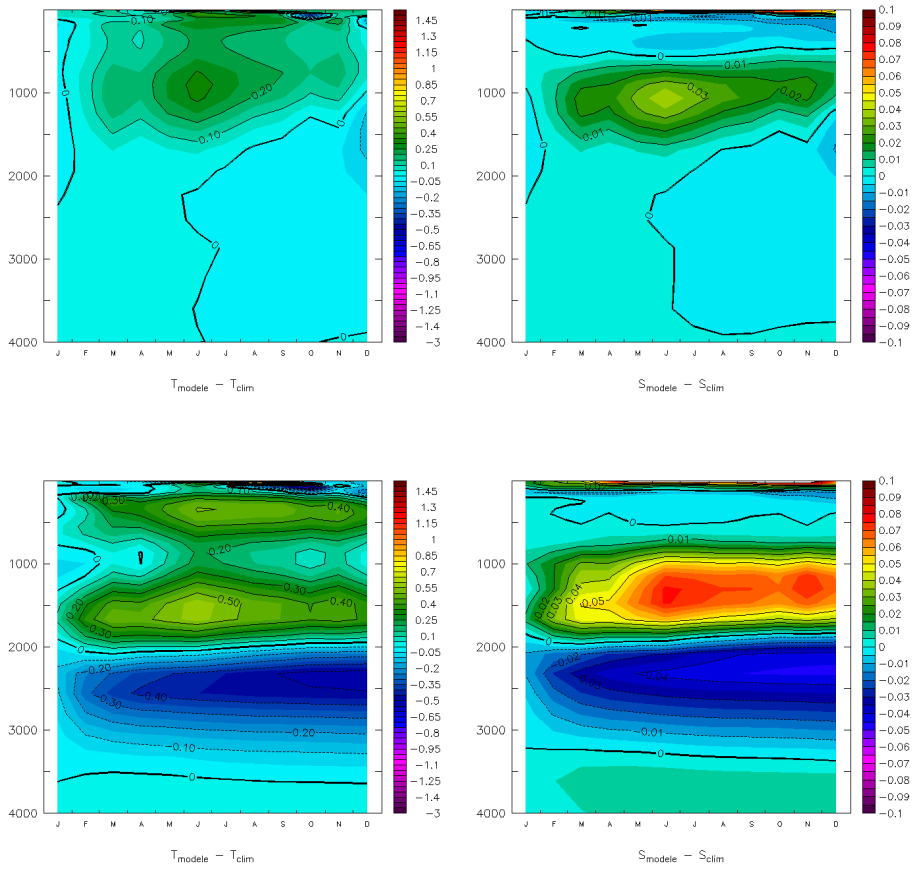

Figure 5.16: Temperature (left panels) and salinity (right panels) differences between each model and PSY2V1. The top panels display the difference in temperature and salinity between NEMO-OPA and PSY2V1, whereas the bottom panels display the difference between MOHID and PSY2V1.

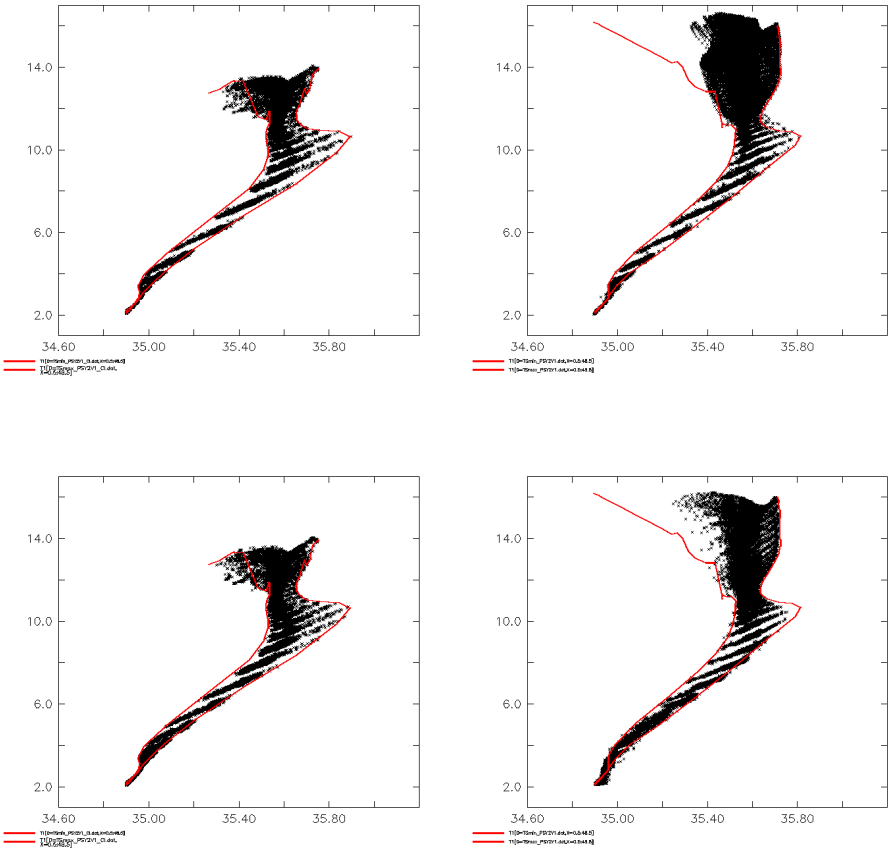

Figure 5.17: TS diagrams of each model. The left panels represent the initial condition. The right panels represent the annual mean. The red contours are the TS minima and maxima from the PSY2V1 reference solution. The top panels represent the results of NEMO-OPA. The bottom panels represent the results of MOHID.

Thermal balance

Heat and salt balance was performed by interpolating/extrapoling all models results, the reference solution and the climatology to a reference grid with the same vertical Cartesian discretization. Naturally, the interpolations will introduce errors in the balances and hence the diagnostics can only hold a qualitative nature. Thermal and haline balances fluctuations are represented in figure 5.2.3.

As can be seen, the reference solution thermal fluctuation is quite different from the climatology, whereas, both models NEMO-OPA and MOHID are in very good agreement, equally, with the climatology.

However, the salt balance is somewhat more complex to analyze. As it must represent the incoming MW, it shouldn't necessarily have a yearly periodicity as the climatology seems to claim. Hence all models, except MOHID, have very different ending values, including the PSY2V1 reference solution. Both NEMO-OPA and MOHID are in phase with the PSY2V1 haline balance variability, however, the haline balance difference relative to the reference solution in MOHID tends to grow, while the NEMO-OPA balance difference is higher during summer and disappears by the end of the year. Thus, while MOHID haline balance follows better the climatology and tends to diverge from the reference solution, the NEMO-OPA is in phase and follows better the reference solution. While this could prove to be a bad feature for MOHID (to diverge from the reference solution), in this case, it shows that MOHID can improve a not-so-good reference solution concerning the haline distribution.

SST bias towards monthly MODIS images

MODIS monthly SST images are very useful for calculating the models biases. The SST biases of each model, in the whole domain and in the Ushant area (Longitude bounded between 6°W and 4°W, and Latitude bounded between 47.5°N and 49°N) are presented in figure 5.2.3. The biases of NEMO-OPA and MOHID are quite in phase. However, due to the thick 8 m depth superficial layer, MOHID was the only model showing a negative cooler bias relative to MODIS during the summer months. Indeed, all the other models, including the reference solution, have a warmer bias trend relative to MODIS SST in their approximately 0.5 meter thick superficial layer.

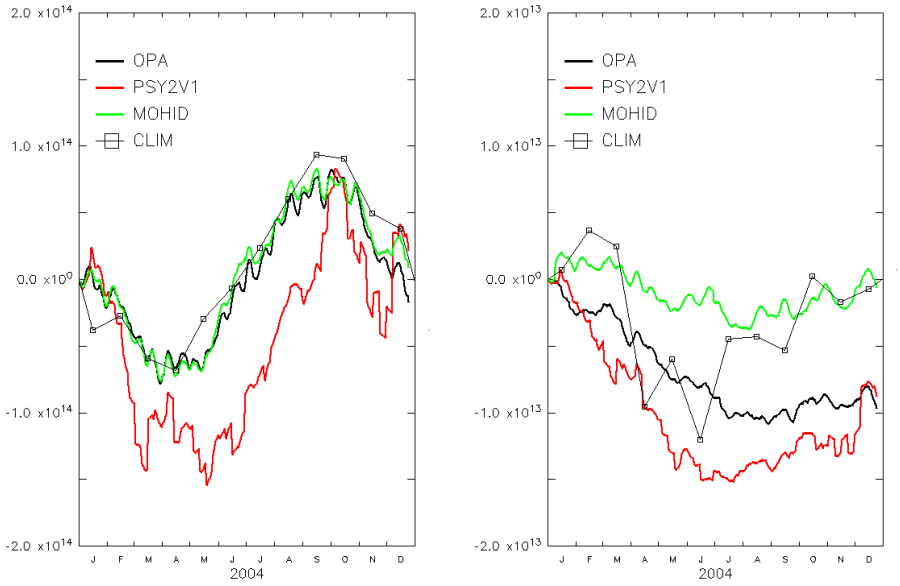

Figure 5.18: Thermal (left panel) and haline (right panel) balance normalized to the initial value obtained for each model. The climatology is also represented.

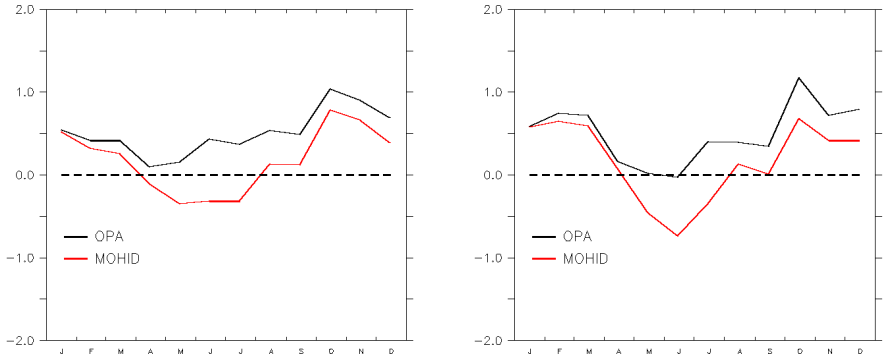

Figure 5.19: SST bias of NEMO-OPA and MOHID relatively to monthly MODIS images. Left panel, bias in the whole region. Right panel, bias in the Ushant area (6°W to 4°W and 47.5°N to 49°N).

Nesting method and global dynamics validation

Nesting a model inside an OGCM is a critical aspect. The objective is to evidence the difficulty of models to manage ingoing (from the OGCM) and outgoing (from the local solution) information, by leveraging on OBC algorithms. Two methods were chosen. The first method consists in calculating the tide-filtered annual mean velocity field at 15 m depth as seen in figure 5.2.3.

Mean annual tide free circulation at 15 m depth obtained with NEMO-OPA and MOHID are hard to be compared. NEMO-OPA is run without tide and MOHID is run with tide. NEMO-OPA does the average of daily instantaneous results, while MOHID performs an online integration for each time-step. Thus please bear in mind that MOHID displays the residual circulation with tide and NEMO-OPA displays the residual circulation without tide.

The globally cyclonic PSY2V1 circulation of the abyssal plain, which contours two anti-cyclonic eddies, presents an excessively intense slope current (that is an already known error of this model). On the shelf however, circulation is overall anti-cyclonic. The mean circulation of the other models, although preserving the same overall cyclonic/anti-cyclonic feature, has qualitatively and quantitatively very distinct traits, namely on the positioning and the intensity of each recirculation pattern. Lack of current data

doesn't allow assessing which model is best. However, the efficiency of the numerical schemes at the OB can be discussed for each model.

As the models evolve and the fields diverge further and further away from the reference solution, due to better atmospheric forcings and better resolution, over-relaxation of salinity and temperature tends to create an artificial front all along the OB that will tend to generate spurious geostrophic residual flow. This residual geostrophic flow will store available potential energy (APE) and enstrophy generated inside the domain, while isolating wave-like information from propagating out-ward and in-ward the domain, thus also deprecating the interior solution away from the OB. Thus the relaxation decay-times are a critical aspect that must be parameterized for each model and each reference solution. They are ill-defined when a geostrophic flow occurs at the OB and when permanent fronts are created after a long enough period of simulation. MOHID was over-relaxed compared to NEMO-OPA by a three-fold factor at the OB, and also used a wider relaxation zone. However NEMO-OPA uses a constant decay-time all along its relaxation zone, while MOHID uses an exponentially growing relaxation time directed away from the OB. As for the results, figure 5.2.3 clearly shows a spurious current in the northern boundary for both models, but much more intense in MOHID, probably due to the relaxation coefficients difference and the wider relaxation area. This is the indication of an intense front generated between the PSY2V1 solution and both models solution, possibly due to an excessive relaxation of the salinity and temperature fields. However, both models perform better at the western boundary, even if MOHID shows the recirculation much more to the interior of the domain. This is probably due to higher relaxation periods and the 30 cells wide relaxation zone that confines the recirculation more on the interior of the domain. Finally, even if MOHID doesn't show a clear spurious geostrophic flow along the OB, it does accuse in figure 5.2.3 a spurious OB front that doesn't show in NEMO-OPA. Probably MOHID is also over-relaxing the salinity and temperature fields at the western OB. Since the rivers runoff are absent in MOHID, the fronts are absent as well and, thus, the model doesn't show the geostrophic frontal anti-cyclonical recirculation over the shelf, along the coastline, that feeds, in the warmpool zone, the abyssal plain cyclonical recirculation, as seen in PSY2V1 and in NEMO-OPA. A second run is being made that will address all these issues in MOHID: adding the river runoff, shortening the relaxation zone, and increasing by a threefold factor the decay time at the western boundary and by a sixfold factor at the northern boundary. This should correct all the OB issues and, expectedly, yield results quite similar to the NEMO-OPA solution.

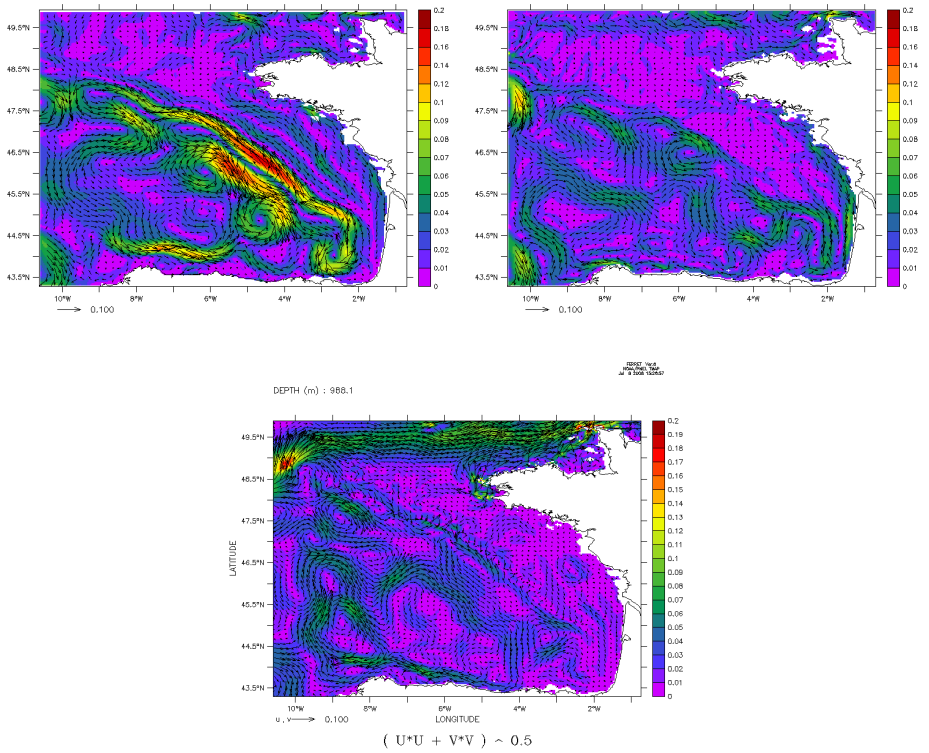

Figure 5.20: Yearly average tide-removed EKE and velocity fields during 2004 at 15 m depth. Top left panel, PSY2V1. Top right panel, NEMO-OPA. Bottom panel, MOHID.

Vertical mixing

In this section, models results are compared against surface buoys temperature data. The buoys are distributed in the Bay of Biscay as shown in figure 5.2.3. There are three types of buoys: i) the buoys moored on the shelf, such as Ushant, Cherbourg and Minquiers; ii) the buoys moored in deep waters, such as Gascogne and Brittany; iii) and finally, the buoys moored on the slope, near the shelf, such as VillanoSisargas, EstacaBares and CaboPenhas. The models performance is expected to remain consistent within each type of buoy, but it can differ completely between the different types of buoys. This is partly due to the influence of the tide and the vertical mixing it induces. Also, the Cherbourg buoy (figure 5.2.3), is very close to the OB, and falls in a relaxation area and/or a sponge area (this is the MOHID case). This means that the accuracy of the models results can be degraded near the sponge area.

Tide will induce vertical mixing. This tide-induced mixing is expected to be more intense on the shelf, than on the abyssal plains, since the tidal barotropic velocity is much more intense over the shelf as a consequence of the reduced depth. Hence we can expect for thicker mixed layers over the shelf than over abyssal plains. Thus models run with tide will present cooler SST over the shelf than models run without tide. This should be particularly true for the NEMO-OPA model, as they have a fine vertical discretization of the superficial 50 m depth, with its superficial layer of only 0.5 m to 1 m depth. Hence it can resolve accurately the mixed-layer. MOHID, however, has a superficial layer 8 m thick. This means that the minimum mixed layer depth will be of 8 m. Hence, MOHID will tend to present cooler SST over deep waters. This bias will be less noticed on shelf waters, however, due to the stronger tide-induced mixing. On deep waters, the barotropic tide and the bathymetry can induce internal tides; which in turn, enhance the vertical mixing. To illustrate the influence of tide on vertical mixing, results of NEMO-OPA with tide and without tide were compared against in-situ surface buoys. Results of MOHID with tide are also presented to compare both models.

In figures 5.2.3 and 5.2.3, the model results with tide (blue line) are directly comparable with the buoy (black line) and the satellite data (black dots). The NEMO-OPA results without tide are also displayed to evidence the mixing induced by the barotropic tide. The more intense summer solar flux tends to create a stratified seasonal thermocline, which in turn, presents higher temperatures at the surface. However this seasonal surface stratification is destroyed with tide-induced mixing. Hence, the NEMO-OPA results

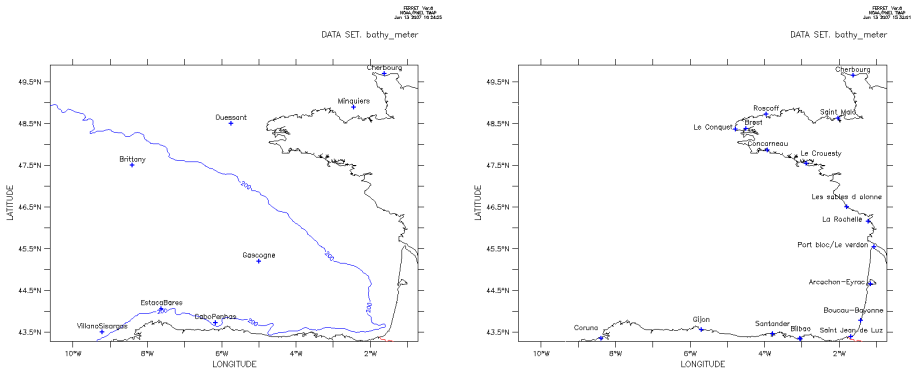

Figure 5.21: Buoys (left panel) and tidal stations (right panel) positions.

with and without tide decorrelate during the months of May to September. Furthermore, MOHID results are consistently cooler relative to NEMO-OPA results with tide. At Cherbourg, the NEMO-OPA results with tide follow more closely the buoy's results, while at Minquiers it's rather the MOHID results that follow slightly more closely the buoy's results.

Tables 5.2.3 to 5.2.3 summarize the results for the 8 buoys whose locations are in the left panel of figure 5.2.3. The tables contain the yearly average, the correlation, the standard deviation and the RMSE between the models and the observations. The standard deviation here is the average error minus the average bias. On the overall both models exhibit similar statistics, NEMO-OPA performs slightly better on some buoys and MOHID performs slightly better on the other buoys.

The June 15th MODIS satellite SST shows a good cloud-free coverage of the area while evidencing clear frontal structures. The comparisons of this satellite image with the models are presented in figure 5.2.3. Figure 5.2.3 contains the same images but the average bias was removed from the models results.

There is a lot of information to be taken from that satellite SST. The lower temperatures on the north shelf (which includes the Ushant front) are highly correlated with strong tidal currents and indicate an area where tidal mixing is maximal. Along the northern part of the continental slope, a thermal front is formed induced by internal waves mixing. The rest of the French continental shelf presents warmer waters and upwelling between the Landes and the mouth of Gironde's estuary. A large upwelling seems to be occurring along the Spanish coast in the models, and probably in the

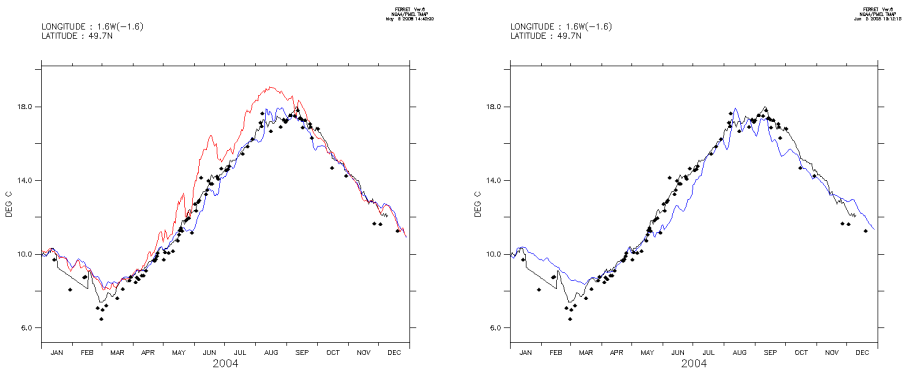

Figure 5.22: Comparison of SST time series between data from the Cherbourg buoy (black line), model results without tide (red line), and model results with tide (blue line). Black dots represent data from cloud-free MODIS images. Left panel, NEMO-OPA. Right panel, MOHID.

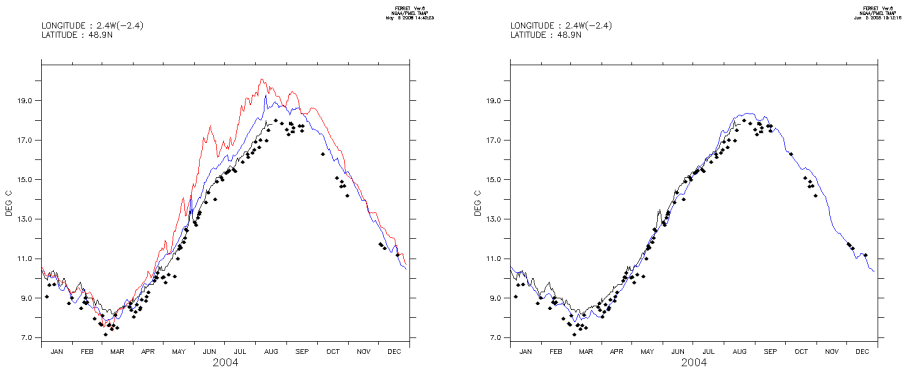

Figure 5.23: Comparison of SST time series between data from the Minquiers buoy (black line), model results without tide (red line), and model results with tide (blue line). Black dots represent data from cloud-free MODIS images. Left panel, NEMO-OPA. Right panel, MOHID.

Table 5.8: Statistical comparison in temperature between the models and the Brittany buoy.

Brittany	NEMO-OPA	MOHID
	Temperature (°C)	
In-situ average SST	14.315	14.315
Average SST TIDE	14.537	14.045
Average SST NOTIDE	14.568	14.045
Standard deviation from in-situ TIDE	0.532	0.448
Standard deviation from in-situ NOTIDE	0.547	0.448
RMSE from in-situ - TIDE	0.532	0.523
RMSE from in-situ - NOTIDE	0.545	0.523
Brittany	NEMO-OPA	MOHID
	Correlation	
Correlation TIDE	0.986	0.982
Correlation NOTIDE	0.992	0.982

Table 5.9: Statistical comparison in temperature between the models and the Cabo Penhas buoy.

Cabo Penhas	NEMO-OPA	MOHID
	Temperature (°C)	
In-situ average SST	15.42	15.42
Average SST TIDE	15.754	15.456
Average SST NOTIDE	15.943	15.456
Standard deviation from in-situ TIDE	0.518	0.520
Standard deviation from in-situ NOTIDE	0.519	0.520
RMSE from in-situ - TIDE	0.616	0.521
RMSE from in-situ - NOTIDE	0.736	0.521
Cabo Penhas	NEMO-OPA	MOHID
	Correlation	
Correlation TIDE	0.985	0.985
Correlation NOTIDE	0.987	0.985

Table 5.10: Statistical comparison in temperature between the models and the Cherbourg buoy.

Cherbourg	NEMO-OPA	MOHID
	Temperature (°C)	
In-situ average SST	12.67	12.67
Average SST TIDE	12.692	12.509
Average SST NOTIDE	13.315	12.509
Standard deviation from in-situ TIDE	0.524	0.729
Standard deviation from in-situ NOTIDE	0.709	0.729
RMSE from in-situ - TIDE	0.525	0.746
RMSE from in-situ - NOTIDE	0.959	0.746
Cherbourg	NEMO-OPA	MOHID
	Correlation	
Correlation TIDE	0.989	0.981
Correlation NOTIDE	0.981	0.981

Table 5.11: Statistical comparison in temperature between the models and the Estacabares buoy.

Estacabares	NEMO-OPA	MOHID
	Temperature (°C)	
In-situ average SST	15.776	15.776
Average SST TIDE	16.182	15.967
Average SST NOTIDE	16.467	15.967
Standard deviation from in-situ TIDE	0.418	0.568
Standard deviation from in-situ NOTIDE	0.521	0.568
RMSE from in-situ - TIDE	0.582	0.560
RMSE from in-situ - NOTIDE	0.866	0.560
Estacabares	NEMO-OPA	MOHID
	Correlation	
Correlation TIDE	0.990	0.982
Correlation NOTIDE	0.987	0.982

Table 5.12: Statistical comparison in temperature between the models and the Gascogne buoy.

Gascogne	NEMO-OPA	MOHID
	Temperature (°C)	
In-situ average SST	15.922	15.922
Average SST TIDE	15.934	15.403
Average SST NOTIDE	15.996	15.403
Standard deviation from in-situ TIDE	0.304	0.402
Standard deviation from in-situ NOTIDE	0.294	0.402
RMSE from in-situ - TIDE	0.304	0.656
RMSE from in-situ - NOTIDE	0.303	0.656
Gascogne	NEMO-OPA	MOHID
	Correlation	
Correlation TIDE	0.996	0.994
Correlation NOTIDE	0.996	0.994

Table 5.13: Statistical comparison in temperature between the models and the Minquiers buoy.

Minquiers	NEMO-OPA	MOHID
	Temperature (°C)	
In-situ average SST	11.797	11.797
Average SST TIDE	12.009	11.591
Average SST NOTIDE	12.670	11.591
Standard deviation from in-situ TIDE	0.478	0.317
Standard deviation from in-situ NOTIDE	1.045	0.317
RMSE from in-situ - TIDE	0.523	0.378
RMSE from in-situ - NOTIDE	1.362	0.378
Minquiers	NEMO-OPA	MOHID
	Correlation	
Correlation TIDE	0.997	0.996
Correlation NOTIDE	0.991	0.996

Table 5.14: Statistical comparison in temperature between the models and the Ushant buoy.

Ushant	NEMO-OPA	MOHID
	Temperature (°C)	
In-situ average SST	14.329	14.329
Average SST TIDE	13.638	13.344
Average SST NOTIDE	14.294	13.344
Standard deviation from in-situ TIDE	0.672	0.805
Standard deviation from in-situ NOTIDE	0.619	0.805
RMSE from in-situ - TIDE	0.964	1.272
RMSE from in-situ - NOTIDE	0.620	1.272
Ushant	NEMO-OPA	MOHID
	Correlation	
Correlation TIDE	0.968	0.954
Correlation NOTIDE	0.97679	0.954

Table 5.15: Statistical comparison in temperature between the models and the Villano-Sisargas buoy.

Villano-Sisargas	NEMO-OPA	MOHID
	Temperature (°C)	
In-situ average SST	15.325	15.325
Average SST TIDE	15.648	15.651
Average SST NOTIDE	15.977	15.651
Standard deviation from in-situ TIDE	0.865	0.630
Standard deviation from in-situ NOTIDE	0.849	0.630
RMSE from in-situ - TIDE	0.923	0.710
RMSE from in-situ - NOTIDE	1.071	0.710
Villano-Sisargas	NEMO-OPA	MOHID
	Correlation	
Correlation TIDE	0.936	0.967
Correlation NOTIDE	0.953	0.967

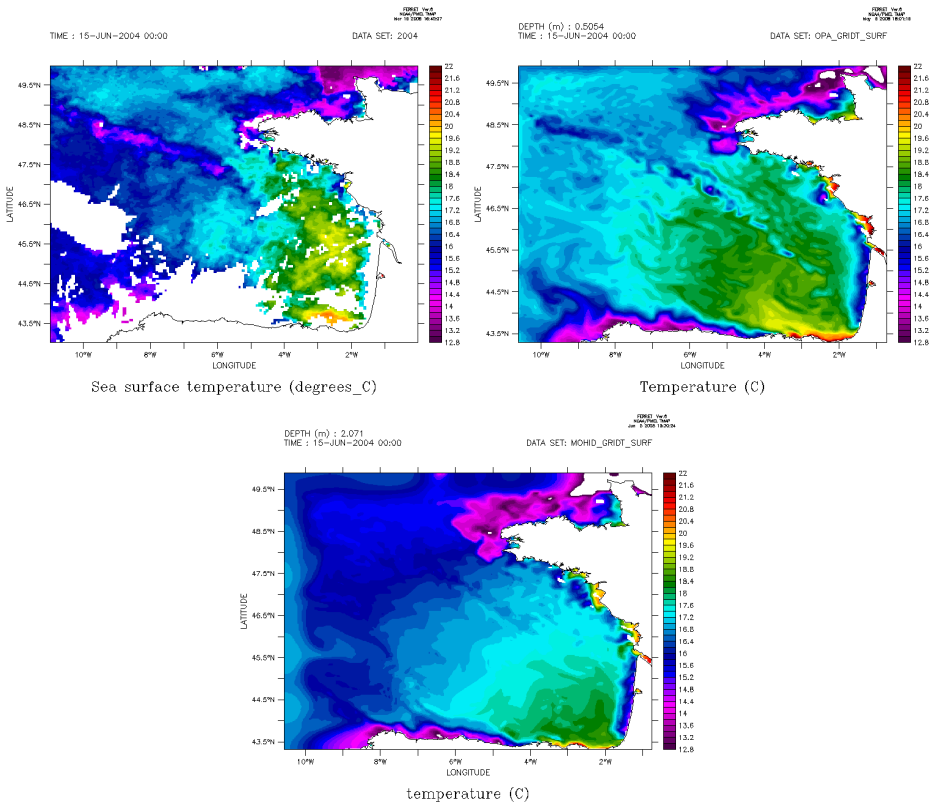

Figure 5.24: SST MODIS comparison with the models NEMO-OPA and MOHID for the June 15th. Top-left panel, MODIS image. Top-right panel, NEMO-OPA model. Bottom panel, MOHID model.

Satellite data despite the cloud cover.

The NEMO-OPA model reproduces appropriately the thermal structures described above. The MOHID results seem to evidence a less variability than could be expected. This may be due to the coarse vertical discretization at the surface. Also, the model is relaxing too strongly to the reference PSY2V1 solution at the western OB. MOHID relaxation time is around 30000 s while, NEMO-OPA are around 90 000 s (1 day). This creates an artificial thermal and haline front at the western OB that will create a spurious geostrophic current inside the domain.

The Ushant front can be well described by satellite imagery even though it is a near-shore process. Cloud-free events were spotted by MODIS near the area on June 3rd (figure 5.2.3) and on July 6th (figure 5.2.3) and were

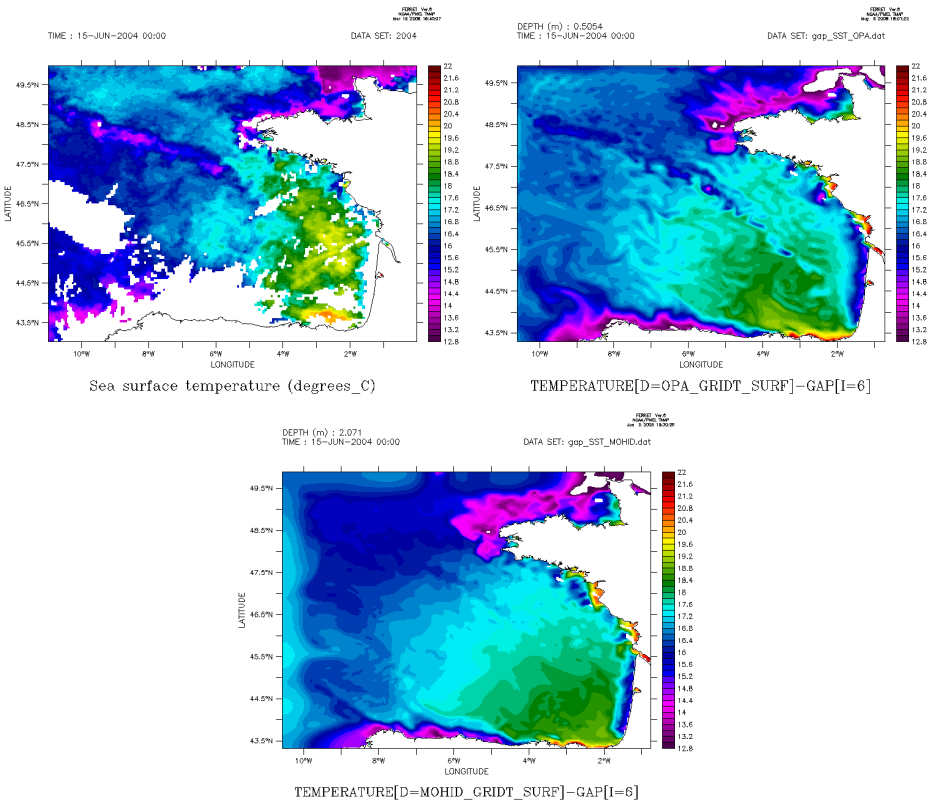

Figure 5.25: SST MODIS comparison with the models NEMO-OPA and MOHID for the June 15th. Top-left panel, MODIS image. Top-right panel, NEMO-OPA model. Bottom panel, MOHID model. The SST average difference between the models and MODIS was removed.

compared with the models with and without bias towards MODIS. Also, the temperature zonal section at 48.15°N (bounded by 6°W to 4°W) is compared with the literature in the rightmost panels of figures 5.2.3 and 5.2.3 for the same dates.

Figures 5.2.3 and 5.2.3 represent the Ushant front, composed of two cold lobes. Both models represent them correctly qualitatively. However, due to the 8 m thick superficial layer, MOHID results are too cold. But, even with the bias corrected (middle panel), MOHID results are still a bit cold for the June 3rd snapshot. The vertical sections are consistent with the scientific description found in the literature for both models.

The offshore distance of the front is an important characteristic of the region. Thus, Hovmuller diagrams along the section SST were created for each model and for the satellite data (figure 5.2.3). To be able to compare the diagrams between model and satellite, the minimum SST was removed from each diagram. Figure 5.2.3 represents the time evolution of temperature minimum in the left panel, in order to representing the temperature evolution of the front. Right panel of figure 5.2.3 represents the time evolution of the position of the temperature minimum, in order to represent the evolution of the front's position.

Observations on the left-panel of figure 5.2.3 show that the minimum of temperature is leaned on the coast during the winter period (January to April and November to December), and is situated around the 5.1°W during the summer period (May to October). During this period, the temperature differences clearly show the presence of a front. During the April and October months, we observe a transient period between the winter/summer states that is characterized by a homogeneous SST.

The results obtained with both models are very consistent showing clearly the seasonal migration of the front. The temperature gradient maxima, however, during summer are too weak for NEMO-OPA, and too strong for MOHID; whereas during winter, they are far too strong for MOHID, and slightly too strong for NEMO-OPA. Finally, the front in MOHID is too thin during winter.

The left panel of figure 5.2.3 shows that, again, the MOHID SST is cooler than the NEMO-OPA SST, probably because of its thick over-mixed superficial layer. However both models results seem to correlate very well with the MODIS data with what looks like an acceptable RMSE. The right panel of figure 5.2.3 shows the evolution of the front position, represented by the SST minimum, between two states, winter and summer. Both NEMO-OPA and MOHID evolve in phase with the obersvations between the winter/summer states. MOHID however performs somewhat better during the transient

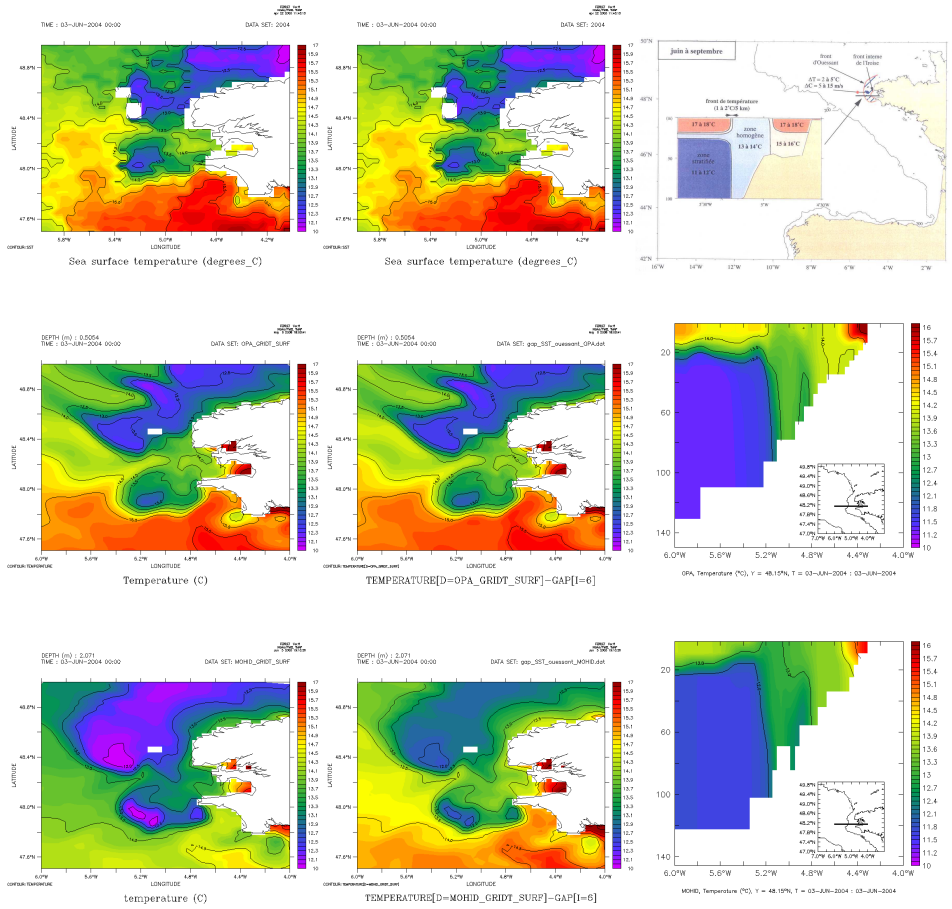

Figure 5.26: June 3rd event in the Ushant area. Top panels: MODIS and litterature data. Middle panels: NEMO-OPA results. Bottom panels: MOHID results. Left panels: SST. Center panels: SST with the average difference with MODIS removed. Right panels: Cross-section at 48.2°N, between 6°W and 4°W.

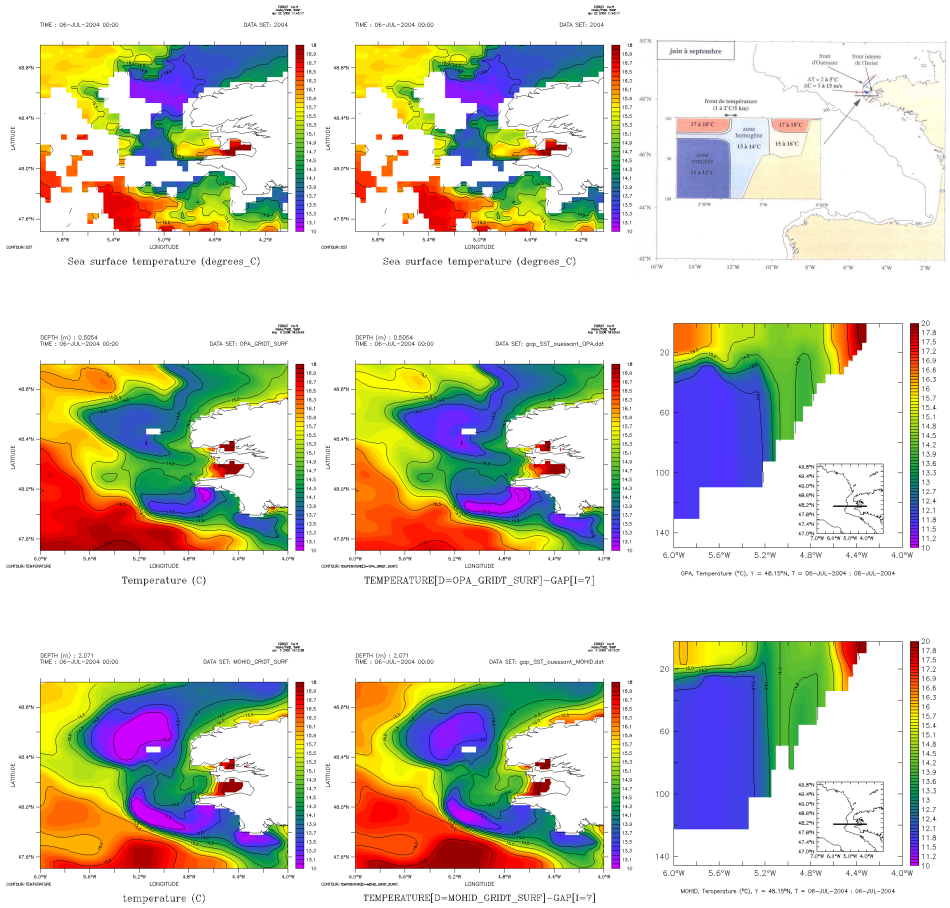

Figure 5.27: July 6th event in the Ushant area. Top panels: MODIS and litterature data. Middle panels: NEMO-OPA results. Bottom panels: MOHID results. Left panels: SST. Center panels: SST with the average difference with MODIS removed. Right panels: Cross-section at 48.2°N, between 6°W and 4°W.

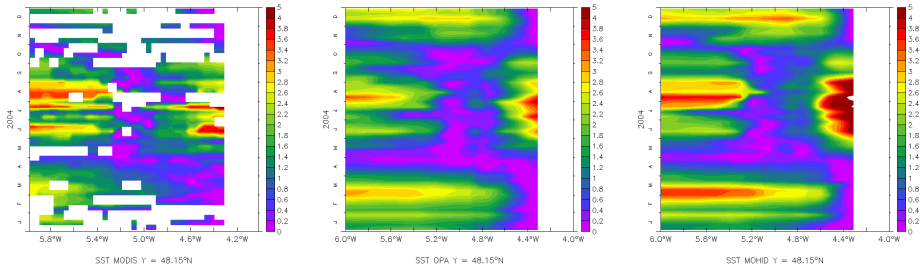

Figure 5.28: Hovmuller diagrams of the temperature offset relatively to the minimal temperature found along the Ushant section (6°W to 4°W at 48.15°N), of the MODIS SST (leftmost panels) and the models SST (middle panel and rightmost panel).

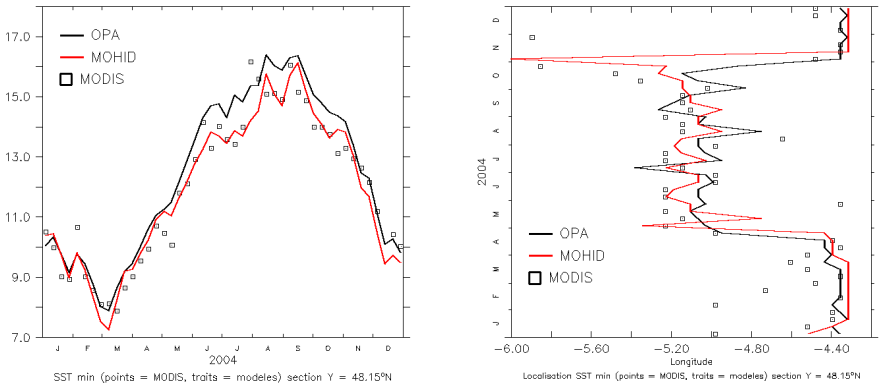

Figure 5.29: left panel: Minimum SST evolution of the Ushant section section (6°W to 4°W at 48.15°N). Right panel: Position evolution of the SST minimum in the Ushant section (right panel).

months of April and October.

Figure 5.2.3 shows that this cold water body is present in the extrapolated/interpolated climatology (top right). The model results (bottom panels) show the presence of the cold water body. However, the MOHID solution doesn't show the folding isopycnics as clearly as does the NEMO-OPA solution. The main reason is that the surface stratification in MOHID cannot be as strong as in NEMO-OPA because of the lack of vertical resolution in the surface and, second, because of the absence of river runoffs. A freshwater plume would intensify the stratification at the surface and inhibit the vertical mixing of the cold water body, thus preserving its form and enhancing the isopycnics folding. This is not the case in NEMO-OPA that does represent more accurately the cold water body.

Sections were built from data from the PELGAS (figure 5.2.3) and EVHOE (figure 5.2.3) cruises. Both sections show the presence of a cold water body. In the PELGAS case (figure 5.2.3), the NEMO-OPA model reproduces quite well the cold water body, with a clear sign of the isopycnics folding; while MOHID tends to be colder overall and shows less evidence of isopycnic folding. In the EVHOE case (figure 5.2.3), MOHID is qualitatively in better agreement than NEMO-OPA, although both models solutions are warmer than the measurements.

Upwellings

There are two upwelling areas in the Bay of Biscay: off the coasts of south-western France, and North-east of the Spanish coast. Several diagnostics are available for measuring upwelling, and none is more relevant than another. In this work, an upwelling index was calculated at latitudes 44°N, 44.5°N and 45°N, representing the SST differences between 1.9°W and 1.4°W, 1.9°W and 1.3°W and 2.2°W and 1.3°W respectively, as seen in figure 5.2.3. Models have similar behaviours, except at latitude 44°N (middle panels of figure 5.2.3), where MOHID fails to show upwelling events as seen on measurements. Both models manage to resolve some measured upwelling events, but not all. This could be due to the weak wind resolution, and the consequent loss of fine-resolution wind vorcitity, that is known to be relevant to induce coastal upwelling.

The warmpool

The warmpool is a surface heat convergence area between south-western France and north-eastern Spain. Thus it is defined as the region with an

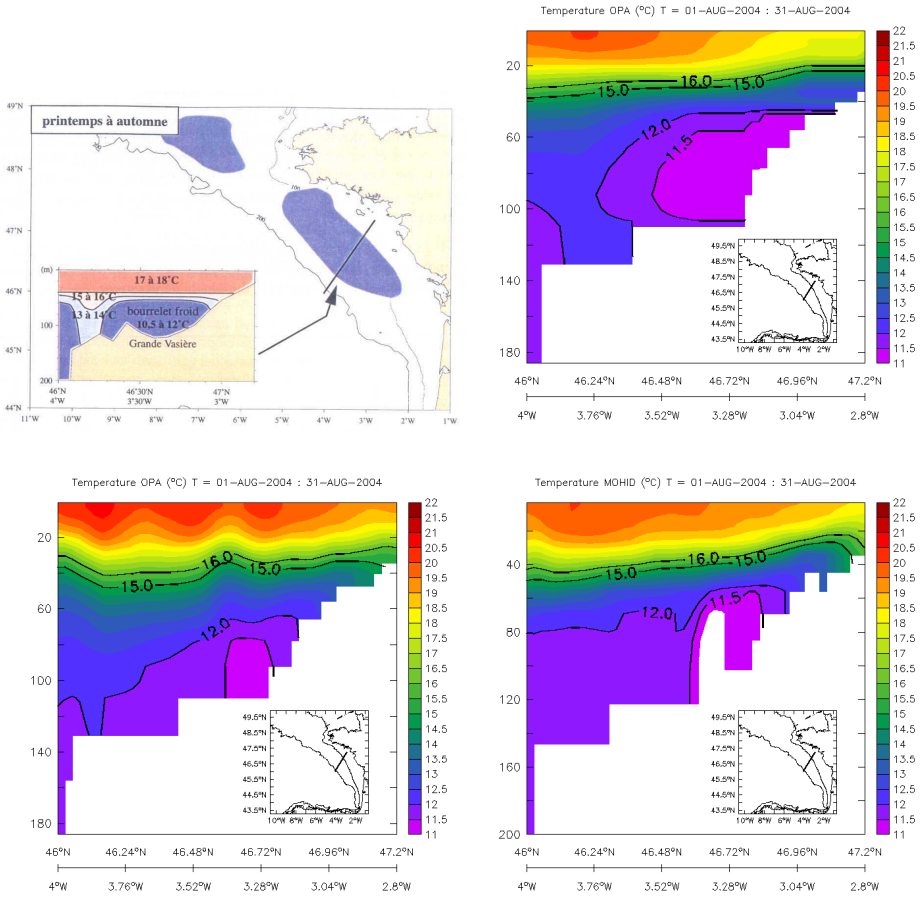

Figure 5.30: Cross-section from 46°N, 4°W to 47.2°N, 2.8°W of the la Vasière cold water mass during August. Temperature comparison between literature (top left), climatology (top right) and the models (bottom).

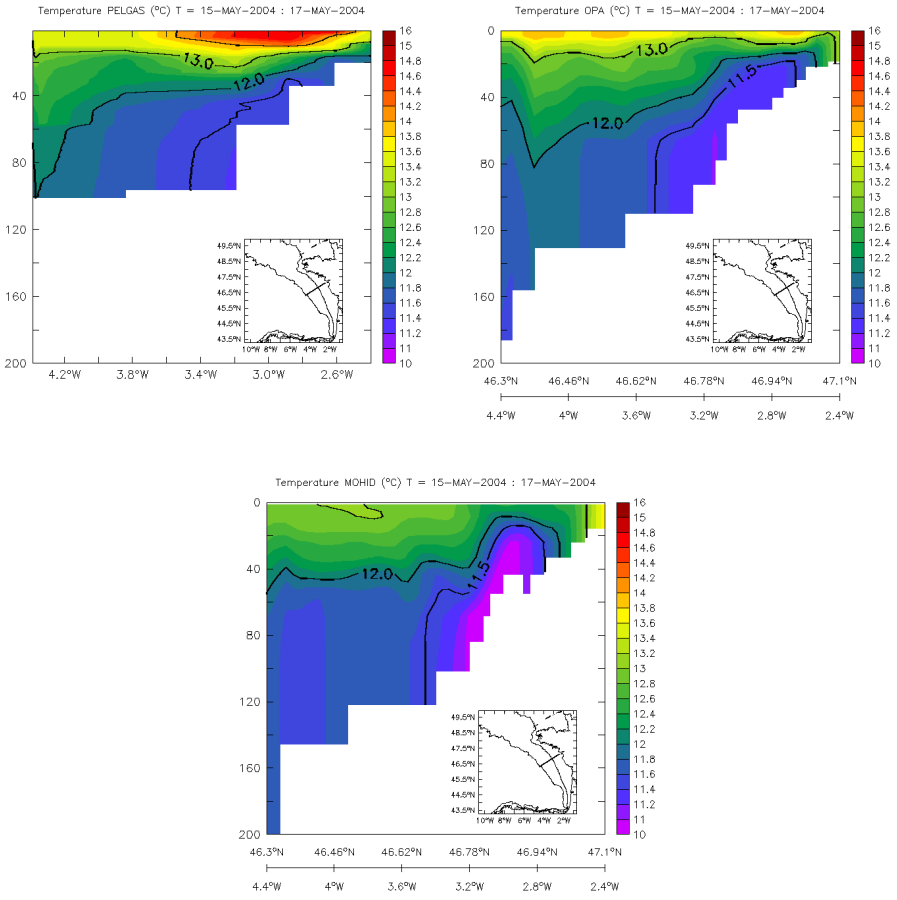

Figure 5.31: Cross-section from 46.5°N, 5°W to 47.6°N, 3°W of the la Vasière cold water mass during PELGAS campaign. Temperature comparison between PELGAS (top left), NEMO-OPA (top right) and MOHID (bottom).

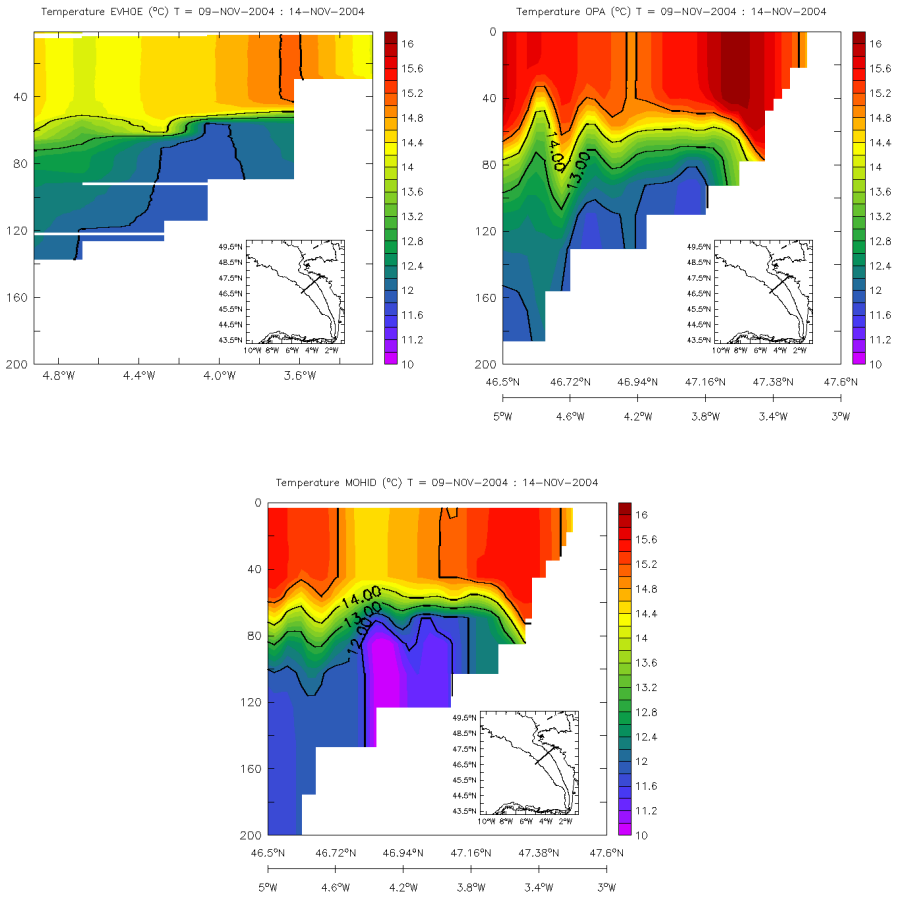

Figure 5.32: Cross-section from 46.3ºN, 4.4ºW to 47.1ºN, 2.4ºW of the la Vasière cold water mass during EVHOE campaign. Temperature comparison between EVHOE (top left), NEMO-OPA (top right) and MOHID (bottom).

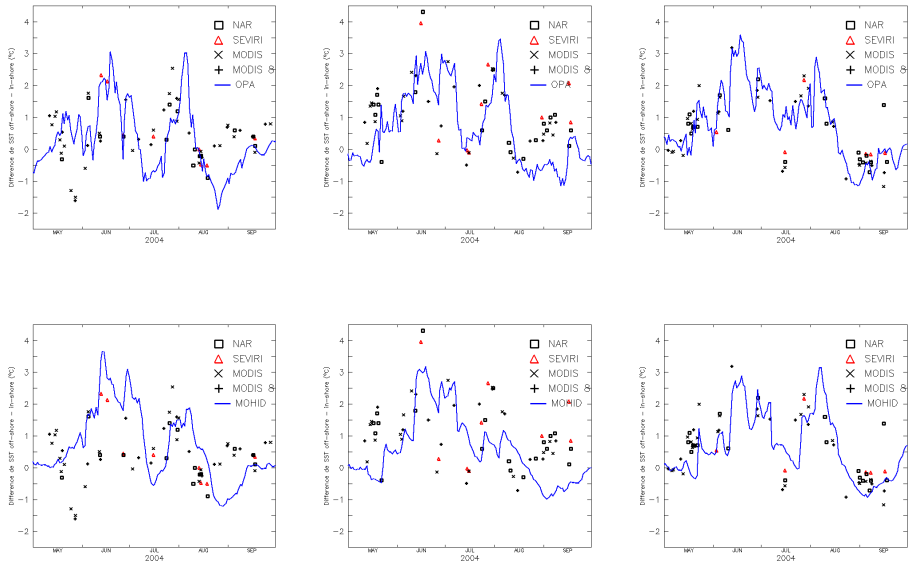

Figure 5.33: Upwelling indexes measured and modelled by NEMO-OPA (top panels) and MOHID (bottom panels) at latitudes 44°N (left), 44.5°N (center) and 45°N (right) between May and September. Superposed are the results from NAR (square), NEVIRI (triangle), MODIS (cross) and MODIS Acqua (vertical cross) satelitte SST imagery.

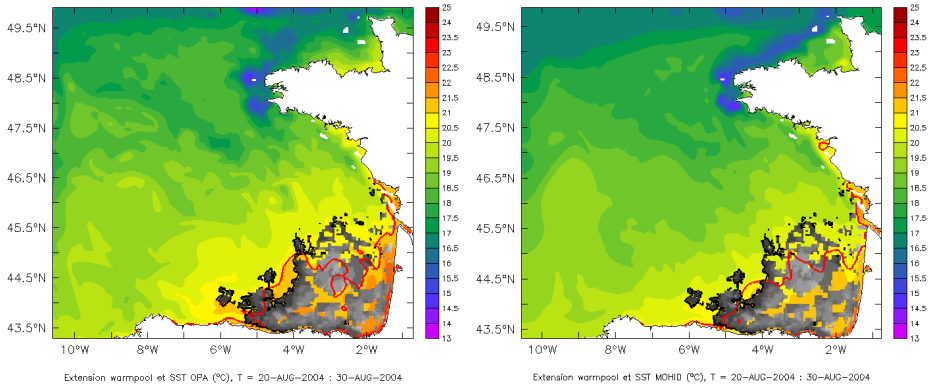

Figure 5.34: Comparing MODIS warmpool (grey area) with the models (red contour and temperature colour scale) NEMO-OPA (left) and MOHId (right) between the 20th and the 30th August.

SST 1.5°C higher than the SST of point 7°W 45°N. Figure 5.2.3 shows the comparison between the warmpool measured by MODIS satellite images (grey area) and the warmpool modelled by NEMO-OPA and MOHID (red contour) over the period comprised between the 20th and the 30th August. Both MOHID and NEMO-OPA provide similar results, but they tend under-estimate the measured warmpool area (MOHID under-estimates slightly more due to its 8 m thick surface layer that tends to over-mix temperature near the surface).

Figure 5.2.3 compares the yearly evolution of the warmpool area (in number of domain cells) of the model (black line) against MODIS (blue line). The blue squares provide the percentage of cloud free area in the MODIS images. Higher percentage means a clearer satellite view and, thus, a more reliable comparison.

Both models generally under-perform by under-estimating the width of the warmpool, except for the October and November months. The July peak in MODIS data is remarkably absent in the models. Other than that, the models try to correlate with the other peaks, but the apparent RMSE seems quite large.

In figure 5.2.3 is shown the yearly evolution of the average SST in the warmpool zone bounded by (4°W to 1°W and 43.5°N to 45°N) of the models (black lines) and of the MODIS snapshots (red dots with error bars). The

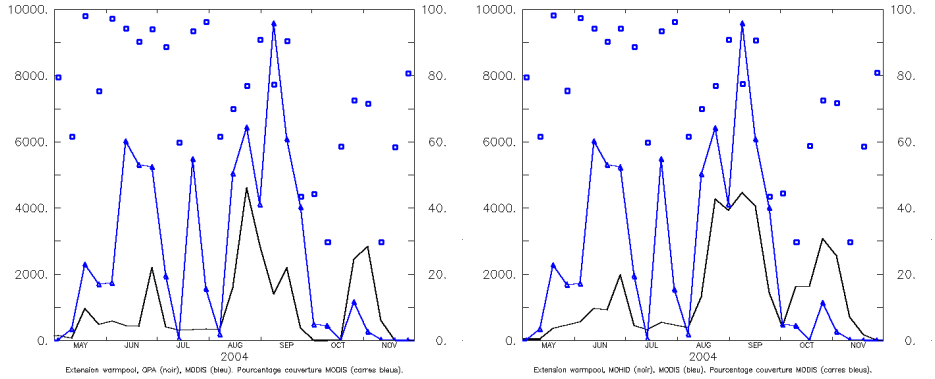

Figure 5.35: Time evolution of the number of cells (vertical axis on the left) defining the warmpool by MODIS (blue line) and by the models (black line). The blue squares stand for the cloud-free area percentage (vertical axis on the right). NEMO-OPA results are on the left panel and MOHID results are on the right panel.

error bar is proportional to the cloud-cover area. The temperature variations are approximately well represented by the models, when compared with the MODIS data, although MOHID looks slightly colder, probably because of its over-mixed 8 m thick superficial layer.

5.2.4 Conclusion

As a general conclusion relative to the intercomparison of models, we can say that NEMO-OPA tends to follow more closely the reference PSY2V1 solution than MOHID. This should be expected since both PSY2V1 and NEMO-OPA share the same source-code. MOHID is generally colder at the surface because of its thicker 8 m depth surface layer that over mixes the surface water. Also, no river run-offs were present in the MOHID simulation, which deteriorated the stratification over the shelf and consequently deteriorated the cold water body characteristics at the la Varsière area. Also, the shelf SST PELGAS and EVHOE data were not interesting to compare with at all for the same reason. MOHID tends to show much less vertical mixing than PSY2V1 or NEMO-OPA, thus creating a stratification dipole in the MW depth and down to 3000 m depth. Otherwise, both models seem to perform quite well, when compared against exhibited in-situ data. On the

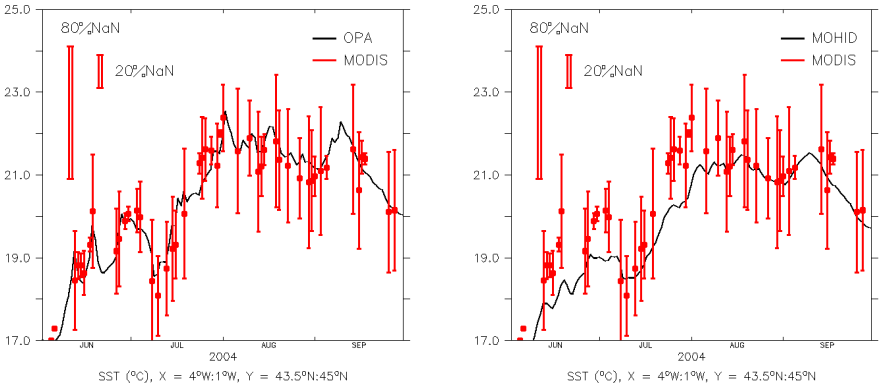

Figure 5.36: Average temperature comparison between MODIS (red) and the models (black) NEMO-OPA (left panel) and MOHID (right panel) in the area bounded by 4°W and 1°W and by 43.5N and 45N. The error bars (in red) are proportional to the cloud-coverage percentage for the area.

downside, MOHID exhibits a too stiff relaxation at the western OB which generates an intense spurious residual geostrophic current. A new run with MOHID is underway with a finer vertical discretization at the surface, river runoffs, and a looser relaxation time at the OB.

For the purpose of downscaling techniques applied to OGCM, the techniques used, independently, by both teams IST and Mercator-Océan proved to be quite similar, differing only in the parameterization terms (such as the relaxation times near the OB, which would influence the quality of the results), and in the numerical schemes. Other initialization techniques could have been tested, such as geostrophic currents initialization. These downscaling techniques, designed to be used with an OGCM in offline, seem to evidence the feasibility of successfully implementing operational systems that can forecast the circulation of regions nested in the OGCM domain, while adding more physics, such as tide, and freshwater river runoffs, improving the existing physics, such as the atmospheric forcing, and yet, yield realistic results. It can be expected to see the implementation of operational regional circulation systems in the years to come; using as offline OGCM the Mercator-Océan forecast solution.

Chapter 6

Conclusion

This thesis studied the possibility of proposing a diagnostic scalar quantity to assess absorbing and radiative open boundary conditions in the scope of regional Ocean modeling. The scalar proposed in this thesis is the scalar of Okubo-Weiss, firstly studied independtly by Okubo (1970) and Weiss (1991), which provides a quick and computationally economic insight on the nature of the flow. It is known that walled boundaries yield elliptic type of flows, whereas areas without boundaries are more prone to hyperbolic eulerian flows. The scalar of Okubo-Weiss easily help diagnose a poor implementation of a boundary condition by accusing an over-elliptic flow, due to undesired reflection of at the boundarie of exiting wave-like perturbations, where otherwise it would have been a predominantly hyperbolic flow.

It is well known that academic test-cases, although they may be exhaustively analyzed and explained, will yield contrary skill assessment to a wide variety of OBCs when compared with their implementation counterpart in realistic complex regional Oceanic models. Hence this thesis needed, beyond academic test-cases, to model realistic regional Ocean domains where the Okubo-Weiss scalar could be given its full expression.

MOHID, which is a full suite of numerical tools for water modeling providing an integrated approach to model any water system to the subplanetary scale, was the model of choice to implement the realistic regional Ocean models. MOHID is a rising tool for regional Ocean modeling (Leitão et al., 2005; Riflet et al., 2007b, 2008), nevertheless, some prior un-exhaustive tests to validate MOHID as a capable model to handle regional Ocean physical processes were undertaken.

The turbulence model in MOHID for the vertical axis was tested in a one-year scenario in an open unbounded Ocean region located at station Papa. This location was chosen due to its large availability of in-situ data. The test revealed that a correction in the Brunt-Vaisalla frequency was required in order for MOHID to yield accurate results. Otherwise, an excessive stratification during the Summer season was occuring. The turbulence model for the vertical axis in MOHID is the GOTM.

The freshwater cylinder experiment of Tartinville et al. (1998) allowed to test and select the best advection scheme (TVD with a superbee flux limiter). It also allowed to test some relaxation OBC schemes. FLA+FRS with a sponge layer proved to provide the best results.

A shallow-water equations model was developed in Matlab in the scope of implementing and testing several OBC schemes. The SWE model featured complex bathymetry and land-masks, Coriolis force, wind and bottom stress, no-slip, closed wall, Flather and gravity wave explicit radiation OBCs. It proved to be a powerful and versatile tool to study simple test-cases which could easily be validated against simple dimensional analysis and simple geometrical considerations. In occurence, a gaussian bump initial elevation was thoroughly studied and interesting relations were deduced, such as the Froude number being equal to the ratio of bump elevation agains water depth, and such as the characteristic time of energy dissipation being equal to $T_\sigma = \frac{\nu}{\sigma^2}$.

The devised numerical experiments consider the basic approach of the large-model/small-model, where a smaller finer or equal resolution model is nested into a larger coarser resolution model. That way, a reference unbounded local flow is always available to compare with the smaller-scale bounded flow and thus provide maximum effectiveness when using the OW scalar in assessing the quality of the OBC prescribed in the small-model.

The shallow-water large-model/small-model experiment yielded a persisting elliptic boundary layer when using a simple GWE (gravity wave explicit) and GWE+FLA radiative OBC, detected by the OW scalar. Testing several boundary conditions, the OW scalar helps to averiguate the best condition for the present system.

The regional models chosen were Western Iberia, for the whole year period of 2007, and the Bay of Biscay, for the whole year period of 2004.

Both models were the downscaling of the Mercator-Océan solution of the North-Atlantic. Both models had realistic atmospheric forcing coming from MM5-ist and from Aladdin, respectively. Both models had realistic time series of the main rivers for their respective regions. The Western Iberia model was validated specifically concerning the presence, depth and behaviour of the MW veins (Riflet et al., 2007b,a), and it served as the basis later for the present operational forecasting system (Riflet et al., 2008), the PCOMS. A master thesis study on the water masses and the fluxes distributions over the Western Iberian region was performed and monitored during the course of the thesis as well.

The Bay of Biscay regional Ocean model was intercompared with another regional Ocean model, NEMO-OPA. Both models yielded interesting results, though MOHID showed better results for the SST comparison with satelite imagery. This is probably due to the cruder vertical resolution at the surface of 2 to 4 meters thichness compared to NEMO-OPA who displays a 0.5 thin layer at the surface. The conclusion of the inter-comparison is that the MOHID model performs quite well, as any other widespread regional Ocean model under the same forcing conditions.

The Okubo-Weiss parameter is yet to be applied to these models, offline. The expected results to appear are the detection, via the Okubo-Weiss scalar diagnostic, of systematic regions where flow type inversions occur (from hyperbolic to elliptic, mostly, but also the other way around) for specific type of boundary conditions. It is expected that the OW scalar be of help as a tool to prescribe alternative configurations to the OBCs, since changing the type of absorbing or radiating scheme (Herzfeld, 2009; Lavelle and Thacker, 2008), to changing the limits of the domain. Another interest aspect of this scalar is that it can be run offline, even after the model was run.

Finally, and as a sideline feature, this thesis proposes an extension and deeper insight on the Reynolds transport theorem, which is a fundamental theorem at the basis of the eulerian formulation of the broad continuum mechanics discipline, with a full suite of proved properties, which may have interesting applications in the multi-phasic fluid flows (Collado, 2007; Brenner, 2005a) or, perhaps, in cases where the control volumes evolve in time, such as the case of free surface numerical models of the primitive Ocean equations.

Bibliography

A. Adcroft, C. Hill, and J. Marshall. Representation of Topography by Shaved Cells in a Height Coordinate Ocean Model. *Monthly Weather Review*, 125(9):2293–2315, 1997. 176, 204

I. Ambar. A shallow core of Mediterranean water off western Portugal. *Deep-Sea Research*, 30(6A):677–680, 1983. 195, 197

I. Ambar and M. R. Howe. Observations of the Mediterranean outflow. I. Mixing in the Mediterranean outflow. *Deep-Sea Research*, 26(1979): 535–554, 1979. 195

I. Ambar, N. Serra, M. J. Brogueira, G. Cabeçadas, F. Abrantes, P. Freitas, C. Gonçalves, and N. Gonzalez. Physical, chemical and sedimentological aspects of the mediterranean outflow off iberia. *Deep Sea Research Part II: Topical Studies in Oceanography*, 19(49):4137–4177, 2002. 179

A. Arakawa. Computational design for long-term numerical integration of the equations of uid motion: Two-dimensional incompressible ow. Part I. *Journal of Computational Physics*, 1(1):119–143, 1966. 3, 115, 117, 120, 128, 149, 176

R. Asselin. Frequency filter for time integrations. *Monthly Weather Review*, 100(6):487–490, 1972. 136, 137

F. Auclair, S. Casitas, and P. Marsaleix. Application of an Inverse Method to Coastal Modeling. *Journal of Atmospheric and Oceanic Technology*, 17 (10):1368–1391, 2000. 187

P. Bahurel, P. De Mey, T. De Prada, E. Dombrowsky, P. Josse, C. Le Provost, P. Y. Le Traon, A. Piacentini, and L. Siefridt. MERCATOR, forecasting global ocean. *AVISO Altimetry Newsletter*, 8:14–16, 2001. 176

P. Baines. On internal tide generation models. *Deep Sea Research Part I: Oceanographic Research*, 29:307–338, 1982. 198

S. Balachandar and J. K. Eaton. Turbulent dispersed multiphase flow. *Annual Review of Fluid Mechanics*, 42(1):111–133, January 2010. ISSN 0066-4189. 31

C. F. Balseiro, P. Carracedo, B. Gómez, P. C. Leitão, P. Montero, L. Naranjo, E. Penabad, and V. Pérez-Munuzuri. Tracking the prestige oil spill: An operational experience in simulation at meteogalicia. *Weather*, 58:452–458, December 2003. 5

C. Basdevant and T. Philipovitch. On the validity of the"Weiss criterion"in two-dimensional turbulence. *Physica D Nonlinear Phenomena*, 73:17–30, 1994. 2

A. Beckmann and D. B. Haidvogel. Numerical simulation of flow around a tall isolated seamount. part i: Problem formulation and model accuracy. *Journal of Physical Oceanography*, 23(8):1736–1753, 1993. 3, 93, 152, 176

J. P. Berenger. A perfectly matched layer for the absorption of electromagnetic waves. *Journal of computational physics*, 114(2):185–200, 1994. 7

B. Blanke and P. Delecluse. Low frequency variability of the tropical Atlantic ocean simulated by a general circulation model with mixed layer physics. *J. Phys. Oceanogr*, 23(8):1736–1753, 1993. 204

E. Blayo and L. Debreu. Revisiting open boundary conditions from the point of view of characteristic variables. *Ocean Modelling*, 9:231–252, 2005. 5, 6, 7, 8, 9, 130, 173, 176, 181, 182

R. Bleck. Finite difference equations in generalized vertical coordinates. Part i. Total energy conservation. *Contrib. Atmos. Phys.*, 51:360–372, 1978. 3, 30, 44

R. Bleck. An oceanic general circulation model framed in hybrid isopycnic-cartesian coordinates. *Ocean Modelling*, 4(1):55–88, 2002. 4, 17, 30

A. F. Blumberg and L. H. Kantha. Open Boundary Condition for Circulation Models. *Journal of Hydraulic Engineering*, 111(2):237–255, 1985. 6, 8, 177, 181, 183

A. F. Blumberg and G. L. Mellor. A description of a three-dimensional coastal ocean circulation model. *Three-dimensional coastal ocean models*, 4:1–16, 1987. 3

J. P. Bourguignon and H. Brezis. Remarks on the euler equation. *Journal of functional analysis*, 15(4):341–363, 1974. 117

J. Boussinesq. Théorie de l'écoulement tourbillant. *Mem. Presentes par divers Savants Acad. Sci. Inst. Fr*, 23:46–50, 1877. 1

A. S. Bower, N. Serra, and I. Ambar. Structure of the mediterranean undercurrent and mediterranean water spreading around the southwestern iberian peninsula. *Journal of Geophysical Research*, 107(C10), 2002. 179, 192, 194

F. Braunschweig, P. Chambel, L. Fernandes, P. Pina, and R. Neves. The object-oriented design of the integrated modelling system MOHID. *Computational Methods in Water Resources International Conference, Chapel Hill, North Carolina, USA*, 2004. 4, 67

F. Braunschweig, F. Martins, P. Chambel, and R. Neves. A methodology to estimate renewal time scales in estuaries: the Tagus Estuary case. *Ocean Dynamics*, 53(3):137–145, 2003. 4

H. Brenner. Is the tracer velocity of a fluid continuum equal to its mass velocity? *Physical Review E*, 70(6):061201+, Dec 2004. 33

H. Brenner. Kinematics of volume transport. *Physica A: Statistical Mechanics and its Applications*, 349(1-2):11–59, April 2005a. ISSN 03784371. 33, 245

H. Brenner. Navier stokes revisited. *Physica A: Statistical Mechanics and its Applications*, 349(1-2):60–132, April 2005b. ISSN 03784371. 33

H. Brenner. Fluid mechanics revisited. *Physica A: Statistical Mechanics and its Applications*, 370(2):190–224, October 2006. ISSN 03784371. 33

D. Brunt. The period of simple vertical oscillations in the atmosphere. *Quart. J. Roy. Meteorol. Soc*, 53:30–32, 1927. 65, 72, 77, 83

K. Bryan. A numerical method for the study of the world ocean. *J. Comput. Phys*, 4:347–376, 1969. 3, 176

H. Burchard. Models of turbulence in the marine environment: a comparative study of two-equation turbulence models. *Journal of Marine Systems*, 21(1-4):29–53, June 1999. ISSN 09247963. 67, 106

H. Burchard. *Applied turbulence modelling in marine waters*. Springer Verlag, 2002. 45, 61

H. Burchard and K. Bolding. Comparative analysis of four second-moment turbulence closure models for the oceanic mixed layer. *Journal of Physical Oceanography*, 31(8):1943–1968, August 2001. 67

H. Burchard, K. Bolding, and M. R. Villarreal. Gotm, a general ocean turbulence model. *Theory, applications and test cases. European Commission Rep. EUR*, 18745, 1999. 66

H. Burchard, K. Bolding, and M. R. Villarreal. Three-dimensional modelling of estuarine turbidity maxima in a tidal estuary. *Ocean Dynamics*, 54(2): 250–265, May 2004. ISSN 1616-7341. 72, 111

H. Burchard and Others. *Applied Turbulence Modelling in Marine Waters*. Springer, 2002. 66, 153, 176

S. Cailleau, V. Fedorenko, B. Barnier, E. Blayo, and L. Debreu. Comparison of different numerical methods used to handle the open boundary of a regional ocean circulation model of the Bay of Biscay. *Ocean Modelling*, 25(1-2):1–16, 2008. 5

A. Canas, A. D. Santos, and P. C. Leitão. Effect of large scale atmospheric pressure changes on water level in the tagus estuary. *Journal of Coastal Research*, SI56:1627–1631, 2009. 5

V. M. Canuto, A. Howard, Y. Cheng, and M. S. Dubovikov. Ocean Turbulence. Part I: One-Point Closure Model Momentum and Heat Vertical Diffusivities. *Journal of Physical Oceanography*, 31(6):1413–1426, 2001a. 69, 72, 176

V. M. Canuto, A. Howard, Y. Cheng, and M. S. Dubovikov. Ocean turbulence. part i: One-point closure model-momentum and heat vertical diffusivities. *Journal of Physical Oceanography*, 31(6):1413–1426, June 2001b. 204

S. C. Chapra. Surface water-quality modeling. *Mcgraw-hill Series In Water Resources And Environmental Engineering*, 1997. 33, 36, 65, 72, 204

E. P. Chassignet and J. Verron. *Ocean weather forecasting: An integrated view of oceanography*. Springer Dordrecht, the Netherlands, 2006. 4, 5

D. B. Chelton, R. A. Deszoeke, M. G. Schlax, E. K. Naggar, and N. Siwertz. Geographical variability of the first baroclinic rossby radius of deformation. *Journal of Physical Oceanography*, 28(3):433–460, 1998. 184

P. C. Chu and F. Chenwu. Finite volume ocean circulation model. *Oceans '02 MTS/IEEE*, 3:1455–1462 vol.3, 2002. 176

H. Coelho, R. J. Neves, M. White, P. C. Leitão, and A. J. Santos. A circulation model for western iberia. *Journal of Marine Systems*, 2001. 203

H. S. Coelho, R. J. J. Neves, M. White, P. C. Leitão, and A. J. Santos. A model for ocean circulation on the iberian coast. *Journal of Marine Systems*, 32(1):153–179, 2002. 175, 183, 193, 194

F. J. Collado. Reynolds transport theorem for a two-phase flow. *Applied Physics Letters*, 90(2):024101+, 2007. 17, 20, 30, 36, 245

R. Courant, K. Friedrichs, and H. Lewy. On the partial difference equations of mathematical physics. *Mathematische Annalen*, 100:32–74, 1928. 119

R. Courant, K. Friedrichs, H. Lewy, and Others. On the partial difference equations of mathematical physics, 1959. xxxv, 3, 138

P. Courtier and J. F. Geleyn. A global numerical weather prediction model with variable resolution: Application to the shallow-water equations. *Quart. J. Roy. Meteor. Soc*, 114:1321–1346, 1988. 206

M. D. Cox and K. Bryan. A numerical model of the ventilated thermocline. *Journal of Physical Oceanography*, 14(4):674–687, 1984. 3, 96

B. Cushman-Roisin and J.-M. Beckers. *Introduction to Geophysical Fluid Dynamics - Physical and numerics aspects*. Academic Press, 2007. 38, 123

H. C. Davies. A lateral boundary formulation for multi-level prediction models. *Quart. J. Roy. Meteor. Soc*, 102(432):405–418, 1976. 6

L. Debreu, E. Blayo, and B. Barnier. A general adaptive multi-resolution approach to ocean modelling: Experiments in a primitive equation model of the North Atlantic. *Adaptive Mesh Refinement: Theory and Applications*, pages 303–314, 2005. 5

E. Deleersnijder. Upwelling and upsloping in three-dimensional marine models. *Applied Mathematical Modelling*, 13:462–467, 1989. 54, 192

E. Deleersnijder and K. Ruddick. A generalized vertical coordinate for 3D marine problems. *Bull. Soc. R. Sci. Li'ege*, 61:486–502, 1992. 44

É. Delhez and É. Deleersnijder. Overshootings and spurious oscillations caused by biharmonic mixing. *Ocean Modelling*, 17(3):183–198, 2007. 204, 210

D. J. J. Domingos and A. R. Trancoso. Meteo - ist. Internet service, 2005. 175

B. E. Doty, J. Wielgosz, J. Gallagher, and D. Holloway. GrADS and DODS/OPENDAP. *Proceedings of the 17th International Conference on Interactive Information and Processing Systems (IIPS) for Meteorology, Oceanography, and Hydrology, American Meteorological Society Albuquerque, NM*, 385, 2001. 175

Y. Drillet, B. R. Badie, L. Siefridt, and C. Le Provost. Meddies in the Mercator North Atlantic and Mediterranean Sea eddy-resolving model. *Journal of Geophysical Research*, 110(C3), 2005. 175, 176, 179, 190, 193, 194

C. Eden and J. Willebrand. Neutral density revisited. *Deep Sea Research Part II: Topical Studies in Oceanography*, 46(1-2):33–54, 1999. 82

V. W. Ekman. *Om jordrotationens inverkan paa vindstrommar i hafvet*. Centraltryck, 1902. 67

W. J. Emery and J. Meincke. Global water masses: summary and review. *Oceanologica Acta*, 9(4):383–391, 1986. 207

B. Engquist and A. Majda. Absorbing boundary conditions for numerical simulation of waves. *Proceedings of the National Academy of Sciences*, 74 (5):1765, 1977. 6, 9

N. Etopo. Bathymetry. *Product Information Catalogue, see also http://www. ngdc. noaa. gov/mgg/global/seltopo. html*, 1988. xxiv, 178, 183, 184

R. A. Flather. A tidal model of the northwest European continental shelf. *Mem. Soc. R. Sci. Liege*, 10(6):141–164, 1976. 8, 9, 93, 111, 130, 137, 162, 177, 181, 183, 210

C. A. J. Fletcher and K. Srinivas. *Computational Techniques for Fluid Dynamics 1*. Springer, 1991. 176

F. Fraga. Upwelling off the Galician coast, northwest Spain. *Coastal upwelling*, pages 176–182, 1981. 196

C. Garcia-Soto, R. D. Pingree, and L. Valdés. Navidad development in the southern Bay of Biscay: climate change and swoddy structure from remote sensing and in situ measurements. *Journal of Geophysical Research-Oceans*, 107(C8):3118, 2002. 198

R. Gerdes. A primitive equation ocean circulation model using a general vertical coordinate transformation 1. Description and testing of the model. *Journal of Geophysical Research-Oceans*, 98(C8):14683–14701, 1993. 3

A. E. Gill. *Atmosphere-ocean dynamics*. Academic Press New York, 1982. xi, 30, 38, 39, 40, 42, 59, 65, 113, 121, 123, 139, 141, 142, 152, 166

W. G. Gray. On the definition and derivatives of macroscale energy for the description of multiphase systems. *Advances in Water Resources*, 25(8): 1091–1104, 2002. 20

G. A. Grell, J. Dudhia, and D. R. Stauffer. A description of the fifth-generation Penn State/NCAR Mesoscale Model (MM5). NCAR Tech. *Note TN-398+ STR*, 122, 1995. 180

S. M. Griffies. *Fundamentals of ocean climate models*. Princeton University Press Princeton, NJ, 2004. 3, 4

D. B. Haidvogel and A. Beckmann. Numerical ocean circulation modeling. *Series On Environmental Science And Management ; Vol. 2*, 1999. 96

R. Hallberg. A thermobaric instability of lagrangian vertical coordinate ocean models. *Ocean Modelling*, 8(3):279–300, 2005. 81

S. M. Hassanizadeh and W. G. Gray. Mechanics and thermodynamics of multiphase flow in porous media including interphase boundaries. *Adv. Water Resour*, 13(4):169–186, 1990. 20, 30

M. Herzfeld. The role of numerical implementation on open boundary behaviour in limited area ocean models. *Ocean Modelling*, 27(1-2):18–32, 2009. ISSN 14635003. 10, 11, 130, 132, 137, 245

F. Q. Hu. A stable, perfectly matched layer for linearized Euler equations in unsplit physical variables. *Journal of Computational Physics*, 173(2): 455–480, 2001. 7

F. Q. Hu. Development of pml absorbing boundary conditions for computational aeroacoustics: A progress review. *Computers & Fluids*, 37(4): 336–348, May 2008. 7

B. L. Hua and P. Klein. An exact criterion for the stirring properties of nearly two-dimensional turbulence. *Physica D: Nonlinear Phenomena*, 113(1):98–110, 1998. 2, 118

H. E. Huppert and J. S. Turner. Double-diffusive convection. *Journal of Fluid Mechanics Digital Archive*, 106:299–329, 2006. 4

M. C. Iorga and M. S. Lozier. Signatures of the Mediterranean outflow from a North Atlantic climatology 1. Salinity and density fields. *Journal of Geophysical Research*, 104(C11):25985–26010, 1999. 179, 180, 192, 194

J. Isern-Fontanet, J. Font, E. Garc'ia-Ladona, M. Emelianov, C. Millot, and I. Taupier-Letage. Spatial structure of anticyclonic eddies in the Algerian basin (Mediterranean Sea) analyzed using the Okubo–Weiss parameter. *Deep-Sea Research Part II*, 51(25-26):3009–3028, 2004. 2, 167

D. R. Jackett and T. J. Mcdougall. Minimal adjustment of hydrographic profiles to achieve static stability. *Journal of Atmospheric and Oceanic Technology*, 12(2):381–389, 1995. 4, 42, 82

I. D. James. Advection schemes for shelf sea models. *Journal of Marine Systems*, 8(3-4):237–254, 1996. 106, 111

A. D. Jenkins and J. A. T. Bye. Some aspects of the work of VW Ekman. *Polar Record*, 42(01):15–22, 2006. 67

N. G. Jerlov. *Optical oceanography*. Elsevier, 1968. 72, 204

L. H. Kantha and C. A. Clayson. An improved mixed layer model for geophysical applications. *Journal of Geophysical Research-Oceans*, 99(C12): 25235–25266, 1994. 77

L. H. Kantha and C. A. Clayson. *Numerical models of oceans and oceanic processes*. Academic Press, 2000. 82, 126, 133, 136, 137, 138, 173

N. Kliem and J. D. Pietrzak. On the pressure gradient error in sigma coordinate ocean models: A comparison with a laboratory experiment. *Journal of Geophysical Research*, 104(C12):29781–29800, 1999. 176

A. N. Kolmogorov. Equations of turbulent motion of an incompressible fluid. *Izv. Akad. Nauk SSSR, Ser. Fiz*, 6(56-58), 1942. 1

A. N. Kolmogorov. A refinement of previous hypotheses concerning the local structure of turbulence in a viscous incompressible fluid at high Reynolds number. *J. Fluid Mech*, 13(1):82–85, 1962. 1

E. B. Kraus and J. A. Businger. *Atmosphere-ocean interaction*. Oxford University Press, USA, 1994. 204

P. K. Kundu and I. M. Cohen. *Fluid mechanics*. Academic Press San Diego, 2002. xi, 30, 116, 142

G. Lapeyre, B. L. Hua, and P. Klein. Dynamics of the orientation of active and passive scalars in two-dimensional turbulence. *Physics of Fluids*, 13: 251, 2001. 2

W. G. Large, J. C. McWilliams, and S. C. Doney. Oceanic vertical mixing: A review and a model with a vertical K-profile boundary layer parameterization. *Rev. Geophys*, 32(4):363–403, 1994. 77, 204

W. G. Large and S. Pond. Open ocean momentum flux measurements in moderate to strong winds. *Journal of Physical Oceanography*, 11(3):324–336, 1981. 43

J. W. Lavelle and W. C. Thacker. A pretty good sponge: Dealing with open boundaries in limited-area ocean models. *Ocean Modelling*, 20(3): 270–292, 2008. 7, 10, 11, 173, 245

J. J. Leendertse. *Aspects of a Computational Model for Long-period Water-wave Propagation*. Rand Corporation for the United States Air Force Project Rand, 1967. 176

J. J. Leendertse and S. K. Liu. A three-dimensional turbulent energy model for nonhomogeneous estuaries and coastal sea systems. In J. C. J. Nihoul, editor, *Hydrodynamics of estuaries and fjords, Volume 23: Proceedings of the 9th International Liège Colloquium on Ocean Hydrodynamics*, volume 23, pages 387–406. Elsevier Science, 1977. 204

P. Leitão, H. Coelho, A. Santos, and R. Neves. Modelling the main features of the algarve coastal circulation during july 2004: A downscaling approach. *Journal of Atmospheric & Ocean Science*, 10(4):421–462, 2005. 4, 5, 11, 203, 210, 212, 243

P. C. Leitão. *Integração de Escalas e Processos na Modelação do Ambiente Marinho*. PhD thesis, Technical University of Lisbon, 2003a. 203

P. C. Leitão. *Integration of Scales and Processes in the marine Environment Modelling*. PhD thesis, Technical Superior Institute, Lisbon, 2003b. 127, 180, 183

B. P. Leonard. A stable and accurate convective modelling procedure based on quadratic upstream interpolation. *Appl. Eng*, 19(1):59–98, January-SeptemberJulySeptember/June 1979. 204

B. P. Leonard. The ULTIMATE conservative difference scheme applied to unsteady one-dimensional advection. *Computer methods in applied mechanics and engineering*, 88(1):17–74, 1991. 204

E. N. Lorenz. Available potential energy and the maintenance of the general circulation. *Tellus*, 7(2):157–167, 1955. 90

F. Lyard, F. Lefevre, T. Letellier, and O. Francis. Modelling the global ocean tides: modern insights from fes2004. *Ocean Dynamics*, 56(5-6):394–415, December 2006. ISSN 1616-7341. 175, 180, 183, 207

P. Lynch and X. Y. Huang. Initialization of the hirlam model using a digital filter. *Monthly Weather Review*, 120(6):1019–1034, June 1992. 187

M. Malhadas, R. Neves, P. Leitão, and A. Silva. Influence of tide and waves on water renewal in Óbidos lagoon, portugal. *Ocean Dynamics*, 60(1): 41–55, February 2010. 5

M. S. Malhadas, P. C. Leitão, and R. Neves. Effect of the bathymetric changes on the hydrodynamics and residence time of the Óbidos lagoon (portugal). *Journal of Coastal Research*, SI56:549–553, 2009a. 5

M. S. Malhadas, P. C. Leitão, A. Silva, and R. Neves. Effect of coastal waves on sea level in Óbidos lagoon, portugal. *Continental Shelf Research*, February 2009b. ISSN 02784343. 5

P. Marchesiello, J. C. McWilliams, and A. Shchepetkin. Open boundary conditions for long-term integration of regional oceanic models. *Ocean Modelling*, 3(1):20, 2001. 7, 8, 207

V. Mariette and B. Le Cann. Simulation of the formation of Ushant thermal front. *Continental Shelf Research*, 4:637–660, 1985. 199

V. H. Marin and F. J. Campuzano. Un modelo hidrodinamico-barotropico para los fiordos australes de chile entre los 41 s y los 46 s. *Revista Ciencia y Tecnologia del Mar*, 31:1, 2008. 5

P. Marsaleix, C. Ulses, I. Pairaud, M. J. Herrmann, J. W. Floor, C. Estournel, and F. Auclair. Open boundary conditions for internal gravity wave modelling using polarization relations. *Ocean Modelling*, 29(1):27–42, 2009. ISSN 14635003. 9, 10, 11, 130

F. Martins, R. J. J. Neves, and P. C. Leitão. A three-dimensional hydrodynamic model with generic vertical coordinate. *Hydroinformatics*, 98: 1403–1410, 1998. 17, 30, 96, 176, 203

H. Martins, A. Santos, Coelho, R. Neves, and T. Rosa. Numerical simulation of internal tides. *Proceedings of the Institution of Mechanical Engineers, Part C: Journal of Mechanical Engineering Science*, 214(6):867–872, 2000. 176

E. A. Martinsen and H. Engedahl. Implementation and testing of a lateral boundary scheme as an open boundary condition in a barotropic ocean model. *Coastal engineering*, 11(5-6):603–627, 1987. 6, 7, 93, 173, 177, 182, 184, 210

M. Mateus and R. Neves. Evaluating light and nutrient limitation in the tagus estuary using a process-oriented ecological model. *Journal of Marine Engineering and Technology*, 2008. 4

T. J. Mcdougall and R. Feistel. What causes the adiabatic lapse rate? *Deep Sea Research Part I: Oceanographic Research Papers*, 50(12):1523–1535, 2003. 82

T. J. Mcdougall, D. R. Jackett, D. G. Wright, and R. Feistel. Accurate and computationally efficient algorithms for potential temperature and density of seawater. *Journal of Atmospheric and Oceanic Technology*, 20 (5):730–741, 2003. 4, 82

G. Mellor. *User's guide for a three-dimensional, primitive equation, numerical ocean model*. Princeton University, 1992. 87

G. L. Mellor. *Introduction to physical oceanography*. AIP Press, 1996. ISBN 156396210. 81

G. L. Mellor and T. Yamada. Development of a turbulence closure model for geophysical fluid problems. *Reviews of Geophysics*, 20(4):851–875, 1982. ISSN 8755-1209. 67

F. Millero, R. Feistel, D. Wright, and T. McDougall. The composition of standard seawater and the definition of the reference-composition salinity scale. *Deep Sea Research Part I: Oceanographic Research Papers*, 55(1): 50–72, January 2008. ISSN 09670637. 42, 74, 80

F. J. Millero and A. Poisson. International one-atmosphere equation of state of seawater. *Deep-Sea Res*, 28:625–629, 1981. 42, 74, 80, 176

R. Miranda, R. Neves, H. Coelho, H. Martins, P. Leitão, and A. Santos. Transport and mixing simulation along the continental shelf edge using a lagrangian approach. *Bol. Inst. Esp. Oceanogr*, 15(1-4):39–60, 1999. 4

W. Munk and C. Wunsch. Abyssal recipes II: energetics of tidal and wind mixing. *Deep-Sea Research Part I*, 45(12):1977–2010, 1998. 198

J. Nycander and K. Doos. Open boundary conditions for barotropic waves. *J. Geophys. Res*, 108(10.1029), 2003. 7, 8, 9

A. Okubo. Horizontal dispersion of floatable particles in the vicinity of velocity singularities such as convergences. *Deep Sea Research and Oceanographic Abstracts*, 17(3):445–454, 1970. 2, 243

I. Orlanski. A simple boundary condition for unbounded hyperbolic flows. *Journal of Computational Physics*, 21:251–269, 1976. 8, 173

I. L. Pairaud, F. Lyard, F. Auclair, T. Letellier, and P. Marsaleix. Dynamics of the semi-diurnal and quarter-diurnal internal tides in the Bay of Biscay. Part 1: Barotropic tides. *Continental Shelf Research*, 2008. 207

E. D. Palma and R. P. Matano. On the implementation of passive open boundary conditions for the Princeton Ocean Model: The barotropic mode. *J. Geophys. Res*, 103:1319–1341, 1998. 7, 8, 207

E. D. Palma and R. P. Matano. Dynamical impacts associated with radiation boundary conditions. *Journal of Sea Research*, 46(2):117–132, 2001. 207, 212

M. P. Papadakis, E. P. Chassignet, and R. W. Hallberg. Numerical simulations of the mediterranean sea outflow: impact of the entrainment parameterization in an isopycnic coordinate ocean model. *Ocean Modelling*, 5(4):325–356, 2003. 190, 193

J. Pedlosky. The spin up of a stratified fluid. *J. Fluid Mech*, 28:463–479, 1967. 90, 110

J. Pedlosky. Axially symmetric motion of a stratified rotating fluid in a spherical annulus of a narrow gap. *J. Fluid Mech*, 36(part 2):401–15, 1969. 90, 111

J. Pedlosky. *Geophysical fluid dynamics*. Springer, 1987. 129

T. Pichevin and D. Nof. The eddy canon. *Deep-Sea Res*, 43(9):1475–1507, 1996. 179

J. Pietrzak, J. B. Jakobson, H. Burchard, H. J. Vested, and O. Petersen. A three-dimensional hydrostatic model for coastal and ocean modelling using a generalised topography following co-ordinate system. *Ocean Modelling*, 4(2):173–205, 2002. 41, 127, 173, 180, 182

R. D. Pingree. The eastern Subtropical Gyre(North Atlantic): Flow rings recirculations structure and subduction. *Journal of the Marine Biological Association of the United Kingdom*, 77(3):573–624, 1997. 196

R. T. Pollard, M. J. Griffttths, S. A. Cunningham, J. F. Read, F. F. Perez, and A. F. Rios. Vivaldi 1991-A study of the formation, circulation and ventilation of Eastern North Atlantic Central Water. *Progress in Oceanography*, 37(2):167–192, 1996. 195, 196

L. Prandtl. On the Role of Turbulence in Technical Hydrodynamics. In *Proceedings of the World Engineering Congress, Tokyo,[bold 6]*, pages 495–507, 1931. 1

I. Puillat, P. Lazure, A. M. Jégou, L. Lampert, and P. I. Miller. Hydrographical variability on the French continental shelf in the Bay of Biscay, during the 1990s. *Continental shelf research*, 24(10):1143–1163, 2004. 199

T. Reynaud, P. Legrand, H. Mercier, and B. Barnier. A new analysis of hydrographic data in the Atlantic and its application to an inverse modelling study. *International WOCE Newsletter*, 32:29–31, 1998. 179

O. Reynolds. On the dynamical theory of incompressible viscous fluids and the determination of the criterion. *Philosophical Transactions of the Royal Society of London. A*, pages 123–164, 1895. 1

G. Riflet, M. Juliano, L. Fernandes, P. C. Leitão, and R. Neves. Operational ocean forecasting of the portuguese waters. *Mercator Quarterly Newsletter*, 30, July 2008. 243, 245

G. Riflet, P. C. Leitão, R. Fernandes, and R. Neves. Assessing the quality of a pre-operational model for the portuguese coast. In *European Geosciences Union 2007*, number 09979 in 1607-7962/gra/EGU2007-A-09979, April 2007a. 11, 245

G. Riflet, P. C. Leitão, R. Fernandes, and R. J. J. Neves. A simple pre-operational model for the portuguese coast. In *CMNE/CILAMCE 2007 porto, 13 a 15 de Junho*. FEUP, June 2007b. 203, 243, 245

A. F. Rios, F. F. Pérez, and F. Fraga. Water masses in the upper and middle North Atlantic Ocean east of the Azores. *Deep-Sea Res*, 39(3/4):645–658, 1992. 195

A. Robinson. *Non-standard analysis*. Princeton University Press, revised edition, 1974. ISBN 0691044902, 9780691044903. 13, 26, 120

L. P. Roed and C. K. Cooper. A study of various open boundary conditions for wind-forced barotropic numerical ocean models. *Elsevier oceanography series*, 45:305–335, 1987. 9

B. C. Roisin. *Introduction to geophysical fluid dynamics*. Prentice Hall Englewood Cliffs, NJ, 1994. 68, 77, 80, 91

S. Saraiva, P. Pina, F. Martins, M. Santos, F. Braunschweig, and R. Neves. Modelling the influence of nutrient loads on portuguese estuaries. *Hydrobiologia*, 587(1):5–18, 2007. 4

A. J. Semtner. An oceanic general circulation model with bottom topography. *Numerical Simulation of Weather and Climate, Technical Report*, 9, 1974. 96

A. Shchepetkin and J. McWilliams. The regional oceanic modeling system (roms): a split-explicit, free-surface, topography-following-coordinate oceanic model. *Ocean Modelling*, 9(4):347–404, 2005. ISSN 14635003. 4

A. F. Shchepetkin. A method for computing horizontal pressure-gradient force in an oceanic model with a nonaligned vertical coordinate. *J. Geophys. Res*, 108(C3):3090, 2003. 173, 176

A. Sommerfeld. *Partial Differential Equations in Physics: lecture on theoretical physics*. Academic Pr, 1949. 6, 7

D. P. Stevens. On open boundary conditions for three dimensional primitive equation ocean circulation models. *Geophysical and astrophysical fluid dynamics*, 51(1-4):103–133, 1990. 184

I. Stevens, M. Hamann, J. A. Johnson, and A. F. G. Fiúza. Comparisons between a fine resolution model and observations in the iberian shelf-slope region. *Journal of Marine Systems*, 26(1):53–74, 2000. 190

C. K. W. Tam, L. Auriault, and F. Cambuli. Perfectly matched layer as an absorbing boundary condition for the linearized Euler equations in open and ducted domains. *Journal of Computational Physics*, 144(1):213–234, 1998. 7

B. Tartinville, E. Deleersnijder, P. Lazure, R. Proctor, K. G. Ruddick, and R. E. Uittenbogaard. A coastal ocean model intercomparison study for a three-dimensional idealised test case. *Applied Mathematical Modelling*, 22 (3):165–182, JanuarySeptemberSeptemberAugust/March 1998. xx, xxix, 10, 88, 90, 91, 93, 95, 96, 99, 106, 107, 109, 110, 111, 112, 244

A. Trancoso, S. Saraiva, L. Fernandes, P. Pina, P. Leitão, and R. Neves. Modelling macroalgae using a 3 d hydrodynamic-ecological model in a shallow, temperate estuary. *Ecological Modelling*, 187(2):232–246, 2005. 4

A. M. Treguier, B. Barnier, A. P. de Miranda, J. M. Molines, N. Grima, M. Imbard, G. Madec, C. Messager, T. Reynaud, and S. Michel. An eddy-permitting model of the Atlantic circulation: Evaluating open boundary conditions. *Journal of Geophysical Research-Oceans*, 106(C10), 2001. 8

L. Umlauf and H. Burchard. Second-order turbulence closure models for geophysical boundary layers. A review of recent work. *Continental Shelf Research*, 25:725–827, 2005. 67, 176

H. M. Van Aken and G. Becker. Hydrography and through-flow in the north-eastern North Atlantic Ocean: the NANSEN project. *Progress in Oceanography*, 38(4):297–346, 1996. 195

N. Vaz, J. M. Dias, P. Leitão, and I. Martins. Horizontal patterns of water temperature and salinity in an estuarine tidal channel: Ria de Aveiro. *Ocean Dynamics*, 55(5):416–429, 2005. 5

N. Vaz, J. Miguel Dias, and P. Chambel Leitão. Three-dimensional modelling of a tidal channel: The Espinheiro Channel (Portugal). *Continental Shelf Research*, 29(1):29–41, 2009. 5

N. Vaz, J. Miguel Dias, P. Chambel Leitão, and R. Nolasco. Application of the Mohid-2D model to a mesotidal temperate coastal lagoon. *Computers and Geosciences*, 33(9):1204–1209, 2007. 5

M. R. Villarreal. *Parameterization of turbulence in the ocean and application of a 3d baroclinic model to the ria de pontevedra*. PhD thesis, Universidade de Santiago de Compostela, 2000. 67

J. Weiss. The dynamics of enstrophy transfer in two-dimensional hydrodynamics. *Physica D Nonlinear Phenomena*, 48:273–294, March 1991. 2, 115, 117, 171, 243

C. Wunsch and R. Ferrari. Vertical mixing, energy, and the general circulation of the oceans. *Annual Review of Fluid Mechanics*, 36:281–314, 2004. 198

L. Zavala Sanson and J. Sheinbaum. Elementary properties of the enstrophy and strain fields in confined two-dimensional flows. *European Journal of Mechanics/B Fluids*, 27(1):54–61, 2008. 2

V. A. Zorich. *Mathematical Analysis II (Universitext)*. Springer, 1 edition, January 2004. ISBN 3540406336. 16, 18

Appendix A

Topics on geometry

A.1 The divergence theorem

A.1.1 Defining the problem

Often in physics, one wishes to calculate the flux of some vectorial quantity flowing through a given cross-section. Such local monitoring provides more insight on the wider area beyond the cross-section. Furthermore, many times, it is required to calculate the flux through a closed surface. Of this necessity derives the famous divergence theorem.

A.1.2 Defining the geometry

Consider $\mathbb{R}^3$, an origin O and a cartesian reference frame composed by the unit vectors $\mathbf{i}$, $\mathbf{j}$, $\mathbf{k}$ which yield in cannonical coordinates (1, 0, 0), (0, 1, 0), and (0, 0, 1).

Consider a vector-field of $\mathbb{R}^3$, $\mathbf{E} = (E_i, E_j, E_k)$.

Consider Ω, a connex open subset of $\mathbb{R}^3$.

Consider $\Delta\Omega$, an element of volume of Ω, whose shape is defined by the edges $\vec{\Delta} \equiv (\Delta x\,\mathbf{i}, \Delta y\,\mathbf{j}, \Delta z\,\mathbf{k})$, whose volume is given by $\Delta\Omega = \Delta x\,\Delta y\,\Delta z$ and whose position P yields coordinates (P_a, P_b, P_c) fixed at its volumic center.

Let the orientation of $\Delta\Omega$ be given by its faces outwards unit vectors $\mathbf{n}_{jk} = -\mathbf{n}_{kj} = (1, 0, 0)$, $\mathbf{n}_{ik} = -\mathbf{n}_{ki} = (0, 1, 0)$, $\mathbf{n}_{ij} = -\mathbf{n}_{ji} = (1, 0, 0)$.

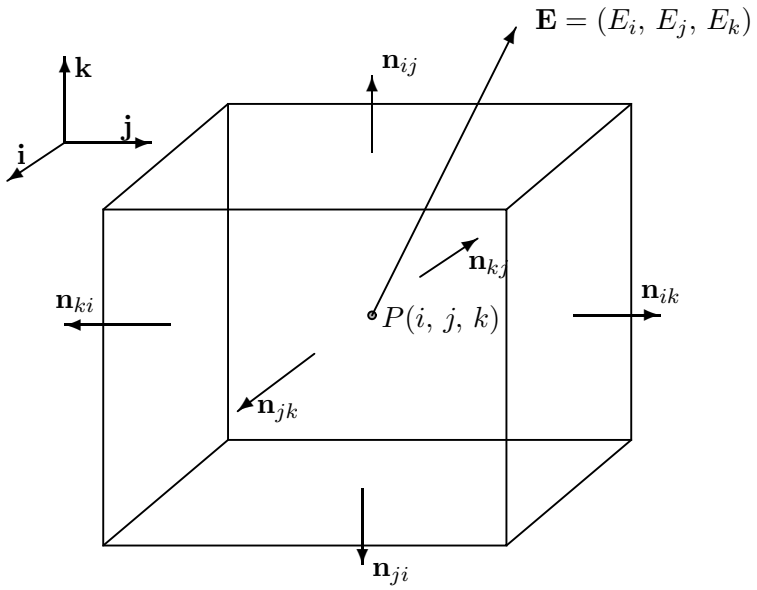

Figure A.1: Cartesian element of volume $\Delta\Omega$ of width, length and height of Δx, Δy and Δz, respectively. The local uniform vector field $\mathbf{E}$ is represented in the volume's center of coordinates $P = (P_i,\, P_j,\, P_k)$.

A.1.3 Calculating the flux of E through one elemental volume

The flux ϕ of $\mathbf{E}$ through the surface of $\Delta\Omega$ can be calculated in the coordinates of the cartesian reference frame. It consists of the sum of the flux through each of the six faces of $\Delta\Omega$, whose geometric centre is given by P_{ij}, and its value is given in equation A.1.

$$\phi = \sum_{i \neq j} \mathbf{E} \cdot \mathbf{n}_{ij}\ \Delta x_i\, \Delta x_j. \tag{A.1}$$

Working out equation A.1, yields:

$$\begin{aligned}
\phi &= \sum_{i \neq j} \mathbf{E}|_{Pij} \cdot \mathbf{n}_{ij}\, \Delta x_i\, \Delta x_j, \\
&= \sum_{i<j,\, i \neq k,\, j \neq k} \left(E_k|_{P_{k+1/2}} - E_k|_{P_{k-1/2}} \right) \Delta x_i\, \Delta x_j, \\
&= \sum_{i<j,\, i \neq k,\, j \neq k} \frac{\left(E_k|_{P_{k+1/2}} - E_k|_{P_{k-1/2}} \right)}{\Delta x_k} \Delta x_i\, \Delta x_j\, \Delta x_k, \qquad \text{(A.2)}
\end{aligned}$$

where P_{ij} is the centred point in $\mathbf{n}_{ij}$'s face, of coordinates defined in equation A.3.

$$\begin{aligned}
P_{ij} &\equiv P + \frac{\vec{\Delta} \cdot \mathbf{n}_{ij}}{2}, \\
&= (P_i,\, P_j,\, P_k) + (0,\, 0,\, \Delta z/2), \\
&= (i\, \Delta x,\, j\, \Delta y,\, k\, \Delta z) + (0,\, 0,\, \Delta z/2), \\
&= (i\, \Delta x,\, j\, \Delta y,\, (k + 1/2)\, \Delta z)\,, \\
&\equiv \left(P_i,\, P_j,\, P_{k+1/2}\right). \qquad \text{(A.3)}
\end{aligned}$$

But of course, what's the point of calculating equation A.1? Well the flux happens to solve a very interesting problem in physics. Given a fluid and given a cross-section through which the fluid flows, the problem lies in determining how much of fluid is flowing through that cross-section. Or, stating it differently, how much volume of water is flowing through the cross-section per unit of time? One can experimentate easily at home, and realize that the volume of fluid that flows through the cross-section per unit of time varies accordingly with the angle that the cross-section makes with the direction of the flow. If the fluid flows perpendicular to the cross-section's plane, then the volume of water is maximum. If the fluid flows tangentially to the cross-section's plane, then the water flows by the cross-section, but not through, thus yielding a null flow, or null volume of water per unit of time. Also, if one intensifies the velocity of the flow, then the volume of water that flows through the cross-section per unit of time also intensifies. And if one diminishes the velocity of the flow, then the volume per unit of time decreases accordingly. Finally, if the cross-section area is increased, then the volume of water that flows per unit of time increases. And if the area is decreased, the volume of water that flows per unit of time decreases. These simple experiments allow the amateur-physicist to speculate that the volume of

fluid ($\left[m^3\right]$) that flows through the cross-section per unit of time ($\left[m^3/s\right]$), depends on the velocity of the flow ($[m/s]$), on the area of cross-section ($\left[m^2\right]$) and on the angle of the flow direction with the cross-section plane (represented by the internal product of the fluid velocity vector-field with the normal vector to the cross-section's plane, $\mathbf{v} \cdot \mathbf{n}$). Thus, our intuition, built from the experimentations, allows to put forward the relation proposed in equation A.4.

$$\begin{aligned}[\text{Flow}] = a\,[\text{Velocity modulus}]^m * b\,[\text{Area}]^n \\ *c\,[\text{Velocity/Cross-section Angle}]^p\,.\end{aligned} \tag{A.4}$$

The dimensional counterpart of equation A.4 is equation A.5.

$$\left[m^3\,s^{-1}\right] = \left[m\,s^{-1}\right]^m * \left[m^2\right]^n\,. \tag{A.5}$$

There's a basic general guideline, in determining Nature's principles, that states that between two plausible laws of Nature regulating the same phenomena, often the simpler and more elegant is correct. Thus, from all the valid combinations of $(m,\, n,\, p)$ in equations A.4 and A.5, $(1,\, 1,\, 1)$ is the most likely hypothesis. By resorting to experimentations, one tries to falsify the hypothesis. However one soon realizes that, in this case, the hypothesis stands unfalsified, and is, thus, proposed as a law of Nature. Note however that $(m,\, n) = (1,\, 1)$ was the only valid hypothesis for the powers of quantities of equation A.5. Next, the dimensionless coefficients $(a,\, b,\, c)$ must be determined. Again, one must experiment. Experimentations, so far, have shown that equation A.4 holds when $(a,\, b,\, c) = (1,\, 1,\, 1)$. Hence, a way to compute the volume of water that flows through the cross-section, per unit of time, shown in equation A.6, has been scientifically determined. It requires the knowledge of the fluid velocity, the cross-section area and the angle between the flow direction and the cross-section.

Definition 4. *The flux of a vector-field through an element of area is linearly proportial to the area of the element, the intensity of the vector-field, and the angle between the vector-field direction and the element's plane.*

$$\Phi = A\,\mathbf{v} \cdot \mathbf{n}. \tag{A.6}$$

Definition 4 was used to calculate equation A.1, that yields the flux of a vector-field, similar to a fluid velocity vector-field, through the six faces of a cube. By conventioning that ingoing flux is negative and that outgoing flux

is positive, then, if the sum of all the fluxes in equation A.1 yields positive, then there is more flow outgoing from the box than ingoing. This means that there must be some source of flow inside the box. If it yields negative, then there is more flow ingoing than outgoing, and this means that a sink term of flow must lie inside the box. If the net flux yields null, then either the source and sink terms balance each other, either there are no source and sink terms inside the box. The net flux, as described herein, is also known as the divergence of the vector-field.

A.1.4 Summing the infinitesimal elements of the open set

Now consider a unit partition of Ω into elements of volume $\Delta\Omega$, such that $\Omega = \bigcup_a \Delta\Omega_a$. In particular, consider a cartesian partition where each $\Delta\Omega = \Delta x\,\Delta y\,\Delta z$. Finally, consider the surface of $\Delta\Omega$ that belongs to the open boundary condition.

Proposition 1. *The sum of the fluxes on the faces of all the elements of volume of Ω, is equal to the sum of the fluxes on all the faces of the boundary of Ω, $\partial\Omega$.*

$$\sum_{\Delta\Omega\,\in\,\Omega} \phi = \sum_{\Delta\partial\Omega\,\in\,\partial\Omega} \phi. \tag{A.7}$$

Proof. The geometry of the problem is such that, $\forall_{\Delta\Omega\,\in\,\Omega}$, each face ij of element volume $\Delta\Omega$ not on the open boundary of Ω, $\partial\Omega$, is shared with one, and only one, other element volume $\Delta\Omega'$, and their normal vectors to the face are symmetric. Thus, the fluxes of the vector-field through the face, for both volumes, are equal, because they are evaluated at the same point; and of opposite signs, because the normal vectors are symmetric. Hence, when summed, they zero out. Hence, if we sum all the fluxes of all the elemental volumes $\Delta\Omega$ of the open set Ω, all the faces fluxes will zero out, except those on $\partial\Omega$. □

Theorem 1. *The divergence theorem states that the flow of a vector-field over the boundary of a volume, is equal to its divergence integrated over the volume.*

$$\oint_{\partial\Omega} \mathbf{E}\cdot\mathbf{n}\; d\,(\partial\Omega) = \int_{\Omega} \nabla\cdot\mathbf{E}\; d\Omega. \tag{A.8}$$

Proof. By inserting equation A.1 into the right-hand side of equation A.7 and equation A.2 into the left-hand side of equation A.7, equation A.9 is obtained.

$$\sum_{\Delta\Omega/\Delta x \,\in\, \partial\Omega} \sum_{i\neq j} \mathbf{E}\cdot\mathbf{n}_{ij}\;\Delta x_i\,\Delta x_j = \tag{A.9}$$

$$\sum_{\Delta\Omega\,\in\,\Omega}\;\sum_{i<j,\,i\neq k,\,j\neq k} \frac{\left(E_k|_{P_{k+1/2}} - E_k|_{P_{k-1/2}}\right)}{\Delta x_k}\;\Delta x_i\,\Delta x_j\,\Delta x_k. \tag{A.10}$$

Then, by taking the limit when $\vec{\Delta} \to 0$, equation A.11 is obtained.

$$\begin{aligned}
\lim_{\vec{\Delta}\to 0} \sum_{\Delta\partial\Omega\,\in\,\partial\Omega} \sum_{i\neq j} \mathbf{E}\cdot\mathbf{n}_{ij}\;\frac{\Delta\Omega}{x_k} &= \lim_{\vec{\Delta}\to 0} \sum_{\Delta\Omega\,\in\,\Omega} \sum_{k} \lim_{\Delta x_k\to 0} \\
&\qquad \frac{\left(E_k|_{P_{k+1/2}} - E_k|_{P_{k-1/2}}\right)}{\Delta x_k}\;\Delta\Omega, \\
\lim_{\vec{\Delta}\to 0} \sum_{\Delta\partial\Omega\,\in\,\partial\Omega} \sum_{i\neq j} \mathbf{E}\cdot\mathbf{n}_{ij}\;\frac{\Delta\Omega}{x_k} &= \lim_{\vec{\Delta}\to 0} \sum_{\Delta\Omega\,\in\,\Omega} \sum_{k} \frac{\partial E_k}{\partial x_k}\;\Delta\Omega, \\
\lim_{\vec{\Delta}\to 0} \sum_{\Delta\partial\Omega\,\in\,\partial\Omega} \sum_{i\neq j} \mathbf{E}\cdot\mathbf{n}_{ij}\;\frac{\Delta\Omega}{x_k} &= \lim_{\vec{\Delta}\to 0} \sum_{\Delta\Omega\,\in\,\Omega} \nabla\cdot\mathbf{E}\;\Delta\Omega.
\end{aligned} \tag{A.11}$$

Finally, let the limit, when the volume element tends to zero, of the finite sum, over all volume elements, of a real function, be defined, in equation A.12, as the integral.

$$\lim_{\vec{\Delta}\to 0} \sum_{\Delta\Omega\,\in\,\Omega} \phi\;\Delta\Omega \equiv \int_{\Omega} \phi\; d\Omega. \tag{A.12}$$

By applying equation A.12 to equation A.11, the single most important result of continuum mechanics, the divergence theorem, is yielded and proved. □

It must be noted, however, that this proof is only partial, as it considers only cartesian coordinates and cartesian elementary control volumes. A full proof would cope with a generic geometry. Typical complete proofs of theorem 1 depart from the integral notation and make use of the *Fundamental Theorem of Calculus*. This proof uses it indirectly, and partially proves it as well. Furthermore, the integral definition we provide in equation A.12 is easily shown to be consistent with the Riemann integral. The more complete Lebesgue integral definition, however, requires the introduction of a measure for the open set Ω.

A.1.5 Summing up

In the equation A.11, we define the divergence notation of $\mathbf{E}$ as $\nabla \cdot \mathbf{E}$. Equation A.11 proves that the divergence represents the net balance of all the fluxes ingoing and outgoing through the open-boundary of the volume element and is, therefore, a useful indicator if there are sinks or source terms within the volume element. The interest of the proof provided for theorem 1, besides the fact that it doesn't resorts to the *Fundamental Theorem of Calculus*, is that it is particularly suited for solving numerical problems by resorting to a numerical cartesian discretization of the medium. This yields direct consequences in the fields of Contiuunm Mechanics as it shows a sound way to derive consistent numerical schemes that can be applied to solve engineering problems in fluid flow and heat and mass transfer.

Index

Adiabatic lapse rate, 82
Advection, 138
Advection-diffusion equation, 33
Arakawa
    B grid, 128
    C grid, 128
    C-grid, 120
Archimedes
    Principle, 82

Bottom stress, 43, 127
Boundary condition, 120, 129
    Absorbing, 9
    Active, 130
    Clamped, 6
    Dirichelet, 6, 129
    Flather, 8
    FRS, 6
    No-slip, 129
    Null-flux, 42, 129
    Null-gradient, 137
    NVIE, 132
    NVOE, 130
    Open, 130, 181
    Orlansky, 8
    Passive, 130
    PML, 7
    PRM, 9
    Radiation, 7
    Radiative, 130
    Relaxation, 6
    Sommerfeld, 7
Boussinesq approximation, 38, 41
Brunt-Vaisalla frequency, 65
Buoyancy, 41, 77

Cells
    T type, 120, 128
    U type, 120, 128
    V type, 128
CFL criterion, 138
Continuity equation, 33, 41
    Extended, 37
Coriolis acceleration, 41, 128
Coriolis frequency, 127
Cross-section, 266
Curl theorem, 14

Diffeomorphism, 18
Diffusion
    Numerical, 152
Divergence theorem, 14, 263, 267
Drag coefficient
    Air, 127
    Bottom, 127

Eddy, 90
Einstein notation, 45
Ekman
    Depth, 68
    Layer, 68
    Spiral, 67
Energy, 54, 141
    Available potential, 90, 141
    Internal, 60

Kinetic, 58, 141
Perturbation potential, 141
Potential, 58
Specific internal, 60
Specific kinetic, 57
Specific potential, 58
Specific total, 61
Total, 58, 141
Enstrophy, 110
Entropy
Specific, 59
Equation of state, 42, 77
Euler
Equations, 113

Fick's law, 68
Field
Vectorial, 263
Finite differences, 119, 133
Flow
Elliptic, 117
Hyperbolic, 117
Mono-phasic, 36
Multi-phasic, 36
Flux, 263, 264, 266
Force
Baroclinic, 122
Barotropic, 120, 122
Fourier's law, 60
Freshwater cylinder experiment, 88
Froude number, 91, 142
Fundamental theorem of calculus, 14, 268

Gauss-Ostrogradsky theorem, *see* Divergence theorem
Gaussian curvature, 117
Gaussian curve, 139
Geostrophic balance, 165
GOTM, 66
Gradient theorem, 15
Gravity constant
Local, 59
Reduced, 91

Half-life, 156
Haline contraction coefficient, 82
Heat flux, 74
Hodge star opeartor, 15
Hooke's law, 83
Hydrostatic approximation, 41, 121
Hydrostatic pressure, 57, 121

Initial condition, 120, 136
Instability
Baroclinic, 90
Barotropic, 90

Kelvin-Stokes theorem, *see* Curl theorem

Lagrangean particle, 116
Lagrangian derivative, 30
Extended, 29
Land mask, 129
Leibniz integral rule, 35
Leibniz integration rule, 15
Length
Roughness, 127
Loss of significance, 152

Material derivative, 27
Extended, 29
Material particle, 31
Mesh, 119, 128
Non-regular, 119
Mixed layer, 65
Mixing
Vertical, 65
Molecular conduction, 59
Musical isomorphisms, 15

Navier-Stokes equations, 20
Newton's second law of motion, 39
Numerical
    Péclet number, 158
    Reynolds number, 158
Numerical error, 151
Numerical instability, 138
Numerical schemes
    CTCS, 133
    Leapfrog, 136
    TVD, 93
    Upwind, 110

Partial differential equation, 119
Pressure
    Correction, 77
    Gradient error, 93
Pressure-gradient error, 152
Primitive ocean equations, 41

Radiative exchange, 59
Reynold's transport theorem, 16
    Extended, 18
Reynolds decomposition, 61
Robert-Asselin filter, 136
Rossby
    Internal radius of deformation, 90
    Potential vorticity, 115
Rotation tensor, 116

Seawater density, *see* Equation of state
Shallow waters equations, 120, 126
Shear strain rate tensor, 116
Specific heat
    Constant pressure, 59
Specific volume, 32
Sponge layer, 7
Stratification, 65
Surface boundary, 42

Temperature
    Potential, 59
    Potential, 82
Thermal conductivity, 59
Thermal expansion coefficient, 82
Thermocline, 65
Thermodynamics
    First law, 59
Thermohaline circulation, 66
Transformation of vertical coordinates, 44

Unit partition, 267

Velocity
    Curl, 114
Vertical coordinates, 44
    Cartesian, 44
    Generalized, 44, 96
    Lagrangean, 93, 96
    Sigma, 44, 96
Viscosity
    Molecular, 62
Volume, 265
    Control, 17
    Specific, 26
von Karman constant, 44, 127
Vortex, 116
Vortice, 90

Wind
    Stress, 127
Wind stress, 43